A Theoretical Investigation of Structural, Electronic and Optical Properties of some Group 10, 11 and 12 Transition-Metal Nitrides

by

Mohammed Suleiman Hussein Suleiman

Mohammed.Suleiman@students.wits.ac.za

مُحَمَّد سُلَيْمَان حُسَيْن سُلَيْمَان

Supervisor

Professor Daniel P. Joubert

daniel.joubert2@wits.ac.za

A thesis submitted for the degree of Doctor of Philosophy (PhD) at the

School of Physics

University of the Witwatersrand

Johannesburg

October 2013

To my late father, my late brother and my late son.

Declaration

I, the undersigned, hereby declare that this dissertation is submitted for the degree of Doctor of Philosophy (PhD) at the School of Physics, University of Witwatersrand. It contains an account of the research carried out between April 2009 and October 2013, under the supervision of Prof. Daniel P. Joubert. The work contained in this thesis and in References [1–7] of the Bibliography are my original works. Any work done in collaboration with or by others or by myself previously has been acknowledged and/or referenced accordingly. No part of this dissertation has been or is currently being submitted for any degree or diploma at this, or any other, University.

Mohammed Suleiman Hussein Suleiman

Student No. 402072

October 2013

Johannesburg

Abstract

Nitrides of late transition metals possess interesting properties leading to different technological applications, yet, due to many factors, synthesis and reliable characterization of the physical properties of these materials constitute a big challenge. In this work, we present a detailed first-principles investigation of the structural, the electronic and the optical properties of the bulk crystalline MN_x (where M = Pd, Pt, Cu, Ag or Au; and $x = 1/3, 1$ or 2) and ZnN.

The studied structural properties include energy-volume equation of state (EOS), equilibrium lattice structural parameters, cohesive and formation energies, relative phase stabilities, bulk modulus and its pressure derivative. By means of the enthalpy-pressure EOS, some possible pressure-induced structural phase transitions are carefully examined. Electronic properties of the energetically most stable phases are investigated via the analysis of their band structure and their total and partial densities of states (DOSs). The frequency-dependent optical constants (absorption coefficient, reflectivity, refractive index, and energy-loss spectrum) of some phases are derived from the calculated frequency-dependent microscopic dielectric tensor.

Our calculations of the structural and the electronic properties are based on density functional theory (DFT) within the projector-augmented wave (PAW) formulation and the generalised-gradient approximation (GGA) to the exchange-correlation functional. In order to improve the calculated electronic structure, and to investigate the optical spectra, we carry out expensive GW0 calculations within the the random-phase approximation (RPA) to the dielectric tensor.

Obtained results are discussed within the employed theoretical methods of calculations. Whenever possible, our obtained results are compared with experiment and with previous theoretical studies. We report the discovery of some possible low-energy competitive phases which are more stable at zero pressure than the synthesized and than other hypothetical structural phases. To the best of our knowledge, our calculated optical spectra may be considered as the first, and thus, the most accurate, calculations within the many-body perturbation GWA calculations, so far.

Contents

1. Introduction

1.1 Motivations

1.1.1 Ab initio Methods and Materials Design and Modeling

There are many reasons for why we need to employ *ab initio* methods:

1. *Ab initio* calculations can be employed to predict the properties of materials when experiments are very difficult to establish (e.g. due to poor stability of the material under consideration) [8].

2. *Ab initio* calculations are used for understanding of the properties of materials [9] and mechanism of different reactions [8] at a fundamental level.

3. *Ab initio* calculations are used for designing new materials for different possible potential applications.

4. Different *Ab initio* methods themselves need to be justified and tested against experiment [8].

5. Compared to experiment, first-principles calculations are cheap and quick when no direct experimental data are available. [10].

And much more.

1.1.2 Late Transition-Metal Nitrides (TMNs)

Because of their unique unusual combination of physical and chemical properties, transition-metal nitrides continue to be a subject of growing interest. They posses outstanding mechanical (e.g. high hardness and good corrosion resistance), thermal (e.g. high melting points and good thermal conductivity), optical, electrical (e.g. good electrical conductivity) and magnetic properties and chemical stability that make them very important in both fundamental science and technological applications [11–17].

These d-block elements nitrides can be used in many applications such as coatings to protect mechanical tools [18], corrosion resistants, optical coatings, electrical contacts, diffusion barriers and superconductors; as well as catalysts, electrode materials for batteries and fuel-cells [15]. They can also be used as materials for magnetic storage devices [19].

In fact, the small number of transition-metal nitrides, compared with the large number of the corresponding oxides, is because of the much more challenging techniques required to prepare nitride phases. Accordingly, computational techniques are believed to be very promising in searching for and characterizing new transition-metal nitrides [19].

Palladium Nitrides

In 2007, Crowhurst *et al.* [20] reported the synthesis of the new palladium nitride compound and argued for its PdN_2 stoichiometry and pyrite (C2) structure. However, many transition-metal nitrides (TMNs) are known to form more than one nitride [21], and first-principles methods are commonly employed to search for possible stable phases.

Platinum Nitrides

Platinum is known to form simple binary compounds with other elements (e.g. PtF_4, PtI_2, PtO and PtS) [22]. However, platinum had not been known to form crystalline solid nitride, but other forms of platinum nitrides (e.g. PtN [22,23], PtN_2 [22], $(PtN)_2$ [22,23] and Pt_2N [23]) had been observed.

In January 2004, Soto [24] reported the preparation of platinum thin films containing up to ~ 14 at. $\%$ nitrogen. The study concluded that platinum can form an incipient nitride phase with composition near to Pt_6N. Few months later, in May 2004, Gregoryanz and co-workers [22] published the discovery and characterization of solid crystalline platinum mono-nitride for the first time. The synthesis was carried out above 45 GPa and $2000\ K$ but with complete recovery of the product at room pressure and temperature. The produced samples have a very high bulk modulus leading to important implications in high-pressure physics and technology. The 1:1 stoichiometry was assigned to the new nitride, and according to their XRD measurements, Gregoryanz et al. proposed three structures: B1, B3 and B17 (for description of the structures see Sec. 5.2 and

App. F), all based on the Pt fcc sub-lattice. Due to some considerations, B1 and B17 were ruled out and B3 was assigned to the new product.

In addition to the well-crystallized and highly ordered regions, a common feature in the synthesized platinum nitrides is the presence of sub- or/and super-stoichiometric phases containing N or Pt vacancies and residual non-stoichiometric material distributed throughout the samples [22,25].

The work of Gregoryanz et al. [22] has stimulated many further theoretical studies [26–28] as expected by Gregoryanz and co-workers [22] themselves. However, theoretical works showed that PtN(B3) is elastically and thermodynamically unstable (see Sec. 10.3). Accordingly, claiming that large errors are generally inevitable in the used experimental characterization methods [27, 29], and due to other paradoxical facts [30] in the original experiment by Gregoryanz et al. [22], theoreticians questioned the chemical stoichiometry and the crystal structure of this new material and started to investigate other possibilities [29–31]. Moreover, the experimentally reported [22] high bulk modulus of the platinum nitride has not been reproduced by any reliable calculations and its mechanism is still an unclear open problem [26, 30, 31].

These investigations led to a kind of consensus that the compound does not crystallize in the proposed PtN(B3) phase [25], but the true stoichiometry and the true crystal structure have become now a matter of debate [27, 30].

In an apparent attempt to respond to this debate, Crowhurst et al. [25] managed, in 2006, to reproduce and characterize platinum nitride. Combining theory with their own observed Raman spectrum, they came up with a conclusion to propose PtN_2(C2) and rejected PtN(B3), proposed by the first platinum nitride synthesizers [22], and PtN_2(C1), proposed in some theoretical works. Like the first proposed structures [22], C1 [29] and C2 [25] structures have the fcc sub-lattice of the metal.

Despite the considerable number of the subsequent theoretical studies, the discrepancy between theory and experiment in the structural and the physical properties of this nitride is not yet satisfactorily understood. Nevertheless, many transition metals can form more than one nitride

[21]. Thus, it is of interest to know if platinum can form nitrides with different stoichiometries and/or crystal structures other than those proposed by the first platinum nitride synthesizers and other researchers.

Copper Nitrides

In 1939, Juza and Hahn succeeded to produce Cu_3N [32] for the first time [33–35]. Since then, copper nitride has been prepared in various techniques [34, 36–38], its properties and applications have been researched, both theoretically and experimentally, and it may now be considered as the most accessible among the noble metal nitrides [35].

Synthesis and reliable characterization of the properties of a stoichiometric copper nitride constitute a big challenge because it is thermally unstable material [34]. However, this low thermal stability results in promising applications in optical memories and laser writing [35, 37].

The viability of using the simple cubic stoichiometric Cu_3N films for write-once optical data storage has been widely explored and confirmed [39–41], superior to other toxic and unstable materials in air at room temperature which are used for the same purpose [40]. Also, the feasibility of using Cu_3N as a coating to generate metal lines by maskless laser writing has been studied; where conducting lines of a few micron in width could be generated with resistivities within an order of magnitude of the bulk Cu metal [42]. This interesting material has been suggested for usage in a number of nano-electronic and nano-photonic devices [38].

Depending on the total sputtering pressure and on the content of nitrogen gas, Hayashi et al. [43] prepared four categories of sputter-deposited Cu–N films: metallic Cu–rich Cu_3N, semiconducting Cu-rich Cu_3N, semiconducting stoichiometric Cu_3N and semiconducting N–rich Cu3N films. In general, it has been reported that it is possible to achieve sub-, over- and stoichiometric copper nitrides [44, 45], and the effect of the nitrogen to copper ratio on the physical properties has been studied by many researchers [36, 44–46].

The structural properties of Cu_3N in the experimentally reported cubic anti-ReO_3 phase are interesting on their own. This structure has many vacant interstitial sites like WO_3. The latter

could be made into a conductor by doping it with some metal ions [47]. This is very suggestive, since one may be able to engineer the physical properties of such technologically important material [18, 46]. In fact, the study of *possible* intercalated copper nitride alloys has been an active subject of research on its own (cf. Ref. [36] and references therein).

Although copper nitride possesses interesting properties leading to different technological applications, there is still a large discrepancy in the formation mechanism and inconsistency in the experimentally reported and in the theoretically predicted physical properties of copper nitrides [34,36,38,46,48]. These differences and contradictions are stemming mainly from the unstable nature (i.e. the metastability and low decomposition temperature) of copper nitride [34,38,49], the experimental conditions [46], the experimental analysis methods [34], the non-stoichiometry of the prepared samples [43] or the lack of knowledge of the real stoichiometry of the prepared samples [38]; and from the different theoretical calculation methods and approximations [46].

Thus, the emerging potential technological applications of copper nitride are faced by the inconsistency in its basic physical properties. This may explain the tremendously increasing interest in further studying this material, especially within first-principles quantum mechanical approaches. Moreover, concerning its optical properties, only a few experiments are available in the literature [50] and there are very few theoretical studies.

To the best of our knowledge, the only experimentally reported stoichiometries of copper nitride are Cu_3N [32, 44, 51] and Cu_4N [44, 51, 52], while CuN and CuN_2 have not been observed yet. However, many transition-metal nitrides (TMNs) are known to form more than one nitride [21, p. 835]. Our interest in the latter two nitride stoichiometries is based on the fact that for other late transition metals close to Cu in the periodic table these 1:1 and 1:2 nitrides have been reported.

Silver Nitrides

Since Juza and Hahn [32] succeeded to synthesize Cu_3N in 1939, copper nitrides have been produced through various techniques and their properties and applications have been the subject of many theoretical and experimental published works [3]. Due to its early discovery, copper nitride

may now be considered as the most investigated among the late TMNs [35].

On the other hand, the nitride of silver, the next element to copper in group 11 of the periodic table, has been known for more than two centuries [53,54]. However, despite its earlier discovery, silver nitride may be the least theoretically studied solid in the late TMNs family. Experimental efforts to investigate structural [54, 55], electronic [54] and formation [53, 55–57] properties of silver nitrides have been made by some researchers.

In 1949, Hahn and Gilbert [55] carried out the first [54] structural study on the reported stoichiometry, Ag_3N. They claimed an fcc structure with $a = 4.369$ Å and $Z = 4/3$ (i.e. 4 Ag atoms in the unit cell). A long time later in 1982, Haisa [58] suggested that the Ag atoms are located at the corners and face centers of the unit cell, while the N atoms, which may be statistically distributed in the octahedral interstices, were given no definite positions [58].

According to the calculated N radius, Ag_3N can be described as an ionic compound, and recent *ab initio* calculations on the proposed structure revealed insulating characteristics with a fundamental band gap close to $1.35\ eV$. On the other hand, due to the similar lattice of the parent Ag and the easily separated N as N_2, it can also be argued that this compound is a metal, supporting its black color [54].

Under ordinary conditions [53], it was found that silver can form Ag_3N [1] from ammoniacal solutions of silver oxide [53,54]. The black metallic-looking solid outcome, Ag_3N, is an extremely sensitive explosive compound [53, 59]. It may explode due to the slightest touch, even from the impact of a falling water droplet [59], but it is relatively easy to handle under water or ethanol [54]. The explosive power is due to the energy released during the decomposition reaction:

$$2Ag_3N \longrightarrow 6Ag + N_2\ . \tag{1.1.2}$$

[1] Ag_3N, formerly termed *fulminating silver* by its discoverers, can be formed from ammoniacal solutions of silver oxide according to the following reaction

$$3Ag_2O + 2NH_3^{(aq)} \longrightarrow 2Ag_3N + 5H_2O. \tag{1.1.1}$$

It can also be formed by means of other reactions [53, 54].

Even in storage at room temperature, this solid compound decomposes slowly according to Eq. 1.1.2 above [54, 59]. From a thermochemical point of view, it was found that there is no stable intermediate stage in this decomposition, but there may be a metastable intermediate species (phase) with a remarkably low decomposition rate [53]. At this point, it may be worth mentioning that the thermochemistry of silver nitride systems is not fully documented in standard handbook data [53].

In their 1991 work, Shanley and Ennis [53] stated: *"Many of the samples ... did not survive the minimum handling required to move them, container and all, to the X-ray stage. ... More vigorously explosive samples propagated throughout their mass leaving no visible residue. Even among supersensitive materials, silver nitride is a striking example of a compound "teetering on the edge of existence". Under the circumstances, we did not succeed in developing data on the proportion of silver nitride required for explosive behavior in these mixtures."*

Thus, beside the potential hazard to lab workers due to its sensitive explosive behavior, characterization of silver nitride is hindered by its extremely unstable (endothermic) nature [53, 54], and we are presented with an incomplete picture of structural, electronic and optical properties of this material. Surprisingly, this lack of detailed knowledge of many physical properties of silver nitride stimulated only very few published *ab initio* studies.

Gold Nitrides

In 2002, Šiller and co-workers [60] at the University of Newcastle[2] reported direct observation of the formation of an Au_xN compound for the first time. Since then, single crystal and polycrystalline gold nitrides have been prepared with different methods [61, 62], and many theoretical [63–66] and experimental [12, 17, 61, 63, 67, 68] investigations on the structural and physical properties of gold nitride have been published. It turned out that gold nitride possesses interesting properties which may lead to potential practical applications [68].

[2] See http://research.ncl.ac.uk/nanoscale/research/goldnitride.html, http://news.bbc.co.uk/2/hi/uk_news/england/tyne/3205959.stm and http://physicsworld.com/cws/article/news/2003/oct/27/gold-plating-on-the-cheap.

So far, the most significant finding may be that of Šiller et. al [12] who, in 2005, reported the production of metallic large area gold nitride films which are $\sim 50\%$ harder than pure gold films produced under similar conditions, making the gold nitride ideal for use in large-scale applications in coatings and in electronics. Moreover, the possibility of patterning gold nitride film surfaces by electron/photon beam lithography was confirmed [68].

From their experimental observations and *ab initio* calculations, Krishnamurthy *et al.* [63] suggested the possibility of formation of more than one gold nitride phase. Although theoretical calculations have predicted several possible structures for AuN, AuN_2 and Au_3N, none of these agrees with experiment [61].

Zinc Nitrides

Zinc nitride was first synthesized by Juza and Hahn [69] in 1940. However, like silver nitride, despite its earlier discovery, zinc nitride remained a relatively unstudied compound for over 50 years, and only little work has been done on it. Furthermore, most properties of this material have not been fully understood or even known. In particular, the optical band gap of zinc nitride has remained a controversial subject for quite long time. As a member of late TMNs family, zinc nitride is expected to exhibit excellent electric and optical properties. Therefore, further intensive investigation is required [70].

As most of the transition metals, different formulas of zinc nitride have been reported: Zn_3N_2, ZnN_2, α-ZnN_6 and β-ZnN_6; each with its own crystal structure [71]. However, it is a common practice in first-principles calculations to study phases that have not been synthesized yet (cf. Refs. [72, 73]). Therefore, it is interesting to investigate zinc nitride in two modifications that are obtained from the replacement of sulfur ion in the well-known ZnS(B3) and ZnS(B4) with an N ion, and perform *ab initio* calculations to study the stability, structural and electronic properties of these hypothetical ZnN(B3) and ZnN(B4) phases; and, as always, to investigate the effect of nitridation on the elemental zinc metal.

1.2 Aims

Motivated by the facts in the previous section, our main objectives of the present work are:

1. Investigate stability, structural and electronic properties of Pd, Pt, Cu, Ag, Au, and Zn nitrides within density functional theory.

2. To investigate the structure preference and identify the most likely candidates for the true stoichiometry and the true crystal structure.

3. To investigate the effect of nitridation on the elemental transition metals.

4. To investigate some possible pressure-induced phase transformations.

5. To sort out the reported discrepancies of previous works.

6. To determine the possible structures and physical properties of those nitrides which have not yet been synthesized.

7. To calculate optical properties and excitation energies of the most stable modifications of these target transition-metal nitrides within the many-body GW approximation; and compare our obtained spectra with the available experimental observations.

8. The obtained results will be used to investigate regularities and trends (if any), and to search for possible transition-metal nitrides for use in electronic devices that can replace pure gold.

9. The results may be used to evaluate to which extent the current different theoretical approaches, computational schemes and codes are capable of describing such kind of electronic systems. (e.g. to what extent DFT and GW methods and VASP package can generate and reproduce the already-reported properties).

10. One of the objectives of the present work is to serve as a reference source for meaningful comparisons which may be made among the largely different calculations, with the view of making results from experiment and from previous calculations available in a single document for any further study.

11. Chapters on theoretical background and calculation methods, namely Part I and Part II, will be flavored with some pedagogical features to serve as a reference source for beginners to learn the use of some of the electronic structure calculations methods and codes, and to deepen the understanding of the most important technical and theoretical aspects.

Obtained results will be discussed within the introduced theoretical framework. However, deep understanding of the concepts and rigorous definitions of the physical quantities that are going to be calculated are basic in analyzing results. On the other hand, comparison with experiment and/or with previous (theoretical) studies is a crucial justifying tool. Success in this work will contribute to fundamental understanding of these technologically important materials as well as benefit their practical applications. Thus, our goal is to provide some transparent physical interpretation for the properties of these materials on the microscopic level and come up with some useful suggestions about how these properties can be further improved.

1.3 Thesis Outline

The Thesis is divided into an introduction and four parts. Part I is devoted to the theoretical methods employed in the calculations. We start this part by defining the general many-body problem of condensed matter physics (Ch. 2). Then, we introduce two solution methods to the problem, namely the density functional theory (Ch. 3) and the so-called GW approximation scheme (Ch. 4).

Part II is devoted to the description of the practical calculations and to the methods of determining and extracting physical properties of solids from first-principles calculations. This part starts with description of the chemical formulas and crystal structures of the materials under investigation (Ch. 5). This is followed by describing the scheme that is employed to solve the electronic problem using density functional theory (Ch. 6). The rest of this Part is devoted to the definitions of, and the methods of calculating the structural (Ch. 7), the electronic (Ch. 8) and the optical (Ch. 9) properties.

Obtained results are presented and analysed in Ch. 10 of Part III, followed by Ch. 11 in which we conclude the whole work and propose directions for future work.

Appendices in Part IV are devoted for some necessary background from basic solid-state theory, classical electromagnetism and mathematics. At the very end of the Thesis, a list of formulated articles out of the present work is presented.

Part I

Theoretical Methods

"The general theory of quantum mechanics is now almost complete, ... The underlying physical laws necessary for the mathematical theory of a large part of physics and the whole of chemistry are thus completely known, and the difficulty is only that the exact application of these laws leads to equations much too complicated to be soluble. It therefore becomes desirable that approximate practical methods of applying quantum mechanics should be developed, which can lead to an explanation of the main features of complex atomic systems without too much computation."

Paul A. M. Dirac [74].

2. The Basic Many-Body Problem of Solids

The description of matter at the atomic scale requires the use of quantum mechanics. In this chapter, we introduce the many-body Schrödinger equation of condensed matter, and we show that this problem can be simplified and decomposed into two subproblems: the nuclear problem and the electronic problem. Each of these two sub-problems is a many-body problem on its own. The solution methods of the latter constitute the field which is known as the electronic structure calculations. Mindful of the big picture, our goal in this chapter is to establish the basis for the succeeding chapters. The discussion and notations here follow closely the presentation in Refs. [75, 76].

2.1 The Basic Hamiltonian

A bulk condensed phase of matter can be looked at as an ensemble of atomic nuclei and electrons that glue the nuclei together and neutralize their electric charge. These positive nuclei and the negative electrons interact with themselves and with each other, giving rise to a clear quantum many-body problem. The time-dependent non-relativistic Schrödinger equation that describes such a coupled system can be written as

$$\boxed{i\hbar\frac{\partial}{\partial t}\Psi(\mathbf{R},\mathbf{r};t)=\hat{\mathcal{H}}\Psi(\mathbf{R},\mathbf{r};t)}\,. \tag{2.1.1}$$

Here $\Psi(\mathbf{R},\mathbf{r};t)$ is the many-body wave function of the electron-ion system, with $\mathbf{R}=\{\mathbf{R}_I,\ I=1,2,3,...\}$ and $\mathbf{r}=\{\mathbf{r}_i,\ i=1,2,3,...\}$ being the spatial coordinates of the nuclei and the electrons, respectively. In the absence of external fields, the time-independent Hamiltonian $\hat{\mathcal{H}}$ is

generally given by [75, 77–79]

$$\hat{\mathcal{H}} = \underbrace{-\frac{\hbar^2}{2m_e}\sum_i \nabla_i^2}_{\hat{T}_e} + \underbrace{\frac{e^2}{2}\sum_i\sum_{j\neq i}\frac{1}{|\mathbf{r}_i-\mathbf{r}_j|}}_{\hat{V}_{\text{ee}}} \underbrace{-\sum_{i,I}\frac{Z_I e^2}{|\mathbf{r}_i-\mathbf{R}_I|}}_{\hat{V}_{\text{en}}} \underbrace{-\sum_I \frac{\hbar^2}{2M_I}\nabla_I^2}_{\hat{T}_n} + \underbrace{\frac{e^2}{2}\sum_I\sum_{J\neq I}\frac{Z_I Z_J}{|\mathbf{R}_I-\mathbf{R}_J|}}_{\hat{V}_{\text{nn}}}, \tag{2.1.2}$$

where m_e and e are the electronic mass and charge, respectively; and M_I and Z_I are the mass and the charge of the I^{th} nucleus, respectively. In general, we denote electrons by lower case subscripts, while nuclei are denoted by upper case subscripts.

The terms in $\hat{\mathcal{H}}$ above are the electronic kinetic energy operator $\hat{T}_e = -\frac{\hbar^2}{2m_e}\sum_i \nabla_i^2$, the nuclear potential acting on electrons $\hat{V}_{\text{en}} = -\sum_I\sum_i \frac{Z_I e^2}{|\mathbf{r}_i-\mathbf{R}_I|}$, the electron-electron repulsion interaction operator $\hat{V}_{\text{ee}} = \frac{e^2}{2}\sum_i\sum_{j\neq i}\frac{1}{|\mathbf{r}_i-\mathbf{r}_j|}$, the nuclear kinetic energy operator $\hat{T}_n = -\sum_I \frac{\hbar^2}{2M_I}\nabla_I^2$, and the nuclear-nuclear repulsion interaction operator $V_{\text{nn}} = \frac{e^2}{2}\sum_I\sum_{J\neq I}\frac{Z_I Z_J}{|\mathbf{R}_I-\mathbf{R}_J|}$.

If the system contains P nuclei and N electrons, then this is an equation with $3(P+N)$ coupled spatial degrees of freedom. Neither analytic nor exact numerical solution is possible. Thus, approximations may be made to lead to a soluble problem, reasonable amount of calculations effort, and should be valid for a wide range of problems of interest [75, 77, 80]. In the next section, we will present such approximations and may discuss their limitations and validity.

2.2 Born-Oppenheimer Approximation

Grouping the terms in the Hamiltonian 2.1.2 as

$$\hat{\mathcal{H}} = \hat{\mathcal{H}}_e + \hat{\mathcal{H}}_I = (\hat{T}_e + \hat{V}_{\text{ee}} + \hat{V}_{\text{en}}) + (\hat{T}_n + V_{\text{nn}}), \tag{2.2.1}$$

one can propose[1] a solution $\Psi(\mathbf{R},\mathbf{r};t)$ to Eq. 2.1.1 in the form

$$\Psi(\mathbf{R},\mathbf{r};t)=\sum_n \Theta_n(\mathbf{R};t)\Phi_n(\mathbf{R},\mathbf{r})\ , \tag{2.2.2}$$

where the time-independent bases $\Phi_n(\mathbf{R},\mathbf{r})$ are assumed to satisfy the electronic Schrödinger equation

$$\hat{\mathcal{H}}_e\ \Phi_n(\mathbf{R},\mathbf{r})=E_n(\mathbf{R})\Phi_n(\mathbf{R},\mathbf{r}) \tag{2.2.3}$$

for any given nuclear configuration $\mathbf{R}$. That is, the nuclear coordinates $\mathbf{R}$ enter Eq. 2.2.3 above only as parameters.

Substituting Eqs. 2.2.2 and 2.2.3 into Eq. 2.1.1, multiplying from the left by $\Phi_q(\mathbf{R},\mathbf{r})$, integrating over all the electronic coordinates $\mathbf{r}$ and rearranging the terms, it is straightforward to find the following infinite set of equations

$$\begin{aligned}&\left(i\hbar\frac{\partial}{\partial t}+\sum_I\frac{\hbar^2}{2M_I}\nabla_I^2-V_{\text{nn}}-E_q(\mathbf{R})\right)\Theta_q(\mathbf{R};t)=\\ &-\sum_I\sum_n\frac{\hbar^2}{2M_I}\left\langle\Phi_q\middle|\nabla_I^2\middle|\Phi_n\right\rangle\Theta_q(\mathbf{R};t)-2\sum_I\sum_n\frac{\hbar^2}{2M_I}\left(\nabla_I\Theta_q(\mathbf{R};t)\right)\left\langle\Phi_q|\nabla_I|\Phi_n\right\rangle .\end{aligned} \tag{2.2.4}$$

The presence of the off-diagonal elements in Eq. 2.2.4 above reveals the fact that along the time evolution electronic states Φ_n will be mixed (i.e. excited) due to the nuclear dynamics. In the so-called "*adiabatic approximation*", these terms are ignored. The validity of this approximation is based on the significant difference (three to five orders of magnitude) in mass between nuclei and electrons [79], leading to a huge difference in the time (or energy) scale associated with the motion of nuclei and electrons [75]. Thus, while nuclei are moving slowly in the configuration space, electrons respond instantaneously to any nuclear motion and adjust themselves to remain in the stationary states of $\hat{\mathcal{H}}_e$, i.e. without undergoing transitions between these stationary states. Within the adiabatic approximation, the last term in Eq. 2.2.4 vanishes due to the normalization requirement $\langle\Phi_n|\Phi_n\rangle=1$. Hence, one can write the *adiabatic* Schrödinger equation for the

[1] No approximation here. Mathematically speaking, this is always possible.

nuclear subsystem as

$$i\hbar\frac{\partial}{\partial t}\Theta_q(\mathbf{R};t)=\left(-\sum_I\frac{\hbar^2}{2M_I}\nabla_I^2+V_{\mathsf{nn}}(\mathbf{R})+\tilde{V}_q(\mathbf{R})\right)\Theta_q(\mathbf{R};t)\ , \tag{2.2.5}$$

where

$$\tilde{V}_q(\mathbf{R})=E_q(\mathbf{R})+\sum_I\sum_n\frac{\hbar^2}{2M_I}\left\langle\Phi_q\middle|\nabla_I^2\middle|\Phi_q\right\rangle\ . \tag{2.2.6}$$

The diagonal correction to the electronic energy levels (the last term in Eq. 2.2.6 above) is due to the remaining coupling between the nuclear and the electronic degrees of freedom, and is found to be proportional to m_e/M. The negligence of this term, known as "*Born-Oppenheimer approximation*" [81], leads to the following Schrödinger equation for the nuclear subsystem

$$i\hbar\frac{\partial}{\partial t}\Theta_q(\mathbf{R};t)=\left(-\sum_I\frac{\hbar^2}{2M_I}\nabla_I^2+V_{\mathsf{nn}}(\mathbf{R})+E_q(\mathbf{R})\right)\Theta_q(\mathbf{R};t)\ . \tag{2.2.7}$$

2.3 The Atomic Structure of Solids

Consider an observable $\mathcal{O}$, the time derivative of its expectation value $\langle\mathcal{O}\rangle$ is given by [75, 82]

$$\frac{d}{dt}\langle\mathcal{O}\rangle=\frac{1}{i\hbar}\langle[\mathcal{O},\hat{\mathcal{H}}]\rangle+\left\langle\frac{\partial\mathcal{O}}{\partial t}\right\rangle\ . \tag{2.3.1}$$

In particular

$$\frac{d}{dt}\langle\mathbf{R}\rangle=\frac{1}{i\hbar}\langle[\mathbf{R},\hat{\mathcal{H}}]\rangle+\left\langle\frac{\partial\mathbf{R}}{\partial t}\right\rangle=\frac{1}{M}\langle\hat{p}\rangle\ , \tag{2.3.2}$$

and

$$\frac{d}{dt}\langle\hat{p}\rangle=\frac{1}{i\hbar}\langle[\hat{p},\hat{\mathcal{H}}]\rangle+\left\langle\frac{\partial\hat{p}}{\partial t}\right\rangle=\langle-\nabla\hat{V}\rangle\ ; \tag{2.3.3}$$

where $\hat{p}$ is the momentum and $\hat{V}$ is the potential of the Hamiltonian $\hat{\mathcal{H}}$. Combining Eqs. 2.3.2 and 2.3.3 above yields

$$M\frac{d^2}{dt^2}\langle\mathbf{R}\rangle = \langle -\nabla\hat{V}\rangle \ , \tag{2.3.4}$$

which is a Newtonian equation of motion for the position mean value $\langle\mathbf{R}\rangle$. In the so-called "*classical nuclei approximation*", the quantum mean value $\langle\mathbf{R}\rangle$ is approximated by spatial coordinates of the classical particle.

$$M\frac{d^2}{dt^2}\mathbf{R} = -\nabla V = F \ , \tag{2.3.5}$$

where $\mathbf{R}$ is now the classical particle position, and F is the force on that particle.

Now, if we apply the classical nuclei approximation to the Born-Oppenheimer nuclear subsystem (Eq. 2.2.5), we obtain

$$M\frac{d^2}{dt^2}\mathbf{R} = -\nabla\hat{V} = -\nabla\left[E_q(\mathbf{R}) + V_{\mathsf{nn}}(\mathbf{R})\right] \ , \tag{2.3.6}$$

where $E_q(\mathbf{R})$, called the q^{th} adiabatic potential energy surface (PES), is given by Eq. 2.2.3. Considering the I^{th} nucleus, and applying the so-called Hellman-Feynman force theorm [78,83–85]

$$\frac{\partial E_q(\lambda)}{\partial\lambda} = \left\langle \Phi_q(\mathbf{R}) \middle| \frac{\partial\hat{\mathcal{H}}_e(\lambda)}{\partial\lambda} \middle| \Phi_q(\mathbf{R}) \right\rangle \ , \tag{2.3.7}$$

where λ is any external parameter coupled to the electronic degrees of freedom, Eq. 2.3.6 above reads

$$M_I\frac{d^2}{dt^2}\mathbf{R}_I = -\left\langle \Phi_q(\mathbf{R}) \middle| \frac{\partial\hat{\mathcal{H}}_e(\mathbf{R})}{\partial\mathbf{R}_I} \middle| \Phi_q(\mathbf{R}) \right\rangle - \frac{\partial V_{\mathsf{nn}}}{\partial\mathbf{R}_I} \ , \tag{2.3.8}$$

The ground-state atomic geometrical structure of a solid is found by solving

$$\left\langle \Phi_q(\mathbf{R}) \middle| \frac{\partial\hat{\mathcal{H}}_e(\mathbf{R})}{\partial\mathbf{R}_I} \middle| \Phi_q(\mathbf{R}) \right\rangle + \frac{\partial V_{\mathsf{nn}}}{\partial\mathbf{R}_I} = 0 \ , \tag{2.3.9}$$

and the procedure is known as *ab initio* or first-principles "*geometry optimization*". Every time the nuclear spatial configuration $\mathbf{R}$ changes, one has to obtain the new PES by solving Eq. 2.2.3. This integration of Eq. 2.3.8 is known as molecular dynamics [75, 86] .

2.4 The Electronic Structure of Solids

Whether the aim is to investigate structural (i.e. solve Eq. 2.3.9), dynamic (i.e. numerically integrate Eq. 2.3.8) or electronic properties, one has to find the adiabatic potential hyper surface $E(\mathbf{R})$. That is, one has to solve the Born-Oppenheimer non-relativistic[2] time-independent Schrödinger equation (Eq. 2.2.3) of the electronic subsystem [75, 86–88]. The solution to Eq. 2.2.3 is known as the "*electronic structure calculations*" [87].

Eq. 2.2.3 involves $3N$ spatial degrees of freedom. To reduce the number of degrees of freedom, one may consider those inner electrons which do not participate effectively in the chemical bonding to be moving rigidly with the nuclei to form the so-called ion core [77]. i.e. one redefines M_I and Z_I. This is the essence of the so-called *pseudopotential* which will be discussed briefly in Subsection 3.6.4. So, from now on we use the term *ion* instead of *nucleus* to refer to this approximation.

Mathematically, the two-particle feature of the Coulomb operator V_{ee} does not allow for the separation of Eq. 2.2.3. Physically, due to the repulsive nature of V_{ee}, the probability of finding an electron at a position $\mathbf{r}$ depends on the positions of the other $N-1$ electrons; that is each electron is affected by the motion of every other electron in the system. This property is known as *correlation* [75, 79]. One of its implications is that, any exact solution $\Phi_n(\mathbf{R},\mathbf{r})$ of Eq. 2.2.3 must contain two-particle degrees of freedom [75].

Moreover, if two electrons of the same spin interchange positions, Φ must change sign; that is any solution $\Phi_n(\mathbf{R},\mathbf{r})$ to Eq. 2.2.3 must be antisymmetric with respect to the exchange of the electronic spatial coordinates [3]. This quantum correlation phenomenon is known as *ex-*

[2] For now, we are not including relativistic, spin, magnetic fields or quantum electrodynamic effects. Some of these will enter our discussion later at different stages. cf. Sec. 3.5 and the very last part of Subsec. 3.6.4 of this Thesis.

[3] This antisymmetry nature of the N-electron total wave function $\Phi_n(\mathbf{R},\mathbf{r})$ is the fundamental manifestation

change [75, 79][4].

In general, it is evident that regardless of what simplifications one introduces, the nature of the electrons makes the issue of solving Eq. 2.2.3 for Φ an extremely difficult task. Consequently, the complexity of the electronic problem invokes many approximations, this in turn leads to different theoretical methods [79]. In the present section, the exchange-correlation problem will be formally addressed, and the electronic Hamiltonian $\hat{\mathcal{H}}_e$ will be rewritten in terms of the density of electrons.

2.4.1 The Electronic Density

For a given ionic configuration $\mathbf{R}(t)$, the many-body wave function of N electrons (Eq. 2.2.3) can be written as

$$|\Phi\rangle = \Phi(\mathbf{r}_1\sigma_1, \mathbf{r}_2\sigma_2, ... \mathbf{r}_N\sigma_N) \ , \tag{2.4.1}$$

where the spin degrees of freedom σ have been included explicitly[5]. The product

$$\Phi^*(\mathbf{r}_1\sigma_1, \mathbf{r}_2\sigma_2, ... \mathbf{r}_N\sigma_N)\Phi(\mathbf{r}_1\sigma_1, \mathbf{r}_2\sigma_2, ... \mathbf{r}_N\sigma_N)$$

determines the probability that the variables of the first electron lie in spatial volume element $\mathrm{d}\mathbf{r}_1$ with spin coordinates σ_1, those of the second simultaneously in $\mathrm{d}\mathbf{r}_2$ with spin coordinates σ_2, etc. [76, 94]. To find $n_\sigma(\mathbf{r})d\mathbf{r}$, the average number of the electrons of spin σ in volume $d\mathbf{r}$ around $\mathbf{r}$, one needs to calculate the probability of finding electron**s** of spin σ at $\mathbf{r}$, i.e. the electronic

of the well-known Pauli exclusion principle [89]. In fact, the original Pauli principle of the year 1925 [90] claims that for identical fermions (particles with half-integer spin [82]) the occupation number for any quantum state cannot exceed the value 1. Later, in 1926, Dirac [91] and Heisenberg [92] showed that the Pauli principle is a consequence of a much deeper statement: the antisymmetry of the many-fermion wave function [93].

[4] Exchange and correlation will be discussed in more details in Subsections 2.4.3 and 3.6.3. However, it may be worth mentioning here that the solution of the nuclear problem $\Theta_q(\mathbf{R};t)$ must, in principle, be symmetric or antisymmetric depending on the species and on the spins of the nuclei. Nevertheless, if the classical nuclei approximation is applied, $\Theta_q(\mathbf{R};t)$ can be represented by a product of Dirac δ-functions [75], i.e. no overlap.

[5] Note that, the subscripts $1 \cdots N$ refer merely to different volume elements while their places, which in principle indicate the particles referred to, are arbitrary owing to the symmetry [94].

density $n_\sigma(\mathbf{r})$ [78]. If $|\Phi\rangle$ are[6] normalized, it is straightforward to show that

$$\begin{aligned} n_\sigma(\mathbf{r}) \equiv \quad & n(\mathbf{r},\sigma) = \langle\Phi|\hat{n}_\sigma(\mathbf{r})|\Phi\rangle \\ = \quad & N\sum_{\sigma_j=\sigma_2}^{\sigma_N}\int \mathrm{d}\mathbf{r}_2\mathrm{d}\mathbf{r}_3\ ...\ \mathrm{d}\mathbf{r}_N\ \ |\Phi(\mathbf{r}\sigma,\mathbf{r}_2\sigma_2,\mathbf{r}_3\sigma_3,...\ \mathbf{r}_N\sigma_N)|^2 \quad , \end{aligned} \tag{2.4.2}$$

with the density operator

$$\hat{n}_\sigma(\mathbf{r}) = \sum_{k=1}^{N}\delta(\mathbf{r}_k-\mathbf{r})\delta(\sigma_k-\sigma)\ , \tag{2.4.3}$$

and

$$\sum_\sigma\int d\mathbf{r}\ n_\sigma(\mathbf{r}) = \int \mathrm{d}\mathbf{r}\ \ (n_\uparrow(\mathbf{r})+n_\downarrow(\mathbf{r})) = N \tag{2.4.4}$$

must be satisfied.

One can also define the joint electronic density by

$$\begin{aligned} n_{\sigma\sigma'}(\mathbf{r},\mathbf{r}') \equiv \quad & n(\mathbf{r}\sigma,\mathbf{r}'\sigma') = \langle\Phi|\hat{n}_{\sigma\sigma'}(\mathbf{r},\mathbf{r}')|\Phi\rangle \\ = \quad & \left\langle\Phi\left|\sum_{j<k}\delta(\mathbf{r}_j-\mathbf{r})\delta(\sigma_j-\sigma)\delta(\mathbf{r}_k-\mathbf{r})\delta(\sigma_k-\sigma)\right|\Phi\right\rangle \\ = \quad & \frac{N(N-1)}{2}\sum_{\sigma_j=\sigma_3}^{\sigma_N}\int \mathrm{d}\mathbf{r}_3\mathrm{d}\mathbf{r}_4\ ...\ \mathrm{d}\mathbf{r}_N\ \ |\Phi(\mathbf{r}\sigma,\mathbf{r}'\sigma',\mathbf{r}_3\sigma_3,...\ \mathbf{r}_N\sigma_N)|^2 \quad , \end{aligned} \tag{2.4.5}$$

which represents the probability of finding electron**s** of spin σ at $\mathbf{r}$ and electron**s** of spin σ' at $\mathbf{r}'$. Its integration

$$\sum_{\sigma\sigma'}\int \mathrm{d}\mathbf{r}\mathrm{d}\mathbf{r}'\ n_{\sigma\sigma'}(\mathbf{r},\mathbf{r}') = \frac{N(N-1)}{2} \tag{2.4.6}$$

[6] Because electrons are Fermions, there are $N!$ distinct electronic configurations. The formula 2.4.2 is true also if one considers the ensemble of these $N!$ states if they are equally probable. Nevertheless, following Refs. [94, 95], here and in what follows, we consider $|\Phi\rangle$ to be a pure state. A straightforward generalization to ensemble case can be found in Chapter 2 of Ref. [76].

gives the number of electron pairs [76, 78, 79, 95, 96].

The definitions above are crucial and have many important consequences. For example the correlation phenomenon, that is introduced in Sec. 2.4, can be quantified in terms of $n_\sigma(\mathbf{r})$ and $n_{\sigma\sigma'}(\mathbf{r},\mathbf{r}')$ by

$$\Delta n_{\sigma\sigma'}(\mathbf{r},\mathbf{r}') = n_{\sigma\sigma'}(\mathbf{r},\mathbf{r}') - n_\sigma(\mathbf{r})n_{\sigma'}(\mathbf{r}') \ , \tag{2.4.7}$$

where, the product represents the joint density of uncorrelated particles [78]. Dividing Eq. 2.4.7 above by $n_\sigma(\mathbf{r})n_{\sigma'}(\mathbf{r}')$ yields

$$\begin{aligned} \frac{\Delta n_{\sigma\sigma'}(\mathbf{r},\mathbf{r}')}{n_\sigma(\mathbf{r})n_{\sigma'}(\mathbf{r}')} &= \frac{n_{\sigma\sigma'}(\mathbf{r},\mathbf{r}')}{n_\sigma(\mathbf{r})n_{\sigma'}(\mathbf{r}')} - \frac{n_\sigma(\mathbf{r})n_{\sigma'}(\mathbf{r}')}{n_\sigma(\mathbf{r})n_{\sigma'}(\mathbf{r}')} \\ h_{\sigma\sigma'}(\mathbf{r},\mathbf{r}') &= g_{\sigma\sigma'}(\mathbf{r},\mathbf{r}') - 1 \quad . \end{aligned} \tag{2.4.8}$$

Here, $g_{\sigma\sigma'}(\mathbf{r},\mathbf{r}')$ is the so-called pair-correlation function (or pair-correlation distribution) which is nothing but a normalized version of the joint density $n_{\sigma\sigma'}(\mathbf{r},\mathbf{r}')$ [75,78]. The normalized correction $h_{\sigma\sigma'}(\mathbf{r},\mathbf{r}') \equiv \frac{\Delta n_{\sigma\sigma'}(\mathbf{r},\mathbf{r}')}{n_\sigma(\mathbf{r})n_{\sigma'}(\mathbf{r}')}$ represents what is known as the exchange correlation hole [76, 78]. More about g and h will be discussed in Subsec. 2.4.3. However, in consideration of local, non-local, one-particle, and two-particle operators, a more formal treatment of these densities based on density matrices is to be utilized. This is the subject of the next subsection.

2.4.2 Density Matrices

In fact, $n_\sigma(\mathbf{r})$ of Eq. 2.4.2 is the diagonal of the first order (or one-particle) reduced density matrix; while $n_{\sigma\sigma'}(\mathbf{r},\mathbf{r}')$ of Eq. 2.4.5 is the the second order (or two-particle) reduced density matrix. The reduced density matrix of the p^{th} order is defined by [76, 95]

$$\begin{aligned} &\gamma_p(\mathbf{r}'_1\sigma'_1, \mathbf{r}'_2\sigma'_2, \cdots \mathbf{r}'_p\sigma'_p, \mathbf{r}_1\sigma_1, \mathbf{r}_2\sigma_2, \cdots \mathbf{r}_p\sigma_p) = \\ &\binom{N}{p} \sum_{\sigma_j=\sigma_{p+1}}^{\sigma_N} \int \mathrm{d}\mathbf{r}_{p+1} \ \cdots \ \mathrm{d}\mathbf{r}_N \ \gamma_N(\mathbf{r}'_1\sigma'_1, \cdots \mathbf{r}'_p\sigma'_p, \mathbf{r}_{p+1}\sigma_{p+1}, \cdots \mathbf{r}_N\sigma_N, \mathbf{r}_1\sigma_1, \cdots \mathbf{r}_p\sigma_p, \cdots \mathbf{r}_N\sigma_N) \end{aligned} \tag{2,4.9}$$

where $\binom{N}{p}$ is the binomial coefficient and the integrand γ_N is the coordinate representation of the density operator

$$\hat{\gamma}_N = |\Phi\rangle\langle\Phi| \; . \tag{2.4.10}$$

That is

$$\begin{aligned} \gamma_N &= \langle \mathbf{r}_1\sigma_1, \; \cdots \; \mathbf{r}_N\sigma_N|\hat{\gamma}_N|\mathbf{r}'_1\sigma'_1, \; \cdots \; \mathbf{r}'_N\sigma'_N\rangle & (2.4.11)\\ &= \langle \mathbf{r}_1\sigma_1, \; \cdots \; \mathbf{r}_N\sigma_N|\Phi\rangle\langle\Phi|\mathbf{r}'_1\sigma'_1, \; \cdots \; \mathbf{r}'_N\sigma'_N\rangle & (2.4.12)\\ &= \Phi\left(\mathbf{r}_1\sigma_1, \; \cdots \; \mathbf{r}_N\sigma_N\right)\Phi^*\left(\mathbf{r}'_1\sigma'_1, \; \cdots \; \mathbf{r}'_N\sigma'_N\right) & (2.4.13) \end{aligned}$$

From the definitions 2.4.10 and 2.4.11 above, it is clear that

$$\text{diagonal element of}\left(\gamma_N\right) \equiv \Phi\left(\mathbf{r}_1\sigma_1, \; \cdots \; \mathbf{r}_N\sigma_N\right)\Phi^*\left(\mathbf{r}_1\sigma_1, \; \cdots \; \mathbf{r}_N\sigma_N\right) \; , \tag{2.4.14}$$

and

$$\text{trace}\left(\hat{\gamma}_N\right) = \sum_{\sigma_j}^{\sigma_N} \int \mathrm{d}\mathbf{r}_1 \; ... \; \mathrm{d}\mathbf{r}_N \Phi\left(\mathbf{r}_1\sigma_1, \; \cdots \; \mathbf{r}_N\sigma_N\right)\Phi^*\left(\mathbf{r}_1\sigma_1, \; \cdots \; \mathbf{r}_N\sigma_N\right) = 1 \; . \tag{2.4.15}$$

According to definition 2.4.9, the first-order (or one-particle) and the second-order (or two-particle) reduced density matrices are given by

$$\gamma_1(\mathbf{r}'_1\sigma'_1, \mathbf{r}_1\sigma_1) = N\sum_{\sigma_2}^{\sigma_N} \int \mathrm{d}\mathbf{r}_2 \; ... \; \mathrm{d}\mathbf{r}_N \; \Phi\left(\mathbf{r}'_1\sigma'_1, \mathbf{r}_2\sigma_2, \; \cdots \; \mathbf{r}_N\sigma_N\right)\Phi^*\left(\mathbf{r}_1\sigma_1, \; \cdots \; \mathbf{r}_N\sigma_N\right) \; , \tag{2.4.16}$$

and

$$\begin{aligned} &\gamma_2(\mathbf{r}'_1\sigma'_1, \mathbf{r}'_2\sigma'_2, \mathbf{r}_1\sigma_1, \mathbf{r}_2\sigma_2) = \\ &\frac{N(N-1)}{2}\sum_{\sigma_3}^{\sigma_N} \int \mathrm{d}\mathbf{r}_3 \cdots \mathrm{d}\mathbf{r}_N \; \Phi\left(\mathbf{r}'_1\sigma'_1, \mathbf{r}'_2\sigma'_2, \mathbf{r}_3\sigma_3, \cdots, \mathbf{r}_N\sigma_N\right)\Phi^*\left(\mathbf{r}_1\sigma_1, \cdots, \mathbf{r}_N\sigma_N\right) . \end{aligned} \tag{2.4.17}$$

It is also evident that γ_1 and γ_2 integrate to the number of electrons and number of electron pairs, respectively

$$\text{trace}(\gamma_1(\mathbf{r}'_1\sigma'_1, \mathbf{r}_1\sigma_1)) = \sum_{\sigma_1} \int \mathrm{d}\mathbf{r}_1 \; \gamma_1(\mathbf{r}_1\sigma_1, \mathbf{r}_1\sigma_1) = N \; , \tag{2.4.18}$$

$$\text{trace}(\gamma_2(\mathbf{r}'_1\sigma'_1, \mathbf{r}'_2\sigma'_2, \mathbf{r}_1\sigma_1, \mathbf{r}_2\sigma_2)) = \sum_{\sigma_1,\sigma_2} \int \mathrm{d}\mathbf{r}_1\mathrm{d}\mathbf{r}_2 \; \gamma_2(\mathbf{r}_1\sigma_1, \mathbf{r}_2\sigma_2, \mathbf{r}_1\sigma_1, \mathbf{r}_2\sigma_2) = \frac{N(N-1)}{2} \; . \tag{2.4.19}$$

Moreover

$$\gamma_1(\mathbf{r}'_1\sigma'_1, \mathbf{r}_1\sigma_1) = \frac{2}{N-1} \sum_{\sigma_2} \int \mathrm{d}\mathbf{r}_2 \; \gamma_2(\mathbf{r}'_1\sigma'_1, \mathbf{r}_2\sigma_2, \mathbf{r}_1\sigma_1, \mathbf{r}_2\sigma_2) \; . \tag{2.4.20}$$

Operators

The major significance of $\hat{\gamma}_1$ (or $n_\sigma(\mathbf{r})$) and $\hat{\gamma}_2$ (or $n_{\sigma\sigma'}(\mathbf{r}, \mathbf{r}')$) lies in the fact that they allow to determine all the expectation values of one-particle and two-particles operators, respectively [95]. To show this, we first notice that for any observable $\hat{\mathcal{O}}$, one can straightforwardly show that

$$\left\langle \hat{\mathcal{O}} \right\rangle = \text{trace}\left(\hat{\mathcal{O}}\hat{\gamma}_N\right) = \text{trace}\left(\hat{\gamma}_N\hat{\mathcal{O}}\right) \tag{2.4.21}$$

Accordingly, the expectation value of a one-electron operator

$$\hat{\mathcal{O}}_1 = \sum_{i=1}^{N} \mathcal{O}(\mathbf{r}_i\sigma_i, \mathbf{r}'_i\sigma'_i) \tag{2.4.22}$$

is given by

$$\left\langle \hat{\mathcal{O}}_1 \right\rangle = \text{trace}(\hat{\mathcal{O}}_1\gamma_N) = \sum_{\sigma'_1,\sigma_1} \int \mathrm{d}\mathbf{r}'_1\mathrm{d}\mathbf{r}_1 \; \mathcal{O}(\mathbf{r}_1\sigma_1, \mathbf{r}'_1\sigma'_1)\gamma_1(\mathbf{r}'_1\sigma'_1, \mathbf{r}_1\sigma_1) \; . \tag{2.4.23}$$

If $\hat{\mathcal{O}}_1$ is local[7], then Eqs. 2.4.22 and 2.4.23 above read

$$\hat{\mathcal{O}}_1 = \sum_{i=1}^{N} \mathcal{O}_1(\mathbf{r}_i\sigma_i) \tag{2.4.24}$$

[7] An operator $\hat{\mathcal{O}}$ is local if $\hat{\mathcal{O}}(\mathbf{r}, \mathbf{r}') = \hat{\mathcal{O}}(\mathbf{r})\delta(\mathbf{r} - \mathbf{r}')$ [76].

$$\left\langle \hat{\mathcal{O}}_1 \right\rangle = \text{trace}(\hat{\mathcal{O}}_1 \gamma_N) = \sum_{\sigma_1} \int \mathrm{d}\mathbf{r}_1 \ [\mathcal{O}_1(\mathbf{r}_1\sigma_1)\gamma_1(\mathbf{r}'_1\sigma'_1, \mathbf{r}_1\sigma_1)]_{\mathbf{r}'_1\sigma'_1=\mathbf{r}_1\sigma_1} \ . \tag{2.4.25}$$

For a local two-electron operator

$$\hat{\mathcal{O}}_2 = \sum_{i<j}^{N} \mathcal{O}_2(\mathbf{r}_i\sigma_i, \mathbf{r}_j\sigma_j) \ , \tag{2.4.26}$$

the expectation value reads

$$\left\langle \hat{\mathcal{O}}_2 \right\rangle = \text{trace}(\hat{\mathcal{O}}_2 \gamma_N) = \\ \sum_{\sigma_1,\sigma_2} \int \mathrm{d}\mathbf{r}_1 \mathrm{d}\mathbf{r}_2 \ [\mathcal{O}_2(\mathbf{r}_1\sigma_1, \mathbf{r}_2\sigma_2)\gamma_2(\mathbf{r}'_1\sigma'_1, \mathbf{r}'_2\sigma'_2, \mathbf{r}_1\sigma_1, \mathbf{r}_2\sigma_2)]_{\mathbf{r}'_1\sigma'_1=\mathbf{r}_1\sigma_1, \mathbf{r}'_2\sigma'_2=\mathbf{r}_2\sigma_2} \ . \tag{2.4.27}$$

The Electronic Hamiltonian

We rewrite the N-electron Hamiltonian $\hat{\mathcal{H}}_e$ as

$$\hat{\mathcal{H}}_e = \sum_{i=1}^{N} \left(-\frac{\hbar^2}{2m_e}\nabla_i^2 + v_{\text{ext}}(\mathbf{r}_i) \right) + \sum_{i=1}^{N}\sum_{j\neq i}^{N} \frac{e^2}{2|\mathbf{r}_i - \mathbf{r}_j|} \ , \tag{2.4.28}$$

where[8]

$$v_{\text{ext}}(\mathbf{r}_i) \equiv -\sum_{I=1}^{P} \frac{Z_I e^2}{|\mathbf{r}_i - \mathbf{R}_I|} \ . \tag{2.4.29}$$

The expectation value of $\hat{\mathcal{H}}_e$ is given by

$$\left\langle \Phi \middle| \hat{\mathcal{H}}_e \middle| \Phi \right\rangle \equiv E = \left\langle \Phi \middle| \hat{T}_e + \hat{V}_{\text{ext}} + \hat{V}_{\text{ee}} \middle| \Phi \right\rangle = \left\langle \Phi \middle| \hat{T}_e \middle| \Phi \right\rangle + \left\langle \Phi \middle| \hat{V}_{\text{ext}} \middle| \Phi \right\rangle + \left\langle \Phi \middle| \hat{V}_{\text{ee}} \middle| \Phi \right\rangle \ . \tag{2.4.30}$$

[8] The subscript "ext", stands for "external", refers to the fact that the ionic subsystem is considered to be external to the electronic subsystem. cf. Ref. [89, p. 338]. As we will shortly see, the last V_{ee} term will be decomposed into Hartree, exchange and correlation contributions, that is $V_{\text{ee}} = V_{\text{Hartree}} + V_X + V_C$, and some authors (cf. [78, p. 54]) refer to it as V_{int}, where the subscript "int" stands for "internal".

From Eq. 2.4.28 above, it is clear that $\hat{T}_e$ and $\hat{V}_{\text{ext}}$ are one-particle operators, while $\hat{V}_{\text{ee}}$ is a two-body operator. Thus, using Eqs. 2.4.21, 2.4.25 and 2.4.27, one obtains

$$T_e = \left\langle \Phi \middle| \hat{T}_e \middle| \Phi \right\rangle = -\frac{\hbar^2}{2m_e} \sum_{i=1}^{N} \left\langle \Phi \middle| \nabla_i^2 \middle| \Phi \right\rangle = -\frac{\hbar^2}{2m_e} \sum_{\sigma_1} \int \mathrm{d}\mathbf{r}_1 \ \left[\nabla_1^2 \gamma_1(\mathbf{r}_1'\sigma_1', \mathbf{r}_1\sigma_1) \right]_{\mathbf{r}_1'\sigma_1'=\mathbf{r}_1\sigma_1} \tag{2.4.31}$$

$$V_{\text{ext}} = \left\langle \Phi \middle| \hat{V}_{\text{ext}} \middle| \Phi \right\rangle = \left\langle \Phi \middle| \sum_{i=1}^{N} v_{\text{ext}}(\mathbf{r}_i) \middle| \Phi \right\rangle = \sum_{\sigma_1} \int \mathrm{d}\mathbf{r}_1 \ \left[v_{\text{ext}}(\mathbf{r}_1) \gamma_1(\mathbf{r}_1'\sigma_1', \mathbf{r}_1\sigma_1) \right]_{\mathbf{r}_1'\sigma_1'=\mathbf{r}_1\sigma_1} \tag{2.4.32}$$

$$\begin{aligned} V_{\text{ee}} = \left\langle \Phi \middle| \hat{V}_{\text{ee}} \middle| \Phi \right\rangle &= \frac{1}{2} \sum_{i=1}^{N} \sum_{j \neq i}^{N} \left\langle \Phi \middle| \frac{e^2}{|\mathbf{r}_i - \mathbf{r}_j|} \middle| \Phi \right\rangle \\ &= \sum_{\sigma_1, \sigma_2} \int \mathrm{d}\mathbf{r}_1 \mathrm{d}\mathbf{r}_2 \ \left[\frac{e^2}{2|\mathbf{r}_1 - \mathbf{r}_2|} \gamma_2(\mathbf{r}_1'\sigma_1', \mathbf{r}_2'\sigma_2', \mathbf{r}_1\sigma_1, \mathbf{r}_2\sigma_2) \right]_{\mathbf{r}_1'\sigma_1'=\mathbf{r}_1\sigma_1, \mathbf{r}_2'\sigma_2'=\mathbf{r}_2\sigma_2} \end{aligned} \tag{2.4.33}$$

Putting all these together, the expectation value of the N-electron Hamiltonian $\hat{\mathcal{H}}_e$ reads [76, 95]

$$\begin{aligned} E \ &= \ \text{trace}(\hat{\mathcal{H}}_e \hat{\gamma}_N) = \sum_{\sigma_1} \int \mathrm{d}\mathbf{r}_1 \ \left[\left(-\frac{\hbar^2}{2m_e} \nabla_1^2 + v_{\text{ext}}(\mathbf{r}_1) \right) \gamma_1(\mathbf{r}_1'\sigma_1', \mathbf{r}_1\sigma_1) \right]_{\mathbf{r}_1'\sigma_1'=\mathbf{r}_1\sigma_1} \\ &+ \ \sum_{\sigma_1, \sigma_2} \int \mathrm{d}\mathbf{r}_1 \mathrm{d}\mathbf{r}_2 \ \left[\frac{e^2}{2|\mathbf{r}_1 - \mathbf{r}_2|} \gamma_2(\mathbf{r}_1'\sigma_1', \mathbf{r}_2'\sigma_2', \mathbf{r}_1\sigma_1, \mathbf{r}_2\sigma_2) \right]_{\mathbf{r}_1'\sigma_1'=\mathbf{r}_1\sigma_1, \mathbf{r}_2'\sigma_2'=\mathbf{r}_2\sigma_2} \end{aligned} \tag{2.4.34}$$

Comparing the form of $\hat{\mathcal{H}}_e$ in Eqs. 2.4.28 and 2.4.34, one notices the significant reduction of the dimensions involved in $\hat{\mathcal{H}}_e$ from $4N$ variables[9] to 8 coordinates $(\mathbf{r}_1\sigma_1, \mathbf{r}_2\sigma_2)$[10]. Noting that the operators in the $\hat{\mathcal{H}}_e$ do not involve spin coordinates, it is possible to further reduce $\gamma_1(\mathbf{r}_1'\sigma_1', \mathbf{r}_1\sigma_1)$ (Eq. 2.4.16) and $\gamma_2(\mathbf{r}_1'\sigma_1', \mathbf{r}_2'\sigma_2', \mathbf{r}_1\sigma_1, \mathbf{r}_2\sigma_2)$ (Eq. 2.4.17) by introducing the spinless density matrix via the integration over the spin coordinates [76].

[9] $3N$ spatial + N spin coordinates.
[10] Yet, one needs to evaluate γ_2 from Φ.

Spin-Free Density Matrices

The first- and the second-order spin-free density matrices are defined by

$$\begin{aligned} n_1(\mathbf{r}_1', \mathbf{r}_1) &= \sum_{\sigma_1} \gamma_1(\mathbf{r}_1'\sigma_1, \mathbf{r}_1\sigma_1) \\ &= N \sum_{\sigma_1}^{\sigma_N} \int \mathrm{d}\mathbf{r}_2 \cdots \mathrm{d}\mathbf{r}_N \; \Phi\left(\mathbf{r}_1'\sigma_1, \mathbf{r}_2\sigma_2, \cdots \mathbf{r}_N\sigma_N\right) \Phi^*\left(\mathbf{r}_1\sigma_1, \; \cdots \; \mathbf{r}_N\sigma_N\right) \end{aligned} \tag{2.4.35}$$

and

$$\begin{aligned} n_2(\mathbf{r}_1', \mathbf{r}_2', \mathbf{r}_1, \mathbf{r}_2) &= \sum_{\sigma_1, \sigma_2} \gamma_2(\mathbf{r}_1'\sigma_1, \mathbf{r}_2'\sigma_2, \mathbf{r}_1\sigma_1, \mathbf{r}_2\sigma_2) \\ &= \frac{N(N-1)}{2} \sum_{\sigma_1}^{\sigma_N} \int \mathrm{d}\mathbf{r}_3 \cdots \mathrm{d}\mathbf{r}_N \; \Phi\left(\mathbf{r}_1'\sigma_1, \mathbf{r}_2'\sigma_2, \mathbf{r}_3\sigma_3, \cdots, \mathbf{r}_N\sigma_N\right) \Phi^*\left(\mathbf{r}_1\sigma_1, \cdots, \mathbf{r}_N\sigma_N\right) \end{aligned} \tag{2.4.36}$$

Accordingly, the expectation values of Eqs. 2.4.25 and 2.4.27 now read for spin-independent operators

$$\left\langle \hat{\mathcal{O}}_1 \right\rangle = \int \mathrm{d}\mathbf{r}_1 \left[\mathcal{O}_1(\mathbf{r}_1) n_1(\mathbf{r}_1', \mathbf{r}_1)\right]_{\mathbf{r}_1' = \mathbf{r}_1} \tag{2.4.37}$$

and

$$\left\langle \hat{\mathcal{O}}_2 \right\rangle = \int \mathrm{d}\mathbf{r}_1 \mathrm{d}\mathbf{r}_2 \; \left[\mathcal{O}_2(\mathbf{r}_1, \mathbf{r}_2) n_2(\mathbf{r}_1'\mathbf{r}_2', \mathbf{r}_1\mathbf{r}_2)\right]_{\mathbf{r}_1' = \mathbf{r}_1, \mathbf{r}_2' = \mathbf{r}_2} \; . \tag{2.4.38}$$

The Electronic Hamiltonian Revisited

Using Eqs. 2.4.21, 2.4.37 and 2.4.38, the expectation values of the $\hat{\mathcal{H}}_e$ components read [75, 76]

$$T_e = \left\langle \Phi \middle| \hat{T}_e \middle| \Phi \right\rangle = -\frac{\hbar^2}{2m_e} \sum_{i=1}^{N} \left\langle \Phi \middle| \nabla_i^2 \middle| \Phi \right\rangle = -\frac{\hbar^2}{2m_e} \int \mathrm{d}\mathbf{r}_1 \; \left[\nabla_{\mathbf{r}_1}^2 n_1(\mathbf{r}_1', \mathbf{r}_1)\right]_{\mathbf{r}_1' = \mathbf{r}_1} \; , \tag{2.4.39}$$

$$V_{\text{ext}} = \left\langle \Phi \middle| \hat{V}_{\text{ext}} \middle| \Phi \right\rangle = \left\langle \Phi \middle| \sum_{i=1}^{N} v_{\text{ext}}(\mathbf{r}_i) \middle| \Phi \right\rangle = \int \mathrm{d}\mathbf{r}_1 \; \left[v_{\text{ext}}(\mathbf{r}_1) n_1(\mathbf{r}_1', \mathbf{r}_1)\right]_{\mathbf{r}_1' = \mathbf{r}_1} \; , \tag{2.4.40}$$

and

$$V_{\text{ee}} = \left\langle \Phi \middle| \hat{V}_{\text{ee}} \middle| \Phi \right\rangle = \frac{1}{2} \sum_{i=1}^{N} \sum_{j \neq i}^{N} \left\langle \Phi \middle| \frac{e^2}{|\mathbf{r}_i - \mathbf{r}_j|} \middle| \Phi \right\rangle = \int \mathrm{d}\mathbf{r}_1 \mathrm{d}\mathbf{r}_2 \left[\frac{n_2(\mathbf{r}_1' \mathbf{r}_2', \mathbf{r}_1 \mathbf{r}_2)}{|\mathbf{r}_1 - \mathbf{r}_2|} \right]_{\mathbf{r}_1' = \mathbf{r}_1,\, \mathbf{r}_2' = \mathbf{r}_2} . \tag{2.4.41}$$

Putting all these together, the expectation value of the N-electron Hamiltonian $\hat{\mathcal{H}}_e$ reads [76, 95]

$$\begin{aligned} E &= E\left[n_1(\mathbf{r}_1', \mathbf{r}_1), n_2(\mathbf{r}_1, \mathbf{r}_2)\right] = E\left[n_2(\mathbf{r}_1, \mathbf{r}_2)\right] \\ &= -\frac{\hbar^2}{2m_e} \int \mathrm{d}\mathbf{r} \, \left[\nabla_{\mathbf{r}}^2 n_1(\mathbf{r}', \mathbf{r})\right]_{\mathbf{r}' = \mathbf{r}} + \int \mathrm{d}\mathbf{r} \, v_{\text{ext}}(\mathbf{r}) n(\mathbf{r}) \quad + \quad \int \mathrm{d}\mathbf{r}_1 \mathrm{d}\mathbf{r}_2 \, \frac{n_2(\mathbf{r}_1, \mathbf{r}_2)}{|\mathbf{r}_1 - \mathbf{r}_2|} \end{aligned} \tag{2.4.42}$$

Here, the shorthand notations $n_1(\mathbf{r}_1) = n(\mathbf{r})$ and $n_2(\mathbf{r}_1, \mathbf{r}_2)$ were used for the diagonal elements of $n_1(\mathbf{r}_1', \mathbf{r}_1)$ and $n_2(\mathbf{r}_1' \mathbf{r}_2', \mathbf{r}_1 \mathbf{r}_2)$, respectively [11]. The square brackets indicate the functional dependence[12] of E on n_1 and n_2. The dependence of E on n_2 alone is evident because

$$n_1(\mathbf{r}_1', \mathbf{r}_1) = \frac{2}{N-1} \int \mathrm{d}\mathbf{r}_2 \, n_2(\mathbf{r}_1' \mathbf{r}_2', \mathbf{r}_1 \mathbf{r}_2) \quad \Longrightarrow \quad n(\mathbf{r}_1) = \frac{2}{N-1} \int \mathrm{d}\mathbf{r}_2 \, n_2(\mathbf{r}_1, \mathbf{r}_2) \tag{2.4.43}$$

as can readily be obtained from Eq. 2.4.20 [75, 76]. Moreover, Eq. 2.4.42 above involves only $n(\mathbf{r})$, a three coordinates function, and $n_1(\mathbf{r}', \mathbf{r})$ and $n_2(\mathbf{r}_1, \mathbf{r}_2)$, six coordinates functions. In addition, with the form of Eq. 2.4.29 for v_{ext}, the second term of Eq. 2.4.42 above may be written as [75]

$$V_{\text{ext}} = \left\langle \Phi \middle| \hat{V}_{\text{ext}} \middle| \Phi \right\rangle = \sum_{I=1}^{P} \left\langle \Phi \middle| \sum_{i=1}^{N} v_I(|\mathbf{r}_i - \mathbf{R}_I|) \middle| \Phi \right\rangle = \sum_{I=1}^{P} \int \mathrm{d}\mathbf{r} \, n(\mathbf{r}) v_I(|\mathbf{r} - \mathbf{R}_I|) \, . \tag{2.4.44}$$

2.4.3 Exchange and Correlation (XC)

If the two-body V_{ee} were purely classical, then the last term in Eq. 2.4.42 would have taken the classical form

$$J[n] = \frac{1}{2} \int \mathrm{d}\mathbf{r}_1 \mathrm{d}\mathbf{r}_2 \, \frac{n(\mathbf{r}_1) n(\mathbf{r}_2)}{|\mathbf{r}_1 - \mathbf{r}_2|} \tag{2.4.45}$$

[11] The diagonal element of $n_1(\mathbf{r}_1', \mathbf{r}_1) = n_1(\mathbf{r}_1) = n(\mathbf{r})$ is just the electronic density defined by Eq. 2.4.2, while the diagonal element of $n_2(\mathbf{r}_1' \mathbf{r}_2', \mathbf{r}_1 \mathbf{r}_2) = n_2(\mathbf{r}_1 \mathbf{r}_2, \mathbf{r}_1 \mathbf{r}_2) = n_2(\mathbf{r}_1, \mathbf{r}_2)$ is the joint density of Eq. 2.4.5, regardless of the spin of the electrons in both cases.

[12] For a compact description of functionals and functional derivatives, cf. Ref. [97], Ref. [75, Subsec. 4.1.1], Ref. [76, Appendix A] and Ref. [78, Appendix A].

known as Hartree term or contribution. The prefactor $\frac{1}{2}$ here is to prevent double counting. Rewriting Eq. 2.4.8 as

$$n(\mathbf{r})n(\mathbf{r}')g(\mathbf{r},\mathbf{r}') = n(\mathbf{r},\mathbf{r}') = n(\mathbf{r})n(\mathbf{r}')\left[1 + h(\mathbf{r},\mathbf{r}')\right] \tag{2.4.46}$$

and reading it together with Eqs. 2.4.41 and 2.4.45 may be suggestive to separate V_{ee} into two terms [75, 76]:

$$\begin{aligned} V_{\text{ee}} &= \int \mathrm{d}\mathbf{r}'\mathrm{d}\mathbf{r}\, \frac{n_2(\mathbf{r},\mathbf{r}')}{|\mathbf{r}-\mathbf{r}'|} \\ &= \frac{1}{2}\int \mathrm{d}\mathbf{r}'\mathrm{d}\mathbf{r}\, \frac{n(\mathbf{r})n(\mathbf{r}')}{|\mathbf{r}-\mathbf{r}'|} + \frac{1}{2}\int \mathrm{d}\mathbf{r}'\mathrm{d}\mathbf{r}\, \frac{n(\mathbf{r})n(\mathbf{r}')}{|\mathbf{r}-\mathbf{r}'|}\left[g(\mathbf{r},\mathbf{r}') - 1\right] \\ &= \frac{1}{2}\int \mathrm{d}\mathbf{r}'\mathrm{d}\mathbf{r}\, \frac{n(\mathbf{r})n(\mathbf{r}')}{|\mathbf{r}-\mathbf{r}'|} + \frac{1}{2}\int \mathrm{d}\mathbf{r}'\mathrm{d}\mathbf{r}\, \frac{n(\mathbf{r})n(\mathbf{r}')}{|\mathbf{r}-\mathbf{r}'|}\left[h(\mathbf{r},\mathbf{r}')\right] . \end{aligned} \tag{2.4.47}$$

Substituting the right hand side of Eq. 2.4.46 for $n(\mathbf{r},\mathbf{r}')$ in Eq. 2.4.43 and rearranging the terms yield

$$\int \mathrm{d}\mathbf{r}'\; n(\mathbf{r}')h(\mathbf{r},\mathbf{r}') = -1 . \tag{2.4.48}$$

The integrand of the sum rule above defines the so-called exchange-correlation hole (or exchange-correlation charge) [76]:

$$n_{\text{xc}}(\mathbf{r},\mathbf{r}') = n(\mathbf{r}')h(\mathbf{r},\mathbf{r}') \quad \Longrightarrow \quad \int \mathrm{d}\mathbf{r}'\; n_{\text{xc}}(\mathbf{r},\mathbf{r}') = -1 . \tag{2.4.49}$$

That is, the integral of the hole density $n_{\text{xc}}(\mathbf{r},\mathbf{r}')$ over all $\mathbf{r}'$ is exactly one missing electron per electron at any point $\mathbf{r}$ [78]. Eq. 2.4.47 in terms of $n_{\text{xc}}(\mathbf{r},\mathbf{r}')$ now reads

$$V_{\text{ee}} = \frac{1}{2}\int \mathrm{d}\mathbf{r}'\mathrm{d}\mathbf{r}\, \frac{n(\mathbf{r})n(\mathbf{r}')}{|\mathbf{r}-\mathbf{r}'|} + \frac{1}{2}\int \mathrm{d}\mathbf{r}'\mathrm{d}\mathbf{r}\, \frac{n(\mathbf{r})}{|\mathbf{r}-\mathbf{r}'|}\, n_{\text{xc}}(\mathbf{r},\mathbf{r}') . \tag{2.4.50}$$

In the so-called Hartree approximation [98], the exchange-correlation potential, i.e. the second term of Eq. 2.4.47 and 2.4.50 is neglected altogether, and electrons are considered to be completely uncorrelated. This is equivalent to take $g(\mathbf{r},\mathbf{r}') = 1$ in Eq. 2.4.47 [75].

Exchange in the Hartree-Fock Approximation

To *exactly* include the exchange interaction, the N-electron wave function Φ can be *approximated* by a properly antisymmetrized product of N orthonormal *one-electron* spin-orbitals $\varphi_i(\mathbf{r}_j\sigma_j)$ in the form of Slater determinant [99–101]

$$\Phi \equiv \Phi_{\mathsf{HF}}\left(\mathbf{r}_1'\sigma_1, \mathbf{r}_2\sigma_2, \cdots \mathbf{r}_N\sigma_N\right) = \frac{1}{\sqrt{N!}} \begin{vmatrix} \varphi_1(\mathbf{r}_1\sigma_1) & \varphi_2(\mathbf{r}_1\sigma_1) & \cdots & \varphi_N(\mathbf{r}_1\sigma_1) \\ \varphi_1(\mathbf{r}_2\sigma_2) & \varphi_2(\mathbf{r}_2\sigma_2) & \cdots & \varphi_N(\mathbf{r}_2\sigma_2) \\ \vdots & \vdots & \ddots & \vdots \\ \varphi_1(\mathbf{r}_N\sigma_n) & \varphi_2(\mathbf{r}_N\sigma_N) & \cdots & \varphi_N(\mathbf{r}_N\sigma_N) \end{vmatrix} , \quad (2.4.51)$$

where the ith orbital φ_i associated with the jth electron is given as a product of spin and spatial components

$$\varphi_i(\mathbf{r}_j\sigma_j) = \psi_i^{\sigma_j}(\mathbf{r}_j)\alpha_i(\sigma_j) \, . \quad (2.4.52)$$

This is called the Hartree-Fock (HF) approximation [76, 78, 98, 100]. The expectation value of $\hat{\mathcal{H}}_e$ (as defined by Eq. 2.4.28) in this scheme is given by [76, 78]

$$E_{\mathsf{HF}} = \left\langle \Phi_{\mathsf{HF}} \middle| \hat{\mathcal{H}}_e \middle| \Phi_{\mathsf{HF}} \right\rangle = \sum_{i=1}^{N} h_{ii} + \frac{1}{2}\sum_{i=1}^{N}\sum_{j=1}^{N}(\mathcal{J}_{ij} - \mathcal{K}_{ij}) \, , \quad (2.4.53)$$

where

$$h_{ii} = \sum_{\sigma}\int \mathrm{d}\mathbf{r} \; \varphi_i^*(\mathbf{r}\sigma) \left(-\frac{\hbar^2}{2m_e}\nabla_{\mathbf{r}}^2 + v_{\mathsf{ext}}(\mathbf{r}\sigma)\right)\varphi_i(\mathbf{r}\sigma) \, , \quad (2.4.54)$$

$$\mathcal{J}_{ij} = \sum_{\sigma_1}\sum_{\sigma_2}\int \mathrm{d}\mathbf{r}_1\mathrm{d}\mathbf{r}_2 \;\; \varphi_i(\mathbf{r}_1\sigma_1)\varphi_i^*(\mathbf{r}_1\sigma_1)\frac{1}{|\mathbf{r}_1 - \mathbf{r}_2|}\varphi_j^*(\mathbf{r}_2\sigma_2)\varphi_j(\mathbf{r}_2\sigma_2) \, , \quad (2.4.55)$$

$$\mathcal{K}_{ij} = \sum_{\sigma_1}\sum_{\sigma_2}\int \mathrm{d}\mathbf{r}_1\mathrm{d}\mathbf{r}_2 \;\; \varphi_i^*(\mathbf{r}_1\sigma_1)\varphi_j(\mathbf{r}_1\sigma_1)\frac{1}{|\mathbf{r}_1 - \mathbf{r}_2|}\varphi_i(\mathbf{r}_2\sigma_2)\varphi_j^*(\mathbf{r}_2\sigma_2) \; \delta_{\sigma_1\sigma_2} \, . \quad (2.4.56)$$

Here, h_{ii} are the single-electron expectation values of the so-called core Hamiltonian

$$\hat{h}(\mathbf{r}_i\sigma_i) = -\frac{\hbar^2}{2m_e}\nabla_{\mathbf{r}_i}^2 + v_{\mathsf{ext}}(\mathbf{r}_i\sigma_i) \quad (2.4.57)$$

which neglects the interaction of the single electron with other electrons. The direct integral $\mathcal{J}_{ij}$ is the same as the one defined by Eq. 2.4.45 which corresponds to the classical Coulomb interaction between two charge distributions. The term $\mathcal{K}_{ij}$, known as the exchange integral, has no classical correspondence [75,76,82]. Mathematically, the minus sign arises from the fact that the $\mathcal{K}_{ij}$ terms correspond to odd permutations in the Slater determinant (Eq. 2.4.51). Physically, this can be seen as a reduction in the Coulomb interaction[13] $\mathcal{J}_{ij}$ because spin-like electrons are prohibited by the of Pauli's principle from being too close to each other [75][14].
Notice that the diagonal terms, $\mathcal{J}_{ii}$ and $\mathcal{K}_{ii}$, are counted in the summations 2.4.55 and 2.4.56, respectively. However, these unphysical self-interactions exactly cancel out in Eq. 2.4.53 due to the clear fact that [75,76,78][15]

$$\mathcal{J}_{ii} = \mathcal{K}_{ii} \ . \tag{2.4.58}$$

With the restrictions of Eq. 2.4.51, the minimization of E_{HF} (Eq. 2.4.53) with respect to all electronic degrees of freedom leads to the so-called Hartree-Fock equations [75,76,78][16]:

$$\hat{\mathcal{F}}\varphi_i(\mathbf{r}\sigma) = \left(\hat{h} + \sum_{j=1}^{N}(\hat{\mathcal{J}}_j - \hat{\mathcal{K}}_j)\right)\varphi_i(\mathbf{r}\sigma) = \varepsilon_i\varphi_i(\mathbf{r}\sigma) \ , \tag{2.4.59}$$

where $\hat{\mathcal{F}}$ is known as the Fock operator, and the Coulomb $\hat{\mathcal{J}}_j$ and the exchange $\hat{\mathcal{K}}_j$ operators are defined by

$$\hat{\mathcal{J}}_j \ \varphi_i(\mathbf{r}_2\sigma_2) = \left(\sum_{\sigma_1}\int \mathrm{d}\mathbf{r}_1 \ \ \varphi_j^*(\mathbf{r}_1\sigma_1)\frac{1}{|\mathbf{r}_1 - \mathbf{r}_2|}\varphi_j(\mathbf{r}_1\sigma_1)\right)\varphi_i(\mathbf{r}_2\sigma_2) \ , \tag{2.4.60}$$

$$\hat{\mathcal{K}}_j \ \varphi_i(\mathbf{r}_2\sigma_2) = \left(\sum_{\sigma_1}\int \mathrm{d}\mathbf{r}_1 \ \ \varphi_j^*(\mathbf{r}_1\sigma_1)\frac{1}{|\mathbf{r}_1 - \mathbf{r}_2|}\varphi_i(\mathbf{r}_1\sigma_1)\right)\varphi_j(\mathbf{r}_2\sigma_2) \ . \tag{2.4.61}$$

Since the solutions $\varphi_i(\mathbf{r}_i\sigma_i)$ to Eqs. 2.4.59 are part of the operator $\hat{\mathcal{F}}$ itself, one must solve Eq. 2.4.59 iteratively. Thus, the HF approach is a self-consistent-field (SCF) method.

[13] Indeed, with respect to the unphysical case where electrons are completely uncorrelated [75].
[14] In terms of the HF exchange density n_{xc} (Eq. 2.4.71), the lowering in the direct Coulomb interaction can be seen as the interaction of each electron with a positive n_{xc} that surrounds it [78].
[15] Note that the case $i = j$ does not correspond to any permutation in the Slater determinant (Eq. 2.4.51) [75].
[16] In fact, Eqs. 2.4.59 are termed as the *canonical representation of the HF equations*. For details, readers are referred to, e.g., Refs. [75,76].

The total electronic energy expectation value E in terms of the Fock operator eigenvalues[17]

$$\varepsilon_i = h_{ii} + \sum_{j=1}^{N} (\mathcal{J}_{ij} - \mathcal{K}_{ij}) \tag{2.4.62}$$

now reads [75, 76]

$$E_{\text{HF}} = \sum_{i=1}^{N} \varepsilon_i - \frac{1}{2} \sum_{i=1}^{N} \sum_{j=1}^{N} (\mathcal{J}_{ij} - \mathcal{K}_{ij}) \, , \tag{2.4.63}$$

To restate the HF method in terms of density matrices (Subsec. 2.4.2), we start by considering the single determinant of Eq. 2.4.51. It is straightforward to show that the p^{th} order reduced density matrix is [76]

$$\gamma_p(\mathbf{r}'_1\sigma'_1, \mathbf{r}'_2\sigma'_2, \cdots \mathbf{r}'_p\sigma'_p, \mathbf{r}_1\sigma_1, \mathbf{r}_2\sigma_2, \cdots \mathbf{r}_p\sigma_p) = \frac{1}{p!} \begin{vmatrix} \gamma_1(\mathbf{r}'_1\sigma'_1, \mathbf{r}_1\sigma_1) & \gamma_1(\mathbf{r}'_1\sigma'_1, \mathbf{r}_2\sigma_2) & \cdots & \gamma_1(\mathbf{r}'_1\sigma'_1, \mathbf{r}_p\sigma_p) \\ \gamma_1(\mathbf{r}'_2\sigma'_2, \mathbf{r}_1\sigma_1) & \gamma_1(\mathbf{r}'_2\sigma'_2, \mathbf{r}_2\sigma_2) & \cdots & \gamma_1(\mathbf{r}'_2\sigma'_2, \mathbf{r}_p\sigma_p) \\ \vdots & \vdots & \ddots & \vdots \\ \gamma_1(\mathbf{r}'_p\sigma'_p, \mathbf{r}_1\sigma_1) & \gamma_1(\mathbf{r}'_p\sigma'_p, \mathbf{r}_2\sigma_2) & \cdots & \gamma_1(\mathbf{r}'_p\sigma'_p, \mathbf{r}_p\sigma_p) \end{vmatrix} , \tag{2.4.64}$$

where the first order reduced density matrix

$$\gamma_1(\mathbf{r}'_1\sigma'_1, \mathbf{r}_1\sigma_1) = \sum_{i=1}^{N} \varphi_i(\mathbf{r}'_1\sigma'_1)\varphi_i^*(\mathbf{r}_1\sigma_1) \, , \tag{2.4.65}$$

known as Fock-Dirac density matrix, can be written in the operator form as [76][18]

$$\hat{\gamma}_1 = \sum_{i=1}^{N} |\varphi_i\rangle\langle\varphi_i| \, . \tag{2.4.66}$$

[17] Sometimes the Fock operator eigenvalues are called "orbital energies". cf. Ref. [76].

[18] It is easy to see that $\hat{\gamma}_1$ is a projector onto the space that is spanned by the N occupied HF orbitals φ_i.

In particular

$$\gamma_2(\mathbf{r}'_1\sigma'_1,\mathbf{r}'_2\sigma'_2) = \frac{1}{2!}\begin{vmatrix}\gamma_1(\mathbf{r}'_1\sigma'_1,\mathbf{r}_1\sigma_1) & \gamma_1(\mathbf{r}'_1\sigma'_1,\mathbf{r}_2\sigma_2)\\ \gamma_1(\mathbf{r}'_2\sigma'_2,\mathbf{r}_1\sigma_1) & \gamma_1(\mathbf{r}'_2\sigma'_2,\mathbf{r}_2\sigma_2)\end{vmatrix}$$
$$= \frac{1}{2}\left[\gamma_1(\mathbf{r}'_1\sigma'_1,\mathbf{r}_1\sigma_1)\gamma_1(\mathbf{r}'_2\sigma'_2,\mathbf{r}_2\sigma_2) - \gamma_1(\mathbf{r}'_1\sigma'_1,\mathbf{r}_2\sigma_2)\gamma_1(\mathbf{r}'_2\sigma'_2,\mathbf{r}_1\sigma_1)\right] . \quad (2.4.67)$$

Inserting 2.4.67 above in Eq. 2.4.34, the expectation value of the N-electron Hamiltonian $\hat{\mathcal{H}}_e$ reads [76]

$$E_{\mathsf{HF}}[\gamma_1] = \sum_{\sigma_1}\int \mathrm{d}\mathbf{r}_1 \left[\left(-\frac{\hbar^2}{2m_e}\nabla_1^2 + v_{\mathsf{ext}}(\mathbf{r}_1\sigma_1)\right)\gamma_1(\mathbf{r}'_1\sigma'_1,\mathbf{r}_1\sigma_1)\right]_{\mathbf{r}'_1\sigma'_1=\mathbf{r}_1\sigma_1}$$
$$+ \frac{1}{2}\sum_{\sigma_1,\sigma_2}\int \mathrm{d}\mathbf{r}_1\mathrm{d}\mathbf{r}_2\, e^2\left[\frac{\gamma_1(\mathbf{r}_1\sigma_1,\mathbf{r}_1\sigma_1)\gamma_1(\mathbf{r}_2\sigma_2,\mathbf{r}_2\sigma_2)}{|\mathbf{r}_1-\mathbf{r}_2|} - \frac{\gamma_1(\mathbf{r}_1\sigma_1,\mathbf{r}_2\sigma_2)\gamma_1(\mathbf{r}_2\sigma_2,\mathbf{r}_1\sigma_1)}{|\mathbf{r}_1-\mathbf{r}_2|}\right] \quad (2.4.68)$$

Eq. 2.4.68 above is to be compared with Eq. 2.4.53.

To express E_{HF} in terms of the spin-free density matrices (Subsec. 2.4.2) one uses the definitions 2.4.35, 2.4.36, 2.4.37, and 2.4.37, and it is straightforward (cf. Ref. [76, p. 39]) to rewrite the expectation value of the N-electron Hamiltonian $\hat{\mathcal{H}}_e$ (Eq. 2.4.42) in the HF picture as [76]

$$E_{\mathsf{HF}}[n_1] = \underbrace{\int \mathrm{d}\mathbf{r}_1 \left[-\frac{\hbar^2}{2m_e}\nabla_1^2 n_1(\mathbf{r}'_1,\mathbf{r}_1)\right]_{\mathbf{r}'_1=\mathbf{r}_1}}_{T_e[n_1]} + \underbrace{\int \mathrm{d}\mathbf{r}\; v_{\mathsf{ext}}(\mathbf{r})n(\mathbf{r})}_{V_{\mathsf{en}}[n]} + \underbrace{\frac{1}{2}\int \mathrm{d}\mathbf{r}_1\mathrm{d}\mathbf{r}_2\, e^2\,\frac{n(\mathbf{r}_1)n(\mathbf{r}_2)}{|\mathbf{r}_1-\mathbf{r}_2|}}_{\mathcal{J}[n]}$$
$$\underbrace{-\frac{1}{2}\int \mathrm{d}\mathbf{r}_1\mathrm{d}\mathbf{r}_2\, e^2\left[\frac{n_1^{\alpha\alpha}(\mathbf{r}_1,\mathbf{r}_2)n_1^{\alpha\alpha}(\mathbf{r}_2,\mathbf{r}_1)}{|\mathbf{r}_1-\mathbf{r}_2|} + \frac{n_1^{\beta\beta}(\mathbf{r}_1,\mathbf{r}_2)n_1^{\beta\beta}(\mathbf{r}_2,\mathbf{r}_1)}{|\mathbf{r}_1-\mathbf{r}_2|}\right]}_{\mathcal{K}[n_1]}$$
$$= T_e[n_1] + V_{\mathsf{en}}[n] + \mathcal{J}[n] - \mathcal{K}[n_1] , \quad (2.4.69)$$

where the n_1 matrices in the last integral have been resolved into components which arise from different spins [76]

$$n_1(\mathbf{r}_i,\mathbf{r}_j) = n_1^{\alpha\alpha}(\mathbf{r}_i,\mathbf{r}_j) + n_1^{\beta\beta}(\mathbf{r}_i,\mathbf{r}_j) \quad (2.4.70)$$

The exchange-correlation hole $n_{\rm xc}$ in the HF approximation can be obtained by comparing the electron-electron interaction terms in Eq. 2.4.69 above with Eq. 2.4.50

$$n_{\rm xc}^{\rm HF}(\mathbf{r}_1,\mathbf{r}_2) = n_{\rm x}^{\rm HF}(\mathbf{r}_1,\mathbf{r}_2) = -\frac{1}{2}\frac{|n_1(\mathbf{r}_1,\mathbf{r}_2)|^2}{n(\mathbf{r}_1)} \ , \tag{2.4.71}$$

and the pair correlation function (Eq. 2.4.49) reads [76]

$$h_{\rm xc}^{\rm HF}(\mathbf{r}_1,\mathbf{r}_2) = h_{\rm x}^{\rm HF}(\mathbf{r}_1,\mathbf{r}_2) = -\frac{1}{2}\frac{|n_1(\mathbf{r}_1,\mathbf{r}_2)|^2}{n(\mathbf{r}_1)n(\mathbf{r}_2)} \ . \tag{2.4.72}$$

It is evident from the foregoing discussion (cf. the $\mathcal{K}[n_1]$ term in Eq. 2.4.69) that the only correlation included in the HF scheme is the exchange interaction among the spin-like electrons. In this sense, the term "correlation" is reserved for further corrections beyond the HF method, excluding the exchange contribution [89]. That is [76]

$$E_{\rm c}^{\rm HF} = E^{\rm exact} - E^{\rm HF} \ . \tag{2.4.73}$$

Thus, while the exact expression for the exchange hole $n_{\rm x}(\mathbf{r},\mathbf{r}')$ can be derived [76], the basic shortcoming of this scheme is that correlation effects, due to the two-electron Coulomb interactions, are not taken into account [75, 102]. Nevertheless, The HF method introduces the idea of separation of interaction effects into exchange and correlation $n_{\rm xc}(\mathbf{r},\mathbf{r}') = n_{\rm x}(\mathbf{r},\mathbf{r}') + n_{\rm c}(\mathbf{r},\mathbf{r}')$ [102].

In first-principles electronic structure calculations, a large amount of work has been devoted to calculations of exchange and correlation, since it turns out that the XC contribution is crucial for describing many physical properties and phenomena. Several methods which can treat correlation with a high accuracy exist. Details about some of these methods and further formal properties of $n_{\rm x}(\mathbf{r},\mathbf{r}')$ will be given in Subsec. 3.6.3 [19].

[19] At this stage, one can go no further beyond this point, simply because the XC energy is considered as the correction to the energy obtained by any approximate method; i.e. $E_{\rm xc} = E^{\rm exact} - E^{\rm approximate}$. Moreover, there is still a correlation piece that stems from the (approximated) kinetic energy [95] which we have not considered

2.5 Summary

Substituting Eq. 2.4.50 into Eq. 2.4.42, the energy of the electronic subsystem reads

$$E(\mathbf{R}) = \langle \hat{\mathcal{H}}_e \rangle = -\frac{\hbar^2}{2m_e} \int \mathrm{d}\mathbf{r} \ \left[\nabla^2_{\mathbf{r}} n_1(\mathbf{r}', \mathbf{r})\right]_{\mathbf{r}'=\mathbf{r}} + \int \mathrm{d}\mathbf{r} \ n(\mathbf{r}) v_{\text{ext}}(\mathbf{r}; \mathbf{R}) + \frac{1}{2} \int \mathrm{d}\mathbf{r}' \mathrm{d}\mathbf{r} \ \frac{n(\mathbf{r}) n(\mathbf{r}')}{|\mathbf{r} - \mathbf{r}'|} + \frac{1}{2} \int \mathrm{d}\mathbf{r}' \mathrm{d}\mathbf{r} \ \frac{n(\mathbf{r})}{|\mathbf{r} - \mathbf{r}'|} \ n_{\text{xc}}(\mathbf{r}, \mathbf{r}') \ . \tag{2.5.1}$$

It is this form of $\langle \hat{\mathcal{H}}_e \rangle$ which we are going to consider and treat in the rest of the present thesis.

Within the assumption that the nuclear and the electronic degrees of freedom can be decoupled, and regardless of the electronic structure calculations method, once the ground-state $E(\mathbf{R})$ of Eq. 2.5.1 above (i.e. the solution of Schrödinger equation of the electrons 2.2.3) is obtained, all physical properties are, in principle, now accessible. For example, one can:

- optimize the geometry (i.e. find the equilibrium structural parameters) by solving the stationary problem of Eq. 2.3.9 (more in Ch. 7);
- apply a varying isotropic pressure to study the energy-volume and enthalpy-pressure equation of states (more in Sections 7.4 and 7.6);
- apply non-isotropic strain to calculate elastic properties (cf. Ref. [103]);
- obtain the eigenstate states from the solution of Eq. 2.2.3 and calculate the electronic properties; e.g. band diagrams (more in Sec. 8.1), density of states (more in Sec. 8.2) and chemical bonds (cf. Ref. [104]);
- or integrate Eq. 2.2.3 to study the dynamical and thermal properties (cf. Ref. [105]).
- Moreover, excitation[20] spectra can be calculated by applying perturbation techniques on top of the obtained ground-state (more in Ch. 4.5).

This idea is depicted schematically in Fig. 2.1. Moreover, it is becoming clear that the electronic density plays a major role in the electronic structure calculations. Using the density matrix

yet.

[20] At this stage it may be worth to mention that it is crucial to distinguish between ground and excited states. Some properties at first sight may be considered as excited states while they are purely ground-state properties [78].

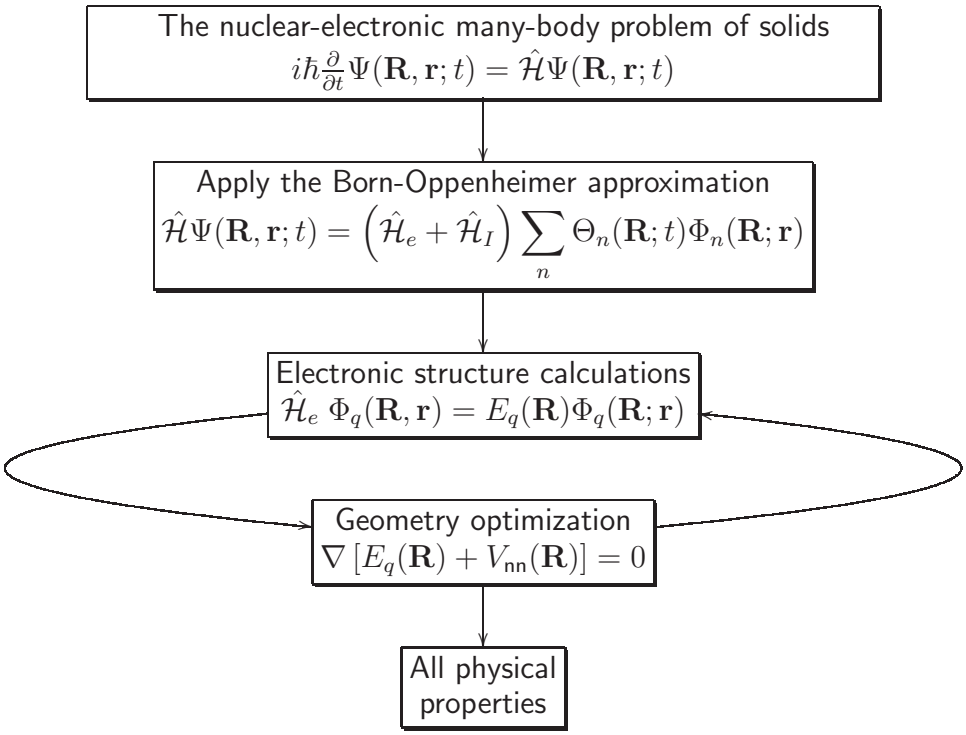

Figure 2.1: A schematic mind mapping of the *big picture* of the electronic structure calculations. The loop indicated in the Figure refers to changing ionic configurations (and not to changing electronic densities and wavefunctions). See the text.

formalism, the components of the exact (Eq. 2.5.1) and of the approximate (Eq. 2.4.69) total electronic energy were written as functionals of the electronic density and of the first-order density matrix. In addition, the canonical representation of the HF equations (Eqs. 2.4.59) and the corresponding total electronic energy (Eq. 2.4.63) may suggest that one can develop a many-electron theory starting from an independent-electron approximation.

A major strategy in the field of electronic structure calculations introduced by the HF method has been developed through out the present chapter. The idea is to resolve the electron-electron interaction term V_{ee} of the original electronic Hamiltonian $\hat{\mathcal{H}}_e$ into three components of decreasing energetic contributions [75, 102][21] and of decreasing importance: (i) The far largest contribution and the exactly known Hartree classical electrostatic Coulomb interaction. (ii) The second large contribution is the exchange term. In principle, it can be calculated exactly, at least in the HF formalism, but it is computationally expensive. (iii) The last and the smallest contribution comes

[21] In atoms and molecules, the exchange energies are found to be an order of magnitude or more bigger than the correlation energies [76].

from the correlation term, and represents the correction to the total electronic energy obtained by any approximate method.

Bearing the foregoing picture in mind, the most widely used ground-state electronic structure calculations approach, density functional theory [76, 106–109], is described in the next chapter, followed by a chapter on the GW approximation [80, 110], a successful approximation for determination of excited states.

3. Density-Functional Theory (DFT)

In Sec. 2.4, we formally addressed the electronic *problem* of matter and introduced some notions, concepts and methods. In particular the electronic density, the single-electron core Hamiltonian, the one electron contribution to the total electronic energy (orbital energy), the exchange and the correlation interactions, and the self-consistent field methods. In the present chapter, we consider an in principle exact *solution* to the problem, the Density-Functional Theory (DFT) method.

Due to its unique combination of reasonable accuracy and low computational cost, DFT may be considered as the most successful and the most widely used theoretical method in the field of electronic structure calculations [87, 111, 112]. In fact, many of the successes of modern condensed-matter physics and chemistry are connected with the development of DFT [113]. Together with the Hellmann-Feynman force theorem (see Sec. 2.3), structural, electronic and dynamic properties can be investigated simultaneously, giving rise to a profound impact on the materials characterization [87]. Within the introduced many-electron problem of the previous chapter, the goal of the present chapter is to undertake a brief review of the DFT approach.

3.1 Thomas-Fermi-Dirac Approximation

The original idea of density functional theory was the proposal of Thomas [114] and Fermi [115] who, independently, suggested that the many-electron wave function can be replaced by the (non-interacting) electrons density $n(\mathbf{r})$ as the fundamental quantity. In the original Thomas-Fermi model, exchange and correlation were neglected, but the former was introduced into the picture later by Dirac [116]. The total energy E in this Thomas-Fermi-Dirac (TFD) model is then given by (compare with Eq. 2.5.1)

$$E^{\mathsf{TFD}}[n(\mathbf{r})] = C_{\mathsf{k}} \int \mathrm{d}\mathbf{r}\; n(\mathbf{r})^{5/3} + \int \mathrm{d}\mathbf{r}\; n(\mathbf{r}) v_{\mathsf{ext}}(\mathbf{r}) + \frac{1}{2} \int \mathrm{d}\mathbf{r}' \mathrm{d}\mathbf{r}\; \frac{n(\mathbf{r}) n(\mathbf{r}')}{|\mathbf{r} - \mathbf{r}'|} - C_X \int \mathrm{d}\mathbf{r}\; n(\mathbf{r})^{4/3} \,. \tag{3.1.1}$$

The terms here are the kinetic, external, Hartree and exchange contribution, respectively; and C_{k} and C_{X} are constants. It is clear that the total energy and each contribution (α) is given as an

explicit functional of the electronic density

$$E_\alpha[n(\mathbf{r})] = C_\alpha \int \mathrm{d}\mathbf{r}\; n(\mathbf{r})\; \varepsilon_\alpha[n(\mathbf{r})]\;, \tag{3.1.2}$$

where $\varepsilon_\alpha[n(\mathbf{r})]$ is the energy density of the α component evaluated locally[1].

To find the ground-state energy and density within this model, one should minimize $E^{\mathsf{TFD}}[n(\mathbf{r})]$ with respect to $n(\mathbf{r})$ under the constraint

$$\int \mathrm{d}\mathbf{r}\; n(\mathbf{r}) = N\;. \tag{3.1.3}$$

Using the Lagrange multipliers method, this minimization reads

$$\frac{\delta}{\delta n(\mathbf{r})}\left(E^{\mathsf{TFD}}[n(\mathbf{r})] - \mu\left[\int \mathrm{d}\mathbf{r}\; n(\mathbf{r}) - N\right]\right) = 0\;. \tag{3.1.4}$$

The original TFD approach is too crude, missing essential physics and chemistry [78], and many modifications, improvements and extensions to it exist. Details can be found in many books and articles; e.g. Ref. [76, Sec. 3.1], Ref. [75, Sec. 4.1], Ref. [78, Sec. 6.1], and references therein. Nevertheless, the realization that the $3N$ degrees of freedom in the Schrödinger wave function can be replaced with only one variable $n(\mathbf{r})$ provided the key step to an exact theory: the Hohenberg-Kohn density functional theory [106].

3.2 The Hohenberg-Kohn Theorems

Recall Eqs. 2.4.30 and 2.4.32; and let E_0 and Φ be the ground state energy and function of $\hat{\mathcal{H}}_e$

$$E_0 = \left\langle \Phi \middle| \hat{\mathcal{H}}_e \middle| \Phi \right\rangle = \left\langle \Phi \middle| \hat{T}_e + \hat{V}_{\mathsf{ee}} + \hat{V}_{\mathsf{ext}} \middle| \Phi \right\rangle = \left\langle \Phi \middle| \hat{T}_e + \hat{V}_{\mathsf{ee}} \middle| \Phi \right\rangle + \int \mathrm{d}\mathbf{r}\; n_0(\mathbf{r}) v_{\mathsf{ext}}(\mathbf{r})\;. \tag{3.2.1}$$

[1] This is the first local density approximation (LDA). Dirac formulated the LDA for the E_X, i.e. the last term in Eq. 3.1.1, which is still being used today [75, 76, 78]. The first term in Eq. 3.1.1 is the famous TF kinetic energy functional, and one should recall that $\hat{T}_e$ is a non-local operator as seen from Eq. 2.4.39 [76, 78].

Also, let E_0' and Φ' be the ground state energy and function of the $\hat{\mathcal{H}}_e'$

$$E_0' = \left\langle \Phi' \middle| \hat{\mathcal{H}}_e' \middle| \Phi' \right\rangle = \left\langle \Phi' \middle| \hat{T}_e + \hat{V}_{\text{ee}} + \hat{V}_{\text{ext}}' \middle| \Phi' \right\rangle = \left\langle \Phi' \middle| \hat{T}_e + \hat{V}_{\text{ee}} \middle| \Phi' \right\rangle + \int \mathrm{d}\mathbf{r}\; n_0(\mathbf{r}) v_{\text{ext}}'(\mathbf{r}) \; . \tag{3.2.2}$$

Here, we have assumed that $[v_{\text{ext}}(\mathbf{r}) - v_{\text{ext}}'(\mathbf{r}) \neq \text{const.}]$ but both $v_{\text{ext}}(\mathbf{r})$ and $v_{\text{ext}}'(\mathbf{r})$ lead to the same ground state density $n_0(\mathbf{r})$. From the variational principle (cf. Ref. [82, Ch. 7]), it follows that

$$E_0 < \left\langle \Phi' \middle| \hat{\mathcal{H}}_e \middle| \Phi' \right\rangle = \left\langle \Phi' \middle| \hat{\mathcal{H}}_e' \middle| \Phi' \right\rangle + \left\langle \Phi' \middle| \hat{\mathcal{H}}_e - \hat{\mathcal{H}}_e' \middle| \Phi' \right\rangle = E_0' + \int \mathrm{d}\mathbf{r}\; n_0(\mathbf{r}) \left(v_{\text{ext}}(\mathbf{r}) - v_{\text{ext}}'(\mathbf{r}) \right) \; , \tag{3.2.3}$$

and

$$E_0' < \left\langle \Phi \middle| \hat{\mathcal{H}}_e' \middle| \Phi \right\rangle = \left\langle \Phi \middle| \hat{\mathcal{H}} \middle| \Phi \right\rangle - \left\langle \Phi \middle| \hat{\mathcal{H}}_e - \hat{\mathcal{H}}_e' \middle| \Phi \right\rangle = E_0 - \int \mathrm{d}\mathbf{r}\; n_0(\mathbf{r}) \left(v_{\text{ext}}(\mathbf{r}) - v_{\text{ext}}'(\mathbf{r}) \right) \; . \tag{3.2.4}$$

Adding inequality 3.2.3 to inequality 3.2.4 leads to the inconsistency

$$E_0 + E_0' < E_0 + E_0' \; , \tag{3.2.5}$$

This *reductio ad absurdum* argument proves the first Hohenberg-Kohn (HK) theorem [106]:

- **Theorem 1** *The external potential $v_{\text{ext}}(\mathbf{r})$ is (up to a constant) a unique functional of the ground state electronic density $n_0(\mathbf{r})$.*
- **Corollary** *Since $n(\mathbf{r})$ univocally determines $v_{\text{ext}}(\mathbf{r})$, and thus fully determines $\hat{\mathcal{H}}_e$, it follows that all (ground and excited state) properties are completely determined given $n_0(\mathbf{r})$* [75, 78].

Now, since Φ is a functional of $n(\mathbf{r})$, let us construct a universal functional $F[n(\mathbf{r})]$, which is valid for any number of particles and for (and independent of) any external potential [106], by

$$F[n(\mathbf{r})] = \left\langle \Phi[n(\mathbf{r})] \middle| \hat{T}_e + \hat{V}_{\text{ee}} \middle| \Phi[n(\mathbf{r})] \right\rangle \; , \tag{3.2.6}$$

where the non-negative density $n(\mathbf{r})$ corresponds to some $v_{\text{ext}}(\mathbf{r})$ and satisfies

$$\int \mathrm{d}\mathbf{r}\; n(\mathbf{r}) = N\;. \tag{3.2.7}$$

Consider a system with the ground state density $n_0(\mathbf{r})$ and wave function $\Phi[n_0(\mathbf{r})]$. Using the definition 3.2.6 above, the ground state energy of this system can be written as

$$\begin{aligned} E_0[n_0(\mathbf{r})] = \Big\langle \Phi[n_0(\mathbf{r})]\Big|\hat{\mathcal{H}}_e\Big|\Phi[n_0(\mathbf{r})]\Big\rangle = F[n_0(\mathbf{r})] + \int \mathrm{d}\mathbf{r}\; n_0(\mathbf{r})v_{\text{ext}}(\mathbf{r}) \\ = T_e[n_0(\mathbf{r})] + V_{\text{ee}}[n_0(\mathbf{r})] + \int \mathrm{d}\mathbf{r}\; n_0(\mathbf{r})v_{\text{ext}}(\mathbf{r})\;. \end{aligned} \tag{3.2.8}$$

Consider a different density $n(\mathbf{r})$ which corresponds to a different wave function $\Phi[n(\mathbf{r})]$. It follows from the variational principle that

$$\begin{aligned} \Big\langle \Phi[n(\mathbf{r})]\Big|\hat{\mathcal{H}}_e\Big|\Phi[n(\mathbf{r})]\Big\rangle = F[n(\mathbf{r})] \;\; + \int \mathrm{d}\mathbf{r}\; n(\mathbf{r})v_{\text{ext}}(\mathbf{r}) = \\ E[n(\mathbf{r})] > E_0[n_0(\mathbf{r})] \\ = \Big\langle \Phi[n_0(\mathbf{r})]\Big|\hat{\mathcal{H}}_e\Big|\Phi[n_0(\mathbf{r})]\Big\rangle = F[n_0(\mathbf{r})] + \int \mathrm{d}\mathbf{r}\; n_0(\mathbf{r})v_{\text{ext}}(\mathbf{r}) \end{aligned} \tag{3.2.9}$$

The inequality 3.2.9 above defines the variational energy $E[n(\mathbf{r})]$ and proves the second HK theorem [106]:

- **Theorem 2** *There exists a universal functional of the density, $F[n(\mathbf{r})]$, independent of $v_{ext}(\mathbf{r})$, such that the expression*

$$E[n(\mathbf{r})] \equiv F[n(\mathbf{r})] + \int \mathrm{d}\mathbf{r}\; n(\mathbf{r})v_{ext}(\mathbf{r}) = T_e[n(\mathbf{r})] + V_{ee}[n(\mathbf{r})] + \int \mathrm{d}\mathbf{r}\; n(\mathbf{r})v_{ext}(\mathbf{r}) \tag{3.2.10}$$

  has as its global minimum value the correct ground state energy associated with $v_{ext}(\mathbf{r})$, and the density $n(\mathbf{r})$ that minimizes $E[n(\mathbf{r})]$ is the exact ground state density $n_0(\mathbf{r})$.

- **Corollary** *The functional $E[n(\mathbf{r})]$ alone is sufficient to determine the ground state energy and density. Electronic excited states may be determined by other means* [78].

The variational search for the ground state density $n_0(\mathbf{r})$ can be achieved by minimization of $E[n(\mathbf{r})]$ with respect to the density $n(\mathbf{r})$ via the Lagrange multipliers method (compare with Eq.

3.1.4 in TFD)

$$\frac{\delta}{\delta n(\mathbf{r})}\left(E^{\mathsf{HK}}[n(\mathbf{r})]-\mu\left[\int \mathrm{d}\mathbf{r}\; n(\mathbf{r})-N\right]\right)=0\;, \tag{3.2.11}$$

where μ is the Lagrange multiplier

$$\mu=\frac{\delta E^{\mathsf{HK}}[n(\mathbf{r})]}{\delta n(\mathbf{r})}=\frac{\delta F[n(\mathbf{r})]}{\delta n(\mathbf{r})}+v_{\mathsf{ext}}(\mathbf{r})\;. \tag{3.2.12}$$

The two Theorems above establish the mathematical basis of the Hohenberg-Kohn density functional theory (DFT) [75]. However, in the spirit of Eqs. 2.5.1 and 2.4.69, we may rewrite the HK total energy functional 3.2.10 as[2]

$$\begin{aligned}E_{\mathsf{HK}}[n(\mathbf{r})]&=T_e[n(\mathbf{r})]+V_{\mathsf{ee}}[n(\mathbf{r})]+\int \mathrm{d}\mathbf{r}\; n(\mathbf{r})v_{\mathsf{ext}}(\mathbf{r})\\&=T_e[n(\mathbf{r})]+\mathcal{J}[n(\mathbf{r})]+\overbrace{V_{\mathsf{ee}}[n(\mathbf{r})]-\mathcal{J}[n(\mathbf{r})]}^{V_{\mathrm{xc}}[n(\mathbf{r})]}+\int \mathrm{d}\mathbf{r}\; n(\mathbf{r})v_{\mathsf{ext}}(\mathbf{r})\\&=T_e[n(\mathbf{r})]+\mathcal{J}[n(\mathbf{r})]+V_{\mathrm{xc}}[n(\mathbf{r})]+V_{\mathsf{ext}}[n(\mathbf{r})]\;.\end{aligned} \tag{3.2.13}$$

3.3 The Constrained Search Formulation of DFT

According to the variational principle, the strict inequality in Eqs. 3.2.3 and 3.2.4 is true only for non-degenerate ground-state [76, 78, 117]. For a degenerate ground state, the ground state density $n_0(\mathbf{r})$, which determines $\hat{H}_e$ and its eigenstate states, may correspond to different wave functions. Moreover, the HK variational search (Eqs. 3.2.9 and 3.2.11) may readily lead to wave functions, which all correspond to the ground state density $n_0(\mathbf{r})$, but they are physically unacceptable, e.g. not antisymmetric [75].

In 1982, an alternative two-step minimization procedure, and thus an alternative definition of the functional $F[n(\mathbf{r})]$ and a reformulation of the HK DFT, was given independently [117] by Levy [118] and Lieb [119,120]. Consider the class of the antisymmetric N-electron wave functions $\Phi(\mathbf{R},\mathbf{r})$ of Eq. 2.2.3 that correspond to the same electronic density $n(\mathbf{r})$. The total electronic energy for each of these Φ's is given by Eq. 2.4.30. Following the traditional Rayleigh-Ritz

[2] Recall the conclusion we made in Sec. 2.5. See also [76, p.52].

variational principle (cf. Ref. [82, Ch. 7]), the first step is to minimize the energy over this class of wave functions Φ with the same density $n(\mathbf{r})$ [3]:

$$E_{\mathsf{LL}}[n] = \min_{\Phi\to n(\mathbf{r})} \left\langle \Phi \middle| \hat{\mathcal{H}}_e \middle| \Phi \right\rangle = \min_{\Phi\to n(\mathbf{r})} \left(\left\langle \Phi \middle| \hat{T}_e + \hat{V}_{\mathsf{ee}} \middle| \Phi \right\rangle + \int \mathrm{d}\mathbf{r}\; n(\mathbf{r}) v_{\mathsf{ext}}(\mathbf{r}) \right)$$
$$= \min_{\Phi\to n(\mathbf{r})} \left\langle \Phi \middle| \hat{T}_e + \hat{V}_{\mathsf{ee}} \middle| \Phi \right\rangle + \int \mathrm{d}\mathbf{r}\; n(\mathbf{r}) v_{\mathsf{ext}}(\mathbf{r}) \; . \tag{3.3.1}$$

Thus, $E_{\mathsf{LL}}[n]$ of Eq. 3.3.1 above is the unique lowest density for that $n(\mathbf{r})$ [78], and defines the universal Levy-Lieb functional

$$F_{\mathsf{LL}}[n] \equiv \min_{\Phi\to n(\mathbf{r})} \left\langle \Phi \middle| \hat{T}_e + \hat{V}_{\mathsf{ee}} \middle| \Phi \right\rangle \; . \tag{3.3.2}$$

That is to say, the functional $F_{\mathsf{LL}}[n]$ searches over all Φ's that yield the input $n(\mathbf{r})$ and then delivers the minimum of $\left\langle \Phi \middle| \hat{T}_e + \hat{V}_{\mathsf{ee}} \middle| \Phi \right\rangle$ [76]. The second step is to consider all the classes of the wave functions Φ and sort them according to the densities $n(\mathbf{r})$ to which they correspond to. The ground state energy E_0 is then found by minimizing $E_{\mathsf{LL}}[n]$ over these densities [78, 117]

$$E_0[n_0(\mathbf{r})] = \min_{n(\mathbf{r})} E_{\mathsf{LL}}[n] = \min_{n(\mathbf{r})} \left(\min_{\Phi\to n(\mathbf{r})} \left\langle \Phi \middle| \hat{T}_e + \hat{V}_{\mathsf{ee}} \middle| \Phi \right\rangle + \int \mathrm{d}\mathbf{r}\; n(\mathbf{r}) v_{\mathsf{ext}}(\mathbf{r}) \right)$$
$$= \left\langle \Phi_0[n_0(\mathbf{r})] \middle| \hat{T}_e + \hat{V}_{\mathsf{ee}} \middle| \Phi_0[n_0(\mathbf{r})] \right\rangle + \int \mathrm{d}\mathbf{r}\; n_0(\mathbf{r}) v_{\mathsf{ext}}(\mathbf{r}) \; , \tag{3.3.3}$$

under the constraint that $\int \mathrm{d}\mathbf{r}\; n(\mathbf{r}) = N$ [80].

Comparing the LL formulation to the HK one, a few remarks must be stated:

- While the HK functional (Eq. 3.2.6) applies only to ground state densities, the LL functional (Eq. 3.3.2) considers a wider class of densities [117].
- While in the HK formalism the search is restricted to non-degenerate states, degenerate states are automatically searched over in the LL formulation [78, 117].
- The LL functional (Eq. 3.3.2) is formally more tractable, its physical meaning is clarified, and, in principle, can be obtained exactly [78].

[3] Recall Eqs. 2.4.30, 2.4.32 and 3.2.1.

- The LL functional is defined for any $n(\mathbf{r})$ derivable from an N-electron wave function Φ [4]; while the HK functional is defined only for densities $n(\mathbf{r})$ that can be generated by some external potential $v_{\text{ext}}(\mathbf{r})$ [5]. The existence of the former Φ's for any $n(\mathbf{r})$'s satisfying simple conditions is known, while the conditions of the latter $n(\mathbf{r})$'s are not known in general [76, 78][6].

- The LL constrained search to the subspace of the antisymmetric N-electron wave functions $\Phi(\mathbf{R}, \mathbf{r})$ eliminates the possibility of considering unphysical wave functions [75].

- Weaker conditions are required to construct F_{LL} than F_{HK}[7].

- Recalling the definition 3.3.2, and comparing the first term in the last part of Eq. 3.3.3 with the corresponding one of inequality 3.2.9, one readily sees that

$$F_{\text{HK}}[n_0(\mathbf{r})] = \min_{\Phi \to n_0(\mathbf{r})} \left\langle \Phi \middle| \hat{T}_e + \hat{V}_{\text{ee}} \middle| \Phi \right\rangle = F_{\text{LL}}[n_0(\mathbf{r})] \tag{3.3.4}$$

  That is to say, for a given $v_{\text{ext}}(\mathbf{r})$, the HK functional is equal to the LL one at the minimum total energy of the system [76, 78].

- The F_{LL} is universal, like F_{HK}, in the sense that it is independent of $v_{\text{ext}}(\mathbf{r})$. Moreover, the part of the total energy (e.g. as given by Eq. 3.3.3) that depends on the (atomic) structure of a given system is $\int \mathrm{d}\mathbf{r}\, n_0(\mathbf{r}) v_{\text{ext}}(\mathbf{r})$, but the same F_{LL} applies to both a giant biological molecule and a stand-alone hydrogen atom [76].

[4] This is known as "N-representability" [76, 78].

[5] This is known as "v-representability" [76, 78].

[6] For a decent discussion of the v- and N-representability of the electronic density, readers are referred to Ref. [76, pp. 53–56]. However, it may be worth mentioning here that, in this sense, the first HK theorem is nothing but a one-to-one mapping between the ground state Φ's and v-representable $n(\mathbf{r})$'s; while the second HK theorem simply says that $\forall$ v-representable $n(\mathbf{r})$'s: $E_v[n(\mathbf{r})] = F_{\text{HK}}[n(\mathbf{r})] + \int \mathrm{d}\mathbf{r}\, n(\mathbf{r}) v_{\text{ext}}(\mathbf{r}) \geq E_v[n_0(\mathbf{r})]$ [76]. Nonetheless, many reasonable densities have been found to be non-v-representable [76, 118, 119].

[7] A density $n(\mathbf{r})$ is said to be N-representable if it can be constructed from an antisymmetric Φ. Therefore, the N-representability condition is weaker than the v-representability condition simply because the former is necessary for the latter.

3.4 Kohn-Sham Approach to DFT

As we have seen in the previous two sections, HK density functional theory, and its LL reformulation, established the fact that a functional $F[n]$ can be defined, and that by minimizing this functional it is possible, in principle, to obtain the exact ground state energy and density of the physical many-body system [78]. It is indeed an extraordinary finding that the 3-dimensional ground state electronic density determines all the physical properties of the ground state [76] and replaces the $3N$-dimensional electronic wave function Φ. However, other than the original definition(s), no practical prescription has been given to find the universal functional 3.2.6 [78]. Moreover, comparing the form of the exact total electronic energy (Eq. 2.5.1) with the HK total electronic energy functional (Eq. 3.2.8), it is clear that, in contrast to the other terms, the only term that is not related to the electron density in any obvious way is the total electronic kinetic energy T_e term [78].

However, while the calculation of the *exact* total electronic kinetic energy T_e of Eq. 2.5.1 invokes the knowledge of the non-local[8] Laplacian of the first order reduced density matrix $\nabla^2_{\mathbf{r}} n_1(\mathbf{r}', \mathbf{r})$, the total electronic kinetic energy T_e of non-interacting electrons system and of HF electrons can be calculated exactly and easily[9] [75].

Starting from this observation, in 1965 Kohn and Sham [107] showed how a practical computational method can be constructed from the density functionals of Hohenberg and Kohn [80, 105].

[8] A very simple way to see the non-locality nature of the Laplacian operator can be obtained by considering a one-dimensional function $f(x)$, and considering a grid of equally spaced discrete set of points x_i with spacings equal to h. The first order finite difference for $\nabla^2 f(x)$ is given by

$$\left(\nabla^2 f(x)\right)_{x_i} = \frac{f(x_{i+1}) + f(x_{i-1}) - 2f(x_i)}{h^2} \,,$$

Thus, the simplest evaluation of $\nabla^2 f(x)$ at x_i requires the evaluation of the function $f(x)$ at x_i and at the neighborhoods x_{i-1} and x_{i+1} (cf. Refs. [121, p. 962] and [75, p. 60]).

[9] This is due to the fact that in both cases the N-electron wave function Φ is a product of N orthonormal one-electron orbitals φ_i in the form of Slater determinant 2.4.51 giving rise to a simple expression for the first order reduced density matrix

$$n_1(\mathbf{r}, \mathbf{r}') = \sum_i f_i \, \varphi_i(\mathbf{r}) \varphi_i^*(\mathbf{r}') \,, \tag{3.4.1}$$

and for the kinetic energy

$$T_e = -\frac{\hbar^2}{2m_e} \sum_i f_i \left\langle \varphi_i \middle| \nabla_i^2 \middle| \varphi_i \right\rangle = -\frac{\hbar^2}{2m_e} \sum_i f_i \int \mathrm{d}\mathbf{r} \, |\nabla_{\mathbf{r}} \varphi_i(\mathbf{r})|^2 \,, \tag{3.4.2}$$

where f_i are the occupation numbers corresponding to the orbitals $\varphi_i(\mathbf{r}_i \sigma_i)$ [75].

The Kohn-Sham ansatz assumes that (i) the exact ground state density $n(\mathbf{r})$ can be represented by the ground state density of *an auxiliary system* of non-interacting particles, and (ii) the auxiliary Hamiltonian is chosen to have the usual kinetic energy operator and an effective potential $v_{\mathrm{R}}^{\sigma}(\mathbf{r})$ acting on an electron of spin σ at point $\mathbf{r}$ [78]:

$$\hat{\mathcal{H}}_{\mathrm{R}} = \sum_i \left[-\frac{\hbar^2}{2m_e} \nabla^2_{\mathbf{r}_i} + v_{\mathrm{R}}^{\sigma}(\mathbf{r}_i) \right] \ . \tag{3.4.3}$$

The auxiliary system of the non-interacting electrons is called the reference system, hence the subscript R in the Hamiltonian 3.4.3 above. Since $\hat{\mathcal{H}}_{\mathrm{R}}$ has no electron-electron term, its eigenstates can be expressed in terms of Slater determinants (Eq. 2.4.51). This has important consequences [75, 76, 78]:

- If the reference system has $N = N_{\uparrow} + n^{\downarrow}$ electrons, its electronic density simply reads

$$n(\mathbf{r}) = \sum_{\sigma} n(\mathbf{r}, \sigma) = \sum_{\sigma} \sum_{i}^{N^{\sigma}} |\varphi_i(\mathbf{r}, \sigma)|^2 = \sum_{i}^{N} \sum_{\sigma} |\varphi_i(\mathbf{r}, \sigma)|^2 \ . \tag{3.4.4}$$

- The *exact* total kinetic energy takes the following simple form[10] [122]

$$\begin{aligned} T_s = -\frac{\hbar^2}{2m_e} \sum_i^N \langle \varphi_i | \nabla^2_{\mathbf{r}_i} | \varphi_i \rangle &= -\frac{\hbar^2}{2m_e} \sum_i^N \sum_{\sigma} \int \mathrm{d}\mathbf{r} \ \varphi_i^*(\mathbf{r}, \sigma) \ \nabla^2_{\mathbf{r}} \ \varphi_i(\mathbf{r}, \sigma) \\ &= -\frac{\hbar^2}{2m_e} \sum_i^N \sum_{\sigma} \int \mathrm{d}\mathbf{r} \, |\nabla_{\mathbf{r}} \varphi_i(\mathbf{r}, \sigma)|^2 \equiv T_s[n(\mathbf{r})] \ . \end{aligned} \tag{3.4.5}$$

  It must be insisted that this is not the *true* kinetic energy of the physical system. The *error* in T_e is discussed below.

- Using the KS kinetic energy functional $T_s[n(\mathbf{r})]$ of the fictitious reference system 3.4.5

[10] Notice that Eqs. 3.4.4 and 3.4.5 are special case of Eqs. 3.4.1 and 3.4.2, respectively, with $f_i = 1$ for the first N orbitals and with $f_i = 0$ for the rest [76].

above, the HK total electronic energy functional 3.2.13 of the physical system now reads

$$E_{\mathsf{KS}}[n(\mathbf{r})] = T_s[n(\mathbf{r})] + \mathcal{J}[n(\mathbf{r})] + \underbrace{\overbrace{T_e[n(\mathbf{r})] - T_s[n(\mathbf{r})]}^{T_C[n(\mathbf{r})]} + \overbrace{V_{ee}[n(\mathbf{r})] - \mathcal{J}[n(\mathbf{r})]}^{V_{\mathrm{xc}}[n(\mathbf{r})]}}_{\tilde{V}_{\mathrm{xc}}[n(\mathbf{r})]} + \int \mathrm{d}\mathbf{r}\; n(\mathbf{r}) v_{\mathsf{ext}}(\mathbf{r})$$

$$= T_s[n(\mathbf{r})] + \mathcal{J}[n(\mathbf{r})] + \tilde{V}_{\mathrm{xc}}[n(\mathbf{r})] + V_{\mathsf{ext}}[n(\mathbf{r})] \equiv E_{\mathsf{KS}}[\{\varphi_i\}]\;, \tag{3.4.6}$$

where $V_{\mathrm{xc}}[n(\mathbf{r})]$ is the exchange-correlation energy defined and discussed in Subsec. 2.4.3, $T_C[n(\mathbf{r})]$ is the kinetic correlation ignored in $T_s[n(\mathbf{r})]$, and $\tilde{V}_{\mathrm{xc}}[n(\mathbf{r})]$ is the resulting KS modification of $V_{\mathrm{xc}}[n(\mathbf{r})]$[11]. The curly brackets in the last term stand for the set of the orbitals φ_i, while the last equality is due to 3.4.4. The functional 3.4.6 above is known as Kohn-Sham energy functional.

- The one-particle wave functions $\varphi_i(\mathbf{r}, \sigma)$ that build up the Slater determinant 2.4.51 must satisfy certain mathematical conditions: (i) For $T_s[n(\mathbf{r})]$ above (Eq. 3.4.5) to be finite, $\varphi_i(\mathbf{r}, \sigma)$ must be continuous. (ii) For $\varphi_i(\mathbf{r}, \sigma)$ to be normalizable, they must be square integrable. (iii) Moreover, for the expression 3.4.5 to be valid, $\varphi_i(\mathbf{r}, \sigma)$ must be orthogonal. That is

$$\langle \varphi_i | \varphi_j \rangle = \delta_{ij} \tag{3.4.7}$$

  Thus, it is such a set of continuous, square integrable and orthonormal functions that are being considered.

For $E_{\mathsf{KS}}[\{\varphi_i\}]$ (Eq. 3.4.6) to be minimum, one applies the variational approach, searching for those orbitals φ_i which minimize the total energy $E_{\mathsf{KS}}[\{\varphi_i\}]$ under the constrained 3.4.7[12]. That is [76, 124]

$$\frac{\delta}{\delta \varphi_i^*} \left(E_{\mathsf{KS}}[\{\varphi_i\}] - \sum_i^N \sum_j^N \varepsilon_{ij} \langle \varphi_i | \varphi_j \rangle \right) = 0\;, \tag{3.4.8}$$

[11] That is, $\tilde{V}_{\mathrm{xc}}[n(\mathbf{r})]$ consists of three parts: (i) the quantum potential energy of exchange, (ii) the potential energy of correlation due to Coulomb interaction, and (iii) the kinetic energy of correlation due to the extra swerving motion of the electrons as they avoid each other. The first two parts are negative, while the third is a smaller positive [123].

[12] Notice that the constraint 3.4.7 is equivalent to 3.4.4. Hence, it is equivalent to the TFD constraint 3.1.3, and the derivative in 3.4.8 can be taken with respect to the density n instead of the one-particle wave functions $\{\varphi_i\}$. However, in that case the Lagrange multiplier is the so-called "chemical potential" μ. It is straightforward to show that μ has the same value in both the KS fictitious system and the true system. cf. Ref. [75, p.62].

where ε_{ij} are the Lagrange multipliers. Bearing in mind that the electronic density is given by Eq. 3.4.4, the functional derivative $\frac{\delta}{\delta\varphi_i^*}$ of the components of $E_{\mathsf{KS}}[\{\varphi_i\}]$ as given by Eq. 3.4.6 are

$$\frac{\delta T_s[n(\mathbf{r})]}{\delta\varphi_i^*} = \frac{\delta}{\delta\varphi_i^*}\left(-\frac{\hbar^2}{2m_e}\sum_i^N \int \mathrm{d}\mathbf{r}\ \varphi_i^*(\mathbf{r},\sigma)\ \nabla_{\mathbf{r}}^2\ \varphi_i(\mathbf{r},\sigma)\right) = \left(-\frac{\hbar^2}{2m_e}\ \nabla_{\mathbf{r}}^2\right)\ \varphi_i(\mathbf{r},\sigma)\ , \tag{3.4.9}$$

$$\frac{\delta\mathcal{J}[n(\mathbf{r})]}{\delta\varphi_i^*} = \frac{\delta}{n(\mathbf{r})}\left(\frac{1}{2}\int \mathrm{d}\mathbf{r}'\mathrm{d}\mathbf{r}\ \frac{n(\mathbf{r})n(\mathbf{r}')}{|\mathbf{r}-\mathbf{r}'|}\right)\frac{\delta n(\mathbf{r})}{\delta\varphi_i^*} = \left(\int \mathrm{d}\mathbf{r}'\ \frac{n(\mathbf{r}')}{|\mathbf{r}-\mathbf{r}'|}\right)\ \varphi_i(\mathbf{r},\sigma)\ , \tag{3.4.10}$$

$$\frac{\delta\tilde{V}_{\mathrm{xc}}[n(\mathbf{r})]}{\delta\varphi_i^*} = \frac{\delta\tilde{V}_{\mathrm{xc}}[n(\mathbf{r})]}{\delta n(\mathbf{r})}\ \frac{\delta n(\mathbf{r})}{\delta\varphi_i^*} = \tilde{v}_{\mathrm{xc}}^{\sigma}[n(\mathbf{r})]\ \varphi_i(\mathbf{r},\sigma)\ , \tag{3.4.11}$$

$$\frac{\delta V_{\mathsf{ext}}[n(\mathbf{r})]}{\delta\varphi_i^*} = \frac{\delta}{\delta n(\mathbf{r})}\left(\int \mathrm{d}\mathbf{r}\ n(\mathbf{r})v_{\mathsf{ext}}(\mathbf{r})\right)\ \frac{\delta n(\mathbf{r})}{\delta\varphi_i^*} = v_{\mathsf{ext}}(\mathbf{r})\ \varphi_i(\mathbf{r},\sigma)\ , \tag{3.4.12}$$

and

$$\frac{\delta}{\delta\varphi_i^*}\left(\sum_i^N\sum_j^N \varepsilon_{ij}\ \langle\varphi_i|\varphi_j\rangle\right) = \sum_j^N \varepsilon_{ij}\varphi_j(\mathbf{r},\sigma)\ . \tag{3.4.13}$$

Here, we used the chain rule $\frac{\delta F}{\delta\varphi_i^*} = \frac{\delta F}{\delta n(\mathbf{r})}\frac{\delta n(\mathbf{r})}{\delta\varphi_i^*}$ wherever the functional dependence on φ_i is not explicit but only through $n(\mathbf{r})$ 3.4.4 [13]. Substituting 3.4.9, 3.4.10, 3.4.11, 3.4.12 and 3.4.13 in 3.4.8, the latter reads

$$\left(-\frac{\hbar^2}{2m_e}\ \nabla_{\mathbf{r}}^2 + \int \mathrm{d}\mathbf{r}'\ \frac{n(\mathbf{r}')}{|\mathbf{r}-\mathbf{r}'|} + \tilde{v}_{\mathrm{xc}}^{\sigma}[n(\mathbf{r})] + v_{\mathsf{ext}}(\mathbf{r})\right)\ \varphi_i(\mathbf{r},\sigma) = \sum_j^N \varepsilon_{ij}\varphi_j(\mathbf{r},\sigma) \tag{3.4.15}$$

Note that, a unitary transformation of the wave functions $\varphi_j(\mathbf{r},\sigma)$ leaves the Slater determinant 2.4.51, and hence the density 3.4.4, invariant. Thus, one can always find a new set of functions

$$\varphi_i(\mathbf{r},\sigma) = \sum_j^N U_{ij}\ \varphi_j(\mathbf{r},\sigma) \qquad \text{with} \qquad \sum_j^N U_{ij}^* U_{jk} = \delta_{ik} \tag{3.4.16}$$

[13] From Eqs. 3.2.6 and 3.4.6 we have

$$\tilde{V}_{\mathrm{xc}} = T_e[n(\mathbf{r})] - T_s[n(\mathbf{r})] + V_{ee}[n(\mathbf{r})] - \mathcal{J}[n(\mathbf{r})] = F_{\mathsf{HK}}[n(\mathbf{r})] - T_s[n(\mathbf{r})] - \mathcal{J}[n(\mathbf{r})]\ . \tag{3.4.14}$$

Since all terms in the LHS are functionals of $n(\mathbf{r})$, $\tilde{V}_{\mathrm{xc}}$ must be a functional of $n(\mathbf{r})$ [78].

such that

$$\boxed{\left(-\frac{\hbar^2}{2m_e}\,\nabla^2_{\mathbf{r}} + \int \mathrm{d}\mathbf{r}'\,\frac{n(\mathbf{r}')}{|\mathbf{r}-\mathbf{r}'|} + \tilde{v}^{\sigma}_{\mathrm{xc}}[n(\mathbf{r})] + v_{\mathsf{ext}}(\mathbf{r})\right)\,\varphi_i(\mathbf{r},\sigma) = \varepsilon_i\varphi_i(\mathbf{r},\sigma)}\,, \tag{3.4.17}$$

where the eigenvalues $\varepsilon_i = \varepsilon_{ii}$ are the diagonal elements of the matrix ε_{ij} [75, 76]. The construction of the Hamiltonian 3.4.3 and of the N-electron wave function 2.4.51 implies that the single-electron orbitals φ_i are the eigenfunctions of the one-body Hamiltonian operator

$$\hat{h}_{\mathsf{KS}} \equiv -\frac{\hbar^2}{2m_e}\,\nabla^2_{\mathbf{r}} + \int \mathrm{d}\mathbf{r}'\,\frac{n(\mathbf{r}')}{|\mathbf{r}-\mathbf{r}'|} + \tilde{v}^{\sigma}_{\mathrm{xc}}[n(\mathbf{r})] + v_{\mathsf{ext}}(\mathbf{r}) \tag{3.4.18}$$

which appears in the RHS of 3.4.17 and defines the summands of the auxiliary Hamiltonian $\hat{\mathcal{H}}_{\mathsf{R}}$ 3.4.3 with

$$v^{\sigma}_{\mathsf{R}}(\mathbf{r}) = \int \mathrm{d}\mathbf{r}'\,\frac{n(\mathbf{r}')}{|\mathbf{r}-\mathbf{r}'|} + \tilde{v}^{\sigma}_{\mathrm{xc}}[n(\mathbf{r})] + v_{\mathsf{ext}}(\mathbf{r})\,. \tag{3.4.19}$$

The set of the one-particle Schrödinger-like equations 3.4.17 above is the famous Kohn-Sham equations. However, sometimes Eqs. 3.4.4, 3.4.17 and 3.4.19, all together, are referred to as Kohn-Sham equations to confirm the fact that these equations must be solved self-consistently. In practice, one usually starts with a reasonable guess of $n(\mathbf{r})$, constructs $v^{\sigma}_{\mathsf{R}}(\mathbf{r})$ using 3.4.19, then solves Eqs. 3.4.17 and makes sure that the obtained density coincides with the guessed input one [75, 76, 78].

In summary, the KS approach to the physical many-electron problem is to rewrite the HK formula for the total electronic energy $E[n(\mathbf{r})]$ 3.2.10 in the form of Eq. 3.4.6. Some ground-state physical properties of the many-electron system are then determined from the solution of the KS independent-electron problem [78]. Methods of solution of the latter, extensions, and related subtleties are the subject of the rest of the present chapter.

3.5 Spin Density-Functional Theory (SDFT)

As already indicated in the previous section (e.g. Eq. 3.4.4), the total electronic density $n(\mathbf{r})$ can be decomposed into two independent spin densities as [122, 125]

$$n(\mathbf{r}) = \sum_{\sigma} N^{\sigma}(\mathbf{r}) = \sum_{\sigma} \underbrace{\sum_{i}^{N^{\sigma}} |\varphi_i^{\sigma}(\mathbf{r})|^2}_{n^{\sigma}(\mathbf{r})} = n^{\uparrow}(\mathbf{r}) + n^{\downarrow}(\mathbf{r}) \; , \tag{3.5.1}$$

and the total number of electrons reads [122]

$$N = N^{\uparrow} + N^{\downarrow} \; . \tag{3.5.2}$$

Each of these densities satisfies the KS equations, and Eq. 3.4.6 becomes [122]

$$E_{\mathsf{KS}}[n^{\uparrow}(\mathbf{r}), n^{\downarrow}(\mathbf{r})] = T_s[n^{\uparrow}(\mathbf{r}), n^{\downarrow}(\mathbf{r})] + \mathcal{J}[n(\mathbf{r})] + \tilde{V}_{\mathrm{xc}}[n^{\uparrow}(\mathbf{r}), n^{\downarrow}(\mathbf{r})] + V_{\mathsf{ext}}[n(\mathbf{r})] \; , \tag{3.5.3}$$

while Eqs. 3.4.17 read [122]

$$\left(-\frac{\hbar^2}{2m_e} \nabla_{\mathbf{r}}^2 + \int \mathrm{d}\mathbf{r}' \, \frac{n(\mathbf{r}')}{|\mathbf{r} - \mathbf{r}'|} + \tilde{v}_{\mathrm{xc}}^{\sigma}[n^{\uparrow}, n^{\downarrow}] + v_{\mathsf{ext}}(\mathbf{r}) \right) \varphi_i^{\sigma}(\mathbf{r}) = \varepsilon_i^{\sigma} \, \varphi_i^{\sigma}(\mathbf{r}) \; , \tag{3.5.4}$$

where the XC potential $\tilde{v}_{\mathrm{xc}}^{\sigma}$ is the functional derivative of the XC energy [122]

$$\tilde{v}_{\mathrm{xc}}^{\sigma}[n^{\uparrow}(\mathbf{r}), n^{\downarrow}(\mathbf{r})] = \frac{\tilde{V}_{\mathrm{xc}}[n^{\uparrow}(\mathbf{r}), n^{\downarrow}(\mathbf{r})]}{\delta n^{\sigma}(\mathbf{r})} \; . \tag{3.5.5}$$

This form of DFT is known as Spin Density Functional Theory (SDFT). In this scheme, one can readily obtain the magnetization (or spin-polarization) density

$$\zeta = n^{\uparrow}(\mathbf{r}) - n^{\downarrow}(\mathbf{r}) \; . \tag{3.5.6}$$

If $\zeta \neq 0$, one has spin-polarized system. On the other hand, if $\zeta \neq 0$, for non-spin-polarized systems, SDFT simply reduces to DFT [75].

SDFT is the most widely used form of DFT [112, 126]. It is useful when one deals with systems (atoms, molecules and solids) with magnetic order, as in finite systems with an odd total number of electrons [78]. Beside its necessity and capability of describing the many-electron systems in the presence of magnetic fields acting on the electronic spins [76], the main advantage of SDFT over Hohenberg-Kohn-Sham DFT is that it allows us to build in more physics into the approximate XC functionals with greater flexibility [76, 102]. For further detailed discussion on SDFT, readers are referred to Ref. [76, Ch. 8]. However, some more will be said about the SDFT formalism in the rest of the present work, especially in Subsec. 3.6.3.

3.6 Solving Kohn-Sham Equations

In the previous two sections we have seen how one can replace the $3N$-dimensional many-electron problem of solids with a problem that requires solving N coupled Kohn-Sham equations self-consistently. Bloch theorem (App. B) shows that within such an independent-particle approach, the many-electron problem of bulk crystalline solids is reduced to the problem of the calculation of the wave function for a finite number of electrons in one unit cell. Hence, applying the same symmetry argument as in Apps. B and C, the band index i in the KS Schrödinger-like equations 3.4.17 must be replaced with the crystal quantum numbers $i \to i, \mathbf{k}$ [78][14] to read

$$\boxed{\left(-\frac{\hbar^2}{2m_e}\,\nabla^2_{\mathbf{r}} + \int \mathrm{d}\mathbf{r}'\,\frac{n(\mathbf{r}')}{|\mathbf{r}-\mathbf{r}'|} + \tilde{v}^{\sigma}_{\mathrm{xc}}[n(\mathbf{r})] + v_{\mathrm{ext}}(\mathbf{r})\right)\,\varphi_{i,\mathbf{k}}(\mathbf{r},\sigma) = \varepsilon_{i,\mathbf{k}}\,\varphi_{i,\mathbf{k}}(\mathbf{r},\sigma)}\,, \qquad (3.6.1)$$

and the spin KS equations 3.5.4 become

$$\boxed{\left(-\frac{\hbar^2}{2m_e}\,\nabla^2_{\mathbf{r}} + \int \mathrm{d}\mathbf{r}'\,\frac{n(\mathbf{r}')}{|\mathbf{r}-\mathbf{r}'|} + \tilde{v}^{\sigma,\mathbf{k}}_{\mathrm{xc}}[n^{\uparrow}, n^{\downarrow}] + v_{\mathrm{ext}}(\mathbf{r})\right)\,\varphi^{\sigma}_{i,\mathbf{k}}(\mathbf{r}) = \varepsilon^{\sigma}_{i,\mathbf{k}}\,\varphi^{\sigma}_{i,\mathbf{k}}(\mathbf{r})}\,. \qquad (3.6.2)$$

The above KS equations can only be solved on computer using numerical methods. To do so, several technical choices have to be made (cf. Refs. [128] and [75, Ch. 6]). For example: (i) The choice of a basis set to expand the KS orbitals $\varphi_{i,\mathbf{k}}(\mathbf{r})$. This is the subject of Subsec. 3.6.1.

[14] This is not the only reason for reciprocal space to come into practical DFT calculations. As we will see, many parts of the mathematical problems posed by DFT are much more convenient to solve in the $\mathbf{k}$ space than in the direct space [127].

(ii) In dealing with bulk crystalline solids, the lattice translation invariance manifests itself in the quantum number $\mathbf{k}$. As a result, eigenstates and eigenvalues depend on $\mathbf{k}$ [129]. Bloch's theorem (App. B) shows that electronic structure calculations for bulk solids can be mapped onto calculating the one-electron wave functions $\varphi_{i,\mathbf{k}}(\mathbf{r})$ at (a discrete set of) $\mathbf{k}$ points lying within the so-called first Brillouin zone (App. C), for a number of bands $i_{\max}$ that is of the order of the number of electrons per unit cell. Expectation values $\langle\hat{\mathcal{O}}\rangle$ of quantum operators $\hat{\mathcal{O}}$, including the density operator, are obtained by integrating over the Brillouin zone (BZ). Hence, one needs to *sample* the BZ. This is discussed briefly in Subsec. 3.6.2. (iii) So far, the form of $\tilde{v}^{\sigma}_{\mathrm{xc}}[n(\mathbf{r})]$ has not been discussed. In practice one needs to choose an approximate $\tilde{v}^{\sigma}_{\mathrm{xc}}[n(\mathbf{r})]$ within the so-called "Jacob's ladder of functionals". This is the subject of Subsec. 3.6.3. (iv) The amount of computational calculations can be further reduced if the interactions between the ionic core and the valence electrons are described either by a pseudopotential or by a full-potential approach. This is discussed in Subsec. 3.6.4. (v) The iterative scheme adopted for the calculations of the eigenstates of the KS Hamiltonian (cf. Sec. 6.3).

In general, *practical* calculations involve far many more subtleties than can be covered here. In this section, only *theoretical* and some *practical* issues closely related to the calculation methods presented in Part II will be considered. Hence, by all means, the discussion in the present section is not meant to be comprehensive, and, from time to time, readers are referred to the original works and other resources for more details.

3.6.1 Basis Sets

The mathematical representation of the KS one-particle orbitals (of Eq. 3.6.1 or Eq. 3.6.2) requires a basis set for expansion in the Hilbert space[15]. Thus, one expands the Kohn-Sham eigenstates $\{|\varphi_{i,\mathbf{k}}\rangle\}$ in a *generic* basis set $\{|\phi_{\mathbf{k},\beta}\rangle\}$ as

$$|\varphi_{i,\mathbf{k}}\rangle = \sum_{\beta=1}^{M} c_{i,\mathbf{k},\beta}\,|\phi_{\mathbf{k},\beta}\rangle \ , \tag{3.6.3}$$

[15] Basis sets are required for the expansion of KS one-particle orbitals, charge densities and potentials [128]. These, and more details about the KS orbitals, will be presented later (cf. Sec. 3.6.4).

where $\langle \mathbf{r}|\varphi_{i,\mathbf{k}}\rangle = \varphi_{i,\mathbf{k}}(\mathbf{r})$ and $\langle \mathbf{r}|\phi_{\mathbf{k},\beta}\rangle = \phi_{i,\mathbf{k}}(\mathbf{r})$ are the representations of the KS orbitals and the basis in the real space, $c_{i,\mathbf{k},\beta} = \langle \phi_{\mathbf{k},\beta}|\varphi_{i,\mathbf{k}}\rangle$ are the expansion coefficients, and M is the dimension of the basis set. Now, substituting 3.6.3 into Eq. 3.6.1 and multiplying from left by $\langle \phi_{\mathbf{k},\alpha}|$, the latter KS Schrödinger-like equations 3.6.1 become a general linear eigenvalue problem of the form

$$\sum_{\beta=1}^{M} c_{i,\mathbf{k},\beta} \left(\hat{h}_{\mathrm{KS}_{\alpha\beta}} - \varepsilon_{i,\mathbf{k}} S_{\alpha\beta} \right) = 0 \,, \tag{3.6.4}$$

where $\hat{h}_{\mathrm{KS}_{\alpha\beta}} = \left\langle \phi_{\mathbf{k},\alpha} \middle| \hat{h}_{\mathrm{KS}} \middle| \phi_{\mathbf{k},\beta} \right\rangle$ is the Hamiltonian matrix element between two basis vectors, and $S_{\alpha\beta} = \langle \phi_{\mathbf{k},\alpha}|\phi_{\mathbf{k},\beta}\rangle$ is the overlap matrix element that takes into account any possibility of non-orthogonality of the basis vectors.

Basis sets can be grouped into four main classes: extended, localized, mixed and augmented basis sets [75, pp. 127–128]. Each class has advantages and disadvantages depending mostly on the type of material (i.e. atoms, molecules or condensed phases) at which they are applied. Falling in the first category, is the plane wave basis sets class, which will be briefly discussed below.

In dealing with crystalline solids it must be ensured that Bloch's theorem is satisfied (see App. B). One of the implications of the theorem is that the one-electron orbitals $\varphi_{i,\mathbf{k}}(\mathbf{r})$ can be expanded in a plane-wave basis. Therefore, to verify the translational symmetry of the crystal, the eigenvectors $\varphi_{i,\mathbf{k}}$ of Eq. 3.6.3 can be chosen to have the form of Bloch's wave functions (Eq. B.0.3), and the periodic part $u_{i,\mathbf{k}}(\mathbf{r})$ can be represented by a Fourier series

$$\langle \mathbf{r}|\varphi_{i,\mathbf{k}}\rangle = \varphi_{i,\mathbf{k}}(\mathbf{r}) = e^{\jmath \mathbf{k}\cdot\mathbf{r}}\, u_{i,\mathbf{k}}(\mathbf{r}) = e^{\jmath \mathbf{k}\cdot\mathbf{r}} \left(\frac{1}{\sqrt{\Omega}} \sum_{\mathbf{K}} c_{i,\mathbf{k}}(\mathbf{K})\, e^{\jmath \mathbf{K}\cdot\mathbf{r}} \right) \,, \tag{3.6.5}$$

where $\mathbf{K}$ are the reciprocal lattice vectors. Comparing 3.6.5 above with the generic form 3.6.3, one can define the *plane wave (PW) basis functions* as

$$\phi_{\mathbf{K}}(\mathbf{r}) = \frac{1}{\sqrt{\Omega}}\, e^{\jmath \mathbf{K}\cdot\mathbf{r}} \,. \tag{3.6.6}$$

So, the KS eigenstates in this basis read

$$\varphi_{i,\mathbf{k}}(\mathbf{r}) = e^{\jmath \mathbf{k}\cdot\mathbf{r}}\, u_{i,\mathbf{k}}(\mathbf{r}) = e^{\jmath \mathbf{k}\cdot\mathbf{r}} \sum_{\mathbf{K}} c_{i,\mathbf{k}}(\mathbf{K})\, \phi_{\mathbf{K}}(\mathbf{r}) \,. \tag{3.6.7}$$

Note that

- The $\mathbf{k}$ vector in the phase factor lies in the first BZ, while the sum runs over all $\mathbf{K}$'s in the reciprocal space. Only $\mathbf{K} = \mathbf{0}$ lies in the BZ.
- The plane waves 3.6.6 are orthonormal

$$\langle \phi_{\mathbf{K}} | \phi'_{\mathbf{K}} \rangle = \frac{1}{\Omega} \int_{\Omega} \mathrm{d}\mathbf{r}\; e^{\jmath (\mathbf{K}-\mathbf{K}')\cdot\mathbf{r}} = \delta_{\mathbf{K},\mathbf{K}'} \,. \tag{3.6.8}$$

- There is an equation of the form 3.6.4 for each $\mathbf{k}$ in the BZ[16]. These are coupled via the electronic density (Eq. 3.6.23).
- Plane waves are the solutions of Schrödinger equation when the external potential v_{ext} is constant. In solids, such solutions may approximate the interstitial regions between ions. However, v_{ext} is far from constant near the ions, and the wave functions $\varphi_{i,\mathbf{k}}(\mathbf{r})$ exhibit fast spatial variations (i.e. peaks and nodes) there. The only way to represent these features in terms of PWs is through linear combinations as in Eq. 3.6.5 with many PW components (i.e. with a very high E_{cut}, see below). This issue will be discussed further in Subsec. 3.6.4.
- The basis functions $\phi_{\mathbf{K}}$ can be made $\mathbf{k}$-dependent by incorporation of the phase factor into the definition 3.6.6

$$\phi_{\mathbf{k},\mathbf{K}}(\mathbf{r}) = \frac{1}{\sqrt{\Omega}}\, e^{\jmath (\mathbf{k}+\mathbf{K})\cdot\mathbf{r}} \,, \tag{3.6.9}$$

  then 3.6.7 reads

$$\varphi_{i,\mathbf{k}}(\mathbf{r}) = \sum_{\mathbf{K}} c_{i,\mathbf{k}}(\mathbf{K})\, \phi_{\mathbf{k},\mathbf{K}}(\mathbf{r}) \,. \tag{3.6.10}$$

- Using PWs basis, it is straightforward to show that the Schrödinger eigenvalue problem

[16] Or two equations in the case of SDFT calculations. See Sec. 3.5.

3.6.4 becomes

$$\sum_{\mathbf{K}'} c_{i,\mathbf{k}}(\mathbf{K}') \left(\hat{h}_{\mathrm{KS}_{\mathbf{K}\mathbf{K}'}} - \varepsilon_{i,\mathbf{k}} S_{\mathbf{K}\mathbf{K}'}\right) = 0 \,, \tag{3.6.11}$$

where

$$S_{\mathbf{K}\mathbf{K}'} = \delta_{\mathbf{K}\mathbf{K}'} \qquad \text{(From Eq. 3.6.8)} \,, \tag{3.6.12}$$

and, with $\hat{h}_{\mathrm{KS}}$ and $v_{\mathrm{R}}^{\sigma}(\mathbf{r})$ as defined in Eqs. 3.4.18 and 3.4.19, respectively, $\hat{h}^{\mathbf{k}}_{\mathrm{KS}_{\mathbf{K}\mathbf{K}'}}$ read

$$\begin{aligned}
\hat{h}^{\mathbf{k}}_{\mathrm{KS}_{\mathbf{K}\mathbf{K}'}} &= \left\langle \phi_{\mathbf{k},\mathbf{K}} \middle| -\frac{\hbar^2}{2m_e}\,\nabla^2_{\mathbf{r}} + v^{\sigma}_{\mathrm{R}_{\mathbf{K}\mathbf{K}'}}(\mathbf{r}) \middle| \phi_{\mathbf{k},\mathbf{K}'} \right\rangle \\
&= \left\langle \phi_{\mathbf{k},\mathbf{K}} \middle| -\frac{\hbar^2}{2m_e}\,\nabla^2_{\mathbf{r}} \middle| \phi_{\mathbf{k},\mathbf{K}'} \right\rangle + \langle \phi_{\mathbf{k},\mathbf{K}} | v^{\sigma}_{\mathrm{R}}(\mathbf{r}) | \phi_{\mathbf{k},\mathbf{K}'} \rangle \\
&= -\frac{\hbar^2}{2m_e}\,\frac{1}{\Omega} \int \mathrm{d}\mathbf{r}\; e^{-\jmath(\mathbf{k}+\mathbf{K})\cdot\mathbf{r}}\, \nabla^2_{\mathbf{r}}\, e^{\jmath(\mathbf{k}+\mathbf{K}')\cdot\mathbf{r}} + \frac{1}{\Omega} \int \mathrm{d}\mathbf{r}\; e^{-\jmath(\mathbf{k}+\mathbf{K})\cdot\mathbf{r}}\, v^{\sigma}_{\mathrm{R}}(\mathbf{r})\, e^{\jmath(\mathbf{k}+\mathbf{K}')\cdot\mathbf{r}} \\
&= \frac{\hbar^2}{2m_e}\,|\mathbf{k}+\mathbf{K}|^2 \delta_{\mathbf{K}\mathbf{K}'} + \tilde{v}^{\sigma}_{\mathrm{R}}(\mathbf{K}-\mathbf{K}') \equiv T^{\mathbf{k}}_{\mathbf{K}\mathbf{K}'} + v^{\sigma}_{\mathrm{R}_{\mathbf{K}\mathbf{K}'}}(\mathbf{r}) \,,
\end{aligned} \tag{3.6.13}$$

where $\tilde{v}^{\sigma,\mathbf{k}}_{\mathrm{R}}(\mathbf{K}-\mathbf{K}')$ is the Fourier transform of $v^{\sigma}_{\mathrm{R}}(\mathbf{r})$.

Now, substituting Eq. 3.6.13 above into Eq. 3.6.11, the latter reads

$$\sum_{\mathbf{K}'} \left(\frac{\hbar^2}{2m_e}\,|\mathbf{k}+\mathbf{K}|^2 \delta_{\mathbf{K}\mathbf{K}'} + \tilde{v}^{\sigma}_{\mathrm{R}}(\mathbf{K}-\mathbf{K}') \right) c_{i,\mathbf{k}}(\mathbf{K}') = \varepsilon_{i,\mathbf{k}}\, c_{i,\mathbf{k}}(\mathbf{K}') \,, \tag{3.6.14}$$

- It is evident from Eq. 3.6.13 above that the kinetic matrix element is diagonal in the reciprocal space, while the potential matrix element is diagonal in the direct space. This is one of the advantages of the PWs expansion, since one can calculate each matrix in the representation where it is diagonal simply by using (e.g. FFT) transformations from reciprocal to direct space and vice versa.

- It is also evident from Eq. 3.6.13 above that the potential matrix element is independent of $\mathbf{k}$ if the potential $v^{\sigma}_{\mathrm{R}}(\mathbf{r})$ itself, as assumed, is local.

- In practical calculations, one has to truncate the expansion 3.6.10 at a finite number of PWs. Fortunately, the expansion coefficients are known to decrease as $|\mathbf{k}+\mathbf{K}|$ increases.

At this stage we define the so-called *PW energy cut-off* E_{cut} as

$$\frac{\hbar^2}{2m_e} |\mathbf{k} + \mathbf{K}|^2 < E_{\text{cut}} \ , \tag{3.6.15}$$

where $\frac{\hbar^2}{2m_e} |\mathbf{k} + \mathbf{K}|^2$ is the largest kinetic energy of the included PWs in the sum 3.6.10.

As in the case of the BZ sampling (Sec. 3.6.2), this truncation introduces an error that can be effectively controlled by increasing E_{cut}, i.e. increasing the number of the included PWs. This increases the size of the basis without changing $\hat{h}_{\text{KS}}$, implying that the total energy E should, in principle, decrease variationaly with increasing E_{cut} [17].

- The usual relation between the direct and the reciprocal space $\Delta x \, \mathbf{K}_{\text{cut}} = 2\pi$, where $\mathbf{K}_{\text{cut}}$ is the largest included reciprocal lattice vector, defines the shortest distance Δx between two points in the real space such that any two points closer than Δx carry no additional information.

- The total energy and its derivatives (i.e. forces and stress) are readily calculated in PWs representation. Moreover, in contrast to atom-centered basis sets, the additional (Pulay) forces arising from the derivation of the basis functions are absent.

3.6.2 k-Space and Brillouin-Zone Integrations

From Eq. 3.6.1 it is clear that expectation values $\langle \mathcal{Q} \rangle$ of all observables $\hat{\mathcal{Q}}$ are given by integrating the matrix elements[18]

$$\mathcal{Q}_{i,\mathbf{k}} = \left\langle \varphi_i(\mathbf{k}) \middle| \hat{\mathcal{Q}} \middle| \varphi_i(\mathbf{k}) \right\rangle \tag{3.6.16}$$

over all the (occupied)[19] bands i and, hence, over the whole BZ [129]

$$\langle \mathcal{Q} \rangle = \frac{1}{N} \sum_i \sum_{\mathbf{k} \in \text{BZ}} f_{i,\mathbf{k}} \, \mathcal{Q}_{i,\mathbf{k}} = \frac{1}{N} \sum_i \sum_{\mathbf{k} \in \text{IBZ}} w_{\mathbf{k}} \, f_{i,\mathbf{k}} \, \mathcal{Q}_{i,\mathbf{k}} \ , \tag{3.6.17}$$

[17] Due to some other practical issues, one may not get a variational curve between E and E_{cut}, even if PWs basis are used. We will return to this point in Subsec. 6.1.

[18] In the eigenvector *symbol* we made the dependence of φ on $\mathbf{k}$ explicit to insure the fact that integration 3.6.16 is carried out in the $\mathbf{k}$ space.

[19] Usually but not always.

where the division by the number of the crystal unit cells N denote that the average is taken per unit cell [78][20] . The weighting factor $w_{\mathbf{k}}$ and the relation between the BZ and the IBZ are described in App. C. The factor $f_{i,\mathbf{k}} = f(\varepsilon_i(\mathbf{k}))$ is the number of electrons that occupy state $i, \mathbf{k}$ and known as the *occupation number* [75]. For spin-unpolarized insulating materials

$$f_{i,\mathbf{k}} = 2\,\Theta\left(\varepsilon_{i,\mathbf{k}} - \mu\right) = \begin{cases} 2 & \text{if} \quad i \leq \frac{N}{2} \\ 0 & \text{if} \quad i > \frac{N}{2} \end{cases} , \tag{3.6.18}$$

where Θ is the step function and μ is the chemical potential[21]. For spin-polarized calculations (Sec. 3.5), there will be two sets of occupation numbers $f^{\sigma}_{i,\mathbf{k}}$, one for each spin projection, and

$$f^{\sigma}_{i,\mathbf{k}} = \begin{cases} 1 & \text{if} \quad i \leq N^{\sigma} \\ 0 & \text{if} \quad i > N^{\sigma} \end{cases} , \tag{3.6.19}$$

where N^{σ} is the number of electrons with spin component σ [75][22]. Then Eq. 3.6.17 above reads

$$\langle \mathcal{Q} \rangle = \frac{1}{N} \sum_{i} \sum_{\sigma} \sum_{\mathbf{k} \in \mathrm{BZ}} f^{\sigma}_{i,\mathbf{k}}\, \mathcal{Q}^{\sigma}_{i,\mathbf{k}} = \frac{1}{N} \sum_{i} \sum_{\sigma} \sum_{\mathbf{k} \in \mathrm{IBZ}} w_{\mathbf{k}}\, f^{\sigma}_{i,\mathbf{k}}\, \mathcal{Q}^{\sigma}_{i,\mathbf{k}} , \tag{3.6.20}$$

where

$$\mathcal{Q}^{\sigma}_{i,\mathbf{k}} = \left\langle \varphi^{\sigma}_{i}(\mathbf{k}) \middle| \hat{\mathcal{Q}}^{\sigma} \middle| \varphi^{\sigma}_{i}(\mathbf{k}) \right\rangle \tag{3.6.21}$$

and

$$\langle \mathcal{Q}^{\sigma} \rangle = \frac{1}{N} \sum_{i}^{N^{\sigma}} \sum_{\sigma} \sum_{\mathbf{k} \in \mathrm{IBZ}} w_{\mathbf{k}}\, f^{\sigma}_{i,\mathbf{k}}\, \mathcal{Q}^{\sigma}_{i,\mathbf{k}} \ . \tag{3.6.22}$$

[20] Or, equivalently, over the $\mathbf{k}$ points, since $N = N_{\mathbf{k}}$, where $N_{\mathbf{k}}$ is the number of $\mathbf{k}$ points [78].

[21] Compare Eqs. 3.6.18 and 3.6.19 with Eq. 3.6.30. For the relation between the chemical potential μ and the Fermi energy E_F, see Sec. 8.1.

[22] The relaxation of the electronic degrees of freedom may result in unbalanced $N^{\uparrow}$ and $N^{\downarrow}$. Such a system is said to be spin-polarized [75].

The electronic density

The most important and the clearest example for integration over the BZ (i.e. Eq. 3.6.17) is the electronic density (which couples Eqs. 3.6.1):

$$n(\mathbf{r}) = \frac{1}{N_{\mathbf{k}}} \sum_i \sum_{\mathbf{k}\in \mathrm{BZ}} f_{i,\mathbf{k}}\, n_{i,\mathbf{k}}(\mathbf{r}) = \frac{1}{N_{\mathbf{k}}} \sum_i \sum_{\mathbf{k}\in \mathrm{BZ}} f_{i,\mathbf{k}}\, |\varphi_{i,\mathbf{k}}(\mathbf{r})|^2 \,. \tag{3.6.23}$$

Using the PWs representation 3.6.5, the $n_{i,\mathbf{k}}(\mathbf{r})$ contributions to the density 3.6.23 above read

$$n_{i,\mathbf{k}}(\mathbf{r}) = |\varphi_{i,\mathbf{k}}(\mathbf{r})|^2 = \frac{1}{\Omega} \sum_{\mathbf{K}} \sum_{\mathbf{K}'} c^*_{i,\mathbf{k}}(\mathbf{K})\, c_{i,\mathbf{k}}(\mathbf{K}')\, e^{\jmath(\mathbf{K}'-\mathbf{K})\cdot\mathbf{r}} \,. \tag{3.6.24}$$

For spin-polarized calculations, the electronic spin density $n^\sigma(\mathbf{r})$ (which couples Eqs. 3.6.2) is given by

$$n^\sigma(\mathbf{r}) = \frac{1}{N} \sum_i^{N^\sigma} \sum_\sigma \sum_{\mathbf{k}\in \mathrm{IBZ}} w_{\mathbf{k}}\, f^\sigma_{i,\mathbf{k}}\, |\varphi^\sigma_{i,\mathbf{k}}(\mathbf{r})|^2 \,, \tag{3.6.25}$$

where the index σ indicates the spin component ($\uparrow$ or $\downarrow$), N^σ is the number of the occupied single-electron eigenstates $\varphi^\sigma_{i,\mathbf{k}}(\mathbf{r})$ with spin projection σ at each $\mathbf{k}$-point of the sampled IBZ [23].

Brillouin zone sampling

In the limit of an infinite crystal, $\mathbf{k}$ becomes a continuous variable (App. C), hence the sum 3.6.17 above reads [129][24]

$$\langle \mathcal{Q} \rangle = \frac{1}{\Omega_{\mathrm{R}}} \sum_i \int_{\mathrm{BZ}} \mathrm{d}\mathbf{k}\, f_{i,\mathbf{k}}\, \mathcal{Q}_{i,\mathbf{k}} = \frac{1}{\Omega_{\mathrm{R}}} \sum_i \int_{\mathrm{IBZ}} \mathrm{d}\mathbf{k}\, w_{\mathbf{k}}\, f_{i,\mathbf{k}}\, \mathcal{Q}_{i,\mathbf{k}} \,, \tag{3.6.26}$$

[23] Note that, since $\int \mathrm{d}\mathbf{r}\, n^\sigma(\mathbf{r}) = N^\sigma$, Eq. 3.6.25 implies that $w_{\mathbf{k}}$ must satisfy $\sum_i^{N^\sigma} \sum_\sigma \sum_{\mathbf{k}\in \mathrm{IBZ}} w_{\mathbf{k}}\, f^\sigma_{i,\mathbf{k}} = N^\sigma$. Compare this with Eq. C.0.8.

[24] Indeed, one can carry out the integration 3.6.26 in the i direction first, then in the $\mathbf{k}$ direction, or vise versa:

$$\langle \mathcal{Q} \rangle = \frac{1}{\Omega_{\mathrm{R}}} \int_{\mathrm{BZ}} \mathrm{d}\mathbf{k}\, \underbrace{\left(\sum_i f_{i,\mathbf{k}}\, \mathcal{Q}_{i,\mathbf{k}} \right)}_{\bar{\mathcal{Q}}_{\mathbf{k}}} = \sum_i \underbrace{\left(\frac{1}{\Omega_{\mathrm{R}}} \int_{\mathrm{BZ}} \mathrm{d}\mathbf{k}\, f_{i,\mathbf{k}}\, \mathcal{Q}_{i,\mathbf{k}} \right)}_{\bar{\mathcal{Q}}_i} \,.$$

where Ω_R is the volume of the BZ as given by Eq. C.0.5.

As discussed in Apps. B and C, the ultimate achievement of any one-electron method is to obtain accurate expectation values using matrix elements (3.6.16 or 3.6.21) that have to be calculated explicitly only within the first BZ. When symmetry is exploited to reduce the space of integration further, we arrived at the irreducible wedge of the first Brilouin zone (IBZ). Nonetheless, Eq. 3.6.26 above tells us that, though restricted to the IBZ, this calculations still must be done, in principle, at an infinite number of $\mathbf{k}$ points. Thus, apparently, the infinite-electrons problem has been mapped -via Bloch theorem- to an infinite-$\mathbf{k}$-points problem. However, the latter infinity problem is less worse, since for $\mathbf{k}$ points that are sufficiently close in the IBZ, one expects that the one-electron wave functions carry similar information. Therefore, a well-chosen set of a finite number of $\mathbf{k}$ points in the IBZ should reproduce the desired physical properties to the required *numerical* accuracy. The set of the chosen $\mathbf{k}$-points is generally referred to as *special points* and the procedure is known as the *Brilouin zone sampling* [75].

The Monkhorst-Pack special $\mathbf{k}$-points method

The Monkhorst and Pack [130] sets of special $\mathbf{k}$-points consist of a uniform (i.e an equispaced) grid of points

$$\mathbf{k}_{r_1,r_2,r_3} = \sum_{i}^{3} r_i \mathbf{b}_i = r_1\mathbf{b}_1 + r_2\mathbf{b}_2 + r_3\mathbf{b}_3 \tag{3.6.27}$$

where $\mathbf{b}_i$ are the primitive reciprocal lattice vectors (App. C), while r_i are given by

$$r_i = \frac{2n_i - q_i - 1}{2q_i} \quad , \quad n_i = 1, 2, 3, ..., q_i \ , \tag{3.6.28}$$

with $q_1 \times q_2 \times q_3$ is the size of the Monkhorst-Pack mesh.

Note that, for even q_i's, the grid will be shifted off the Γ point[25] but still centered *around* it. This may break the symmetry in certain cell geometries, as in the case of hexagonal cells, and symmetrization may result in a mesh of non-equally distributed $\mathbf{k}$ points. For odd q_i's, the mesh

[25] Γ point is the point where $\mathbf{k} = 0$.

will be centered *at* Γ, and symmetry is preserved.

Indeed, the sampling of an integral such as 3.6.26 introduces an error which can be reduced by using denser meshes, i.e. larger q_i's [75]. In fact, the integrand in Eq. 3.6.26 can be Fourier expanded (compare with Eq. C.0.6)

$$\mathcal{Q}_{i,\mathbf{k}} \equiv \mathcal{Q}_i(\mathbf{k}) = \sum_{\mathbf{R}} \mathcal{Q}_i(\mathbf{R})\, e^{j\mathbf{k}\cdot\mathbf{R}}\,, \tag{3.6.29}$$

where $\mathbf{R} = \sum_i^3 n_i\, \mathbf{a}_i$ are the translation vectors as defined by Eq. A.0.1. If the sum 3.6.29 above is truncated, due to the exponentially decreasing contributions from terms with large $\mathbf{R}$, at $q_i\mathbf{a}_i$ in each direction, then the error in sampling 3.6.26 must vanish [78].

Metallic systems

In dealing with metals, occupation numbers $f^\sigma_{i,\mathbf{k}}$ should, in principle, be determined by the Fermi-Dirac distribution function *at zero temperature*

$$f^\sigma_{i,\mathbf{k}} = \Theta\left(\varepsilon^\sigma_{i,\mathbf{k}} - E_F\right) = \begin{cases} 1 & \text{if} \quad \varepsilon^\sigma_{i,\mathbf{k}} \le E_F \\ 0 & \text{if} \quad \varepsilon^\sigma_{i,\mathbf{k}} > E_F \end{cases}\,, \tag{3.6.30}$$

where E_F is the Fermi energy (see Sec. 8.1). Due to the sharp variation of $f^\sigma_{i,\mathbf{k}}$ from 1 to 0 in crossing the Fermi surface, a slightly different choice of a Monkhorst-Pack mesh may lead to states (with matrix elements $\mathcal{Q}^\sigma_{i,\mathbf{k}}$) that exit or enter the sum 3.6.20 depending on whether $\varepsilon^\sigma_{i,\mathbf{k}} > E_F$ or $\varepsilon^\sigma_{i,\mathbf{k}} < 0$, respectively. A very fine dense Monkhorst-Pack grid of $\mathbf{k}$ points would, in principle, solve the problem, but this is computationally impracticable [75], since the discontinuity (i.e. the step function $f^\sigma_{i,\mathbf{k}} = \Theta(\varepsilon^\sigma_{i,\mathbf{k}} - E_F)$) of the integrand makes the sum 3.6.20 *converge* exceedingly slow with the number of $\mathbf{k}$ points included. To overcome this significant complication, several practical schemes have been proposed to speed up the *convergence* without destroying the *accuracy* of the integral [87, 127]. Some of these methods are briefly described below.

The tetrahedron interpolation method

A widely used integration scheme which is equally applicable to insulators and metals is the tetrahedron methods [129, 131, 132]. The main idea is that, if one knows $\varphi^{\sigma}_{i,\mathbf{k}}$ and $\varepsilon^{\sigma}_{i,\mathbf{k}}$ at a set of mesh points, it is always possible to approximate the variation between the mesh points by an interpolation method using tetrahedra [78, 129]. Therefore, in the traditional implementation of the (linear) tetrahedron method [131, 132], the IBZ is divided into and filled out with tetrahedra. Matrix elements $\mathcal{Q}^{\sigma}_{i,\mathbf{k}}$ and eigenvalues $\varepsilon^{\sigma}_{i,\mathbf{k}}$ are calculated explicitly only for the $\mathbf{k}$ points at the four vertices of each tetrahedron. Inside each tetrahedron, linear interpolations are performed. For the details of the method, readers are referred to the original works [131, 132]; however, it is worth to mention here that in this method:

- Tetrahedra can be used to fill out the reciprocal space for any mesh of $\mathbf{k}$ points, even for an irregular mesh with more points near the Fermi surface and less points far from it [78].
- Due to the (linear) approximation, the integration can be performed analytically, and, thus, the often complicated shape of the Fermi surface and its exquisite details are taken into account [129].
- Another important superiority of the tetrahedron method over the special $\mathbf{k}$-points schemes is that it provides spectral functions [129].

Blöchl *et al.* [129] introduced several improvements to the traditional (linear) tetrahedron method for BZ integrations:

- The suggested uniform mesh of $\mathbf{k}$ points and tetrahedra render the obtained results for insulators identical to those obtained with the Monkhorst-Pack pecial $\mathbf{k}$-points scheme with the same density of $\mathbf{k}$ points.
- Going beyond the linear approximation of the matrix elements within the tetrahedra, simple correction formula that significantly improves the results for metals was introduced, leading, for a required accuracy, to reduction of the $\mathbf{k}$ mesh density by orders of magnitude.
- Requiring only the space-group operations as input, the tetrahedra and the irreducible $\mathbf{k}$ points are chosen by a fully automated procedure.

- For a given band structure, the integration 3.6.20 effective weights $f^{\sigma}_{i,\mathbf{k}}$ are calculated using the tetrahedron method *once*. Therefore, the efficient use of the tetrahedron method in plane-wave-based DFT calculations (see Sec. 3.6.1) is evident.

For accurate calculations of the total energy in bulk materials and for a smooth nice electronic density of states (see Sec. 8.2), especially in metals, the above *tetrahedron method with Blöchl corrections* is widely used. However, the method has a serious shortcoming: it is not variational with respect to $f^{\sigma}_{i,\mathbf{k}}$, hence the calculated *forces* (see Sec. 2.3 and Sec. 7.3) may not be correct for metals. In fact, for metals, the calculated forces and the stress tensor can be wrong by up to 5 to $10\ \%$. Nevertheless, for insulators, the calculated forces are always correct, since $f^{\sigma}_{i,\mathbf{k}}$ do not vary (Eq. 3.6.18 or 3.6.19) [87].

Smearing methods

To mitigate the problem of metals, one may replace the step function 3.6.30 with another *smooth* distribution function for $f^{\sigma}_{i,\mathbf{k}}$ that *smears* out the discontinuity at the Fermi surface. Such schemes are known as *smearing methods*. A practical illustrating example is the Fermi-Dirac distribution function

$$f^{\sigma}_{i,\mathbf{k}} = \frac{1}{e^{(\varepsilon^{\sigma}_{i,\mathbf{k}} - E_F)/\mathrm{t}_e} + 1} \quad , \tag{3.6.31}$$

where the fictitious electronic temperature $\mathrm{t}_e = k_{\mathrm{B}}\theta_e$ here has no *physical* meaning (at least at $0\ K$), but *mathematically* it is the *smearing width* of the distribution and it turns out that it controls the speed of the convergence in a proportional manner [75].

It is easy to see that this method leads to an error in the integration [133]. In fact, smearing schemes suffer from two main shortcomings:

- It turns out that the total energy E is no longer variational, and the calculated forces are now the derivatives of a generalized free energy

$$F = E - \sum_{i} \sum_{\mathbf{k}\in \mathrm{BZ}} w_{\mathbf{k}}\ \mathrm{t}_e\ \mathcal{S}(f_{i,\mathbf{k}})\ . \tag{3.6.32}$$

  Therefore, the scheme is not the best choice for geometry optimization. However, compared to the tetrahedron method with Blöchl corrections, the error in the calculated forces is small

and acceptable, in general.

Despite this drawback of the scheme, it is still possible to get a physical quantity using the formula

$$E\left(\mathfrak{t}_e \to 0\right) = E_0 = \frac{1}{2}\left(E + F\right) \ , \tag{3.6.33}$$

and obtain an accurate extrapolation for $\mathfrak{t}_e \to 0$ [87].

- From practical point of view, $\mathfrak{t}_e$ is treated as a convergence parameter that has to be handled with great care, since fast convergence, i.e. large $\mathfrak{t}_e$ value, may result in an incorrect total energy $E(\mathfrak{t}_e \to 0)$ [75, 87] even for an extremely dense $\mathbf{k}$-points mesh [87]. On the other hand, a small $\mathfrak{t}_e$ requires a dense grid of $\mathbf{k}$ points. Thus, $\mathfrak{t}_e$ can be chosen as large as possible, as far as the difference between F and E, that is the entropy term $\sum_i \sum_{\mathbf{k}\in \mathrm{BZ}} w_{\mathbf{k}}\, \mathfrak{t}_e\, \mathcal{S}(f_{i,\mathbf{k}})$ in Eq. 3.6.33, is negligible[26] [87].

The Methfessel-Paxton scheme

The foregoing two problems can be solved at once by employing a more sophisticated method proposed by Methfessel and Paxton [75, 87, 133]. In their original work [133], they started by writing the integral in 3.6.26 as [27]

$$I = \int_{\mathrm{BZ}} \mathrm{d}\mathbf{k}\ f_{\mathbf{k}}\ \mathcal{Q}_{\mathbf{k}} = \int_{\mathrm{BZ}} \mathrm{d}\mathbf{k}\ \Theta\left(\varepsilon(\mathbf{k}) - E_F\right)\ \mathcal{Q}(\mathbf{k}) = \int_{-\infty}^{\infty} \mathrm{d}\varepsilon\ \Theta\left(\varepsilon - E_F\right)\ Q(\varepsilon) \tag{3.6.34}$$

where

$$Q(\varepsilon) = \int_{\mathrm{BZ}} \mathrm{d}\mathbf{k}\ \mathcal{Q}(\mathbf{k})\ \delta\left(\varepsilon(\mathbf{k}) - E_F\right) \ . \tag{3.6.35}$$

Then, working with a dimensionless energy $x = \left(\varepsilon - E_F\right)/\mathfrak{t}_e$, Methfessel and Paxton searched for successive approximations $\Theta_N(x)$ to the step function $\Theta(x)$ which are smooth and for which the

[26] Practically, the difference between F and E is considered to be negligible if it is less than $1\ meV/\text{atom}$. The only way to obtain an optimal $\mathfrak{t}_e$ value is by performing several calculations with different $\mathfrak{t}_e$ values and different $\mathbf{k}$-point meshes [87]. See also Sec. 6.1.

[27] Note that, since we are only after the Methfessel-Paxton form of $f_{i,\mathbf{k}}$, we dropped out the irrelevant index i, factors and sums.

error vanishes if $Q(\varepsilon)$ is a polynomial with some order in the energy range that is determined by the width $\mathfrak{t}_e$. By expanding the δ function (of Eq. 3.6.35 above) in a complete set of orthonormal smooth functions

$$\delta(x) = \sum_{n=0}^{\infty} A_n \, H_{2n}(x) \, e^{-x^2} \quad , \tag{3.6.36}$$

where H_m is the Hermite polynomial of the mth degree, and the coefficients A_m are numbers depend on m, the central result Methfessel and Paxton arrived at is

$$\Theta_0(x) = \frac{1}{2}\left(1 - \mathrm{erf}(x)\right) \quad , \tag{3.6.37}$$

$$\Theta_N(x) = \Theta_0(x) + \sum_{n=1}^{N} A_n \, H_{2n-1}(x) \, e^{-x^2} \quad . \tag{3.6.38}$$

Note that the zero-order approximation Θ_0 corresponds to the foregoing Fermi-Dirac smearing approximation 3.6.31. Errors inherent in such scheme are corrected for by the higher order terms $(N = 1, 2, ...)$ of 3.6.38.

In similarity to the smearing methods, the total energy E must be replaced with a generalized free energy F as 3.6.33. However, in contrast to the smearing methods the entropy term is usually very small for any reasonable value of $\mathfrak{t}_e$. Therefore, to calculated forces, stress tensor and phonon frequencies based on forces, the Methfessel-Paxton $(N > 0)$ is recommended (see also Sec. 7.3). Nonetheless, one still has to choose the smearing width $\mathfrak{t}_e$ carefully [87].

The method results in very accurate values of the integral 3.6.26 even when small number of $\mathbf{k}$ points is used [75]. It is also the choice for large super cells, especially when the tetrahedron methods are not applicable if less than 3 $\mathbf{k}$ points are to be used [87].

At the end of the present subsection, we refer readers to Ref. [87] for complete discussion on the subject.

3.6.3 Exchange and Correlation Functionals

The problem of exchange and correlation in electronic structure calculations was carefully addressed in Subsec. 2.4.3. In Sec. 3.4, the electronic exchange-correlation potential $\tilde{V}_{\rm xc}[n^{\uparrow}(\mathbf{r}), n^{\downarrow}(\mathbf{r})]$ has been redefined (Eq. 3.4.6) within the KS-DFT to include the kinetic correlation piece. Here, after we give some formal properties that must be satisfied by $\tilde{V}_{\rm xc}$, we give some examples of the available $\tilde{V}_{\rm xc}$ approximations and concentrate on two of them.

Recall from Sec. 2.5 and Eqs. 2.4.56 and 3.4.6 that within the one-particle approaches (e.g. Kohn-Sham DFT) the exchange contribution $V_{\rm x}$ can be calculated exactly, but it is computationally expensive. Moreover, it turns out that if $V_{\rm x}$ is treated exactly, it will not compensate for the error introduced by the approximate $V_{\rm c}$. Therefore, in practice, both terms $V_{\rm x}$ and $V_{\rm c}$ are treated at the same level of approximation [75].

Using Eq. 2.4.50, one can write the KS-DFT XC contribution to the total electronic energy (Eq. 3.4.6) as

$$\tilde{V}_{\rm xc}[n(\mathbf{r})] = \frac{1}{2}\int \mathrm{d}\mathbf{r}\ \mathrm{d}\mathbf{r}'\ \frac{n(\mathbf{r})\tilde{n}_{\rm xc}(\mathbf{r},\mathbf{r}')}{|\mathbf{r}-\mathbf{r}'|}\ . \tag{3.6.39}$$

In the sense of this equation, one can interpret $\tilde{V}_{\rm xc}[n(\mathbf{r})]$ as a Coulomb interaction between the electronic density $n(\mathbf{r})$ and a fictitious charge depletion $\tilde{n}_{\rm xc}(\mathbf{r},\mathbf{r}')$. The latter quantity, known as the XC hole density (Eq. 2.4.49), now includes the kinetic correlation contribution T_C [75]. The XC charge $\tilde{n}_{\rm xc}(\mathbf{r},\mathbf{r}')$ is related to the XC hole $\tilde{h}(\mathbf{r},\mathbf{r}')$ and to the pair correlation distribution $\tilde{g}(\mathbf{r},\mathbf{r}')$ via Eqs. 2.4.49 and 2.4.46, respectively, and it can be shown that the three quantities

have the following properties [75, 112]

$$\tilde{g}(\mathbf{r},\mathbf{r}') = \tilde{g}(\mathbf{r}',\mathbf{r}) \ , \tag{3.6.40}$$

$$\int \mathrm{d}\mathbf{r}\ n(\mathbf{r})\tilde{g}(\mathbf{r},\mathbf{r}') = N-1 \ , \tag{3.6.41}$$

$$\int \mathrm{d}\mathbf{r}\ \tilde{n}_{\mathrm{xc}}(\mathbf{r},\mathbf{r}') = -1 \ , \tag{3.6.42}$$

$$\int \mathrm{d}\mathbf{r}\ \tilde{n}_{\mathrm{x}}(\mathbf{r},\mathbf{r}') = -1 \ , \tag{3.6.43}$$

$$\int \mathrm{d}\mathbf{r}\ \tilde{n}_{\mathrm{c}}(\mathbf{r},\mathbf{r}') = 0 \ . \tag{3.6.44}$$

The first property simply says that $\tilde{g}(\mathbf{r},\mathbf{r}')$ is symmetric under the exchange of $\mathbf{r}$ and $\mathbf{r}'$. The second is a normalization condition (Eq. 2.4.49). The third property, may be the most important sum rule, shows that the XC hole contains exactly one missing electron. The exchange hole density $\tilde{n}_{\mathrm{x}}(\mathbf{r},\mathbf{r}')$ and the correlation hole density $\tilde{n}_{\mathrm{c}}(\mathbf{r},\mathbf{r}')$ in the fourth and the last sum rules are defined by

$$\tilde{n}_{\mathrm{xc}}(\mathbf{r},\mathbf{r}') = \tilde{n}_{\mathrm{x}}(\mathbf{r},\mathbf{r}') + \tilde{n}_{\mathrm{c}}(\mathbf{r},\mathbf{r}') \ , \tag{3.6.45}$$

and integrals 3.6.42, 3.6.43 and 3.6.44 together tell us that the $\tilde{V}_C$ corresponds to the interaction of the charge density with a natural charge distribution [75]. More precisely, the correlation repulsion changes the shape of the XC hole but not its integral [134].

Approaches to construction and selection of density functional *approximations* to the exchange-correlation energy have been a subject of active research. In general, XC functionals can be constructed either non-empirically via satisfaction of known exact constraints, or semi-empirically via adjusting parameters to a given set of experimental data [112, 128]. Attempts to improve DFT calculations have led to the development of an entire hierarchy of exchange-correlation functionals, which is sometimes referred to as the *Jacob's ladder* [112, 135]. The first four rungs on Jacobs ladder are (i) the local density approximation (LDA), (ii) the generalized gradient approximation (GGA), (iii) the meta-GGA, and (iv) hybrid functionals mixing DFT and exact Hartree-Fock exchange [128] [28].

[28] Users should always say which functional they used and why [112], since any reported failure of a DFT application is in fact a failure of a given density functional approximation [123].

The local spin density approximation (LSDA)

The main idea of the local spin density approximation (LSDA) [107, 125] is that one treats a general inhomogeneous system as locally homogeneous [29]. Then, one uses the XC hole of the homogeneous electron gas, since the latter is known to an excellent degree of accuracy [75]. The XC energy in the local spin density approximation (LSDA) [107, 125] is written as [112, 122, 135, 136]

$$\begin{aligned}\tilde{V}_{\rm xc}^{\rm LSDA}[n^{\uparrow}(\mathbf{r}), n^{\downarrow}(\mathbf{r})] &= \int \mathrm{d}\mathbf{r}\; n(\mathbf{r})\; \varepsilon_{\rm xc}^{\rm unif}(n(\mathbf{r}), \zeta) = \int \mathrm{d}\mathbf{r}\; n(\mathbf{r})\; \varepsilon_{\rm xc}^{\rm unif}(n^{\uparrow}(\mathbf{r}), n^{\downarrow}(\mathbf{r})) \\ &= \int \mathrm{d}\mathbf{r}\; n(\mathbf{r})\; \left(\varepsilon_{\rm x}^{\rm unif}(n^{\uparrow}(\mathbf{r}), n^{\downarrow}(\mathbf{r})) + \varepsilon_{\rm c}^{\rm unif}(n^{\uparrow}(\mathbf{r}), n^{\downarrow}(\mathbf{r}))\right) \;, \end{aligned} \tag{3.6.46}$$

where the first equality shows that $\tilde{V}_{\rm xc}$ can be equivalently written in terms of the local polarization[30]

$$\zeta = \frac{n^{\uparrow}(\mathbf{r}) - n^{\downarrow}(\mathbf{r})}{n(\mathbf{r})} \;, \tag{3.6.47}$$

and the total density $n(\mathbf{r})$. The superscript "unif" stands for "uniform" or homogeneous, and refers to the fact that the XC energy density $\varepsilon_{\rm xc}$ at each point is assumed to be the same as in the homogeneous electron gas with the same density n [78]. In other words, in LSDA, the $\varepsilon_{\rm xc}$ of a real, spatially inhomogeneous system at each point $\mathbf{r}$ is approximated by that of a homogeneous electron gas with spin densities equal to the local $n^{\uparrow}(\mathbf{r})$ and $n^{\downarrow}(\mathbf{r})$ [122].

While based upon approximations and numerical fittings to $\varepsilon_{\rm c}^{\rm unif}(n^{\uparrow}(\mathbf{r}), n^{\downarrow}(\mathbf{r}))$, the LSDA scheme uses explicit and exact expression for $\varepsilon_{\rm x}^{\rm unif}(n^{\uparrow}(\mathbf{r}), n^{\downarrow}(\mathbf{r}))$ [78]

$$\varepsilon_{\rm x}^{\rm unif}(n, \zeta) = \varepsilon_{\rm x}(n, 0)\, (\varepsilon_{\rm x}(n, 1) - \varepsilon_{\rm x}(n, 0))\, F_{\rm x}(\zeta) \;, \tag{3.6.48}$$

with

$$F_{\rm x}(\zeta) = \frac{1}{2} \frac{(1+\zeta)^{4/3} + (1-\zeta)^{4/3} - 2}{2^{1/3} - 1} \;. \tag{3.6.49}$$

[29] When dealing with different $\tilde{V}_{\rm xc}$ functionals, the term *local* refers to the case where the value of $\varepsilon_{\rm xc}$ at $\mathbf{r}$ is determined by the electron density at $\mathbf{r}$ (as in the L(S)DA). When the value of $\varepsilon_{\rm xc}$ at $\mathbf{r}$ is determined by the electron density in an infinitesimal neighborhood of $\mathbf{r}$ (as in the GGAs), the term *semi-local* is used. When dealing with exact exchange, $\varepsilon_{\rm x}$ at $\mathbf{r}$ is determined by the electron density at a finite displacement away from $\mathbf{r}$, and $\tilde{V}_{\rm x}$ is said to be *non-local* [122].

[30] ζ is also known as fractional spin-polarization density. Compare Eq. 3.5.6.

Using the second equality in Eq. 3.6.46, the LSDA expression for the Kohn-Sham XC potential $\tilde{v}^{\sigma}_{\rm xc}[n(\mathbf{r})]$ (Eq. 3.4.11) can be found from

$$\delta\tilde{V}^{\rm LSDA}_{\rm xc}[n(\mathbf{r})] = \sum_{\sigma}\int {\rm d}\mathbf{r}\left[\varepsilon^{\rm unif}_{\rm xc}(n^{\uparrow}(\mathbf{r}),n^{\downarrow}(\mathbf{r})) + n(\mathbf{r})\,\frac{\partial\varepsilon^{\rm unif}_{\rm xc}(n^{\uparrow}(\mathbf{r}),n^{\downarrow}(\mathbf{r}))}{\partial n^{\sigma}(\mathbf{r})}\right]_{\mathbf{r},\sigma}\delta n(\mathbf{r},\sigma)\;, \tag{3.6.50}$$

which means that

$$\tilde{v}^{\sigma}_{\rm xc}[n(\mathbf{r})] = \tilde{v}^{\sigma}_{\rm xc}(\mathbf{r}) = \left[\varepsilon^{\rm unif}_{\rm xc}(n^{\uparrow}(\mathbf{r}),n^{\downarrow}(\mathbf{r})) + n(\mathbf{r})\,\frac{\partial\varepsilon^{\rm unif}_{\rm xc}(n^{\uparrow}(\mathbf{r}),n^{\downarrow}(\mathbf{r}))}{\partial n^{\sigma}(\mathbf{r})}\right]_{\mathbf{r},\sigma}\;. \tag{3.6.51}$$

The subscripts $\mathbf{r},\sigma$ refer to the fact that the quantity in the square brackets is evaluated at $n^{\sigma} = n(\mathbf{r},\sigma)$. While the expression for $\tilde{v}^{\sigma}_{\rm x}$ is very simple, the expression for $\tilde{v}^{\sigma}_{\rm c}$ depends upon the form of $\varepsilon_{\rm c}$ [78].

In SDFT (Sec. Spin Density-Functional Theory (SDFT)) the external and Hartree potentials depend only on the total electronic density $n(\mathbf{r})$, and the kinetic energy splits trivially into two spin components (Eq. 3.4.5). The only term in the KS one-electron Hamiltonian that depends on the individual spin densities is the XC potential (Eq. 3.5.5) [75]. Open-shell and magnetics systems are better treated with spin-polarized calculations. On the other hand, for closed-shell and non-magnetic systems, LDA is sufficient. By simply setting $n^{\uparrow}(\mathbf{r}) = n^{\downarrow}(\mathbf{r}) = n(\mathbf{r})/2$, one can obtain the LDA for unpolarized systems [78].

Electronic densities of real *solid* materials are not uniform, and the scheme is expected to work better only for materials like nearly-free-electron metals[31] [75,78,137]. The success of the simple L(S)DA in practical applications to systems that lie outside the formal domain of validity (very slowly varying densities) can be attributed to the fact that L(S)DA satisfies many formal properties of the exact XC energy functional (as the foregoing sum rules) [122]. However, among other obvious faults, the cancellation of the self-interaction in the Hartree term by the LDA exchange term is only approximate (compare Eqs. 2.4.53 and 2.4.58) [75,78]. Nevertheless, comparing the

[31] At some stage, most of the available DFT approximations were derived from the uniform electron gas local density. May be this was the reason why it took the quantum chemistry community too long time before applying DFT to atomic and molecular systems, where the density is far from homogeneous [75,78,112,122].

results of the LDA and LSDA calculations with experiment or with exact calculation methods is a crucial justifying tool of the performance of these approximations, and any other approximation [78]. Performance, trends and limitations of the L(S)DA can be found in many articles and books (cf. Refs. [75, pp. 80–84], [138], [122] and [135]).

The generalized gradient approximation (GGA)

The natural way to address the issue of the inhomogeneity of the electronic density is to consider the gradient and higher order derivatives of the density [78, 112, 122, 135]

$$\begin{aligned}\tilde{V}_{\text{xc}}^{\text{GE}}[n^{\uparrow}(\mathbf{r}), n^{\downarrow}(\mathbf{r})] &= \int \mathrm{d}\mathbf{r}\; n(\mathbf{r})\; \varepsilon_{\text{xc}}^{\text{GE}}(n^{\uparrow}(\mathbf{r}), n^{\downarrow}(\mathbf{r}), |\nabla n^{\uparrow}(\mathbf{r})|, |\nabla n^{\downarrow}(\mathbf{r})|, \cdots) \\ &\equiv \int \mathrm{d}\mathbf{r}\; n(\mathbf{r})\; \varepsilon_{\text{xc}}^{\text{unif}}(n(\mathbf{r}))\; F_{\text{xc}}(n^{\uparrow}(\mathbf{r}), n^{\downarrow}(\mathbf{r}), |\nabla n^{\uparrow}(\mathbf{r})|, |\nabla n^{\downarrow}(\mathbf{r})|, \cdots)\;, \quad (3.6.52)\end{aligned}$$

where $\varepsilon_{\text{xc}}^{\text{unif}}(n(\mathbf{r}))$ is the XC energy density (as in the LDA above) of the unpolarized uniform gas, and F_{xc} is a dimensionless enhancement factor depends on the spin densities and their derivatives [78] and modifies the LDA expression [75].

Using Eq. 3.6.52 above, the expression of the so-called *generalized gradient approximation* (GGA) for the Kohn-Sham XC potential $\tilde{v}_{\text{xc}}^{\sigma}[n(\mathbf{r})]$ of Eq. 3.4.11 can be found from

$$\delta\tilde{V}_{\text{xc}}^{\text{GGA}}[n(\mathbf{r})] = \sum_{\sigma} \int \mathrm{d}\mathbf{r} \left[\varepsilon_{\text{xc}}^{\text{GGA}} + n(\mathbf{r})\; \frac{\partial \varepsilon_{\text{xc}}^{\text{GGA}}}{\partial n^{\sigma}(\mathbf{r})} + n(\mathbf{r})\; \frac{\partial \varepsilon_{\text{xc}}^{\text{GGA}}}{\partial \nabla n^{\sigma}(\mathbf{r})}\; \nabla \right]_{\mathbf{r},\sigma} \delta n(\mathbf{r}, \sigma)\;. \quad (3.6.53)$$

There are in general three ways to treat the last term, one of these methods yields

$$\begin{aligned}\tilde{v}_{\text{xc}}^{\sigma}[n(\mathbf{r})] = &\sum_{\sigma} \int \mathrm{d}\mathbf{r} \left[\varepsilon_{\text{xc}}^{\text{GGA}} + n(\mathbf{r})\; \frac{\partial \varepsilon_{\text{xc}}^{\text{GGA}}}{\partial n^{\sigma}(\mathbf{r})} + n(\mathbf{r})\; \frac{\partial \varepsilon_{\text{xc}}^{\text{GGA}}}{\partial \nabla n^{\sigma}(\mathbf{r})}\; \nabla \right]_{\mathbf{r},\sigma} \\ &+ \sum_{\sigma} \int \mathrm{d}\mathbf{r}\mathrm{d}\mathbf{r}'\; n(\mathbf{r}) \left[\frac{\partial \varepsilon_{\text{xc}}^{\text{GGA}}}{\partial \nabla n^{\sigma}(\mathbf{r})} \right]_{\mathbf{r},\sigma} \frac{\delta \nabla n(\mathbf{r}')}{\delta n(\mathbf{r})} \quad (3.6.54)\end{aligned}$$

Again, the subscripts $\mathbf{r}, \sigma$ refer to the fact that the quantities in the square brackets are evaluated at $n^{\sigma} = n(\mathbf{r}, \sigma)$ [78].

The PBE-GGA functional

There are many different forms for the GGA, each follows a different philosophy in its constructions [122]. The Perdew-Burke-Ernzerhof (PBE) form [138–140] is probably the simplest [78] and the most widely used GGA functional [32]. Here, the enhancement factor F_{x} over the LDA exchange, as defined by Eq. 3.6.52, is chosen to be [135, 138–140]

$$F_{\mathsf{x}}(s) = 1 + \kappa - \frac{\kappa}{1 + \mu s^2/\kappa} \, , \tag{3.6.55}$$

where [75, 78]:

- The dimensionless density gradient $s = \frac{|\nabla n(\mathbf{r})|}{2\, \mathsf{k_F}\, n(\mathbf{r})}$ is chosen to recover the LDA: $F_{\mathsf{x}}(0) = 1$.
- $\kappa = 0.804$ satisfies the so-called local Lieb-Oxford bound [141].
- $\mu = 0.21951$ is chosen to recover the linear response of the LDA.

The PBE-GGA correlation part is given by [78]

$$\tilde{V}_{\mathsf{c}}^{\text{PBE-GGA}}\left[n^{\uparrow} + n^{\downarrow}\right] = \int \mathrm{d}\mathbf{r}\; n(\mathbf{r})\; \left(\varepsilon_c^{\text{unif}}(\mathbf{r}_s, \zeta) + H(\mathbf{r}_s, \zeta, t)\right) \, , \tag{3.6.56}$$

where the local Seitz radius $\mathbf{r}_s = \left(\frac{3}{4\pi n}\right)^{1/3}$ is the mean electronic distance [75, 89] and $t = \frac{|\nabla n(\mathbf{r})|}{2\, \phi\, \mathsf{k_{TF}}\, n(\mathbf{r})}$ with the spin scaling factor $\phi = \frac{(1+\zeta)^{2/3} + (1-\zeta)^{2/3}}{2}$ and $\mathsf{k_{TF}}$ is the Thomas-Fermi screening wave number. The additive correction term H is given by

$$H(\mathbf{r}_s, \zeta, t) = \frac{e^2}{a_0} \gamma \phi^3 \ln\left(1 + \frac{\beta}{\gamma} t^2 \left(\frac{1 + At^2}{1 + At^2 + A^2 t^4}\right)\right) \, , \tag{3.6.57}$$

where a_0 is the Bohr radius, $\beta = 0.066725$, $\gamma = 0.031091$ [75] and [78]

$$A = \frac{\beta}{\gamma} \left(e^{\left(\frac{-\varepsilon_c^{\text{unif}}}{\gamma \phi^3 \frac{e^2}{a_0}}\right)} - 1\right)^{-1} \, . \tag{3.6.58}$$

[32] Within the Physical Review family of journals, the most-cited physics paper between 1994 and 2005 was Ref. [139] by Perdew, Burke and Ernzerhof (From [112]).

Trends of L(S)DA and GGA

From the results of extensive numerical tests and the applications of the various GGAs and L(S)DA to different systems (atoms, molecules, surfaces, and bulk solids.), the following general trends are common

- The total atomic energies, the atomic first ionization energies and binding energies are more accurate in GGA than in the L(S)DA [75, 137].
- The L(S)DA tends to underestimate the experimental equilibrium volume V_0, while the GGAs tend to overestimate it [137]. However, L(S)DA underestimates (probably without exception) the lattice constant, while the PBE-GGA produces mixed results, but tend toward overestimation of the lattice constant [135]. The PBE-GGA provides the least overestimation in the GGA family of functionals [137].

  It is believed that this error originates from the core-valence interaction, where the density varies rapidly [122, 135]. Thus, it can, in principle, be removed by constructing a potential (see Subsec. 3.6.4) that goes beyond the level of semi-local approximations [122].
- Because the bulk modulus B_0 is evaluated at V_0 (see Subsec. 7.2), any error in V_0 translates into a larger error in B_0. In fact uncertainties in the calculated bulk moduli can easily be as large as 10% [135].

In general, for most bulk solid properties, the GGA is a significant improvement over the L(S)DA [135], though the improvements are statistical and not always uniform [78, 122]. Nevertheless, it is a challenge for all functionals to perform well for both extended systems (e.g. surfaces and bulk solids) and small systems (e.g. atoms and molecules). Some popular GGA functionals give good results for atoms and molecules but perform poorly for surface correlation energies. However, this challenge is often best met by those functionals which are designed to incorporate key exact properties (e.g. PBE-GGA) [122].

3.6.4 Pseudopotentials and PAW Methods

In Subsec. 3.6.1, we mentioned that one needs to distinguish between the one-electron core wave functions $|\varphi^c_{\mathbf{k}}\rangle$ and the one-electron valence wave functions $|\varphi^v_{\mathbf{k}}\rangle$. This is due to the fact that

$|\varphi^v_{\mathbf{k}}\rangle$ have appreciable probability in the interstitial regions between nuclei (i.e. between lattice cites $\mathbf{R}$), while $|\varphi^c_{\mathbf{k}}\rangle$ are well localized about the lattice cites $\mathbf{R}$ [89]. Moreover, due to the rapid spatial variations of $|\varphi^v_{\mathbf{k}}\rangle$ in the core region, it is difficult to obtain *convergence* (see Subsections 3.6.1 and 6.1) using a small number of plane waves (PWs) to represent $|\varphi^v_{\mathbf{k}}\rangle$ *everywhere* in the space [89].

The orthogonalized plane waves (OPWs) method

With the hope to reproduce the rapid oscillatory behavior of the valence orbitals in the core region, Herring [142] suggested that the *simple* plane waves (in the expansions 3.6.3, 3.6.7 and 3.6.10) should be replaced, right from the start, by a set of plane waves that *made* orthogonal to the core eigenfunctions. The new basis set is known as the *orthogonalized plane waves* (OPWs) and is given by [89, 142]:

$$
\begin{aligned}
|\phi_{\mathbf{k}}\rangle &= \left|\tilde{\phi}_{\mathbf{k}}\right\rangle + \sum_c b^c_{\mathbf{k}}\, |\varphi^c_{\mathbf{k}}\rangle \\
\phi_{\mathbf{k}}(\mathbf{r}) = \langle \mathbf{r}|\phi_{\mathbf{k}}\rangle &= \; e^{j\mathbf{k}\cdot\mathbf{r}} + \sum_c b^c_{\mathbf{k}}\; \varphi^c_{\mathbf{k}}(\mathbf{r})\;.
\end{aligned}
\tag{3.6.59}
$$

Here, the sum runs over all the core levels (hence the superscript "c") with Bloch wave vector $\mathbf{k}$. By requiring

$$
\langle \varphi^c_{\mathbf{k}}|\phi_{\mathbf{k}}\rangle = \int \mathrm{d}\mathbf{r}\; \varphi^{c*}_{\mathbf{k}}(\mathbf{r})\; \phi_{\mathbf{k}}(\mathbf{r}) = 0 \tag{3.6.60}
$$

one obtains

$$
b^c_{\mathbf{k}} = -\int \mathrm{d}\mathbf{r}\; \varphi^{c*}_{\mathbf{k}}(\mathbf{r})\; e^{j\mathbf{k}\cdot\mathbf{r}}\;. \tag{3.6.61}
$$

This construction of the OPWs $\phi_{\mathbf{k}}(\mathbf{r})$ give them the following properties

- The OPWs $\phi_{\mathbf{k}}(\mathbf{r})$ have the required rapidity in the core region. This can be seen from the imposed condition 3.6.60 where $\phi_{\mathbf{k}}(\mathbf{r})$ is orthogonal to all core wave functions $\varphi^c_{\mathbf{k}}(\mathbf{r})$.
- The second term in 3.6.59 has a small contribution in the interstitial region. This is because the core wave functions $\varphi^c_{\mathbf{k}}(\mathbf{r})$ are localized about the lattice cites $\mathbf{R}$.
- The property above implies that the OPW in the interstitial region is very close to the single plane wave $e^{j\mathbf{k}\cdot\mathbf{r}}$, i.e. the first term of 3.6.59.

- Because both $e^{j\mathbf{k}\cdot\mathbf{r}}$ and $\varphi^c_{\mathbf{k}}(\mathbf{r})$ satisfy the Bloch condition (see App. B), so does $\phi_{\mathbf{k}}(\mathbf{r})$.

In his original work, Herring discussed the rapidity of convergence of his new OPW expansion and gave expressions for the matrix elements [142]. It turned out that the OPWs matrix element of the potential is much smaller than the corresponding PWs one. Moreover, while it is hopeless to get convergence using simple PWs, the convergence of the OPWs expansion turned out to be very much faster [89].

Pseudopotentials

So far, the OPW approach may look nothing more than a method of construction of basis functions. However, the fact is that the OPW method is the prescience to all modern pseudo potentials and PAW methods (discussed below). To see this, we start from the last property of the OPWs above [78]. The property suggests that one can expand the one-electron[33] (Bloch or KS) eigenstates $\varphi_{\mathbf{k}}(\mathbf{r})$ linearly in the OPW basis (compare with PWs expansion 3.6.10):

$$\begin{aligned}
\varphi_{\mathbf{k}}(\mathbf{r}) &= \sum_{\mathbf{k}} c(\mathbf{K})\ \phi_{\mathbf{k}+\mathbf{K}}(\mathbf{r}) \\
&= \sum_{\mathbf{k}} c(\mathbf{K}) e^{j(\mathbf{k}+\mathbf{K})\cdot\mathbf{r}} + \sum_{\mathbf{k}} c(\mathbf{K}) \sum_c \left(- \int \mathrm{d}\mathbf{r}'\ \varphi^{c*}_{\mathbf{k}}(\mathbf{r}')\ e^{j(\mathbf{k}+\mathbf{K})\cdot\mathbf{r}'} \right)\ \varphi^c_{\mathbf{k}}(\mathbf{r}) \\
&= \sum_{\mathbf{k}} c(\mathbf{K}) e^{j(\mathbf{k}+\mathbf{K})\cdot\mathbf{r}} - \sum_c \int \mathrm{d}\mathbf{r}'\ \varphi^{c*}_{\mathbf{k}}(\mathbf{r}') \left(\sum_{\mathbf{k}} c(\mathbf{K})\ e^{j(\mathbf{k}+\mathbf{K})\cdot\mathbf{r}'} \right)\ \varphi^c_{\mathbf{k}}(\mathbf{r})\ ,
\end{aligned}$$

that is

$$\boxed{\varphi_{\mathbf{k}}(\mathbf{r}) = \tilde{\varphi}_{\mathbf{k}}(\mathbf{r}) \quad - \sum_c \left(\int \mathrm{d}\mathbf{r}'\ \varphi^{c*}_{\mathbf{k}}(\mathbf{r}')\tilde{\varphi}_{\mathbf{k}}(\mathbf{r}') \right)\ \varphi^c_{\mathbf{k}}(\mathbf{r})}\ , \tag{3.6.62}$$

where we wrote the *smooth* plane wave part as

$$\tilde{\varphi}_{\mathbf{k}}(\mathbf{r}) = \sum_{\mathbf{k}} c(\mathbf{K}) e^{j(\mathbf{k}+\mathbf{K})\cdot\mathbf{r}}\ , \tag{3.6.63}$$

and we made use of Eq. 3.6.61 in the second line.

[33] In this context, the one-electron orbitals are referred to as *all-electron* (AE) wave functions, to distinguish them from the so-called *pseudo* (PS) wave functions that will appear shortly in the discussion.

Now, suppose that we are dealing with a valence orbital, that is $\varphi_{\mathbf{k}}(\mathbf{r}) = \varphi^v_{\mathbf{k}}(\mathbf{r})$, then we rewrite Eq. 3.6.62 above as[34]

$$\varphi^v_{\mathbf{k}}(\mathbf{r}) = \tilde{\varphi}^v_{\mathbf{k}}(\mathbf{r}) - \sum_c \left(\int \mathrm{d}\mathbf{r}\ \varphi^{c*}_{\mathbf{k}}(\mathbf{r}) \tilde{\varphi}^v_{\mathbf{k}}(\mathbf{r}) \right)\ \varphi^c_{\mathbf{k}}(\mathbf{r}') \ . \tag{3.6.64}$$

Recall that the exact one-electron valence $\varphi^v_{\mathbf{k}}(\mathbf{r})$ and core $\varphi^c_{\mathbf{k}}(\mathbf{r})$ wave functions satisfy the KS eigenvalue equations 3.6.1:

$$\hat{h}_{\mathsf{KS}}\ \varphi^v_{\mathbf{k}}(\mathbf{r}) = \varepsilon^v_{\mathbf{k}} \varphi^v_{\mathbf{k}}(\mathbf{r}) \qquad \text{and} \qquad \hat{h}_{\mathsf{KS}}\ \varphi^c_{\mathbf{k}}(\mathbf{r}) = \varepsilon^c_{\mathbf{k}} \varphi^c_{\mathbf{k}}(\mathbf{r}) \ . \tag{3.6.65}$$

Accordingly,

$$\hat{h}_{\mathsf{KS}}\ \varphi^v_{\mathbf{k}}(\mathbf{r}) = \hat{h}_{\mathsf{KS}}\ \tilde{\varphi}^v_{\mathbf{k}}(\mathbf{r}) - \sum_c \left(\int \mathrm{d}\mathbf{r}\ \varphi^{c*}_{\mathbf{k}}(\mathbf{r}) \tilde{\varphi}^v_{\mathbf{k}}(\mathbf{r}) \right)\ \hat{h}_{\mathsf{KS}}\ \varphi^c_{\mathbf{k}}(\mathbf{r}')$$

$$\begin{aligned} \varepsilon^v_{\mathbf{k}} \left(\tilde{\varphi}^v_{\mathbf{k}}(\mathbf{r}) - \sum_c \left(\int \mathrm{d}\mathbf{r}\ \varphi^{c*}_{\mathbf{k}}(\mathbf{r}) \tilde{\varphi}^v_{\mathbf{k}}(\mathbf{r}) \right)\ \varphi^c_{\mathbf{k}}(\mathbf{r}') \right) &= \hat{h}_{\mathsf{KS}}\ \tilde{\varphi}^v_{\mathbf{k}}(\mathbf{r}) \\ &\quad - \sum_c \left(\int \mathrm{d}\mathbf{r}\ \varphi^{c*}_{\mathbf{k}}(\mathbf{r}) \tilde{\varphi}^v_{\mathbf{k}}(\mathbf{r}) \right)\ \varepsilon^c_{\mathbf{k}}\ \varphi^c_{\mathbf{k}}(\mathbf{r}') \ . \end{aligned} \tag{3.6.66}$$

That is

$$\hat{h}_{\mathsf{KS}}\ \tilde{\varphi}^v_{\mathbf{k}}(\mathbf{r}) + \sum_c (\varepsilon^v_{\mathbf{k}} - \varepsilon^c_{\mathbf{k}}) \left(\int \mathrm{d}\mathbf{r}\ \varphi^{c*}_{\mathbf{k}}(\mathbf{r}) \tilde{\varphi}^v_{\mathbf{k}}(\mathbf{r}) \right)\ \varphi^c_{\mathbf{k}} = \varepsilon^v_{\mathbf{k}}\ \tilde{\varphi}^v_{\mathbf{k}}(\mathbf{r}) \ . \tag{3.6.67}$$

More compactly

$$\boxed{\left(\hat{h}_{\mathsf{KS}} + v^{\mathfrak{R}} \right) \tilde{\varphi}^v_{\mathbf{k}}(\mathbf{r}) = \left(-\frac{\hbar^2}{2m_e}\ \nabla^2_{\mathbf{r}} + v^{\mathsf{PS}} \right) \tilde{\varphi}^v_{\mathbf{k}}(\mathbf{r}) = \varepsilon^v_{\mathbf{k}}\ \tilde{\varphi}^v_{\mathbf{k}}(\mathbf{r})} \ , \tag{3.6.68}$$

[34] Notice that here we trivially shifted the primes from the integrand of 3.6.62 to $\varphi^c_{\mathbf{k}}(\mathbf{r})$.

where the potential $v^{\mathfrak{R}}$ is defined via

$$v^{\mathfrak{R}} f = \sum_c (\varepsilon^v_{\mathbf{k}} - \varepsilon^c_{\mathbf{k}}) \left(\int \mathrm{d}\mathbf{r}\ \varphi^{c*}_{\mathbf{k}}\ f \right)\ \varphi^c_{\mathbf{k}}\ , \tag{3.6.69}$$

while the *pseudopotential* v^{PS} is defined to be the sum of v_{R} (Eq. 3.4.19) and $v^{\mathfrak{R}}$.

Eq. 3.6.68 we arrived at is an effective Schrödinger equation satisfied by the *pseudo wave functions* $\tilde{\varphi}^v_{\mathbf{k}}(\mathbf{r})$, i.e. the smooth part of the wave function $\varphi^v_{\mathbf{k}}(\mathbf{r})$.

At this point, we must mention that there are many ways, other than Eq. 3.6.69, to define a potential $v^{\mathfrak{R}}$ such that $(\hat{h}_{\mathrm{KS}} + v^{\mathfrak{R}})$ has the same valance eigenvalues as $\hat{h}_{\mathrm{KS}}$ [89]. This leads people to search for new ideas, clever choices and constructions of the potentials [78].

The Projector Augmented Wave (PAW) Method

In the projector augmented wave (PAW) method [143–145], a sphere with radius r_c (known as core or cut-off radius and, in practice, is usually chosen to be about half the nearest-neighbor distance [144]) is constructed around each atom in the crystal, and the term *augmentation regions* Ω_{aug} is attached to these spheres. The *interstitial regions* between the Ω_{aug}'s are denoted by the symbol Ω_{int}. Then the true *all-electron (AE) wave functions*[35] $|\varphi_{i\mathbf{k}}\rangle$ are derived from the *Pseudo (PS) wave functions* $|\tilde{\varphi}_{i\mathbf{k}}\rangle$ via the following linear transformation:

$$\boxed{\underbrace{|\varphi_{i\mathbf{k}}\rangle}_{\mathrm{AE}} = \underbrace{|\tilde{\varphi}_{i\mathbf{k}}\rangle}_{\mathrm{PS}} + \underbrace{\sum_\beta c_{i\mathbf{k},\beta}\ |\phi_\beta\rangle}_{\text{AE on-site}} - \underbrace{\sum_\beta c_{i\mathbf{k},\beta}\ |\tilde{\phi}_\beta\rangle}_{\text{PS on-site}}}\ , \tag{3.6.70}$$

As in the OPW method (Eqs. 3.6.62 and 3.6.63), the PS wave function $|\tilde{\varphi}_{i\mathbf{k}}\rangle$ is expanded in a plane wave basis set. That means it is smooth in the whole space. However, the difference now

[35] A true Kohn-Sham *single-electron* wave function $|\varphi_{i\mathbf{k}}\rangle$ will be called an *all-electron* (AE) wave function and may take the superscript "AE": $|\varphi^{\mathrm{AE}}_{i\mathbf{k}}\rangle$. The term is used, in this context, in contrast to the *Pseudo* (PS) wave functions $|\tilde{\varphi}_{i\mathbf{k}}\rangle$, and must not to be confused with the *many-electron* wave function $\Phi(\{\mathbf{r}\};\{\mathbf{R}\})$. Following Blöchl [143], all *Pseudo* (PS) wave functions, and related quantities, in the present subsection are marked with a tilde "~", i.e. $|\tilde{\varphi}_{i\mathbf{k}}\rangle$.

is that

$$|\tilde{\varphi}_{i\mathbf{k}}\rangle = \sum_{\mathbf{k}} c(\mathbf{K}) e^{j(\mathbf{k}+\mathbf{K})\cdot\mathbf{r}} = |\varphi_{i\mathbf{k}}\rangle \quad \text{in } \Omega_{\text{int}} \text{ only} , \tag{3.6.71}$$

while the true $|\varphi_{i\mathbf{k}}\rangle$ oscillates rapidly in Ω_{aug}. These PS wave functions, $|\tilde{\varphi}_{i\mathbf{k}}\rangle$, are the variational quantities in the PAW formalism[36].

The second term of the expansion 3.6.70 is *added* in order to take care for the rapid spatial variation of the true AE $|\varphi_{i\mathbf{k}}\rangle$ in Ω_{aug}, The summand of this term constitutes the on-site *all-electron (AE) partial wave functions* $|\phi_\beta\rangle$. These are the one-electron exact solutions to KS equations for a reference spherical atom. Beside the principal quantum number n, the index β is used to refer to a collection of indexes and quantum numbers: the atomic site $\mathbf{R}$, atom type M, angular momentum quantum numbers $L = (l, m)$, and to an additional index ν that represents an atomic energy reference $\mathcal{E}_{\nu,l}$.

By now, two *errors* have been introduced: The error within Ω_{aug} introduced by the smooth PS $|\tilde{\varphi}_{i\mathbf{k}}\rangle$, and the error within Ω_{int} introduced by the AE on-site $|\phi_\beta\rangle$. To get rid of both errors simultaneously, the *pseudo (PS) partial wave functions* $\left|\tilde{\phi}_\beta\right\rangle$ are introduced in the summand of the *subtracted* term in the expansion 3.6.70. These $\left|\tilde{\phi}_\beta\right\rangle$ are constructed such that

$$\sum_\beta c_{i\mathbf{k},\beta} \, |\tilde{\phi}_\beta\rangle = |\tilde{\varphi}_{i\mathbf{k}}\rangle \quad \text{within } \Omega_{\text{aug}} , \tag{3.6.72a}$$

$$\left|\tilde{\phi}_\beta\right\rangle = |\phi_\beta\rangle \quad \text{within } \Omega_{\text{int}} , \tag{3.6.72b}$$

This can be achieved by means of constructing the PS partial waves as

$$\tilde{\phi}_{\beta=L\nu}(\mathbf{r}) = \langle \mathbf{r}|\tilde{\varphi}_\beta\rangle = Y_L(\mathbf{r}-\mathbf{R})\tilde{\phi}_{l\nu}(|\mathbf{r}-\mathbf{R}|) , \tag{3.6.73}$$

and expanding the spherical harmonics $Y_L(\mathbf{r}-\mathbf{R})$ in terms of Bessel functions.

[36] It is this *pseudo part* of the wave function people really refer to when they say: "We expanded the KS *wave functions* in PWs with E_{cut} ... ". See Subsections 3.6.1 and 6.1.

In order to obtain proper cancellations and matchings, the coefficients $c_{i\mathbf{k},\beta}$ must be constructed carefully. It turned out that these coefficients are scalar products

$$c_{i\mathbf{k},\beta} = \langle \tilde{p}_\beta | \tilde{\varphi}_{i\mathbf{k}} \rangle \ , \tag{3.6.74}$$

where the *projector* functions $|\tilde{p}_\beta\rangle$ are chosen to be localized in the Ω_{aug}, dual to $|\tilde{\phi}_{i\mathbf{k},\alpha}\rangle$, and obey

$$\left\langle \tilde{p}_\beta \middle| \tilde{\phi}_{i\mathbf{k},\alpha} \right\rangle = \delta_{\alpha\beta} \ . \tag{3.6.75}$$

Now, we can rewrite Eq. 3.6.70 in a full form as

$$\boxed{\underbrace{|\varphi_{i\mathbf{k}}\rangle}_{\text{AE}} = \underbrace{|\tilde{\varphi}_{i\mathbf{k}}\rangle}_{\text{PS}} + \underbrace{\sum_\beta \langle \tilde{p}_\beta | \tilde{\varphi}_{i\mathbf{k}} \rangle \ |\phi_\beta\rangle}_{\text{AE on-site}} - \underbrace{\sum_\beta \langle \tilde{p}_\beta | \tilde{\varphi}_{i\mathbf{k}} \rangle \ |\tilde{\phi}_\beta\rangle}_{\text{PS on-site}}} \ , \tag{3.6.76}$$

which shows explicitly that the basic ingredients of the PAW method (compared i.e. to the OPW method) are partial waves and the projectors. Starting from this equation, it is straightforward to show that the AE charge density, in the PAW method, has approximately a similar form as the AE wave function:

$$n(\mathbf{r}) = \underbrace{\sum_i \sum_{\mathbf{k}\in \text{BZ}} f_{i,\mathbf{k}} \langle \tilde{\varphi}_{i\mathbf{k}} | \mathbf{r} \rangle \langle \mathbf{r} | \tilde{\varphi}_{i\mathbf{k}} \rangle}_{\tilde{n}(\mathbf{r})} + \underbrace{\sum_{(\alpha,\beta)} \rho_{\alpha\beta} \langle \phi_\alpha | \mathbf{r} \rangle \langle \mathbf{r} | \phi_\beta \rangle}_{n^1(\mathbf{r})} - \underbrace{\sum_{(\alpha,\beta)} \rho_{\alpha\beta} \left\langle \tilde{\phi}_\alpha \middle| \mathbf{r} \right\rangle \left\langle \mathbf{r} \middle| \tilde{\phi}_\beta \right\rangle}_{\tilde{n}^1(\mathbf{r})} \ , \tag{3.6.77}$$

where

$$\rho_{\alpha\beta} = \sum_{(\alpha,\beta)} f_{i,\mathbf{k}} \langle \tilde{\varphi}_{i\mathbf{k}} | \tilde{p}_\alpha \rangle \langle \tilde{p}_\beta | \tilde{\varphi}_{i\mathbf{k}} \rangle \tag{3.6.78}$$

are the occupancies of each augmentation channel (α, β).

Indeed, the brief discussion above introduces only some basic ideas of the PAW method. However, the topic is broad, and many issues have to be considered, such as: details about which approxi-

mations are required in real calculations; the expressions for $\hat{h}_{\mathrm{KS}}$ and forces; the implementation in first-principles molecular dynamics schemes; formal description and construction of the basic ingredients used in the method, such as partial waves and projector functions; analysis of the errors introduced in the practical implementation of the method; numerical test calculations; and details about the relation between the PAW method and the other existing electronic structure calculations approaches. Interested readers are referred to Refs. [143–145].

Relativistic Effects

If heavy elements present in a solid, Dirac equation [146] (with Darwin, mass-velocity and spin-orbit terms included) must be solved. On the other hand, non-relativistic calculations are well justified for solids containing light elements. For the third class of medium atomic numbers (up to about 54), the so-called *scalar relativistic calculations* [147] are commonly performed. In this scheme, the main expansion and contraction of orbitals due to the Darwin and the mass-velocity terms are incorporated, but spin-orbit splittings are neglected [148].

In practice inclusion of the spin-orbit term is computationally demanding. This is due to the fact that spin-down and spin-up wave functions are coupled by this spin-orbit term. If we have M basis functions without spin-orbit coupling, then inclusion of the spin-orbit term in the Hamiltonian leads to a $2M \times 2M$ matrix equation. Due to the M^3 scaling relation, the latter, in turn, requires about eight times as much computer time as the former [148].

In general, valence states carry small spin-orbit effects, and essential relativistic effects originate deep inside the atomic core. Therefore, it is often sufficient to carry out fully relativistic calculations for spherical atomic geometry. Obtained results are expected to be transferable to solids and molecules with no change. Therefore, in actual calculations fully relativistic effects of the atomic core are built-in the (pseudo)potential [78].

For brief discussion of Dirac equation and spin-orbit coupling, we refer to Ref. [78, Sec. 10.4 and p. 218]. For a decent survey on relativistic density functional theory (RDFT), we recommend Ref. [149] and original articles referred to therein.

3.7 Summary

The topic of this chapter was the density functional theory (DFT). The original idea beyond the theory, the Thomas-Fermi-Dirac model was discussed in Sec. 3.1, then the Hohenberg-Kohn DFT was introduced in Sec. 3.2. Some subtleties were discussed in Sec. 3.3, and the clever Kohn-Sham approach to DFT was discussed in Sec. 3.4. The latter leads to a set of Schrödinger-like equations that must be solved self-consistently, with special handling to their ingredients. Basis sets for the expansion of the one-electron orbitals $\varphi^{\sigma}_{i,\mathbf{k}}$ of the one-electron KS equations 3.6.2 was discussed in Subsec. 3.6.1. The one-electron kinetic energy (Eqs. 3.4.5 and 3.4.9) and the Hartree interaction (Eq. 3.4.10) terms in Eq. 3.6.2 are by now known exactly. The biggest unknown part $\tilde{v}^{\sigma}_{\mathrm{xc}}$ was treated approximately in Subsec. 3.6.3. the quantum numbers σ and $\mathbf{k}$ were treated in Sec. 3.5 and Subsec. 3.6.2, respectively. The only piece in Eq. 3.6.2 that we have not considered so far is the electron-nuclei interaction $v_{\mathrm{ext}}(\mathbf{r})$. This was the subject of the last subsection. Many related practical issues are deferred to Part II. One of the limitations of DFT and an approach to overcome are the subject of the next chapter.

4. The GWA Approach

Properties of matter can be grouped into two main categories determined by the electronic ground states (such as: total energy, electron density, equilibrium crystal structure and elastic constants.) and electronic exited states (e. g. optical properties, spectra of adding and removing electrons.). This distinction determines the framework for theoretical understanding and development of the entire field of electronic calculations [78].

4.1 Excited States in KS-DFT

The widely used DFT, described in Ch. 3, is a reasonably successful approach for determination of structural and some *ground-state* physical properties of many solids [1]. The ground-state density in particular is, in principle, exact [78–80]. However, a well-known failure of DFT is that it does not describe the *excited states* accurately [80]. In particular, it is well known that the calculated band gaps in semiconductors and insulators are too small in comparison to experiment [105], the Fermi surface of metals are in general not correct [78], and sometimes even the general qualitative features of the conduction band is not correct [150]. Compared to experiment, *Optical spectra* calculated within DFT show significant deviations. The position of the energy characteristic peaks and their corresponding amplitudes can be wrong [151].

This striking failure of DFT is intimately linked to the fact that the KS one-electron eigenvalues (*band structure*) ϵ_i and wave functions φ_i are in principle nothing but mathematical constructs [75,78,79,150], while the fundamental quantities in DFT are the ground state total energy and the electron density [105]. Neither these KS eigenvalues correspond to true electron removal or addition energies nor their differences correspond to optical (neutral) excitations[2] [78, 152].

A successful approach to solve the foregoing problem is to go beyond DFT using KS eigenstates as basis for *many-body perturbation theory* (MBPT) calculations. The approach is based on the

[1] To see why single-particle approximations are successful, see for example [79, pp. 66–67]

[2] In 1985 it was shown that in exact DFT the highest occupied eigenvalue (highest occupied molecular orbital level, or HOMO) does have a physical interpretation: it corresponds to the ionization potential [78, 152].

concept of the so-called *quasi-particle*, the *Green's function* and the *self-energy* [77, 80, 150].

4.2 Quasi-Particles (QP)

The Coulomb repulsion between *bare* electrons leads to a depletion of negative charge around a given electron and the ensemble of this electron and its surrounding positive screening charge forms a *quasi-particle* [80]. This concept of quasi-particles was first introduced by Landau [77,79]. The advantage of the notion is evident, since instead of dealing with a complicated system of strongly interacting particles, one can treat the system as constitutes of weakly interacting quasi-particles. In such a case, one formulate a *perturbation theory* starting from non-interacting particles (usually KS particles) as the *unperturbed* state [79].

4.3 Green's functions

The mathematical description of quasi-particles is based on the single-particle Green's function G [80]. In mathematics, Green's function of a linear operator $\mathcal{L}$ is defined by [121, 126]

$$[z - \mathcal{L}(r)]G(x, x'; z) = \delta(x - x') \ , \tag{4.3.1}$$

with $\delta(x - x')$ being the Dirac's delta function. For example, a single particle in an external potential $v_{\text{ext}}(\mathbf{r})$ satisfies [126]

$$\left[-\frac{\hbar^2}{2m}\nabla^2 + v_{\text{ext}}(\mathbf{r}) - \epsilon\right] G^{(0)}(\mathbf{r}, \mathbf{r}'; \epsilon) = -\delta(\mathbf{r} - \mathbf{r}') \ . \tag{4.3.2}$$

For a many-electron system, it can be shown that the one-particle Green's function $G(\mathbf{r}, \mathbf{r}'; E)$ of the system satisfies [75]

$$\left\{ -\frac{\hbar^2}{2m}\nabla^2 + v_{\text{ext}}(\mathbf{r}) - \epsilon \right\} G(\mathbf{r}, \mathbf{r}'; \epsilon) + \int d\mathbf{r}'' \ \Sigma(\mathbf{r}, \mathbf{r}''; \epsilon) G(\mathbf{r}'', \mathbf{r}'; \epsilon) = -\delta(\mathbf{r} - \mathbf{r}') \ . \tag{4.3.3}$$

In this expression, we have written G in the energy domain. This is possible because when the Hamiltonian is time-independent, G depends only on the time difference $t - t'$, i.e. $G \equiv$

$G(\mathbf{r},\mathbf{r}';t-t')$. A Fourier transformation of $G(\mathbf{r},\mathbf{r}';t-t')$ w.r.t. $t-t'$ then yields $G(\mathbf{r},\mathbf{r}';\epsilon)$ [126]. Physically, the one-particle Green's function $G(\mathbf{r},\mathbf{r}';t-t')$ gives the probability of finding an electron at $\mathbf{r}$ at time t given that there was an electron at $\mathbf{r}'$ at time t'. In some sense, $G(\mathbf{r},\mathbf{r}';t-t')$ represents a kind of extension of the *static* pair correlation function $g(\mathbf{r},\mathbf{r})$, introduced in Sec. 2.4, to the time domain [3]. If Eq. 4.3.3 can be solved exactly, i.e. if $G(\mathbf{r},\mathbf{r}';t-t')$ is known, all physical properties are, in principle, accessible [75].

If the exact $G_0(\mathbf{r},\mathbf{r}';\epsilon)$ of related reference (e.g. KS reference system) is known exactly, then $G(\mathbf{r},\mathbf{r}';\epsilon)$ of the true system can obtained by means of MBPT using Dyson's equation

$$G(\mathbf{r},\mathbf{r}';\epsilon) = G_0(\mathbf{r},\mathbf{r}';\epsilon) + \int \mathrm{d}\mathbf{r}_1\mathrm{d}\mathbf{r}_2\; G_0(\mathbf{r},\mathbf{r}_1;\epsilon)\;\Delta\Sigma(\mathbf{r}_1,\mathbf{r}_2;\epsilon)\;G(\mathbf{r}_2,\mathbf{r}';\epsilon)\;, \tag{4.3.4}$$

where the perturbation $\Delta\Sigma$ is given in terms of the interaction potential of the reference system v_0 by[4]

$$\Delta\Sigma(\mathbf{r}_1,\mathbf{r}_2;\epsilon) = \Sigma(\mathbf{r}_1,\mathbf{r}_2;\epsilon) - v_0(\mathbf{r}_1,\mathbf{r}_2)\;. \tag{4.3.5}$$

If one takes the KS system as the reference system, the Green's function assumes the exact form

$$G_0(\mathbf{r},\mathbf{r}';\epsilon) = \sum_i \frac{\varphi_i(\mathbf{r})\varphi_i^*(\mathbf{r}')}{\epsilon-\epsilon_i}\;. \tag{4.3.6}$$

4.4 The Self-Energy

The quantity Σ that appears in Eqs. 4.3.3 and 4.3.4 is known as the self-energy. Generally, it is an energy dependent, non-local, and in general non-Hermitian operator [75, 77, 80]. Physically, it represents the difference between the bare particle and the quasi-particle. The name, *self-energy*, emerges from the fact that Σ is equal to the energy of the bare particle interacting with itself through the polarization cloud which the particle induces in the many-body system. Hence, Σ

[3] Recall that in Ch. 2 we proceeded from the pair correlation function to the *reduced density matrix*. The latter quantity does *not* contain explicit information about the coordinates of every single particle in the system, yet it can replace the complicated many-body wave function since it contains *all* the relevant information about the system. The Green's function G is another object which has the same property [126].

[4] Notice that $v_0(\mathbf{r}_1,\mathbf{r}_2)=0$ for a non-interacting reference system [75].

accounts for all the exchange and correlation interactions, static and dynamic, including those effects neglected in the reference system (see Eq. 4.3.5). With such many-body complexities, an exact determination of Σ is *not* possible, and a numerical determination of the Σ can only be approximate [80].

4.5 The GW Approximation

A practical scheme for the quantitative calculations of Σ in metals, semiconductors and insulators is the so-called dynamically screened interaction, or the GW approximation (GWA), first proposed by Hedin in 1965 [110]. In this approximation, the self-energy Σ is expanded linearly in terms of the screened interaction

$$\Sigma_{GW}(\mathbf{r},\mathbf{r}';t) \approx jG(\mathbf{r},\mathbf{r}';t)W(\mathbf{r},\mathbf{r}';t)\ , \tag{4.5.1}$$

which explains the name of the approximation [80], or in the energy domain

$$\Sigma_{GW} = j\int d\epsilon'\ G(\mathbf{r},\mathbf{r}';\epsilon+\epsilon')W(\mathbf{r},\mathbf{r}';\epsilon), \tag{4.5.2}$$

where the screened interaction W can be obtained from the bare Coulomb interaction v via

$$W(\mathbf{r},\mathbf{r}';\epsilon) = j\int d\mathbf{r}_1\varepsilon^{-1}(\mathbf{r},\mathbf{r}_1;\epsilon)v(\mathbf{r}_1,\mathbf{r}'), \tag{4.5.3}$$

with ε the dielectric function; or equivalently

$$W(\mathbf{r},\mathbf{r}';\epsilon) = v(\mathbf{r}_1,\mathbf{r}') + \int \mathrm{d}\mathbf{r}_1\ \mathrm{d}\mathbf{r}_1\ W(\mathbf{r},\mathbf{r}_1;\epsilon)\ P(\mathbf{r}_1,\mathbf{r}_2;\epsilon)\ v(\mathbf{r}_2,\mathbf{r}') \tag{4.5.4}$$

where the polarization $P(\mathbf{r}_1,\mathbf{r}_2;\epsilon)$ is given by

$$P(\mathbf{r},\mathbf{r}';\epsilon) = -jG(\mathbf{r},\mathbf{r}';\epsilon)\ G(\mathbf{r}',\mathbf{r};\epsilon)\ . \tag{4.5.5}$$

In practice, the set of the four equations 4.3.5, 4.5.2, 4.5.4, and 4.5.5 are solved self-consistently [75].

4.6 The Quasi-Particle Equations

Within the GWA method, the quasi-particle energies $\epsilon^{\mathsf{QP}}_{i,\mathbf{k}}$ are the solutions of the following quasi-particle (QP) equations, which can be written for a periodic crystal as [80, 153]

$$\left\{ -\frac{\hbar^2}{2m}\nabla^2 + \int d\mathbf{r}' \frac{n(\mathbf{r}')}{|\mathbf{r}-\mathbf{r}'|} + v_{\mathsf{ext}}(\mathbf{r}) \right\} \varphi^{\mathsf{QP}}_{i,\mathbf{k}}(\mathbf{r}) + \int d\mathbf{r}' \Sigma(\mathbf{r},\mathbf{r}';\epsilon^{\mathsf{QP}}_{i,\mathbf{k}}) \varphi^{\mathsf{QP}}_{i,\mathbf{k}}(\mathbf{r}') = \epsilon^{\mathsf{QP}}_{i,\mathbf{k}} \varphi^{\mathsf{QP}}_{i,\mathbf{k}}(\mathbf{r}) \ . \tag{4.6.1}$$

In practice, the orbitals $\varphi^{\mathsf{QP}}_{i,\mathbf{k}}(\mathbf{r})$ are taken from the ground-state KS-DFT calculations, and the corresponding QP eigenvalues read

$$\epsilon^{\mathsf{QP}}_{i,\mathbf{k}} = \mathfrak{Re}\left(\left\langle \varphi^{\mathsf{QP}}_{i,\mathbf{k}} \middle| H_{\mathsf{KS}} - v^{\sigma}_{\mathsf{XC}} + \Sigma_{GW} \middle| \varphi^{\mathsf{QP}}_{i,\mathbf{k}} \right\rangle \right) \ . \tag{4.6.2}$$

4.7 Further Technical Details

The presentation of the subject in this Chapter is meant to be very brief and phenomenological. A proper discussion of Σ and G requires second quantization formalism and via Feynman diagrams [126]. For comprehensive discussion of such topics, interested readers are referred to Ref. [77]. Article [80] is a very good review of quasi-particle calculations in the GWA. For details on the implementation of the GWA scheme within the PAW framework, we refer readers to Ref. [150]. Nevertheless, more practical issues (e.g. the self-consistent iteration and the calculation of the dielectric matrix) will be discussed in Ch. 9.

Part II

Calculation and Characterization Methods

"... non of the methods we shall describe can be carried through analytically ... . All require modern, high-speed computers for their execution. ... and the kinds of approximations one is likely to consider are influenced by available computational techniques."

Neil W. Ashcroft and N. David Mermin [89, p. 193].

"... nevertheless it is not easy to set all parameters correctly"!

VASP the GUIDE [154].

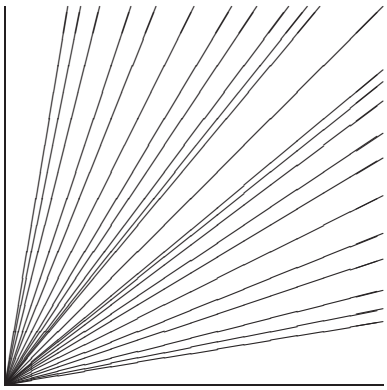

5. Chemical Formulas and Crystal Structures

As a part of the transition-metal pnictides, transition-metal nitrides (TMNs) crystallize in a large number of different structural types. This exhibited structural richness is translated into their physical properties. Among TMNs one can find metals, semiconductors, superconductors and different types of magnetic behavior [155]. Probably, then, the main reason why researchers (within the electronic structure calculations community) test different chemical stoichiometries and crystal structures of transition-metal nitrides (TMNs) is that many TMNs are known to form more than one nitride [21, p. 835].

Our target materials in the present investigation (see Ch. 1) are the nitrides of the late transition metals: Pd, Pt, Cu, Ag, Au and Zn. We start this chapter (i.e. Sec. 5.1) by presenting the procedure we followed in this study to choose certain molecular formulas for these materials. In Sec. 5.2, we propose a loose procedure to assign crystal structures to the chosen stoichiometric compounds. Then we tabulate the output of our application of these two procedures and give some additional information about the considered crystal structures. In Sec. 5.3, the problem of this study (fisrt posed in Sec. 1.2) will be formally reposed within the introduced motivations (Sec. 1.1), theoretical framework (Part I) and within the chosen chemical formulas and crystal structures (the present chapter).

5.1 Stoichiometries and Chemical Formulas

The term *stoichiometric compound* is used in general to refer to kind of materials that have chemical combination in simple integral ratios. That is, such a compound has no excess of reactants or products, and it balances the chemical equation that represents the given chemical reaction [156]. On the other hand, the term *solid solution*, or *mixed crystal*, refers to a crystal which contains a second chemical constituent (considered as a *defect*) that fits into and is distributed in the lattice of the host crystal [156].

In the present chapter, we use the symbol M_mN_n to refer to a general TMN with an m:n ratio of a transition metal M to nitrogen N, where m and n are generally integers. It is well known that many (if not most) real transition-metal nitrides behave as (non-stoichiometric) solid solutions, with chemical formulas MN_x, where "x" as a rule is a variable quantity. That means N atoms in such phases occupy interstitial sites of the closed-packed metal host lattices. Within first-principle calculations, researchers usually consider a wide range for the variable "x" in order to study the physical properties of such materials and to be able to interpret the experimental observations [36, 157].

In dealing with such compounds, one has no specific rules to determine their stoichiometry. Nevertheless, some crystalline stoichiometric TMNs were experimentally reported (e.g. Cu_3N [32]), some others have been theoretically proposed and studied (e.g. AuN [65], AuN_2 [64], and Au_3N [63]), while the true stoichiometry and crystal structure of some others are still a matter of debate (cf. Ref. [1] and references therein).

In the present study, we consider the nitrides of group 10 (Ni, Pd and Pt), group 11 (Cu, Ag and Au) and of Zn (which belongs to group 12) of the periodic table. We assign three chemical formulas to each nitride: M_3N, MN and MN_2. These selected molecular formulas for a given TMN are chosen according to the following simple loose systematic procedure: First, we choose the already reported (either from experiment or calculations) stoichiometries. Second, we assign every chosen studied stoichiometry to the nitrides of all the other considered metals. When discussing the crystal structures in the following section, we will give some information about which formula was experimentally reported, theoretically proposed by other researchers, which is hypothetical, and which is still controversial.

5.2 Crystal Structure Descriptions

The electronic structure of the outer shells of atoms is a crucial controlling factor in deciding which crystal structure to be assumed [58]. In the present study, the proposed crystal structures for a given metal nitride and for a given molecular formula are chosen according to the following

procedure: First, we choose the already reported (either experimentally reported or theoretically investigated) structures. Second: we assign every chosen reported structure to the nitrides of all the other considered metals. By following these two steps, we will be able to study trends, if any, since our compounds under study share the same geometrical structure(s) within any considered molecular formula. Last: we consider some *prototype* compounds that have our chosen stoichiometries and assign their structures to our materials. We do this even if these structures have not been reported (see Subsec. 1.1.1).

Table 5.1 below shows the outputs of our application of the two procedures proposed in Sec. 5.1 and Sec. 5.2 on the nitrides of group 10, 11 and 12 elements of the periodic table. Information about each chosen crystal structure are summarized in Table 5.1, unit cells are depicted in Figs. 5.1, 5.2 and 5.3 and more data are given about some structures follows. Presented information include:

- Strukturbericht designation (symbols): The Strukturbericht Designation is a very simple partly systematic useful system of nomenclature for describing relatively simple structures [185]. We try to stick to these Strukturbericht structure symbols in this chapter and through out the study. However, some of the considered structures (ϵ-Fe_3N, RhF_3, NiTi, $CoSb_2$) do not have Strukturbericht symbols.
- The underlying Bravais lattice (BL). For definition, see App. A.
- The prototype compound(s): These are well known compounds with the same structure under consideration. However, some TMNs that have one of the considered structures will be pointed out.
- The space group and its sequential number as given in the International Tables for Crystallography [173]. For more information, see App. A.
- The number of M_mN_n chemical formulas per unit cell (Z).
- Sources where one can obtain the presented data and more are cited. However, Information about crystal structures can be found at various useful on-line sites. One example is the

Table 5.1: The studied structural phases of MN_n (n = 0, 1/3, 1, 2). Presented are the Strukturbericht designation (symbol), the underlying Bravais lattice (BL), a prototype compound, the space group and its sequential number as given in International Tables for Crystallography, number of M_mN_n formulas per unit cell Z, and references where one can obtain the presented information and more.

Symbol	BL	Prototype(s)	Space group	Z	References
			M Structures		
A1	fcc	Cu	$Fm\bar{3}m$ (#225)	1	[158] [159, p. 12-19]
A3	hexagonal	Mg	$P6_3mmc$ (#194)	1	[158]
			M_3N Structures		
$D0_3$	fcc	$AlFe_3$	$Fm\bar{3}m$ (#225)	1	[158, 160] [161, p. 323] [21, p. 254]
A15	sc	Cr_3Si	$Pm\bar{3}n$ (#223)	2	[158, 162] and [163, pp. 217-220]
$D0_9$	sc	anti-ReO_3 (α), Cu_3N	$Pm\bar{3}m$ (#221)	1	[155, 164, 165] [21, p. 208 and p. 265]
$L1_2$	sc	Cu_3Au	$Pm\bar{3}m$ (#221)	1	[158, 166, 167] [21, pp. 1297–1298]
$D0_2$	bcc	$CoAs_3$ (skutterudite)	$Im\bar{3}$ (#204)	4	[155, 158, 168] [21, pp.267–268]
ϵ-Fe_3N	hexagonal	ϵ-Fe_3N, Ni_3N	$P6_322$ (#182)	2	[169, 170]
RhF_3	trigonal (rhombohedric)	RhF_3	$R\bar{3}c$ (#167)	2	[171] [21, p. 417]
			MN Structures		
B1	fcc	NaCl	$Fm\bar{3}m$ (#225)	1	[158, 172] [173, p. 734] [21, p. 238]
B2	sc	CsCl	$Pm\bar{3}m$ (#221)	1	[158, 172] [173, p. 873] [21, p. 245]
B3	fcc	ZnS (zincblende)	$F\bar{4}3m$ (#216)	1	[158, 172] and [174, pp. 112-114]
$B8_1$	hexagonal	NiAs	$P6_3/mmc$ (#194)	2	[158, 175] and [174, pp. 124-132]
B_k	hexagonal	BN	$P6_3/mmc$ (#194)	2	[158, 176] [21, pp. 1060–1061]
B_h	hexagonal	WC	$P\bar{6}m2$ (#187)	1	[158, 175]
B4	hexagonal	ZnS (wurtzite)	$P6_3mc$ (#186)	2	[158, 177] and [174, pp. 118-124]
B17	s tetragonal	PtS (cooperite)	$P4_2/mmc$ (#131)	2	[158, 178, 179] [21, p. 755]
B24	fc orthorhombic	TlF	$Fmmm$ (#69)	1	[158, 180]
			MN_2 Structures		
C1	fcc	CaF_2 (fluorite)	$Fm\bar{3}m$ (#225)	1	[158, 168], [21, p. 252]
C2	sc	FeS_2 (pyrite)	$Pa\bar{3}$ (#205)	4	[168, 181, 182] [21, p. 759 and p.242]
C18	s orthorhombic	FeS_2 (marcasite)	$Pnnm$ (#58)	2	[158, 168, 182, 183] [21, p. 759 and p.250]
$CoSb_2$	s monoclinc	$CoSb_2$	$P2_1/c$ (#14)	4	[168, 182, 184]

on-line Crystal Lattice Structures database of the Center for Computational Materials Science (CCMS) [http://cst-www.nrl.navy.mil/lattice/] which offers a concise index of common crystal lattice structures. In this web page, structures are indexed by Strukturbericht Designation, Pearson symbol, space group, and prototype. The CCMS on-line information about each prototype includes : Pearson symbol, Strukturbericht designation, space group, references, other compounds with the same structure, primitive vectors, and basis vectors; as well as graphical representations and more useful information about the crystals.

- Relations between some structures and some more useful informations will be given wherever appropriate.

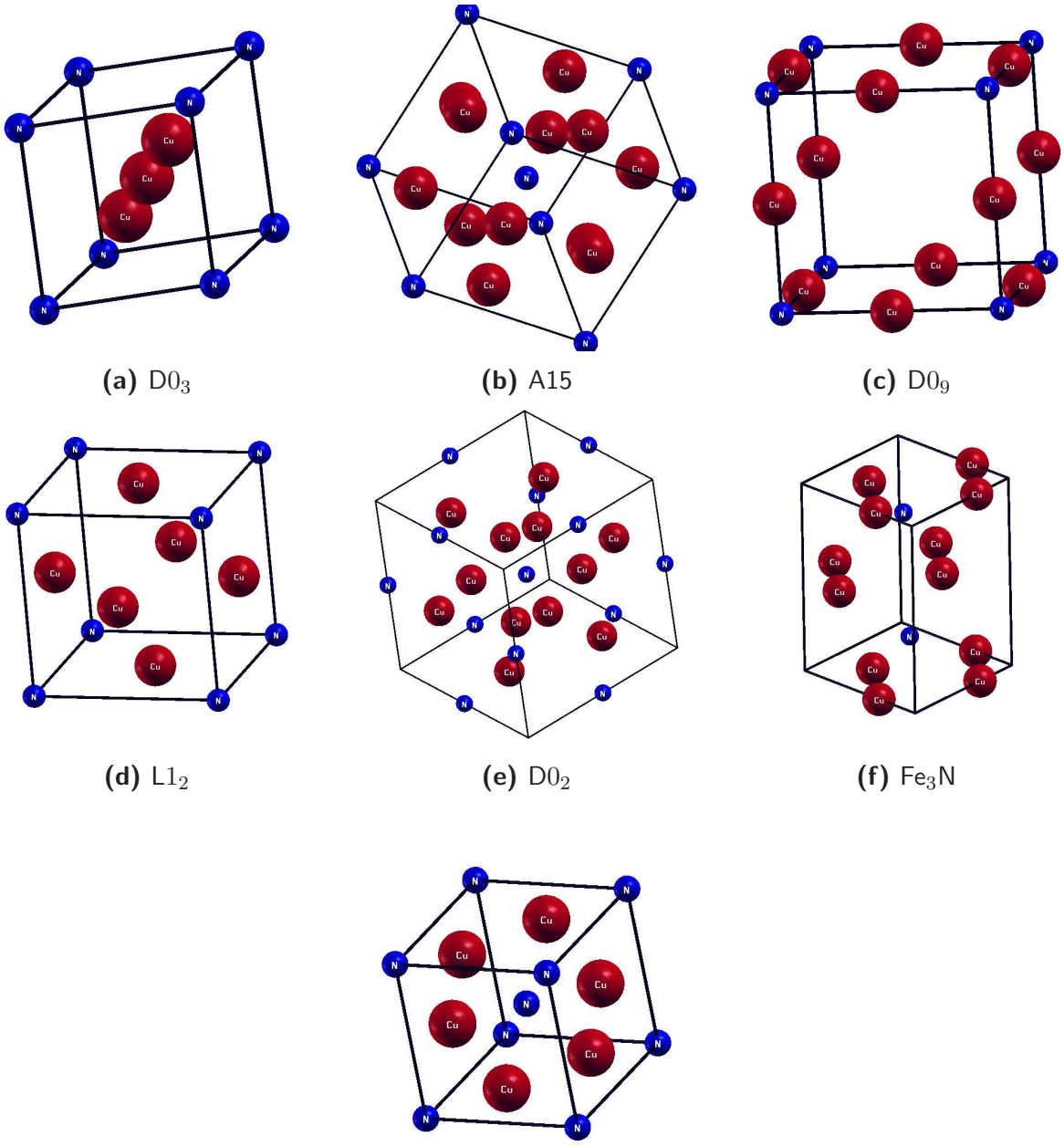

(a) $D0_3$ **(b)** A15 **(c)** $D0_9$

(d) $L1_2$ **(e)** $D0_2$ **(f)** Fe_3N

(g) RhF_3

Figure 5.1: (Color online.) M_3N structures considered in this work. The large (red) and the small (blue) spheres represent metallic and nitrogen atoms, respectively. All figures were created using the XCrySDen software. Dimenssions of different unit cells are not in the same scale. For numerical data, i.e. primitive and basis vectors, see App. F.

5.2.1 M_3N structures

1. **$D0_3$:** The $D0_3$ structure of $AlFe_3$ is sometimes referred to as BiF_3 structure. However, A. F. Wells claims that this might not be true [21, p. 255 and p. 422]. $D0_3$ structure was proposed and tested for the synthesized Au_3N [63].

2. **A15:** This structure is sometimes refered to as GeV_3 structure (cf. Refs. [63] and [21, p. 1283]). It was proposed and tested for the synthesized Au_3N [63].

3. **$D0_9$:** Two substances are said to be anti-isomorphous when their crystal structures are geometrically identical but with the position of the corresponding atoms or ions interchanged [186, p. 194]. Hence the prefix *anti* in anti-ReO_3. This $D0_9$ structure is the most symmetrical [21, p. 208] and the simplest structure for MX_3 compounds [155] including Cu_3N [32]. While the N atoms occupy the corners of the cell, the M atoms occupy the middle of the cubic edges, leading to many vacant interstitial sites. The electrical and optical properties of a TMN in this structure can be modified by hosting additional (or other) M atoms within these sites [187].

4. **$L1_2$:** Both $D0_9$ and $L1_2$ structures belong to the same space group, and N atoms occupy 1a Wyckoff sites. M atoms on the other hand are in the 3d sites for $D0_9$ but occupy the 3c sites in the case of $L1_2$. Cu_3N is found to prefer the latter structure over the former at high pressure [188].

5. **$D0_2$:** This structure was proposed and tested for the synthesized Au_3N [63]. However, we set $Z = 4$, while $Z = 8$ in Ref. [63].

6. **ϵ-Fe_3N:** This structure is based on an hcp sub-lattice of M atoms, while N atoms occupy the octahedral sites. ϵ-Fe_3N structure is quite common for binary nitrides of 3d metals; particularly, it was experimentally confirmed for Ni_3N [170].

7. **RhF_3:** For the relation between $D0_9$, $D0_2$ and RhF_3 structures, see Ref. [21, p. 265 and pp. 267–268] and Ref. [155]. This structure was proposed and tested for the synthesized Au_3N [63].

5.2.2 MN structures

1. **B1:** In this structure N atoms occupy all the four octahedral sites of the FCC metal sub-lattice [64]. It is the most popular structure for many early TMNs, e.g. ScN, TiN, VN, CrN, FeN, ZrN and HfN [64,189,190], and it has been theoretically proposed for most late TMNs. In particular, it was experimentally claimed for PdN [10] and NiN [191].

2. **B2:** This structure was theoretically tested for NiN [192], PdN [193], PtN [194], CuN, AgN and AuN [65]. Of all the listed MN structures here, the most dominated among the AB binary compounds are B1, B2 and B3 [180].

3. **B3:** In this structure all of the NM_4 tetrahedra are corner-sharing [30]. In B1, B2 and B3 structures, N atoms fill in the same fcc sub-lattice formed by the metal atoms. However, the volume of the octahedral interstitial cites, at which the N atoms in B1 are located, is larger than that of the tetrahedral interstitial ones occupied by the N atoms in B3 [192]. FeN [195] and CoN [196] were experimentally synthesized in this structure.

4. **B8$_1$:** Electronic and magnetic properties of CuN and NiN in this structure have been studied [192].

5. **B$_k$:** See Table 5.1.

6. **B$_h$:** See Table 5.1.

7. **B4:** AlN and GaN are known to crystallize in this structure [22].

8. **B17:** Non-metal atoms in this structure are tetrahedrally coordinated, while the Pt atoms have square-planar coordination environments [30]. B17 structure has a distorted fcc M sub-lattice [22]. The structure is adopted by PtS and PtO and was theoretically proposed to be the ground-state structure of PtN [30].

9. **B24:** This is the least symmetric considered structure. In an apparently similar trial to test such low symmetry structure possibility, Patil et al. [178] investigated the mechanical stability of PtN in a face-centered orthorhombic structure (space group Fddd), but it is not the same as our studied face-centered orthorhombic B24 structure (space group Fmmm).

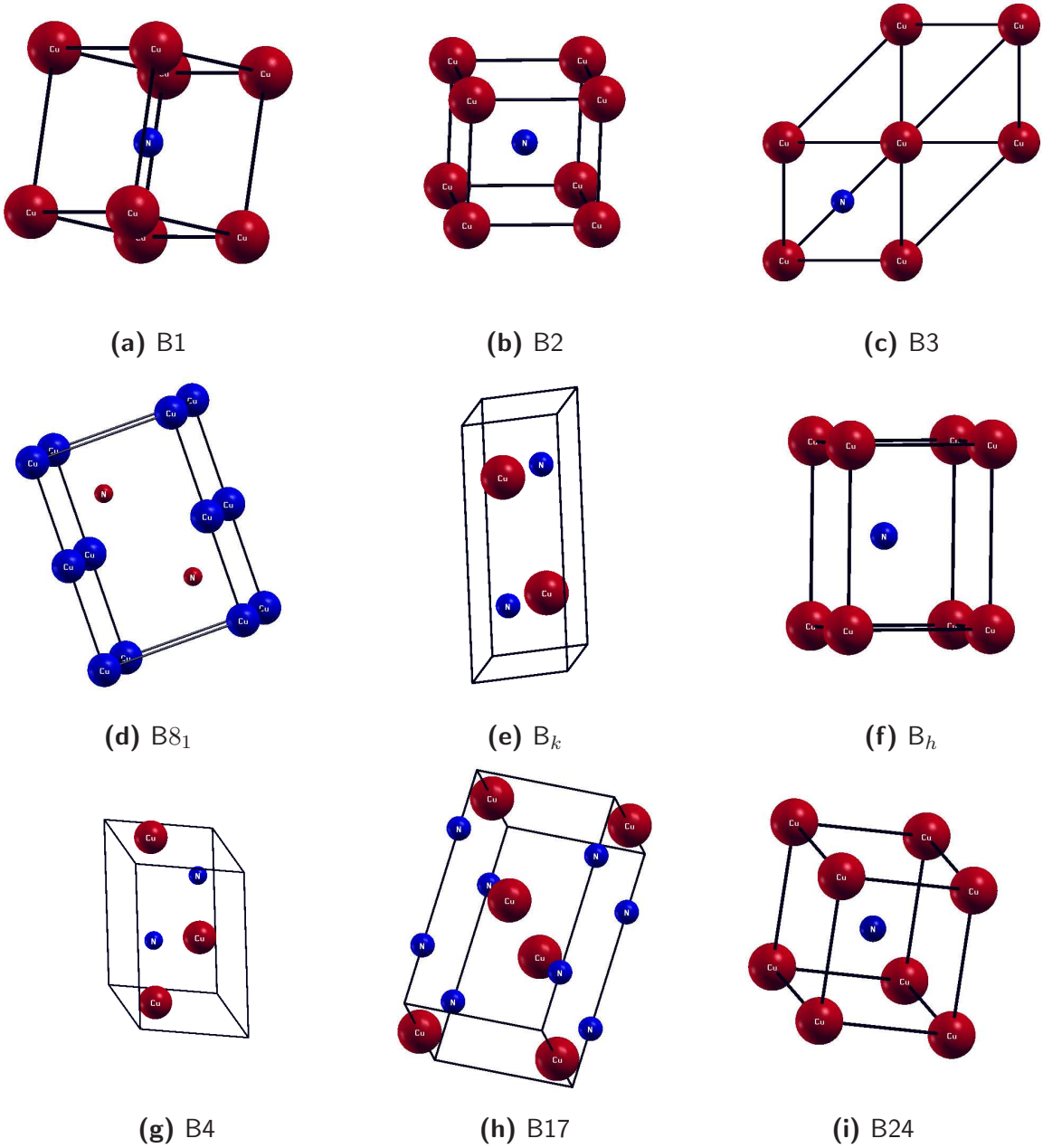

(a) B1 **(b)** B2 **(c)** B3

(d) $B8_1$ **(e)** B_k **(f)** B_h

(g) B4 **(h)** B17 **(i)** B24

Figure 5.2: (Color online.) MN structures considered in this work. The large (red) and the small (blue) spheres represent metallic and nitrogen atoms, respectively. All figures were created using the XCrySDen software. Dimenssions of different unit cells are not in the same scale. For numerical data, i.e. primitive and basis vectors, see App. F.

5.2.3 MN_2 structures

1. **C1:** In the C1 structure, N atoms occupy all the tetrahedral interstitial sites of the fcc metal sub-lattice, giving rise to a stoichiometry of MN_2 [25]. One can start by a B3 structure, in which the N atoms occupy half of the tetrahedral interstitial sites of the M sub-lattice, then fill the remaining tetrahedral sites with another four N atoms to obtain the C1 structure (cf. Fig. 1 in Ref. [197]). For the relation between $D0_3$ and C1 structures, see Ref. [21, p. 254].

2. **C2:** This structure can be described as a B1 structure, in which N atoms are replaced with N_2 units (i.e. nitrogen pairs) [25,30]. It has 12 atoms per primitive unit cell with M atoms occupying the 4a Wyckoff positions and N atoms occupying the 8b positions. Moreover, the structure has one free parameter (u) that determines the bond length between the N_2 units. The C1 structure is a special high-symmetry phase of C2 with $u = 0.25$ [25]. Chen, Tse and Jiang [66] claim that there is a consensus on the crystal structure of PtN_2 and PdN_2 to be this C2 structure.

3. **C18:** Chen, Tse and Jiang [66] also claim that there is a consensus on the crystal structure of OsN_2 to be the C18 structure.

4. **$CoSb_2$:** This structure is related to the FeAsS-arsenopyrite structure and is very close to the C43 structure of ZrO_2. The C2, C18 and $CoSb_2$ structures can be looked at as composed of PdN_6 octahedra. In C2, the octahedra are corner shared, while in C18 and $CoSb_2$ the octahedra are both edge and corner shared [66]. From first-principles calculations and comparison with experimental data, $CoSb_2$ structure was assigned to IrN_2 [198]. Chen, Tse and Jiang [66] went further and claimed that there is a consensus on the crystal structure of IrN_2 to be this $CoSb_2$ structure.

5.3 Re-Posing the Problem

As a starting point of the present investigation, we assigned in the previous two sections certain crystal structures to the bulk nitrides under investigation. The procedures we have followed in proposing the chemical formulas and crystal structures, though loose, allow us to

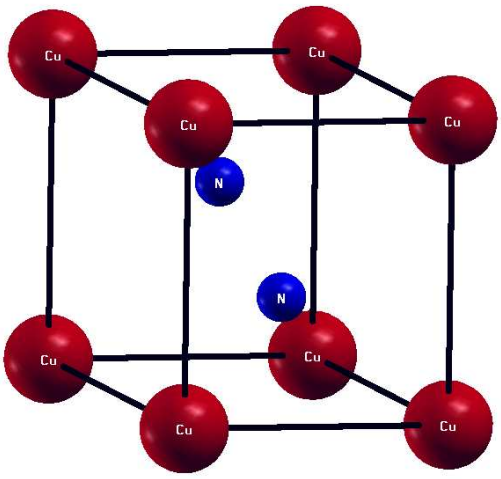

(a) C1

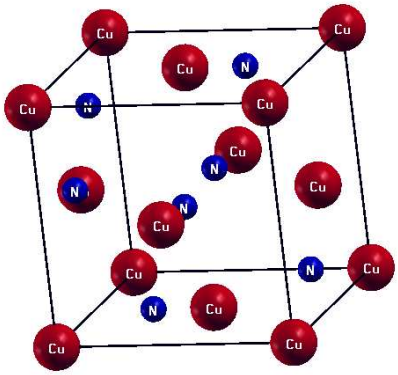

(b) C2

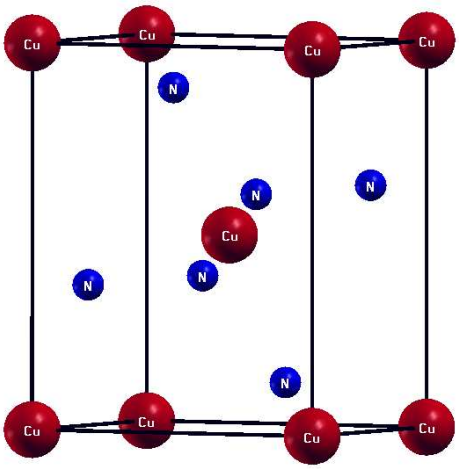

(c) C18

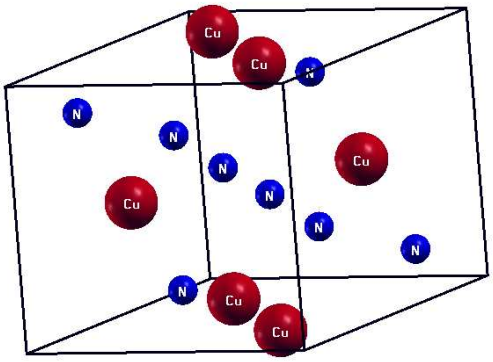

(d) $CoSb_2$

Figure 5.3: (Color online.) MN_2 structures considered in this work. The large (red) and the small (blue) spheres represent metallic and nitrogen atoms, respectively. All figures were created using the XCrySDen software. Dimenssions of different unit cells are not in the same scale. For numerical data, i.e. primitive and basis vectors, see App. F.

- compare our results with experiment and with previous theoretical studies; and to
- use our results to investigate regularities and trends (if any) among these nitrides. This, in turn, helps in identifying and in searching for the most appropriate TMN(s) for use in a given application (e.g. replacing gold in electronic devices), or that TMN in which certain physical properties (e.g. bulk modulus) can be enhanced.

Therefore, the next natural step is to search, within a given stoichiometry, for the most stable TMNs which might be the most likely candidates for the true crystal structure [1]. This can be done by studying their energy-volume equation of state (EOS). Equilibrium cohesive energy and formation energy are common crucial measures of relative stabilities. Lattice parameters at equilibrium control the physical properties of materials and should be identified. Equilibrium bulk modulus and its pressure derivative are very important properties for many applications. Upon application of external pressure, structural phase transition may take place. This can be examined by means of the enthalpy-pressure EOS. Band structure and total and partial density of states (DOS) of the energetically most stable phases contain most information about the electronic properties of these TMNs. Optical characterization can be achieved by finding a way to derive the frequency-dependent optical constants (e.g. absorption coefficient, reflectivity and refractive index) of these phases.

Within the theoretical methods introduced in Part I, the rest of the present Part is devoted to definitions and technical details of methods of calculations of these desired properties.

[1] However, even if one examines a wide range of structures, this, of course, does not mean that we have determined the global minimum. However, it is worth eliminating those structures which are not energetically favorable. This is usually the issue of structure optimization problem (cf. Refs. [63, p.4] and [78, sec. 2.2]).

6. Electronic Relaxation Details

In Subec. 3.6.2 we established the fact that the Kohn-Sham approach to DFT leads to $N_{\mathbf{k}}$ (number of $\mathbf{k}$ points) equations of the form 3.6.2 that should be solved self-consistently. The present chapter is devoted to the practical settings and technical details of our KS-DFT calculations. At this point, it must be mentioned that all calculations at the electronic structure level (i.e. DFT and GWA) in this study were carried out using the all-electron plane-wave *Vienna ab initio Simulation Package* (VASP) [87, 128, 144, 154, 199–201].

6.1 Convergence Issues

A numerical calculation is considered to be *well-converged* when the true solution of the (DFT) mathematical problem is accurately approximated by the numerically derived solution [127] [1]. As already pointed out in Subsections 3.6.2 and 3.6.1, convergence of the calculated total energy with respect to the plane waves energy cut-off E_{cut} and with respect to the number of $\mathbf{k}$ points is essential to be achieved *before* doing any real DFT (or GWA) calculations.

6.1.1 Plane-wave cut-off convergence

For the VASP expansion of the pseudo part of the KS one-electron spin orbitals $\varphi^{\sigma}_{i,\mathbf{k}}(\mathbf{r})$, we included only those PWs with kinetic energy $\frac{\hbar^2}{2m_e}|\mathbf{k}+\mathbf{G}| < E_{\text{cut}}$ such that the change in E_{cut} causes a change in the total electronic energy E and in the Fermi energy (or the chemical potential) E_F that is always less than $0.003\ eV$/atom and $0.002\ eV$, respectively. This can always be achieved using $E_{\text{cut}} = 600\ eV$ for all systems under investigation. A set of samples of convergence tests of E and E_F with respect to E_{cut} are depicted in Figs. 6.1. In contrast to what we have mentioned in Subsec. 3.6.1, Fig. 6.1a shows clearly that E does not decrease monotonically with increasing E_{cut}, which is an apparent violation of the variational principle. However, this is because VASP takes into account the approximate error according to the RRKJ [202] kinetic energy criterion when cohesive energies are calculated. For details on this issue, interested readers are referred to Refs. [154], [202], [75, pp. 153–154].

[1] It may be worth to recall here that the accuracy of DFT in describing physical reality is quite separate from the concept of numerical convergence. cf. Ref. [127, pp. 49-50 and Ch. 10].

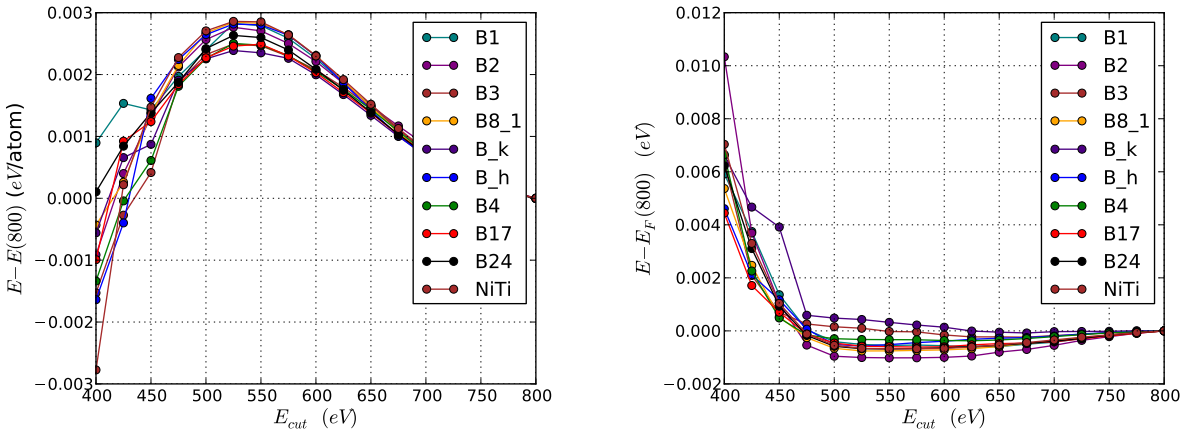

(a) **(b)**

Figure 6.1: (Color online.) (a) Total energy E per atom, and (b) Fermi energy E_F, for CuN in different structures (see Table 5.1), each versus the energy cut-off E_{cut}, using $15 \times 15 \times 15$ $\mathbf{\Gamma}$-centered Monkhorst-Pack $\mathbf{k}$ mesh, $\mathrm{t}_e = 0.2\ eV$ and the Methfessel-Paxton 2nd order smearing method. For a given structure, each value is given relative to that evaluated at the highest trial $E_{\text{cut}} = 800\ eV$. (For notations, see Subsec. 3.6.2).

6.1.2 $\mathbf{k}$-points convergence

All our BZs were sampled using $\mathbf{\Gamma}$-centered Monkhorst-Pack meshes (see Sec. 3.6.2). To determine the size of the mesh, convergence tests of the total energy E with respect to the size of the mesh (i.e. with respect to the number of $\mathbf{k}$ points) were always carried out prior to any calculations. All tests were carried out at plane waves cut-off energy $E_{\text{cut}} = 600\ eV$ using the smearing method of Methfessel-Paxton of the 2nd order, with the smearing width set to $\mathrm{t}_e = 0.2\ eV$. A set of samples of such test are depicted in Fig. 6.2a. In all cases, total energy E is considered to be well converged with respect to the number of $\mathbf{k}$ points (i.e. independent of the number of $\mathbf{k}$ points) when any increase in the density of the mesh produces a change in the total energy less than $0.002\ eV/\text{atom}$. Also, Fig. 6.2b below shows that the Fermi surface E_F (or the chemical potential μ) has been carefully treated such that any increase in the density of the mesh produces a change in E_F less than $0.02\ eV$. Moreover, the smearing width t_e was chosen such that the fictitious entropy - introduced by the smearing occupation scheme (see Sec. 3.6.2) - has always been kept below $0.001\ eV/\text{atom}$.

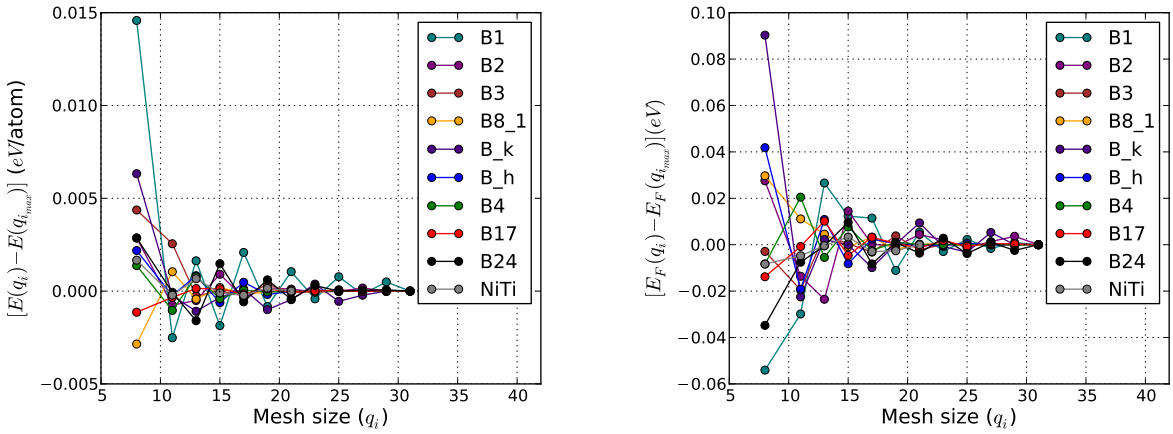

(a) **(b)**

Figure 6.2: (Color online.) (a) Total energy E per atom, and (b) Fermi energy E_F, for CuN in different structures (see Table 5.1), each versus the size of the $\mathbf{\Gamma}$-centered Monkhorst-Pack $\mathbf{k}$ mesh q_i, using $E_{\text{cut}} = 600\ eV$, $\mathrm{t}_e = 0.2\ eV$ and the Methfessel-Paxton 2nd order smearing method. For a given structure, each value is given relative to that evaluated at the highest trial mesh size $q_{i_{max}}$. (For notations, see Subsec. 3.6.2).

After all, different mesh densities and occupation schemes were employed according to the following different cases:

- *Geometry relaxation*: A $13\times13\times13$ mesh and the smearing method of Methfessel-Paxton (MP) were always used (See also Sec. 7.3 and Sec. 7.4).

- *Static calculations*: After each ionic relaxation, a static calculations step with a $17\times17\times17$ mesh and the tetrahedron interpolation method with Blöchl corrections are employed (see also Sec. 7.4).

- *DOS calculations*: At least a $21 \times 21 \times 21$ mesh with partial occupancies $f^{\sigma}_{i,\mathbf{k}}$ set using the tetrahedron method with Blöchl corrections were used (see also Sec. 8.2).

- *Band structure calculations*: Non-self-consistent calculations are always performed on top of the above mentioned self-consistent DOS calculations. The coordinates of the high-symmetry $\mathbf{k}$-points with respect to the reciprocal lattice basis vectors (and their labeled according to Ref. [203]) are supplied explicitly (see also Sec. 8.1).

- *GWA calculations*: These are computationally demanding (see Chs. 4 and 9). Therefore, in consideration of computational cost, that is, depending on the available computational

resources and time, we used $12 \times 12 \times 12$ or $10 \times 10 \times 10$ mesh of $\mathbf{k}$-points (see Ch. 10 and the appended articles).

6.2 XC Functional and PAW Potentials

For all calculations that are related to the structural and electronic properties, the The PBE-GGA functional (see Sec. 3.6.3) was employed for the XC potentials $\tilde{v}_{\text{xc}}[n^{\uparrow}(\mathbf{r}), n^{\downarrow}(\mathbf{r})]$. The VASP implemented PAW method (see Sec. 3.6.4) was used to describe the core-valence interactions $v_{\text{ext}}(\mathbf{r})$. Which electrons are treated as core electrons and which are treated as valance ones for each element in consideration is mentioned explicitly in Ch. 10 and in the appended articles [1–3, 6, 7].

Concerning relativistic effects (see the very last part of Subsec. 3.6.4), VASP, in its standard mode, performs full relativistic calculations for the core electrons and treats the valence electrons in an approximate scalar relativistic fashion [128]. Due to the large number of phases we should deal with, and due to the computationally demanding nature of its calculations, no effort to consider spin-orbit interaction of the valence electrons were made. Nonetheless, other researchers have tested the spin-orbit contributions to the macro-physical properties of some of our target materials, and found it to be negligible. See our article [1], Ref. [204] and [P. Philipsen and E. Baerends, Phys. Rev. B, 61: 1773 (2000)] cited therein.

6.3 Numerical Optimization Schemes

In this section we mention the algorithms implemented in VASP to calculate the electronic ground state and briefly discuss the corresponding self-consistency cycle. The discussion here follows [154]. For detailed analysis, readers are referred to [87].

Generally, two nested loops present: the outer one for charge density optimization, and the inner one for wave functions optimization. Accordingly, we have two sets of algorithms: The matrix-diagonalization iterative schemes including the conjugate gradient (CG) scheme [205, 206], block Davidson scheme [207] and a residual minimization scheme - direct inversion in the iterative

subspace (RMM-DIIS) [208, 209]. The other set of algorithms is for the charge density mixing. This includes an efficient Broyden/Pulay mixing scheme [209, 210] .

At the beginning, the wave functions and the charge density are completely independent quantities. Later, the charge density is used to set up the Hamiltonian within each self-consistency loop; then the wave functions are updated iteratively such that they get closer and closer to the exact wave functions of *this* Hamiltonian. The optimized wave functions are now used to calculate the *new* charge density. Then the new and the old densities are *mixed* to create a new input density, ...

The combination of the above mentioned traditional self-consistency cycle with these efficient numerical algorithms leads to fast, efficient and robust scheme for solving the KS system. The implemented blocked Davidson and RMM-DISS are among the fastest currently available methods.

For a given ionic configuration, we chose the implemented blocked Davidson iteration scheme [207] for the relaxation of the electronic degrees of freedom. Convergence was considered to be arrived at when the difference in the total (or free) energy and in the eigenvalues between two successive self-consistent (SC) loops are both less than $1 \times 10^{-4}\ eV$.

7. Calculations of Structural Properties

It is well known now that structural properties, crystal stabilities and pressure-induced phase transformations in bulk solids can be accurately described employing first-principles calculations [211]. In the present chapter, we demonstrate, how we utilized the theoretical methods introduced in Part I to study these properties.

7.1 Cohesive Energy

Cohesive energy E_{coh} of a solid is the energy required to decompose the soild into its atomic constituent with all atoms neutral and infinitely separated [89, 212–215]. Thus, in *ab initio* calculations practice, it corresponds to the difference between the calculated total crystal energy per unit cell and the total energy of the isolated atoms [36, 135, 215, 216]

$$E_{\text{coh}} = E(\text{crystal}) - E(\text{atoms}) = E(\text{crystal}) - \sum_{\text{atom}} E_{\text{atom}}^{\text{isolated}} \,. \tag{7.1.1}$$

That is, the cohesive energy *per atom* for our target nitrides M_mN_n can be expressed as[1]

$$E_{\text{coh}}^{\text{M}_m\text{N}_n} = \frac{E_{\text{solid}}^{\text{M}_m\text{N}_n} - Z \times \left(mE_{\text{atom}}^{\text{M}} + nE_{\text{atom}}^{\text{N}}\right)}{Z \times (m+n)} \,. \tag{7.1.2}$$

Here, Z is the number of M_mN_n per unit cell, as defined in Sec. 5.2, $E_{\text{atom}}^{\text{M}}$ and $E_{\text{atom}}^{\text{N}}$ are the atomic energies, and $m, n = 1, 2$ or 3 are the stoichiometric weights.

It should be clear that, for Eq. 7.1.2 above to have a physical meaning, both crystal energy and atomic energies must be calculated at the same level of accuracy [36,217]. However, total energies in VASP are calculated with respect to non spin-polarized spherical atomic references [154]. Moreover, VASP, as a solid-state code, performs calculations periodic systems only. Therefore, we placed each atom in in an orthorhombic cell with 13 Å $\times$ 14 Å $\times$ 15 Å dimensions and carried out SDFT calculations. Electronic configurations of these isolated spin-polarized pseudo-atom were set to be the same as they enter the RHS of Eq. 7.1.2 above. By imposing large dimensions

[1] Eq. 7.1.2 results in a negative E_{coh}. However, another convention with positive E_{coh} is also common, where energy signs in Eq. 7.1.2 change.

to the unit cell, one is certain that there is no significant interaction between the atom in the cell and its neighbor replicants. Moreover, by imposing the symmetry of the orthorhombic cell, the physically incorrect spherical states are avoided[2] (cf. Ref. [204] and Ref. 28 therein.). We used Γ point and Gaussian smearing method with a small width of $0.002\ eV$. We then manually subtracted the obtained atomic energies from the cohesive energies $E_{\text{solid}}^{\text{Cu}_m\text{N}_n}$ calculated by VASP.

7.2 Bulk Modulus B and its Pressure Derivative B'

Given the DFT calculated total energy E (or, equivalently cohesive energy E_{coh}), the external pressure on the unit cell can be calculated from [89, 219]

$$P = -\frac{\partial E}{\partial V}\ . \tag{7.2.1}$$

When the pressure vanishes ($P = 0$), we say the bulk system is at *equilibrium*, and all quantities at that state are denoted by subscript "0". The equilibrium isotropic elastic properties of a bulk system are described by its compressibility K_0 [89, 219]

$$\frac{1}{K_0} = B_0 = -V\frac{\partial P}{\partial V}\bigg|_{V=V_0} = -V\frac{\partial^2 E}{\partial V^2}\bigg|_{V=V_0}\ , \tag{7.2.2}$$

where B_0, the ratio between the small decrease in pressure P to the resulting fractional increase in volume V, is the equilibrium bulk modulus (or incompressibility) [82, 89, 220]. Its pressure derivative is given by [219]

$$B_0' = \frac{\partial B}{\partial P}\bigg|_{P=0} = \frac{\partial B}{\partial V}\frac{\partial V}{\partial P}\bigg|_{V=V_0} = \frac{1}{B_0}\left(-V\frac{\partial B}{\partial V}\right)\bigg|_{V=V_0} = \frac{1}{B_0}\left(V\frac{\partial}{\partial V}(V\frac{\partial^2 E}{\partial V^2})\right)\bigg|_{V=V_0} \tag{7.2.3}$$

It is clear that B_0' measures the dependence of the equilibrium bulk modulus B_0 on pressure [219]. From experimental point of view, B_0' is a measurable quantity[3], is related to some important

[2] It is also well known that GGA may slightly lower the ground-state energy when a non-spherical ground-state density is allowed for (cf. Ref. [218] and Ref. 46 therein).

[3] Theoretically, B_0' can be obtained from first-principles calculations, as in the present work, or through the *so-called* method of model potentials. In either approaches, and from eq. 7.2.2, eq. 7.2.1 and eq. 7.2.3, the main required quantity is the total energy E [219]. For summary of the experimental and semi-empirical methods of determining B_0', interested readers are referred to the work by Raju, Mohandas and Raghunathan [219]. In that

thermo-physical properties, and it is of great physical significance in high pressure physics [219, and Ref. (1) therein]. Therefore, the measurable B_0 and B_0' can be used to directly test our total-energy *ab initio* calculations against experiment.

7.3 Forces on Ions and Cell

The general theory of force has been established in Sec. 2.3. For expressions of force within the PAW formalism, we have already referred interested readers to Refs. [143–145]. Here, we emphasize that the assumption that total energy of a system E depends on a single geometrical parameter λ may be valid only in the case of cubic crystals and only when the constituent atomic basis has no internal degrees of freedom. In the general case, however, one should -in principle- consider the $E(\lambda_1, \lambda_2, ..., \lambda_n)$ hyper-surface over all possible deformations of the lattice that are described by $\lambda_1, \lambda_2, ..., \lambda_n$ [213]. A general expression for the force F_λ is thus given by the Hellman-Feymann force theorm (Eq. 2.3.7).

Given a certain crystal structure, the dependence of its total electronic energy E on a geometrical parameter λ with linear dimension (such as lattice parameter, distance between nearest neighbors, cube root of the molar volume, etc.), we define the equilibrium structural parameter λ_{min} as the value of λ which satisfies $E(\lambda_{min}) = E_{min}$. That is, the first derivative satisfies $(\partial E/\partial\lambda)|_{\lambda_m} = 0$, while the second derivative is related to the bulk modulus B by

$$B = -V\frac{\partial P}{\partial V} = V\frac{\partial^2 E}{\partial V^2} = V\frac{\partial^2 E}{\partial \lambda^2}\frac{\partial^2 \lambda}{\partial V^2}, \tag{7.3.1}$$

where V is the volume of the cell, P the hydrostatic pressure and the derivatives are to be evaluated at λ_{min} [213].

As in the most available soild-state codes, in using VASP one needs only to input the chemical symbols of the constituent atomic elements, lattice vectors and basis vectors (See App. A and Sec. 5.2). Then, in general, the total energy E should be minimized with respect to the

work, they pointed out that these different methods agree poorly among themselves! On the other hand, B_0 can be measured with great accuracy at $T \neq 0$ and extrapolated to $T = 0$ [78].

volume (*volume relaxation*), with respect to the shape of the unit cell (*cell external relaxation*), and with respect to the position of the atoms within the cell (*cell internal relaxation*) [8,128,154].

In our calculations, we did not relax the shape of the unit cell (i. e. angles and lattice parameters *ratios* are kept fixed), and we relaxed the volume manually (see Sec. 7.4). However, employing the implemented conjugate-gradient (CG) algorithm (which is regarded as the most reliable backup routines in the present), we allowed every ion with free parameter(s) to search for local minima on the Born-Oppenheimer potential hyper-surface (see Sec.2.2) until all Hellmann-Feynman force components on every and each ion are smaller than $0.01\ eV/$Å.

If a position of an individual atom in a crystal is changed by a small amount, $\delta\mathbf{r}$, then the corresponding change in total energy is roughly $|\delta E| \approx |\mathbf{F}||\delta\mathbf{r}|$, with $\mathbf{F}$ being the force on that atom. If we set $\delta\mathbf{r} = 0.01$ Å, a relatively significant distance at the atomic scale, our *stopping criterion* $|\mathbf{F}| \leq 0.01\ eV/$Å will produce $|\delta E| \leq 0.0001\ eV$. Thus, this small amount of energy justifies our relaxation stopping condition (cf. [127]).

7.4 Equation of State (EOS) and Lattice Constants

It is clear from the last parts to the right in Eq. 7.2.2 and Eq. 7.2.3 that: (i) B_0 and B_0' are a second- and a third-order energy derivative with respect to the externally imposed volume, respectively. (ii) The only DFT calculated quantity is the total energy E (or, equivalently E_{coh}) at $T = 0$. Therefore, B_0 and B_0' are directly related to the energy versus volume curve $E(V)$, and both measures its curvature about the equilibrium volume, V_0. Since it is very straight forward to carry out electronic structure calculations at fixed V, the $E(V)$ equation of state (EOS) has become the most convenient for theoretical analysis [78].

To determine the equilibrium lattice parameters of each structure and to study its energy-volume $E(V)$ equation of state (EOS) we perform a two-step energy calculations at several different volumes: First, atoms with internal degrees were relaxed as in Sec.7.3 above. Second, a static calculation (i.e. with atomic positions fixed) with tetrahedron method with Blöchl corrections (see Subsec. 3.6.2). We then calculated E_{coh} and the obtained values as a function of volume

V *per atom* were least-squares-fitted [221] to the integration

$$E(V) = E(V_0) + \frac{9V_0B_0}{16}\left(\left[\left(\frac{V_0}{V}\right)^{\frac{2}{3}} - 1\right]^3 B_0' + \left[\left(\frac{V_0}{V}\right)^{\frac{2}{3}} - 1\right]^2 \left[6 - 4\left(\frac{V_0}{V}\right)^{\frac{2}{3}}\right]\right) \quad (7.4.1)$$

of the isothermal Birch-Murnaghan 3rd-order EOS [220, 222]

$$P(V) = \frac{3}{2}B_0\left(\left(\frac{V_0}{V}\right)^{7/3} - \left(\frac{V_0}{V}\right)^{5/3}\right)\left(1 + \frac{3}{4}\left(B_0' - 4\right)\left[\left(\frac{V_0}{V}\right)^{2/3} - 1\right]\right), \quad (7.4.2)$$

where V_0, E_0, B_0 and B_0' here are the fitting parameters. The *equilibrium* structural parameters and energetic and elastic properties are are readily then deduced by performing the calculations again at V_0.

7.5 Formation Energy

Since the driving force for the formation of a solid may lie in the energy liberated when the elements condense to form the solid [223], it has become a common practice in first-principles calculations to calculate the so-called heat or energy of formation[4] in order to test the possibility of formation of materials under consideration [224] as well as to measure the relative thermodynamic stabilities of different phases [36, 225].

We can formally define the formation heat E_f of a solid as the energy required to separate the solid compound into elements (not necessarily atoms) in their standard state [212]. Within *ab initio* calculations, formation energy E_f can be obtained from the difference between the cohesive energy (or enthalpy) of the products $E_{\text{coh}}(\text{products})$ and the cohesive energy (or enthalpy) of the reactants $E_{\text{coh}}(\text{reactants})$ [8, 215, 226]

$$E_f = \sum E_{\text{coh}}(\text{products}) - \sum E_{\text{coh}}(\text{reactants}); \quad (7.5.1)$$

where $E_{\text{coh}}(\text{reactants})$ should be given in the reference states of the reactants; that is, at their

[4] Note that, we use the term *energy of formation* not *enthalpy of formation* because the latter is *defined* only at $T = 273.15\ K = 0\ ^oC$ [215].

most stable state at specified temperature and pressure [226].

Assuming that the bulk solid M_mN_n results from the interaction between the gaseous N_2 and the solid M(*structure*) metal (where *structure* = **A3** for Zn and = **A1** for Ni, Pd, Pt, Cu, Ag and Au. See Table 5.1 and Refs. [161, 168, 227].) through the chemical reaction

$$m\mathrm{M}^{\mathrm{solid}} + \frac{n}{2}\mathrm{N}_2^{\mathrm{gas}} \quad \rightleftharpoons \quad \mathrm{M}_m\mathrm{N}_n^{\mathrm{solid}} \ , \tag{7.5.2}$$

Eq. 7.5.1 translates as

$$E_f(\mathrm{M}_m\mathrm{N}_n^{\mathrm{solid}}) = E_{\mathrm{coh}}(\mathrm{M}_m\mathrm{N}_n^{\mathrm{solid}}) - \frac{mE_{\mathrm{coh}}(\mathrm{M}^{\mathrm{solid}}) + \frac{n}{2}E_{\mathrm{coh}}(\mathrm{N}_2^{\mathrm{gas}})}{m+n} \ , \tag{7.5.3}$$

where $E_{\mathrm{coh}}(\mathrm{M}_m\mathrm{N}_n^{\mathrm{solid}})$ is the cohesive energy *per atom* as obtained from Eq. 7.1.2[5].

To determine the equilibrium cohesive energy of the elemental metals $E_{\mathrm{coh}}(\mathrm{Cu}^{\mathrm{solid}})$ each in its well-known standard crystal structure, we followed the same procedures described in Sec. 7.1 and Sec. 7.4. The obtained energy-volume EOS curves are displayed in Sec. 10.1. The obtained structural parameter(s) and cohesive energy of each metal M are given with the obtained results for the corresponding nitride, M_mN_n.

To calculate the cohesive energy of the gaseous diatomic molecular nitrogen ($E_{\mathrm{coh}}(\mathrm{N}_2^{\mathrm{gas}})$), we generally followed the method described in Sec. 7.1. However, we placed one N atom at a corner of a cubic cell of edge $a = 14$ Å, while we displaced the second atom along the diagonal direction, and, following the implemented conjugate gradient algorithm, the latter atom was allowed to move searching for the optimal point on this one-dimensional potential surface. In this calculation, we set $E_{\mathrm{cut}} = 800\ eV$ and employed Γ point and Gaussian smearing method with $\mathrm{t}_e = 0.002\ eV$. With comparison to experiment and to previous calculations, obtained equilibrium cohesive energy and equilibrium bond length are given in Table II of the appended article (Ref. [3]).

[5] If E_{coh} is used with a positive sign convention, i.e. negative of Eqs. 7.1.1 and 7.1.2, then signs in Eq. 7.5.3 must be reversed.

7.6 Pressure-Induced Structural Phase Transitions

At $T = 0\ K$, a (structural) phase transition between, say, phase 1 and phase 2 takes place when the enthalpies

$$H = E(V) + PV \tag{7.6.1}$$

of the two structures are equal, that is when [213]

$$E_1(V_1) + P_t V_1 = E_2(V_2) + P_t V_2. \tag{7.6.2}$$

This condition defines the *transition pressure* P_t, the pressure at which the transition occurs, as

$$P_t = -\frac{E_2 - E_1}{V_2 - V_1} = -\left[\frac{\mathrm{d}E_1}{\mathrm{d}V}\right]_{V=V_1} = -\left[\frac{\mathrm{d}E_2}{\mathrm{d}V}\right]_{V=V_2}, \tag{7.6.3}$$

where we made use of Eq. 7.2.1. Geometrically, Eq. (7.6.3) above defines a common tangent line that connects point V_1 on the $E(V)$ EOS of phase 1 to point V_2 on the $E(V)$ EOS of phase 2.

Thus, to determine the transition pressure P_t, one can either use Eq. (7.6.2), plot the $H(P)$ curves and the point where the two curves (of two modifications with the same chemical stoichiometry [228]) cross is P_t; or use Eq. (7.6.3), plot the $E(V)$ curves and the the slope of the common tangent line to the two curves defines P_t. The later approach is known in the literature as Gibbs construction [78].

Surely the direction of transition is from the higher H to the lower H, and only the phase with the lower H will survive above P_t, since systems under pressure always adjust themselves toward a lower point on the potential surface. The P_t itself is a point at which polymorphism occurs [213].

In the present investigation, we plotted the $H(P)$ curves for a *selected* set of nitrides, determine the P_t's, if any, and carefully analyzed the stabilities (see Sec. 7.7).

7.7 Phase Stabilities

In general, a phase is said to be *stable* if it is resistant to changes of condition. Such phase lives in a deep energy-well. A phase is said to be *metastable* if it cannot maintain its condition. Such phase lives in a shallow energy-well [215]. If a phase has a positive cohesive energy E_{coh} or a positive formation energy E_f, it is *unstable*.

The concepts and methods of calculations of the *cohesive energy* E_{coh} and *formation energy* E_f were established in Sec. 7.1 and Sec. 7.5, respectively. The significance of both quantities is that they can be used as useful measures of *relative* stabilities. That is, those structural phases with the lower E_{coh} are relatively more favorable than those with higher E_{coh}; and those structural phases with the lower E_f are thermodynamically more stable[6]. For non-zero pressure states, we employed enthalpy H as a measure of stability, since it a natural extension to E_{coh}. We have not considered *elastic stability*, but refer it whenever results are available in the literature.

[6] From its definition, E_f may give an evidence about the spontaneous decomposition of the bulk solid phase, yet E_f cannot be used as a sharp restriction of the synthesizability and alloying ability of the phase [215].

8. Calculations of Electronic Properties

The electronic energy band diagram is the fundamental quantity that characterizes the electronic structure of a solid and determines its ground state and a series of excitations involving electronic states [148]. In the present chapter, we first summarize several basic concepts from solid-state physics in order to establish the notation used to characterize the materials under investigation and to show how these quantities are calculated within the context of the theoretical methods introduced in Part I, especially DFT. Introduced and derived equations and the analysis lead to them will be applied in Part III to characterize the materials under investigation.

8.1 Band Structure

Within an independent-particle approximation to the many-electron problem of bulk crystalline solids, Bloch's theorem, we summarize the basic notions of *band structure* in App. B. In the present section, we will discuss related issues like Fermi surface, band gap, and how can one make use of the band diagrams to classify materials into metals, insulators and semiconductors.

The ground state of N independent electrons (e.g. Bloch and Kohn-Sham electrons) is constructed by populating the lowest one-electron states $\varepsilon_{i,\mathbf{k}}$. When all electrons are accommodated, three distinct configurations can result [89]:

1. Certain number of bands are completely filled, while the rest are completely empty. The difference in energy between the highest occupied band (called valence band maximum (VBM)) and the bottom of the lowest unoccupied band (called conduction band minimum (CBM)) is referred to as the band gap E_g[1]. If $E_g >> k_\mathrm{B}T$, where k_B is the Boltzmann constant and T is about room temperature, one has an insulator [89].

2. As in 1 above but $E_g \sim k_\mathrm{B}T$. In that case one has an intrinsic semiconductor [89][2].

3. A band or more may be partially filled, and one has a metallic material [89].

[1] At $T = 0\ K$, the collection of all occupied electronic states is known as the valence band, while the collection of all the unoccupied electronic states is known as the conduction band [127].

[2] In fact, the distinction between insulators and semiconductors is somewhat arbitrary. However, $E_g > 3\ eV$ are typically considered wide band gaps [127].

Note that, the number of levels (i.e. number of allowed $\mathbf{k}$'s) in each band is just twice the number of primitive cells in the crystal (see App. B). Therefore, only in solids with an even number of electrons per primitive cell all bands can be filled or empty. However, the converse is not true and it is common to find conducting solids with an even number of electrons per primitive cell. This happens because the overlap of band energies can lead to a ground state in which several bands are partially filled.

In the latter configuration above, the highest occupied level is known as *Fermi level*, ε_F. The set of constant energy surfaces $\varepsilon_{i,\mathbf{k}} = \varepsilon_F$ in $\mathbf{k}$-space is known as *Fermi surface*. A Fermi surface arising from a single partially filled band is known as a *branch* of Fermi surface.

As $T \to 0$, the *chemical potential* μ of a solid with E_g approaches the energy in the middle between the VBM and the CBM. It is this μ which is referred to when the term *Fermi energy* ε_F is used to describe a solid with E_g. However, strictly speaking, a solid with E_g has no ε_F (cf. [89, App. B, p. 142 and p. 575]).

For spin-polarized calculations (Sec. 3.5), one obtains two sets of bands, one for each spin.

8.2 Density of States (DOS)

The density of the electronic states (DOS) as a function of energy is a very useful concept in analyzing the electronic states of solids [79]. It condenses the properties of the band structure for all possible positions in reciprocal space into a simple form [127]. The DOS is defined as the number of one-electron states (in Bloch, HF, or DFT schemes) per unit energy interval and per unit cell volume [148]. Thus, for energies in the range $\varepsilon + \mathrm{d}\varepsilon$, the DOS is given by a sum over all states with energy in that range [79]. An explicit relation between the DOS and the band

structure $\varepsilon_i(\mathbf{k})$ can be seen in the following expression for DOS [79, 89]

$$g(\varepsilon) = \frac{1}{\Omega}\sum_i 2\sum_{\mathbf{k}}\delta(\varepsilon-\varepsilon_{i,\mathbf{k}}) = \sum_i 2\int\frac{\mathrm{d}\mathbf{k}}{(2\pi)^3}\,\delta(\varepsilon-\varepsilon_{i,\mathbf{k}})$$
$$= \sum_i \underbrace{2\int_{\varepsilon_{i,\mathbf{k}}=\varepsilon}\frac{\mathrm{d}S_{\mathbf{k}}}{(2\pi)^3}\,\frac{1}{|\nabla_{\mathbf{k}}\,\varepsilon_{i,\mathbf{k}}|}}_{g_i(\varepsilon)} \tag{8.2.1}$$

where Ω is the volume of the solid. The presence of the prefactor 2 is due the fact that each $i,\mathbf{k}$ level can accommodate two electrons (one of each spin in the non-spin-polarized case). In the limit of bulk material (i.e. large crystal with an infinite number of unit cells) the spacings between the allowed $\mathbf{k}$ vectors become very small; hence the sum over $\mathbf{k}$ in the first expression is replaced with an integral in the second expression. The volume integral in the second expression can be expressed as a surface integral as in the last expression, where $S_{\mathbf{k}}$ is a constant-energy surface in $\mathbf{k}$-space and $\nabla_{\mathbf{k}}\,\varepsilon_i(\mathbf{k})$ is a vector normal to $S_{\mathbf{k}}$ with magnitude equal to the rate of change of $\varepsilon_i(\mathbf{k})$ in that normal direction.

Because $\varepsilon_i(\mathbf{k})$ is bound (see App. B), there must exist, for each i, at least two points $\mathbf{k}_0$ at which $\nabla_{\mathbf{k}}\,\varepsilon_i(\mathbf{k}) = 0$. These vanishing gradients lead to singularities, known as van Hove singularities, in the integrand of $g(\varepsilon)$ 8.2.1[3]. Typical van Hove singularities introduce sharp features in the $g_i(\varepsilon)$ diagrams [79, 89] in a number of places where the slope of the DOS changes discontinuously [127]. Moreover, with valence and conduction bands separated, the $g_i(\varepsilon)$ also reflects the presence of the E_g. On the other hand, a simple observation is that metals have a nonzero DOS at the Fermi level [127].

For practical purposes, let us define the *integrated* DOS by [148]

$$I(\varepsilon) = \int_{-\infty}^{\varepsilon}\mathrm{d}\varepsilon\; g(\varepsilon)\;. \tag{8.2.2}$$

Now, by imposing that $I(\varepsilon_F) = N$, where N is the number of (valence) electrons per unit cell,

[3] It can be shown that such singularities are integrable [89, p.145]. For brief treatments of this point see [79, Sec. 5.1].

Fermi energy ε_F can be obtained readily from Eqs. 8.2.1 and 8.2.2. On computer (and in VASP), however, it is easier to calculate the DOS from $I(\varepsilon)$ as [154]

$$g(\varepsilon_i) = \frac{I(\varepsilon) - I(\varepsilon_{i-1})}{\Delta\varepsilon} \,, \tag{8.2.3}$$

where $\Delta\varepsilon$ is the energy difference between each two points in the energy grid. This scheme should conserve the total number of electrons N exactly.

As always, for spin-polarized calculations (Sec. 3.5), it is straightforward to calculate spin-projected DOS using $\varepsilon_{i,\sigma}(\mathbf{k})$ instead of $\varepsilon_i(\mathbf{k})$ in Eq. 8.2.1 (and replacing the prefactor 2 with 1) and $g_i^\sigma(\varepsilon)$ instead of $g_i(\varepsilon)$ in the subsequent equations. At the end, one obtains two sets of DOS's, one for each spin.

$$\begin{aligned} g^\sigma(\varepsilon) = \frac{1}{\Omega}\sum_i \sum_{\mathbf{k}} \delta(\varepsilon - \varepsilon^\sigma_{i,\mathbf{k}}) &= \sum_i \int \frac{\mathrm{d}\mathbf{k}}{(2\pi)^3}\, \delta(\varepsilon - \varepsilon^\sigma_{i,\mathbf{k}}) \\ &= \sum_i \underbrace{\int_{\varepsilon^\sigma_{i,\mathbf{k}}=\varepsilon} \frac{\mathrm{d}S_{\mathbf{k}}}{(2\pi)^3}\, \frac{1}{\left|\nabla_{\mathbf{k}}\, \varepsilon^\sigma_{i,\mathbf{k}}\right|}}_{g_i^\sigma(\varepsilon)} \quad . \end{aligned} \tag{8.2.4}$$

8.3 Partial (Projected) Density of States (PDOS)

The DOS we have discussed in the previous section is known in the literature as the total DOS (TDOS). However, the TDOS can be resolved into *spin-projected* DOS (Eq. 8.2.4) when spin-plorized calculation are performed. One can go further and rewrite the expression for TDOS 8.2.1 as

$$g(\varepsilon) = \frac{1}{\Omega}\sum_i 2 \sum_{\mathbf{k}} \langle \varphi_{i,\mathbf{k}} | \varphi_{i,\mathbf{k}} \rangle\, \delta(\varepsilon - \varepsilon_{i,\mathbf{k}}) \,, \tag{8.3.1}$$

where $|\varphi_{i,\mathbf{k}}\rangle$ are the KS eigenstates corresponding to the eigenvalues $\varepsilon_{i,\mathbf{k}}$. Insertion of a *complete* set of orthonormal basis, say $|\mathbf{r}\rangle$ with $\int \mathrm{d}\mathbf{r}\ |\mathbf{r}\rangle\langle\mathbf{r}| = \mathbb{1}$, yields

$$\begin{aligned} g(\varepsilon) &= \frac{1}{\Omega}\sum_i 2\sum_{\mathbf{k}}\langle\varphi_{i,\mathbf{k}}|\left(\int \mathrm{d}\mathbf{r}\ |\mathbf{r}\rangle\langle\mathbf{r}|\right)|\varphi_{i,\mathbf{k}}\rangle\ \delta(\varepsilon-\varepsilon_{i,\mathbf{k}}) \\ &= \int \mathrm{d}\mathbf{r}\ \underbrace{\left(\frac{1}{\Omega}\sum_i 2\sum_{\mathbf{k}}\langle\varphi_{i,\mathbf{k}}|\mathbf{r}\rangle\langle\mathbf{r}|\varphi_{i,\mathbf{k}}\rangle\ \delta(\varepsilon-\varepsilon_{i,\mathbf{k}})\right)}_{g(\varepsilon,\mathbf{r})} = \int \mathrm{d}\mathbf{r}\ g(\varepsilon,\mathbf{r})\ . \end{aligned} \tag{8.3.2}$$

The projection of DOS on the configuration space, $g(\varepsilon,\mathbf{r})$, is known as the *local (or site-projected) density of states* (LDOS). For a general *complete* orthonormal basis $\{|a\rangle\}$ with $\sum_a |a\rangle\langle a| = \mathbb{1}$, the *projected (or partial) density of states* (PDOS), $g^a(\varepsilon)$, is defined by

$$\begin{aligned} g(\varepsilon) &= \frac{1}{\Omega}\sum_i 2\sum_{\mathbf{k}}\langle\varphi_{i,\mathbf{k}}|\left(\sum_a |a\rangle\langle a|\right)|\varphi_{i,\mathbf{k}}\rangle\ \delta(\varepsilon-\varepsilon_{i,\mathbf{k}}) \\ &= \sum_a \underbrace{\left(\frac{1}{\Omega}\sum_i 2\sum_{\mathbf{k}}\langle\varphi_{i,\mathbf{k}}|a\rangle\langle a|\varphi_{i,\mathbf{k}}\rangle\ \delta(\varepsilon-\varepsilon_{i,\mathbf{k}})\right)}_{g^a(\varepsilon)} = \sum_a g^a(\varepsilon)\ . \end{aligned} \tag{8.3.3}$$

One can choose to project the TDOS onto the all-electron partial waves of the isolated atoms (see Subsec. 3.6.4), to get the *atom-projected* DOS. One can also choose to project the TDOS onto the atomic orbitals (e.g. s, p and d) to obtain the *atomic orbital (or ℓ-) projected* DOS [145,229].

The significance of ℓ-PDOS is evident, since the interactions between different atoms or orbital components in a soild manifest themselves in the alignment of peaks in their PDOS spectra. This in turn, provides a very useful tool to investigate the nature of interactions and electronic bonding in a solid [229, 230]. Spin PDOS give a clue about the magnetic nature of a solid (cf. Eq. 3.5.6). Moreover, PDOS may give a clue about the electrons dynamics under perturbation (cf. Ch. 9).

VASP gives access to different kinds of PDOS: TDOS, spin-PDOS, site-PDOS and ℓ-PDOS. For each target TMNs, and within each stoichiometry, we carried out band-structure and DOS

calculations on the most energetically favorable phase(s). Electronic properties of some other phases have been also investigated. The SDFT calculated band diagrams (i.e. $\epsilon_i^\sigma(\mathbf{k})$ curves), spin-projected DOS and ℓ-PDOS (decomposed into each atomic type) for the selected phases have been presented graphically. In order to closely investigate the details of their electronic structure, we plotted the energy bands along densely sampled high-symmetry string of neighboring $\mathbf{k}$-points (listed in Table 8.1). Moreover, the orbital character of the bands were extracted by plotting the (*integrated*) ℓ-PDOS (*of each atomic type*) at the same energy scale as the energy bands and side by side.

Table 8.1: High-symmetry $\mathbf{k}$-points along which band diagrams are calculated. Points are labeled according to Ref. [203] and coordinates are given w.r.t. the reciprocal lattice basis vectors. The common $\Gamma(0.0, 0.0, 0.0)$ point is not shown.

Structure	$\mathbf{k}$-points
M_3N Structures	
$D0_9$	$M(0.5, 0.5, 0.0)$, $X(0.0, 0.5, 0.0)$, $R(0.5, 0.5, 0.5)$.
$D0_2$	$N(0.0, 0.0, 0.5)$, $P(0.25, 0.25, 0.25)$, $H(0.5, -.5, 0.5)$.
ϵ-Fe_3N	$A(0, 0, 0.5)$, $H(-0.333, 0.667, 0.5)$ $K(-0.333, 0.667, 0)$, $M(0, 0.5, 0)$, $L(0, 0.5, 0.5)$.
RhF_3	$F(0.5, 0.5, 0.0)$, $Q(0.375, 0.625, 0.0)$, $B(0.5, 0.75, 0.25)$, $Z(0.5, 0.5, 0.5)$, $L(0.0, 0.5, 0.0)$, $Y(0.25, 0.5, -.25)$, $\Sigma(0.0, 0.5, -.5)$.
MN Structures	
B3	$X(0.0, 0.5, 0.0)$, $W(0.75, 0.25, 0.5)$, $L(0.5, 0.5, 0.5)$, $K(0.750, 0.375, 0.375)$, $U(0.625, 0.250, 0.625)$.
B17	$X(0.0, 0.5, 0.0)$, $M(0.5, 0.5, 0.0)$, $Z(0.0, 0.0, 0.5)$, $A(0.5, 0.5, 0.5)$, $R(0.0, 0.5, 0.5)$.
B24	$Z(0.5, 0.5, 0.0)$, $X(0.5, 0.0, 0.5)$, $Y(0.0, -.5, -.5)$, $L(0.5, 0.0, 0.0)$.
MN_2 Structures	
C18	$X(0.0, 0.5, 0.0)$, $S(-.5, 0.5, 0.0)$, $Y(-.5, 0.0, 0.0)$, $Z(0.0, 0.0, 0.5)$, $U(0.0, 0.5, 0.5)$, $R(-.5, 0.5, 0.5)$, $T(-.5, 0.0, 0.5)$.
$CoSb_2$	$B(-.5, 0.0, 0.0)$, $A(-.5, 0.5, 0.0)$, $E(-.5, 0.5, 0.5)$, $Z(0.0, 0.0, 0.5)$, $Y(0.0, 0.5, 0.0)$, $D(-.5, 0.0, 0.5)$, $C(0.0, 0.5, 0.5)$.

9. Calculations of Optical Properties

"Response functions are the bread and butter of theoretical physics and the connection to important experimental measurements."

Richard M. Martin [78, p. 486]

A vast amount of useful information and extremely powerful investigation and characterization methods of solid materials are provided by their *optical excitation spectra*. Moreover, optical spectra supply us with the basis for a wide range of technological applications, e.g. in opto-electronics [151]. From a fundamental point of view, the evaluation of the static and frequency-dependent dielectric response functions is important for the interpretation of the optical properties measured for bulk solids as well as their surfaces [231]. An efficient calculation of the frequency-dependent microscopic density repose matrix χ (Sec. 9.2.1) is crucial for the implementation of most post-DFT approaches (e.g. GW and the Bethe-Salpeter) which constitute the main routes toward a high-level description of the optical properties in extended systems. In GW, in particular, the frequency-dependent macroscopic dielectric function is required for analytically integrating the $\mathbf{q} = \mathbf{0}$ Coulomb singularity of the correlation and self-energy. If excitonic effects are included, dielectrically screened interaction potentials are also necessary [231].

Following the clear presentation of Ref. [153, Ch. 2] and Refs. [150, 231], the present chapter is devoted to the employed methods of evaluation of the dielectric matrix ε. We emphasize that we only sketch the general derivation procedures, quote results and define some important terminologies in the subject. Technical details can be found in the original works [150, 153, 231–235] and in many texts [78, 86, 89, 236, 237].

9.1 Preliminary Remarks

In Appendix D, it is shown that all the frequency-dependent optical constants of a material can be calculated if the complex dielectric function $\varepsilon(\mathbf{q}, \omega)$ is known. However, before we move to show how $\varepsilon(\mathbf{q}, \omega)$ itself can be obtained from DFT-GW calculations, we should mention some points:

1. As in the usual spectroscopic experiments, we are limiting the discussion here to the linear response. That is, we are considering the influence of weak external perturbations compared to the electric fields caused by the ions [153]; in which case the material parameters are independent of the strength of the electric field.

2. It is also assumed that these parameters do not depend on the change of an external applied magnetic field, i.e. no magneto-resistive effects are considered.

3. In principle, the dielectric function has a tensorial nature, that is Eq. D.1.4a should be written as

$$D_\alpha = \sum_\beta \varepsilon_{\alpha\beta} E_\beta \ . \tag{9.1.1}$$

However, in experiment isotropy is normally assumed. Therefore, in order to make comparison with experiment, we averaged out the diagonal terms of the obtained $\varepsilon_{\alpha\beta}$. It is this average which is substituted in the relations of Appendix D [1].

9.2 Dynamical Linear Response

9.2.1 The Density Response Function (χ)

The central quantity in the so-called "linear response theory" is the density response function:

$$\chi(\mathbf{r}, \mathbf{r}', t - t') = \frac{\delta n(\mathbf{r}, t)}{\delta v_{\text{ext}}(\mathbf{r}', t')} \ , \tag{9.2.1}$$

where $\delta n(\mathbf{r}, t)$ is the induced change in the electronic density at $(\mathbf{r}, t)$ due to a small change δv_{ext} in the external potential at $(\mathbf{r}', t')$ [78, 153]. Therefore,

$$\delta n(\mathbf{r}, t) = \int \mathrm{d}t' \int \mathrm{d}\mathbf{r}' \ \chi(\mathbf{r}, \mathbf{r}', t - t') \ \delta v_{\text{ext}}(\mathbf{r}', t') \ . \tag{9.2.2}$$

In the static DFT approach (Ch. 3), it is required that the electron density of the KS system and of the physical system must be the same. Similarly, one may require that any change δn in

[1] For cubic crystals diagonal terms are equal and there is no need for approximation.

the time-dependent density $n(\mathbf{r},t)$ of the reference system[2] to be equal to that of the physical system. Therefore, one can define the density response function of the KS system $\chi^{\mathrm{KS}}(\mathbf{r},\mathbf{r}',t-t')$ to any small change in the KS potential (defined by Eqs. 3.4.17 and 3.4.19)[3] as

$$\chi^{\mathrm{KS}}(\mathbf{r},\mathbf{r}',t-t') = \frac{\delta n(\mathbf{r},t)}{\delta v_{\mathrm{R}}(\mathbf{r}',t')} \ , \tag{9.2.3}$$

$$\delta n(\mathbf{r},t) = \int \mathrm{d}t' \int \mathrm{d}\mathbf{r}' \ \chi^{\mathrm{KS}}(\mathbf{r},\mathbf{r}',t-t') \ \delta v_{\mathrm{R}}(\mathbf{r}',t') \ . \tag{9.2.4}$$

Substituting for v_{R} from Eq. 3.4.19, Eq. 9.2.4 reads

$$\delta n(\mathbf{r},t) = \int \mathrm{d}t' \int \mathrm{d}\mathbf{r}' \ \chi^{\mathrm{KS}}(\mathbf{r},\mathbf{r}',t-t') \ \left(\delta v_{\mathrm{H}}(\mathbf{r},t) + \delta v_{\mathrm{ext}}(\mathbf{r},t) + \delta \tilde{v}_{\mathrm{xc}}(\mathbf{r},t)\right) \ . \tag{9.2.5}$$

9.2.2 The Exchange-Correlation Kernel (f_{xc})

In order to obtain an explicit relation between χ and χ^{KS}, one may write the *time-dependent* exchange correlation functional $\tilde{v}_{\mathrm{xc}}(\mathbf{r},t)$ in terms of the ground state density *time-independent* $n_0(\mathbf{r})$ as

$$\tilde{v}_{\mathrm{xc}}(\mathbf{r},t) = \tilde{v}_{\mathrm{xc}}[n_0+\delta n](\mathbf{r},t) = \tilde{v}_{\mathrm{xc}}[n_0](\mathbf{r}) + \int \mathrm{d}t' \int \mathrm{d}\mathbf{r}' \ f_{\mathrm{xc}}[n_0](\mathbf{r},\mathbf{r}',t-t') \ \delta n(\mathbf{r}',t') \ , \tag{9.2.6}$$

where the so-called exchange-correlation kernel f_{xc} is the functional derivative of the $\tilde{v}_{\mathrm{xc}}$ potential with respect to the electron density evaluated at the unperturbed ground state [234]

$$f_{\mathrm{xc}}[n_0](\mathbf{r},\mathbf{r}',t-t') = \left.\frac{\delta \tilde{v}_{\mathrm{xc}}(\mathbf{r},t)}{\delta n(\mathbf{r}',t')}\right|_{n=n_0} \ . \tag{9.2.7}$$

Now, substituting Eq. 9.2.7 in Eq. 9.2.6 and equating Eqs. 9.2.2 and 9.2.5 one obtains a Dyson equation

$$\boxed{\chi(\mathbf{r},\mathbf{r}',\omega) = \chi^{\mathrm{KS}}(\mathbf{r},\mathbf{r}',\omega) + \int \mathrm{d}\mathbf{r}_1\mathrm{d}\mathbf{r}_2 \ \chi^{\mathrm{KS}}(\mathbf{r},\mathbf{r}_1,\omega)\left(\frac{e^2}{|\mathbf{r}_1-\mathbf{r}_2|} + f_{\mathrm{xc}}(\mathbf{r}_1,\mathbf{r}_2,\omega)\right)\chi(\mathbf{r}_2,\mathbf{r}',\omega) \ ;} \tag{9.2.8}$$

[2] In fact, by considering n to be a time-dependent quantity, one has already migrated from the static KS-DFT formalism to a time-dependent DFT formalism.

[3] Dropping the spin superscript, for now.

where we have moved from the time domain to the frequency domain, and the chain rule have been employed on $\delta v_{\rm H}$ and $\delta v_{\rm xc}$ (For further explanation, see Ref. [153, p.14]).

9.2.3 Random Phase Approximation (RPA)

Dyson equation 9.2.8 above is a key equation in the subject, telling us how to calculate the response function of a many-body system from that of the reference KS system. However, the exchange-correlation kernel $f_{\rm xc}$, like its parent $\tilde{v}_{\rm xc}$, has to be approximated. The simplest approximation is the well-known random phase (or Hartree) approximation (RPA) [236], in which exchange and correlation effects *on the response* are neglected: $f_{\rm xc} = 0$ [234]. In this approximation, electrons are considered to respond to the total (external plus induced) field independently [238]. Only Hartree term $\delta v_{\rm H}$ contributes to 9.2.8, while other interactions felt by the electrons average out because of their random phases [78].

9.2.4 Explicit Forms of χ and $\chi^{\rm KS}$

By introducing the time-dependent external perturbation $\delta\hat{\mathcal{H}}_e(t)$ into the picture, the many-body electronic Schrödinger equation reads

$$i\hbar\frac{\partial}{\partial t}|\Phi(t)\rangle = \left(\hat{\mathcal{H}}_e + \delta\hat{\mathcal{H}}_e(t)\right)|\Phi(t)\rangle \;, \tag{9.2.9}$$

where $\delta\hat{\mathcal{H}}_e$ can be written in terms of the time-dependent induced potential δv as

$$\delta\hat{\mathcal{H}}_e(t) = e^{\eta t}\sum_{i=1}^{N}\delta v(\mathbf{r}_i,t) \;; \qquad 0<\eta\ll 1 \;, \tag{9.2.10}$$

or, in the frequency domain

$$\delta\hat{\mathcal{H}}_e(t) = \int \mathrm{d}\mathbf{r}\int\frac{\mathrm{d}\omega}{2\pi}\; e^{-j(\omega+j\eta)t}\,\delta v(\mathbf{r},\omega)\,\hat{n}(\mathbf{r}) \;. \tag{9.2.11}$$

It is then a routine matter to solve Eq. 9.2.9 to linear order by perturbation theory (See Ref. [153, Sec. 2.2]) to obtain

$$\chi(\mathbf{r},\mathbf{r}',\omega) = -\sum_{i\neq 0}\left(\frac{\langle\Phi_i^0|\hat{n}(\mathbf{r}')|\Phi_0^0\rangle\langle\Phi_0^0|\hat{n}(\mathbf{r})|\Phi_i^0\rangle}{\omega_i^0-\omega-j\eta}+\frac{\langle\Phi_0^0|\hat{n}(\mathbf{r}')|\Phi_i^0\rangle\langle\Phi_i^0|\hat{n}(\mathbf{r})|\Phi_0^0\rangle}{\omega_i^0+\omega+j\eta}\right); \quad (9.2.12)$$

where $|\Phi_i^0\rangle$ are the eigenstates of the unperturbed Schrödinger equation (Eq. 2.2.3), and $\omega_i^0 = E_i^0 - E_0^0$ are the differences between the corresponding eigen energies E_i^0 and the ground state energy E_0^0.

In the (KS) independent-particle picture, where $|\Phi_i^0\rangle$ is given by Eq. (2.4.51), it can be shown straightforwardly that (See Ref. [153, Sec. 2.2])

$$\chi^{\mathrm{KS}}(\mathbf{r},\mathbf{r}',\omega) = -\sum_i\sum_{i'} 2f_i(1-f_{i'})\left(\frac{\varphi_{i'}^*(\mathbf{r}')\varphi_i(\mathbf{r}')\varphi_i^*(\mathbf{r})\varphi_{i'}(\mathbf{r})}{\epsilon_{i'}-\epsilon_i-\omega-j\eta}+\frac{\varphi_i^*(\mathbf{r}')\varphi_{i'}(\mathbf{r}')\varphi_{i'}^*(\mathbf{r})\varphi_i(\mathbf{r})}{\epsilon_{i'}-\epsilon_i+\omega+j\eta}\right); \quad (9.2.13)$$

where $f_i = 0$ for unoccupied states and $f_i = 1$ for occupied states, while all other quantities are defined as in Ch. 3.

9.2.5 Periodic Solids

Due to the lattice translation invariance in periodic solids $\chi(\mathbf{r}+\mathbf{R},\mathbf{r}'+\mathbf{R},\omega) = \chi(\mathbf{r},\mathbf{r}',\omega)$, it can be shown that the Fourier transform $\chi(\mathbf{k},\mathbf{k}',\omega)$ of $\chi(\mathbf{r},\mathbf{r}',\omega)$ is non-zero only if $\mathbf{k}$ and $\mathbf{k}'$ differ by a vector $\mathbf{K}$ in the reciprocal lattice (see App. C). Therefore, the following replacements are valid: $\mathbf{k}\to\mathbf{k}+\mathbf{K}$ and $\mathbf{k}'\to\mathbf{k}+\mathbf{K}'$, where $\mathbf{K}$ and $\mathbf{K}'$ are in the reciprocal lattice, and $\mathbf{k}$ and $\mathbf{K}'$ are inside the BZ. Also, as we did in Sec. 3.6, the indices i and i' must be replaced with the crystal quantum numbers $i\to i,\mathbf{k}$ and $i'\to i',\mathbf{k}$, respectively. Considering all this and doing some mathematical manipulations (See Ref. [153, Sec. 2.2]), the response function can be obtained in the $\mathbf{k}$-space as [150, 231]

$$\boxed{\chi_{\mathbf{q}}^{\mathrm{KS}}(\mathbf{K},\mathbf{K}',\omega) = \frac{1}{\Omega}\sum_{i,i',\mathbf{k}} 2w_{\mathbf{k}}\left(f_{i',\mathbf{k}-\mathbf{q}}-f_{i,\mathbf{k}}\right)\frac{\left\langle\varphi_{i',\mathbf{k}-\mathbf{q}}|e^{i(\mathbf{q}+\mathbf{K})\cdot\mathbf{r}}|\varphi_{i,\mathbf{k}}\right\rangle\left\langle\varphi_{i,\mathbf{k}}|e^{i(\mathbf{q}+\mathbf{K}')\cdot\mathbf{r}'}|\varphi_{i',\mathbf{k}-\mathbf{q}}\right\rangle}{\omega+\epsilon_{i',\mathbf{k}-\mathbf{q}}-\epsilon_{i,\mathbf{k}}+j\eta\,\mathrm{sgn}\left(\epsilon_{i',\mathbf{k}-\mathbf{q}}-\epsilon_{i,\mathbf{k}}\right)}}. \quad (9.2.14)$$

To summarize, within DFT, one can define the independent-electron density response function χ^{KS} as the functional derivative of the electron density with respect to the total KS potential (Eq. 9.2.3) evaluated at the unperturbed ground state (Eqs. 9.2.7 and 9.2.8). In a periodic medium, χ^{KS} is, at any given $\mathbf{k}$ point in the Brillouin zone (BZ), a matrix (Eq. 9.2.14)[4] over reciprocal lattice vectors (see also Ref. [234]).

9.3 The Dielectric Function (ε)

9.3.1 Macroscopic Dielectric Function ($\varepsilon_{\mathrm{mac}}$)

For a bulk crystalline solid and at a coarse scale, both χ and ε are homogeneous, while the periodicity of the external perturbation $\mathbf{E}_{\mathrm{ext}}$ is followed by the total field $\mathbf{E}$. The two fields are formally related via

$$\mathbf{E}(\mathbf{r},\omega) = \int \mathrm{d}\mathbf{r}' \;\; \varepsilon^{-1}_{\mathrm{mac}}(\mathbf{r}-\mathbf{r}',\omega)\mathbf{E}_{\mathrm{ext}}(\mathbf{r}',\omega) \; . \tag{9.3.1}$$

Due to the homogeneity of the bulk material, the *macroscopic* dielectric function ε depends only on the difference $\mathbf{r}-\mathbf{r}'$. Therefore, Eq. 9.3.1 has a simple Fourier-transformed form:

$$\mathbf{E}(\mathbf{q},\omega) = \varepsilon^{-1}_{\mathrm{mac}}(\mathbf{q},\omega)\mathbf{E}_{\mathrm{ext}}(\mathbf{q},\omega) \; . \tag{9.3.2}$$

The $\mathbf{E}_{\mathrm{ext}}$ field is caused only by an external source. That is, $\mathbf{E}_{\mathrm{ext}}$ is independent of the material and its value at any point is the same as if the material were not present [78]. To properly investigate the situation, usually the total potential v_{tot} is divided into *external* and *induced*:

$$v_{\mathrm{tot}} = v_{\mathrm{ext}} + v_{\mathrm{ind}} \; . \tag{9.3.3}$$

Here, the *screened* potential v_{tot} is due to the external charge density n_{ext} *plus* the induced charge density $n_{\mathrm{ind}} = \delta n$. Therefore, in terms of potentials, Eq. 9.3.2 can be rewritten (in the long-wavelength limit) in momentum space as

$$v_{\mathrm{tot}} = \varepsilon^{-1} v_{\mathrm{ext}} \; ; \tag{9.3.4}$$

[4] Adler [233] and Wiser [235] were the first to give such an expression for χ in the context of the self-consistent field (SCF) approximation [234].

and, within the linear response limit, the definitions of the response function χ (known also as the reducible polarizability) and the screened response function P (known also as the irreducible polarizability) read

$$n_{\rm ind} = \chi\, v_{\rm ext}\ , \tag{9.3.5}$$

$$v_{\rm ind} = P\, v_{\rm tot}\ . \tag{9.3.6}$$

Moreover, it is straightforward to show that:

$$\varepsilon^{-1} = 1 + \nu\chi \quad , \tag{9.3.7}$$

$$\varepsilon = 1 - \nu P \quad , \tag{9.3.8}$$

$$\chi = P + P\nu\chi\ . \tag{9.3.9}$$

It is now clear that ε can be obtained if the response of the system to the change in either the external potential (Eq. 9.3.7) or the total potential (Eq. 9.3.8) is known. Eq. 9.3.9 is a Dyson equation (c.f. Eq. 9.2.8).

9.3.2 Microscopic Dielectric Function ($\varepsilon_{\rm mic}$)

At the atomic scale, the total *microscopic* field $\mathbf{e}(\mathbf{r},\omega)$ oscillates rapidly, and Eq. 9.3.1 becomes

$$\mathbf{e}(\mathbf{r},\omega) = \int {\rm d}\mathbf{r}'\ \ \varepsilon^{-1}_{\rm mic}(\mathbf{r},\mathbf{r}',\omega)\mathbf{E}_{\rm ext}(\mathbf{r}',\omega)\ , \tag{9.3.10}$$

where now the *microscopic* dielectric function ε is invariant only under the translation by a lattice vector. It is straightforward to shown that this kind of invariance implies that

$$\boxed{e(\mathbf{q}+\mathbf{K},\omega) = \sum_{\mathbf{K}'} \varepsilon^{-1}(\mathbf{q}+\mathbf{K},\mathbf{q}+\mathbf{K}',\omega)\ \mathbf{E}_{\rm ext}(\mathbf{q}+\mathbf{K}',\omega) = \sum_{\mathbf{K}'} \varepsilon^{-1}_{\mathbf{K},\mathbf{K}}(\mathbf{q},\omega)\ \mathbf{E}_{\rm ext}(\mathbf{q}+\mathbf{K}',\omega)\ .} \tag{9.3.11}$$

Eqs. 9.3.10 and 9.3.11 above are to be compared with Eqs. 9.3.1 and 9.3.2, respectively.

9.3.3 Relation Between $\varepsilon_{\mathrm{mac}}$ and $\varepsilon_{\mathrm{mic}}$

The macroscopic and microscopic fields are connected via the integration over the unit cell Ω around $\mathbf{R}$:

$$\mathbf{E}(\mathbf{R},\omega) = \frac{1}{\Omega}\int_{\Omega(\mathbf{R})} \mathrm{d}\mathbf{r}\ \ \mathbf{e}(\mathbf{r},\omega)\ . \tag{9.3.12}$$

At this point, it may be worth mentioning that the *microscopic* dielectric function is the accessible quantity through *ab initio* calculations. However, the long-wavelength limit($\mathbf{q}\to\mathbf{0}$) of the dielectric matrix determines the optical properties in the regime accessible to optical probes.

Starting from Eq. 9.3.12 above and considering the relations in the previous subsections, one can straightforwardly arrive at the fact that the evaluation of $\varepsilon_{\mathrm{mac}}$ requires the inversion of the full $\varepsilon_{\mathrm{mic}}$ matrix and taking the limit $\mathbf{q}\to\mathbf{0}$

$$\frac{1}{\varepsilon_{\mathrm{mac}}(\hat{\mathbf{q}},\omega)} = \lim_{\mathbf{q}\to\mathbf{0}} \varepsilon^{-1}_{0,0}(\mathbf{q},\omega)\ , \tag{9.3.13}$$

where $\hat{\mathbf{q}} = \mathbf{q}/q$ is the direction which is used to approach the Γ point [231]. At this point, it may be worth mentioning that:

- The *microscopic* dielectric function is the accessible quantity through *ab initio* calculations. Eq. 9.3.13, however, shows that one can obtain $\varepsilon_{\mathrm{mac}}$ from the first-principles-calculated $\varepsilon_{\mathrm{mic}}$ by inverting the latter w.r.t. $\mathbf{K},\mathbf{K}'$ and taking the head[5] of the resulting matrix, then invert this 3×3 tensor.

- The long-wavelength limit ($\mathbf{q}\to\mathbf{0}$) of the dielectric matrix determines the optical properties in the regime accessible to optical probes.

9.3.4 Local Field Effects

In a real solid, the microscopic electric field varies rapidly over the unit cell. The average of the microscopic field over a region large compared with the lattice constant but small compared with the wave-length $2\pi/q$ is what we call the macroscopic field. These two quantities are not in

[5] The terms "head", "body" and "wing" refer to ($\mathbf{K}=\mathbf{K}'=0$), ($\mathbf{K}\neq 0$ and $\mathbf{K}'\neq 0$) and ($\mathbf{K}=0$ or $\mathbf{K}'=0$) of the dielectric matrix, respectively.

general the same; the difference between them give rise to non-vanishing off-diagonal elements in the macroscopic response matrices and is usually referred to as "crystal local fields" or "local field effects" [233, 234].

9.3.5 Longitudinal and Transversal ε

The external perturbation with frequency ω and spatial periodicity $\mathbf{q}$ induces two kinds of potentials in the material, longitudinal and transversal fields. The former results from slowly moving charges and is parallel to the wave vector $\mathbf{q}$. On the other hand, $\mathbf{q}$ and the transversal field vector are perpendicular. As a consequence, ε has two corresponding components: longitudinal and transversal, linking the longitudinal/transversal component of the external electric field to the longitudinal/transversal component of the total electric field. However, in the limit $\mathbf{q} \to 0$, i.e. for slowly varying fields, the two components are equal [153][6]. Furthermore, It has been found that the transversal and longitudinal expressions for the dynamic response function yield identical energy peaks positions in the optical absorption spectrum. This is due to the fact that the optical transitions positions are determined from the ground state band diagrams by applying the optical *selection rules* regardless of $\varepsilon_{\mathrm{mic}}$ type of expression [231].

However, if non-local pseudopotentials or non-local exchange interactions are applied, the simpler transversal approximation breaks down, and the longitudinal or appropriate corrections to the transversal expression have to be used. Furthermore, within PAW formalism, the one-center terms in the standard PAW potentials are truncated at low angular momenta $(l = 1)$ leading to an inaccurate transversal expression. However, instead of including higher angular components, the rigorous treatment using the exact longitudinal form has the advantage of a more rapid convergence with the one-center basis set. Moreover, the extension of the longitudinal expression to non-local XC functionals is readily achievable (see Ref. [231] for details). In the next subsection, we follow Ref. [153] and quote the *longitudinal expressions* as derived by Gajdoš et. al. [231] within PAW formalism.

[6] For formal derivation of the longitudinal ε, cf. Ref. [153, Sec.2.5] and Ref. [20] therein. For formal derivation of the transversal ε, cf. Ref. [233].

9.3.6 Derivation of ε from Band Diagrams

Using Poisson equation

$$j\ \mathbf{q}\cdot\mathbf{E}(\mathbf{q}) = \frac{e}{\epsilon_0}\ n(\mathbf{q})\ , \tag{9.3.14}$$

where e is the charge unit, one can replace the fields in Eq. 9.3.11 by the densities to get

$$n_{\rm ext}(\mathbf{q}+\mathbf{K}) = \sum_{\mathbf{K}'}(\mathbf{q}+\mathbf{K})\ \varepsilon(\mathbf{q}+\mathbf{K},\mathbf{q}+\mathbf{K}')\ (\mathbf{q}+\mathbf{K}')\ \frac{n_{\rm ext}(\mathbf{q}+\mathbf{K}')+n_{\rm ind}(\mathbf{q}+\mathbf{K}')}{(\mathbf{q}+\mathbf{K}')^2}\ . \tag{9.3.15}$$

From this relation, one can, after some mathematical manipulations (See Ref. [153, Sec. 2.5]), arrive at the following expressions for the microscopic dielectric function and its inverse:

$$\begin{aligned}\varepsilon^{-1}_{\mathbf{K},\mathbf{K}'}(\mathbf{q},\omega) := \varepsilon^{-1}(\mathbf{q}+\mathbf{K},\mathbf{q}+\mathbf{K}',\omega) &= \delta_{\mathbf{K},\mathbf{K}'} + \overbrace{\frac{4\pi e^2}{|\mathbf{q}+\mathbf{K}||\mathbf{q}+\mathbf{K}'|}}^{\nu_{\mathbf{K},\mathbf{K}'}(\mathbf{q})}\ \overbrace{\frac{\partial n_{\rm ind}(\mathbf{q}+\mathbf{K},\omega)}{\partial v_{\rm ext}(\mathbf{q}+\mathbf{K}',\omega)}}^{\chi_{\mathbf{K},\mathbf{K}'}(\mathbf{q},\omega)} \\ &= \delta_{\mathbf{K},\mathbf{K}'} + \nu_{\mathbf{K},\mathbf{K}'}(\mathbf{q})\ \chi_{\mathbf{K},\mathbf{K}'}(\mathbf{q},\omega)\end{aligned} \tag{9.3.16}$$

$$\begin{aligned}\varepsilon_{\mathbf{K},\mathbf{K}'}(\mathbf{q},\omega) := \varepsilon(\mathbf{q}+\mathbf{K},\mathbf{q}+\mathbf{K}',\omega) &= \delta_{\mathbf{K},\mathbf{K}'} - \overbrace{\frac{4\pi e^2}{|\mathbf{q}+\mathbf{K}||\mathbf{q}+\mathbf{K}'|}}^{\nu_{\mathbf{K},\mathbf{K}'}(\mathbf{q})}\ \overbrace{\frac{\partial n_{\rm ind}(\mathbf{q}+\mathbf{K},\omega)}{\partial v_{\rm tot}(\mathbf{q}+\mathbf{K}',\omega)}}^{P_{\mathbf{K},\mathbf{K}'}(\mathbf{q},\omega)} \\ &= \delta_{\mathbf{K},\mathbf{K}'} - \nu_{\mathbf{K},\mathbf{K}'}(\mathbf{q})\ P_{\mathbf{K},\mathbf{K}'}(\mathbf{q},\omega)\end{aligned} \tag{9.3.17}$$

Note that Eqs. 9.3.16 and 9.3.17 are the same as Eqs. 9.3.7 and 9.3.8, respectively; while the corresponding Dyson equation, Eq. 9.3.9, can be obtained by combining Eqs. 9.3.16 and 9.3.17 to give

$$\begin{aligned}\chi_{\mathbf{K},\mathbf{K}'}(\mathbf{q},\omega) &= P_{\mathbf{K},\mathbf{K}'}(\mathbf{q},\omega) + \sum_{\mathbf{K}_1,\mathbf{K}_2} P_{\mathbf{K},\mathbf{K}_1}(\mathbf{q},\omega)\ \overbrace{\frac{4\pi e^2}{|\mathbf{q}+\mathbf{K}_1||\mathbf{q}+\mathbf{K}_2|}}^{\nu_{\mathbf{K}_1,\mathbf{K}_2}(\mathbf{q})}\ \chi_{\mathbf{K}_2,\mathbf{K}'}(\mathbf{q},\omega) \\ &= P_{\mathbf{K},\mathbf{K}'}(\mathbf{q},\omega) + \sum_{\mathbf{K}_1,\mathbf{K}_2} P_{\mathbf{K},\mathbf{K}_1}(\mathbf{q},\omega)\ \nu_{\mathbf{K}_1,\mathbf{K}_2}(\mathbf{q})\ \chi_{\mathbf{K}_2,\mathbf{K}'}(\mathbf{q},\omega)\ .\end{aligned} \tag{9.3.18}$$

Now, everything is in order: Eqs. 9.3.16 and 9.3.17 show that for one to obtain the exact $\varepsilon^{-1}_{\mathbf{K},\mathbf{K}'}(\mathbf{q},\omega)$ or $\varepsilon_{\mathbf{K},\mathbf{K}'}(\mathbf{q},\omega)$, one has to know the exact χ or P, respectively. Yet neither χ nor P

of the physical system is known exactly. The only quantity one can access so far is $\chi^{\rm KS}$ through Eq. 9.2.14 for the KS unphysical system. Therefore, one of the following two approximations is to be chosen:

- Replacing χ by $\chi^{\rm KS}$ in Eq. 9.3.16: In this choice, one is actually assuming that the physical system responds to changes in $v_{\rm ext}$ exactly as an independent-particles system.

- Replacing P by $\chi^{\rm KS}$ in Eq. 9.3.17: Using the foregoing relations between the external, induced, total and the effective KS potentials, the following relation can be shown to hold

$$P_{\mathbf{K},\mathbf{K}'}(\mathbf{q},\omega) = \chi^{\rm KS}_{\mathbf{K},\mathbf{K}'}(\mathbf{q},\omega) + \sum_{\mathbf{K}_1,\mathbf{K}_2} \chi^{\rm KS}_{\mathbf{K},\mathbf{K}_1}(\mathbf{q},\omega)\; f_{{\rm xc};\mathbf{K},\mathbf{K}'}(\mathbf{q},\omega)\; P_{\mathbf{K}_2,\mathbf{K}'}(\mathbf{q},\omega)\;. \quad (9.3.19)$$

If one applies the random phase approximation (Subsection 9.2.3) by letting $f_{{\rm xc};\mathbf{K},\mathbf{K}'}(\mathbf{q},\omega) = 0$, Eq. 9.3.19 above reads

$$P_{\mathbf{K},\mathbf{K}'}(\mathbf{q},\omega) = \chi^{\rm KS}_{\mathbf{K},\mathbf{K}'}(\mathbf{q},\omega)\;. \quad (9.3.20)$$

Therefore, replacing P by $\chi^{\rm KS}$ in Eq. 9.3.17 is exactly the random phase approximation to the dielectric tensor, and Eq. 9.3.17 yields

$$\boxed{\varepsilon^{\rm RPA}_{\mathbf{K},\mathbf{K}'}(\mathbf{q},\omega) = \delta_{\mathbf{K},\mathbf{K}'} - \nu_{\mathbf{K},\mathbf{K}'}(\mathbf{q})\; \chi^{\rm KS}_{\mathbf{K},\mathbf{K}'}(\mathbf{q},\omega)}\;. \quad (9.3.21)$$

From physical point of view, this replacement assumes that the response to the *screened* external perturbation P equals the independent particle response function $\chi^{\rm KS}$. Therefore, in this RPA, the electron-electron interaction is taken *at least partly* into account, and thus it is more accurate than the ($\chi = \chi^{\rm KS}$) approximation.

9.3.7 Imaginary and Real Parts of ε

The imaginary part $\varepsilon^{\rm im}(\hat{\mathbf{q}},\omega)$ of the *macroscopic* dielectric function ($\varepsilon = \varepsilon^{\rm re} + j\;\varepsilon^{\rm im}$) can be evaluated as a sum over δ-like peaks at transition energies $\omega = \epsilon_{c,\mathbf{k}} - \epsilon_{v,\mathbf{k}}$, which are weighted by the transition probability $|\langle u_{c,\mathbf{k}+\mathbf{q}}|u_{v,\mathbf{k}}\rangle|^2$

$$\varepsilon^{\rm im}_{\rm mac}(\hat{\mathbf{q}},\omega) = \frac{4\pi^2 e^2}{\Omega} \lim_{\mathbf{q}\to\mathbf{0}} \frac{1}{q^2} \sum_{c,v,\mathbf{k}} 2w_{\mathbf{k}}\; \delta(\epsilon_{c,\mathbf{k}+\mathbf{q}} - \epsilon_{v,\mathbf{k}} - \omega)\; \langle u_{c,\mathbf{k}+\mathbf{q}}|u_{v,\mathbf{k}}\rangle \langle u_{c,\mathbf{k}+\mathbf{q}}|u_{v,\mathbf{k}}\rangle^* \quad (9.3.22)$$

where the indices v and c stand for valence and conduction, respectively, $u_{c\mathbf{k}}$ is the usual cell periodic part (see App. B) of the orbitals at $\mathbf{k}$ [153, 231]. The dependence of the dielectric function on the direction $\hat{\mathbf{q}}$ via the dielectric tensor $\varepsilon_{\alpha\beta}$ can be given by

$$\varepsilon_{\mathrm{mac}}(\hat{\mathbf{q}},\omega) = \lim_{\mathbf{q}\to\mathbf{0}} \varepsilon_{\mathrm{mac}}(\mathbf{q},\omega) =: \sum_{\alpha,\beta} \hat{\mathbf{q}}_\alpha \, \varepsilon_{\alpha\beta}(\omega) \, \hat{\mathbf{q}}_\beta \; , \tag{9.3.23}$$

where $\hat{\mathbf{q}}_\alpha$ is one Cartesian component of the unit vector $\hat{\mathbf{q}}$. With $\mathbf{e}_\alpha$ being the unit vectors for the three Cartesian directions, the 3×3 Cartesian tensor $\varepsilon^{\mathrm{im}}_{\alpha\beta}(\omega)$ is defined as [153, 231]

$$\varepsilon^{\mathrm{im}}_{\alpha\beta}(\omega) = \frac{4\pi^2 e^2}{\Omega} \lim_{\mathbf{q}\to\mathbf{0}} \frac{1}{q^2} \sum_{c,v,\mathbf{k}} 2w_{\mathbf{k}} \, \delta(\epsilon_{c,\mathbf{k}} - \epsilon_{v,\mathbf{k}} - \omega) \, \langle u_{c,\mathbf{k}+\mathbf{e}_\alpha q} | u_{v,\mathbf{k}} \rangle \langle u_{c,\mathbf{k}+\mathbf{e}_\beta q} | u_{v,\mathbf{k}} \rangle^* \; . \tag{9.3.24}$$

Employing the useful Kramers-Kronig transformation

$$\varepsilon^{\mathrm{re}}_{\alpha\beta}(\omega) = 1 + \frac{2}{\pi} \mathcal{P} \int_0^\infty \mathrm{d}\omega' \, \frac{\varepsilon^{\mathrm{im}}_{\alpha\beta}(\omega')\omega'}{\omega'^2 - \omega^2 + j\eta} \; , \tag{9.3.25}$$

is a cheep way to obtain the real part $\varepsilon^{\mathrm{re}}_{\alpha\beta}(\omega)$ of the dielectric tensor [231].

9.4 The GW_0 Routine

Within the introduced PAW-GW scheme (Subsec. 3.6.4 and Ch. 4), the dynamically screened Coulomb interaction $W(\mathbf{K},\mathbf{K}',\omega)$ can be obtained from the multiplication of the bare Coulomb kernel $4\pi e^2 \, \frac{1}{\mathbf{q}+\mathbf{K}}$ with the inverse dielectric matrix $\varepsilon^{-1}(\mathbf{K},\mathbf{K}',\omega)$ in Fourier space [150]:

$$W(\mathbf{K},\mathbf{K}',\omega) = 4\pi e^2 \, \frac{1}{|\mathbf{q}+\mathbf{K}|} \, \varepsilon^{-1}(\mathbf{K},\mathbf{K}',\omega) \, \frac{1}{|\mathbf{q}+\mathbf{K}'|} \; . \tag{9.4.1}$$

The dielectric matrix ε, for a crystalline solid, is calculated at the random phase approximation (RPA) [80] level via Eq. 9.3.21, while the time-ordered independent-particle irreducible polarizability $\chi^{\mathrm{KS}}_{\mathbf{q}}(\mathbf{K},\mathbf{K}',\omega)$ is given by Eq. 9.2.14 [150, 231].

The method described above requires, in practice, an appreciable number of empty conduction

states. Therefore, in all our calculations we double or triple the default number of bands supplied by VASP. We start by performing normal DFT calculation to obtain the unperturbed KS eigenstates and eigenenergies. However, because of the demanding computational nature of the scheme, we used a smaller meshes of $\mathbf{k}$ points: either $12 \times 12 \times 12$ or $10 \times 10 \times 10$. We employed the implemented GW_0 self-consistent routine on G, in which the quasi-particle eigenvalues are updated four times in the calculations of G, while W is kept at the original DFT level [7]. The dielectric matrix ε is recalculated after the final update of G.

9.5 Calculations of Optical Spectra

Using the relations derived in App. D, we managed to derive all the optical constants from the *updated* real $\varepsilon^{\mathrm{re}}(\omega)$ and imaginary $\varepsilon^{\mathrm{im}}(\omega)$ parts of this frequency-dependent dielectric tensor.

[7] With only one exception in the case of PdN(24), where we used a less dense $\mathbf{k}$ mesh and performed single shot G_0W_0 calculations. See Sec. 10.2.

Part III

Results, Discussions and Conclusions

10. Results and Discussions

In this chapter, the obtained results are presented and discussed within the framework of the introduced theoretical approaches (Part I) and characterization methods (Part II).

10.1 Reference Systems

By *reference systems* we mean those systems which their energies are required to calculate cohesive energy (Eq. 7.1.2) and formation energy (Eq. 7.5.3) of the TMN different phases. Namely, these are the *isolated atoms*, the *nitrogen dimer* and the *elemental crystalline metals*. Methods of calculating their energies are described in Sections 7.1 and 7.5.

10.1.1 Isolated Atom

The obtained energies for the non-spherical spin-polarized isolated atomic systems are

```
N     -3.1247041 eV
Pd    -1.4776848 eV
Pt    -.60627956 eV
Cu    -.24231365 eV
Ag    -.33908628 eV
Au    -.28759991 eV
Zn    -.16458042 eV
```

These values are considered as corrections to the energies determined by VASP, and should be compared with those calculated by the VASP authors [154].

10.1.2 Molecular Nitrogen

Obtained cohesive and structural energies of the gaseous diatomic molecular nitrogen ($E_{\text{coh}}(\text{N}_2^{\text{gas}})$) are given in Table 10.1 and compared with experiment and with previous calculations therein. The source of the difference between theory and experiment, and the consequence of that, are

touched in Subsection 10.4.4.

Table 10.1: Calculated and experimental cohesive energy $E_{\text{coh}}(eV)$ and bond length $d(\text{Å})$ of the gaseous diatomic molecular nitrogen (N_2^{gas}). The presented data are of the current work (*Pres.*), experimentally reported (*Expt.*) and of previous calculations (*Comp.*).

	Pres.	Expt.	Comp.
$E_{\text{coh}}(eV)$	-10.392	$-(9.797658 \pm 0.0061149)$[a]	10.49[b], 11.75[c], 11.57[d], 10.69[e]
$d(\text{Å})$	1.113	(1.0976 ± 0.0002)[6]	1.102[b], 1.085[c], 1.095[d], 1.095[e]

[a] This bond strength in nitrogen diatomic molecule is taken from Ref. [159, p. 9:55] where it is given there as $(945.33 \pm 0.59$ KJ/mol) with positive sign convention and at $298\ K$. In p. 9:76 of the same reference, the force constant for bond stretching in nitrogen diatomic molecule is given to be 22.95 N/cm.
[b] Ref. [218], PBE(GGA)-LAPW, with spherical ground-state density of the N free atom.
[c] Ref. [218], LDA-PP, with spherical ground-state density of the N free atom.
[d] Ref. [218], LDA-LAPW, with spherical ground-state density of the N free atom.
[e] Ref. [218], PBE(GGA)-PP, with spherical ground-state density of the N free atom.
[f] Ref. [239, p. S7].

10.1.3 Elemental Crystalline Metals

Structural and energetic properties of the elemental crystalline metals are required to study the effect of nitridation on these pure elemental crystalline metals. Therefore, we present our obtained equilibrium properties of each metal in the first row of the table that includes our obtained equilibrium properties of the corresponding TMN. As a benchmark for the accuracy of the rest of the calculations, we always make comparison with experiment and with previous calculations. Within the accuracy of the employed calculation methods, excellent agreement between our findings and experiment and previous calculations usually achieved.

The energy-volume EOS curves of these metals are displayed in Fig. 10.1. It should be noted that we used the experimental value $c/a = 1.856$ for bulk Zn, however, this ratio may change slightly when Zn is prepared in form of a thin film [240, p. 225].

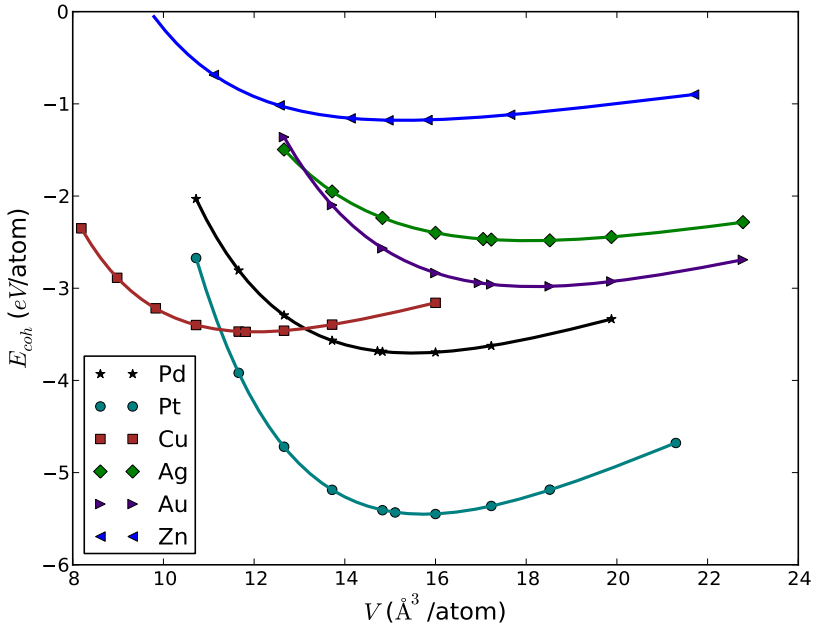

Figure 10.1: (Color online.) Cohesive energy $E_{\text{coh}}(eV/\text{atom})$ versus atomic volume V (Å^3/atom) of the elemental crystalline metals Pd, Pt, Cu, Ag, Au and Zn. Zn is in the hcp A3 structure, while the rest are in the fcc A1 structure.

10.2 Palladium Nitrides

Cohesive energy E_{coh} versus atomic volume V_0 equation of state (EOS) for the considered modifications of Pd_3N, PdN and PdN_2 are displayed graphically in Figs. 10.2a, 10.2b and 10.2c, respectively. The corresponding calculated equilibrium structural, energetic and mechanical properties of these twenty phases and of Pd(A1)are presented in Table 10.2. Modifications in this table are ordered in the same way as in Table 5.1. Our results are compared with experiment and with previous calculations. In the latter case, the calculations methods and the XC functionals are indicated in the Table footnotes whenever possible.

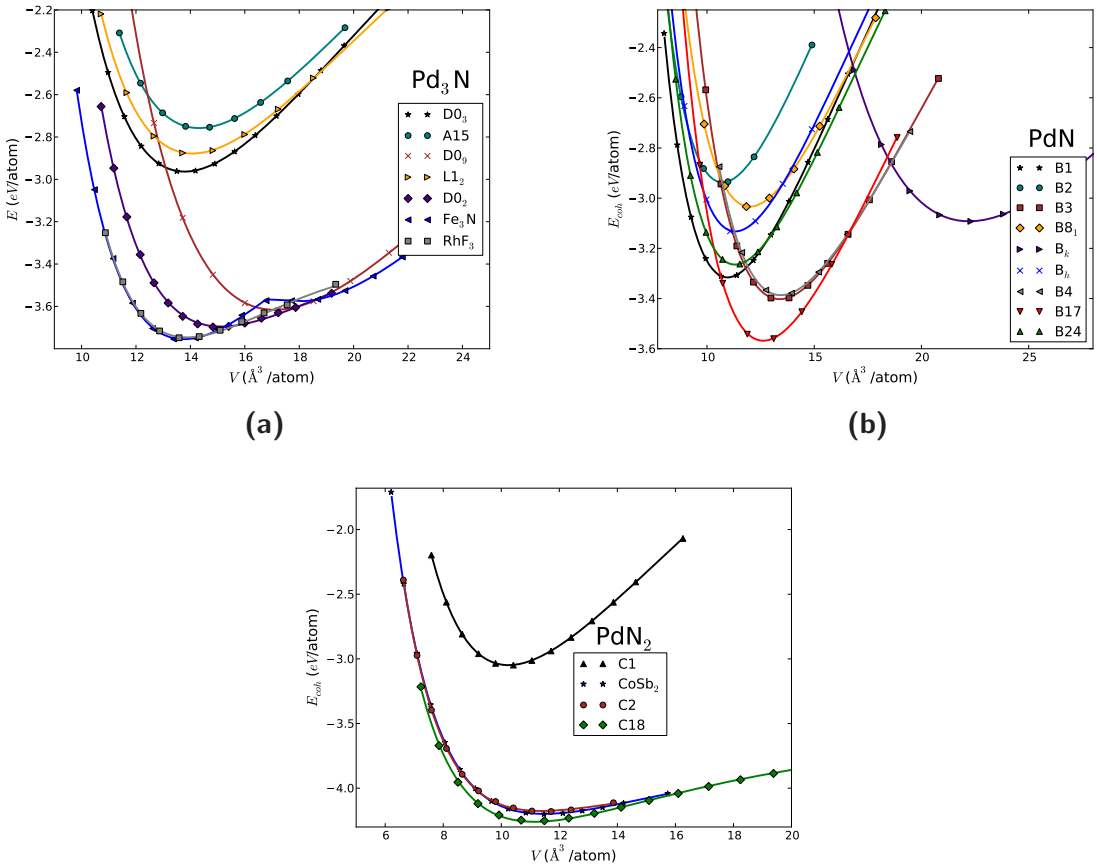

Figure 10.2: (Color online.) Cohesive energy $E_{\rm coh}(eV/{\rm atom})$ versus atomic volume V (Å^3/atom) for: **(a)** Pd_3N in seven different structural phases; **(b)** PdN in nine different structural phases; and **(c)** for PdN_2 in four different structural phases.

Table 10.2: Calculated and experimental zero-pressure properties of Pd(A1) and of the twenty studied phases of Pd_3N, PdN and PdN_2**:** Lattice constants (a(Å), b(Å), c(Å), $\alpha(^\circ)$ and $\beta(^\circ)$), atomic volume V_0(Å^3/atom), cohesive energy $E_{\text{coh}}(eV/\text{atom})$, bulk modulus $B_0(GPa)$ and its pressure derivative B_0', and formation energy $E_{\text{f}}(eV/\text{atom})$. The presented data are of the current work (*Pres.*), experimentally reported (*Expt.*) and of previous calculations (*Comp.*).

Structure		$a(\AA)$	$b(\AA)$	$c(\AA)$	$\alpha(^\circ)$ or $\beta(^\circ)$	$V_0(\AA^3/\text{atom})$	$E_{\text{coh}}(eV/\text{atom})$	B_0(GPa)	B_0'	$E_f(eV/\text{atom})$
						Pd				
A1	*Pres.*	3.957	–	–	–	15.49	−3.703	163.626	5.549	
	Exp.	3.8900[a]	–	–	–	14.716[b]	−3.89[c]	180.8[c], 184[d]	5.42[e]	
	Comp.	3.85[f,g]	–	–	–		−5.06[h],	212[f], 220[g]	5.50[i], 6.40[j],	
			–	–	–		−3.74[k,l]		5.29[m]	
						Pd_3N				
D0$_3$	*Pres.*	6.043	–	–	–	13.79	−2.965	162.895	5.353	1.111
A15	*Pres.*	4.857	–	–	–	14.32	−2.758	148.123	5.321	1.318
D0$_9$	*Pres.*	4.089	–	–	–	17.09	−3.617	132.499	5.255	0.459
L1$_2$	*Pres.*	3.834	–	–	–	14.09	−2.880	148.697	5.402	1.196
D0$_2$	*Pres.*	7.828	–	–	–	14.99	−3.698	111.276	9.361	0.378
ϵ-Fe$_3$N	*Pres.*	5.135	–	4.785	–	13.66	−3.758	168.259	8.694	0.318
RhF$_3$	*Pres.*	5.627	–	–	$\alpha = 54.640$	13.78	−3.749	130.415	9.837	0.327
						PdN				
B1	*Pres.*	4.444	–	–	–	10.97	−3.317	207.787	4.978	1.132
	Comp.	4.145[n]	–	–	–		−4.585[o]			0.400[q]
		4.33[r]	–	–	–		−11.90[r]	297.67[r]	4.15[r]	
			–	–	–		−4.027[p]			
B2	*Pres.*	2.779	–	–	–	10.73	−2.947	210.200	4.931	1.502
	Comp.	2.71[r]	–	–	–		−12.25[r]	251.03[r]	4.70[r]	
B3	*Pres.*	4.748	–	–	–	13.38	−3.404	167.804	5.015	1.045
	Comp.	4.67[r]	–	–	–		−8.89[r]	192.33[r]	4.07[r]	
B8$_1$	*Pres.*	3.416	–	4.751	–	12.00	−3.034	187.954	5.021	1.415
B$_k$	*Pres.*	3.378	–	8.986	–	22.20	−3.092	88.897	4.830	1.357
B$_h$	*Pres.*	2.992	–	2.921	–	11.32	−3.135	201.682	5.037	1.314
B4	*Pres.*	3.360	–	5.503	–	13.45	−3.387	164.169	4.978	1.062
	Comp.	3.37[r]	–	5.26[r]	–		−11.43[r]	171.34[r]	4.63[r]	
B17	*Pres.*	3.061	–	5.389	–	12.62	−3.570	190.426	4.993	0.879
B24	*Pres.*	4.173	4.427	4.898	–	11.31	−3.265	197.566	4.997	1.184
						PdN_2				
C1	*Pres.*	4.975	–	–	–	10.26	−3.050	221.734	4.809	1.648
C2	*Pres.*	5.169	–	–	–	11.51	−4.181	68.462	5.611	0.517
	Comp.	4.975[s]	–	–	–	10.267[s]		135[s]		
		4.843[t]	–	–	–			156[t]	9.48[t]	
C18	*Pres.*	3.173	4.164	5.082	–	11.19	−4.254	76.615	6.102	0.444
	Comp.	3.911[s]	4.975[s]	3.133[s]	–	10.333[s]	–	100[s]		
CoSb$_2$	*Pres.*	5.608	5.304	9.630	$\beta = 151.225$	11.49	−4.200	71.792	6.511	0.498
	Comp.	5.071[s]	5.005[s]	5.071[s]	–	10.433[s]		93[s]		

Notes to Table 10.2 :

[a] Ref. [240]: This is an average of 21 experimental values, at $20\ ^{\circ}C$, with a deviation ± 0.0007 Å.

[b] Ref. [240]: At $20^{\circ}C$.

[c] Ref. [172]: Cohesive energies are given at $0\ K$ and 1 atm $= 0.00010$GPa; while bulk moduli are given at room temperature.

[d] Ref. (25) in [219]: at room temperature.

[e] See Refs. (8)–(11) in [219].

[f] Ref. [241]. LAPW-TB.

[g] Ref. [241]. LAPW-LDA.

[h] Ref. [242]: PAW-LDA.

[i] Ref. [219]: Using the so-called method of transition metal pseudopotential theory; a modified form of a method proposed by Wills and Harrison to represent the effective interatomic interaction.

[j] Ref. [219]: Using a semi-empirical estimate based on the calculation of the slope of the shock velocity *vs.* particle velocity curves obtained from the dynamic high-pressure experiments. The given values are estimated at $\sim 298\ K$.

[k] Ref. [242]: PAW-PW91.

[l] Ref. [242]: PAW-PBE.

[m] Ref. [219]: Using a semi-empirical method in which the experimental static $P - V$ data are fitted to an EOS form where B_0 and B_0' are adjustable parameters. The given values are estimated at $\sim 298\ K$.

[n] Ref. [10]: Estimated by extrapolation of the (experimental) average volume per atom Ω_{MN} for nitrides of other $4d$ transition metals.

[o] Ref. [10]: Using the linear-muffin-tin-orbitals (LMTO) method and the local-spin-density approximation (LSDA).

[p] Ref. [10]: (± 0.150) Semi-empirical calculations.

[q] Ref. [10]: This is enthalpy of formation (± 0.145) from Pd and N in their stable modifications at one atmosphere and $T = -298.15\ K$.

[r] Ref. [193]: Using separable norm-conserving pseudopotentials within LDA.

[s] Ref. [243]: Using the Vanderbilt ultrasoft pseudopotential within GGA.

[t] Ref. [244]: Using PAW within LDA.

To compare and to deeper analyze the obtained equilibrium properties of the three stoichiometries series with respect to one another, the calculated equilibrium properties are depicted graphically in Fig. 10.3. All quantities in this figure are given relative to the corresponding ones of Pd(A1) given in Table 10.2. In this way, one will be able to investigate the effect of nitridation on the

parent crystalline Pd as well [1].

10.2.1 EOS and Relative Stabilities

In Fig. 10.2a, the energy-volume EOSs of the seven considered Pd_3N modifications are displayed. This figure, and the values of the equilibrium cohesive energy $E_{\rm coh}$ (Table 10.2 and Fig. 10.3) reveal that the Fe_3N structure (of the Ni_3N) is the most energetically favored modification, as we expected. However, the rhombohedric RhF_3 phase has a very similar EOS curve before and around the equilibrium, with very close $E_{\rm coh}$ value to that of Fe_3N. Cubic systems ($D0_3$, A15, $D0_9$, $L1_2$ and $D0_2$) seem not to be energetically competing in this stoichiometry.

It is clear that the simple tetragonal structure of cooperite (B17) would be the energetically most stable phase of PdN (Fig. 10.2b). To the best of our knowledge, this structure has not been considered for PdN in any earlier work, though it was theoretically predicted to be the ground-state structure of the nitrides of the elements surrounding Pd in the periodic table: PtN [3, 30], CuN [3], AgN [2], and AuN [6]. Nevertheless, Fig. 10.3 shows clearly that no PdN phase, even PdN(B17), has a tendency to lower the cohesive energy of the parent metal.

In Ref. [193] the $E(V)$ EOS for PdN in the B1, B2, B3 and B4 structures was studied. Within this parameter sub-space, the relative stabilities arrived at in that work agree very well with ours. However, their obtained $E_{\rm coh}$ are more than twice the values we obtained, and the bulk moduli differ considerably (see Table 10.2)!

In the studied parameter sub-space of PdN_2, the marcasite structure (C18) is the most energetically stable. The relative stability of C2 and $CoSb_2$ phases may be compared with Crowhurst *et al.* [20] who found PdN_2 in the baddeleyite structure (which is very close to $CoSb_2$ structure [198]) to be more stable than PdN_2(C2).

From a combined theoretical and experimental investigation, Åberg *et al.* [245] showed that for PdN_2(C2) both the electronic and the structural degrees of freedom have a strong pressure dependence. They claimed that the EOS *cannot* be accurately described within the GGA. Earlier calculations showed that PdN_2(C2) is very soft (see Ref. 22 in [20]). These two facts may explain the difficulty we found in relaxing this structure as well as they may explain the considerable differences found with and among the earlier reported structural properties.

[1] In Table 10.2, our computed properties of the elemental Pd are compared with experiment and with previous calculations as well. This may benchmark the accuracy of the rest of our calculations.

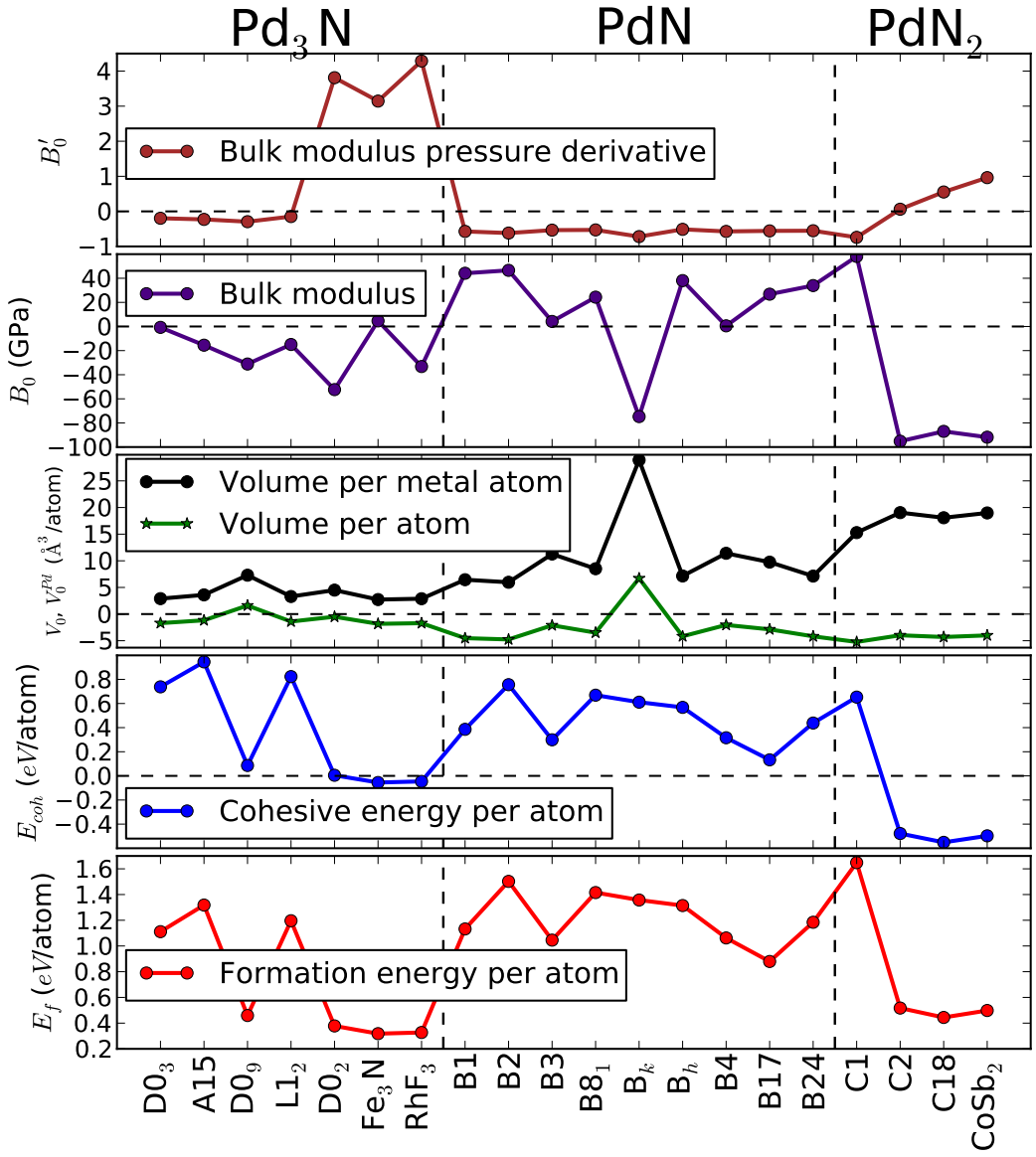

Figure 10.3: (Color online.) Calculated equilibrium properties of the twenty studied phases of palladium nitrides. All quantities are given relative to the corresponding ones of the *fcc* crystalline elemental palladium given in the first row of Table 10.2. The vertical dashed lines separate between the different stoichoimetries.

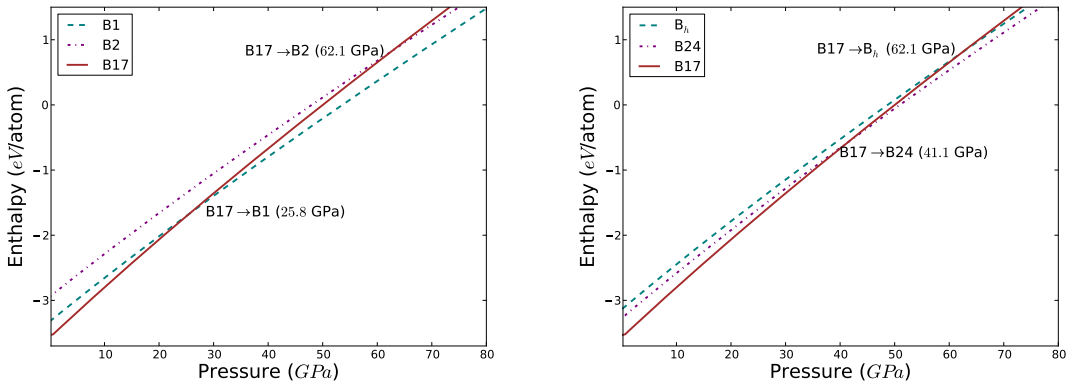

Figure 10.4: (Color online.) Enthalpy *vs.* pressure for some PdN modifications in the region where: B17→B1 and B17→B2 (top) and B17→B_h and B17→B24 (bottom) phase transitions occur.

10.2.2 Volume per Atom and Lattice Parameters

From Fig. 10.3 one can see clearly that except $Pd_3N(D0_9)$ and $PdN(B_k)$, all phases tend to lower the *volume per atom* of their parent metal. The metal-metal bond length, as represented by the volume per *metal* atom V_0^{Pd}, increases (on average) in the direction of increasing nitrogen content and decreasing structural symmetry.

10.2.3 Pressure-Induced Phase Transitions

Enthalpy-pressure relations for PdN in some of the considered structures are displayed in Figs. 10.4. A point at which enthalpies $H = E_{\rm coh}(V) + PV$ of two structures are equal defines the transition pressure P_t, where transition from the phase with higher enthalpy to the phase with lower enthalpy may occur.

Some possible transitions and the corresponding P_t's are depicted in Fig. 10.4. From the top subfigure, it is clear that, in this parameter sub-space, B17 structure is preferred at pressures below ~ 25 GPa, while B1 structure, the most popular structure for transition-metal mono-nitrides, is favoured at higher pressures. The bottom subfigure reveals that B24 is favored over B17 and B_h at pressures higher than 41 GPa.

10.2.4 Bulk Modulus and its Pressure Derivative

Fig. 10.3 shows that the bulk moduli of the Pd_3N phases, except $Pd_3N(Fe_3N)$, tend to be lower than that of Pd, while 1:1 nitrides, except (B_k) tend to increase it. Despite the lower V_0 and the lower $E_{\rm coh}$ possessed by the last three PdN_2 phases, they have ~ 100 GPa lower B_0 than their parent metal. This can be understood only in terms of the increase in the metal-metal bond length (represented by $V_0^{\rm Pd}$).

Upon application of external pressure, the first four Pd_3N phases, all PdN phases and PdN_2(C1) phase tend to lower their B_0. PdN_2(C2) has the same sensitivity of its parent metal. PdN_2(C18 and $CoSb_2$) tend to increase their B_0. Pd_3N($D0_2$, Fe_3N and RhF_3), however, are far more sensitive to external pressure, and their bulk moduli tend to increase significantly under pressure.

10.2.5 Thermodynamic Stability

Interestingly, Fig. 10.3 reveals that Pd_3N(Fe_3N and RhF_3) phases have lower formation energy than all PdN and PdN_2. That is, Pd_3N(Fe_3N and RhF_3) are thermodynamically favored over PdN and PdN_2. Nevertheless, the PdN_2 modifications, except C1, have significantly lower cohesive energy than the most favored Pd_3N phases. The numerical values of the formation energy (Table 10.2) and and their graphical representation (Fig. 10.3) reveal that it may be relatively harder to form a 1:1 palladium nitride.

10.2.6 Electronic Properties

With the Fermi surface crossing the partly occupied bands, it is evident from Figs. 10.6 and 10.5 that Pd_3N(Fe_3N and RhF_3) are metals. In both cases, the strong Pd(d)-N(p) mixture is in the range ($-7.7 \sim -5.7\ eV$). The Pd(d)-N(p) hybridization in the range ($-5 \sim E_F\ eV$) has very little contribution from the N(p) states.

The DFT(GGA) calculated electronic band structures for PdN(B17), PdN(B24) and PdN_2(C18) and their corresponding total and partial DOS are displayed in Figs. 10.7, 10.8 and 10.9, respectively. All phases show clear metallic feature, though PdN_2(C18) has a very low TDOS around Fermi level E_F coming mainly from the d states of the Pd atoms.

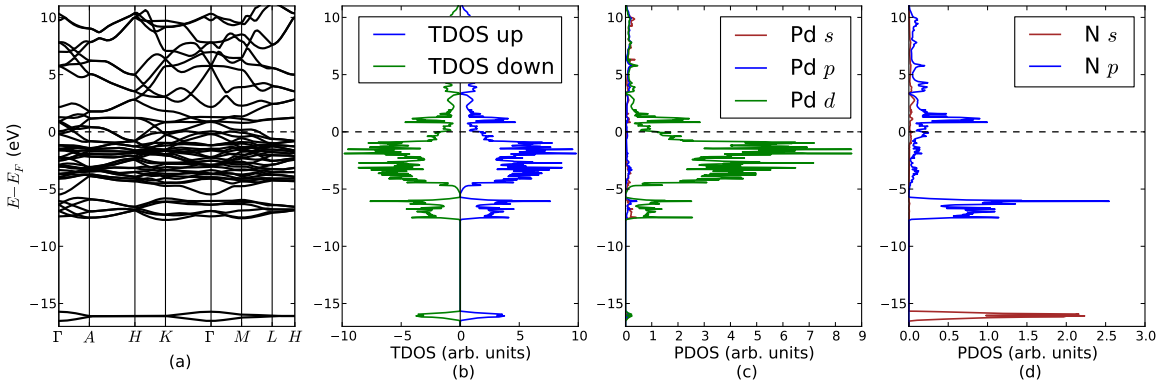

Figure 10.5: (Color online.) DFT calculated electronic structure for Pd_3N in the Fe_3N structure: **(a)** band structure along the high-symmetry $\mathbf{k}$-points (see Table 8.1); **(b)** spin-projected total density of states (TDOS); **(c)** partial density of states (PDOS) of Pd(s, p, d) orbitals in Pd_3N; and **(d)** PDOS of N(s, p) orbitals in Pd_3N.

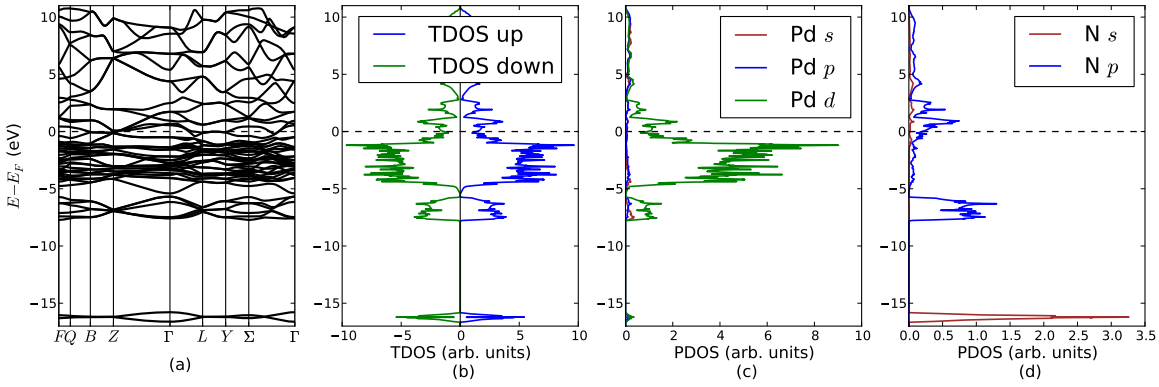

Figure 10.6: (Color online.) DFT calculated electronic structure for Pd_3N in the RhF_3 structure: **(a)** band structure along the high-symmetry $\mathbf{k}$-points (see Table 8.1); **(b)** spin-projected total density of states (TDOS); **(c)** partial density of states (PDOS) of Pd(s, p, d) orbitals in Pd_3N; and **(d)** PDOS of N(s, p) orbitals in Pd_3N.

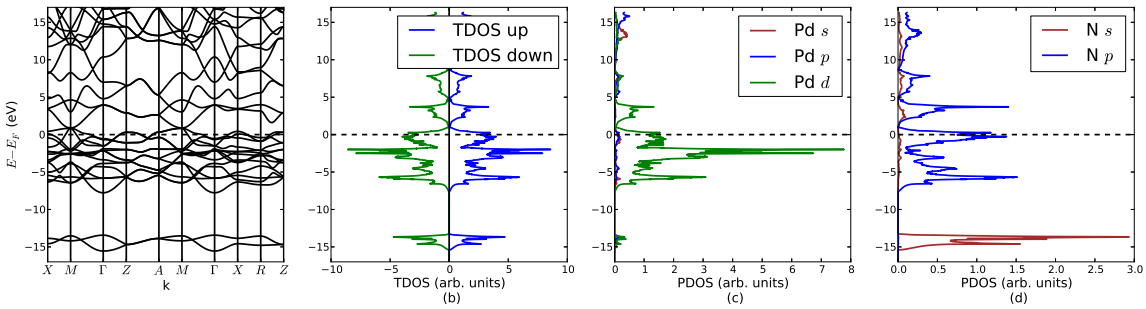

Figure 10.7: (Color online.) DFT calculated electronic structure for PdN in the B17 structure: **(a)** band structure along the high-symmetry $\mathbf{k}$-points (see Table 8.1); **(b)** spin-projected total density of states (TDOS); **(c)** partial density of states (PDOS) of Pds, p, d) orbitals in PdN; and **(d)** PDOS of N(s, p) orbitals in PdN.

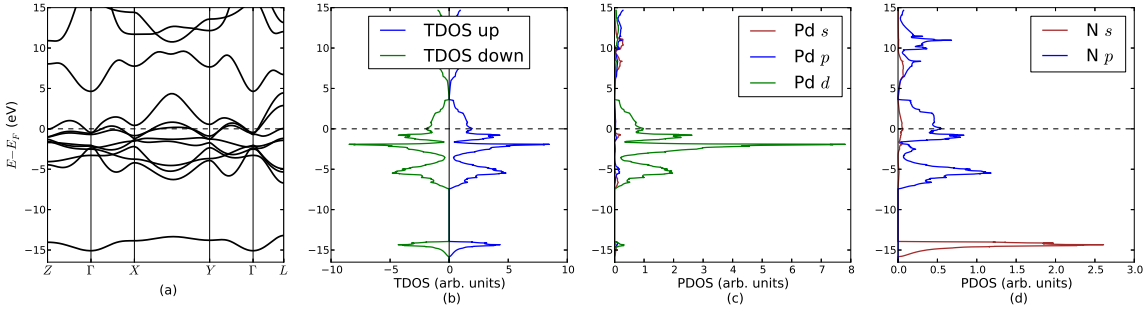

Figure 10.8: (Color online.) DFT calculated electronic structure for PdN in the B24 structure: **(a)** band structure along the high-symmetry $\mathbf{k}$-points (see Table 8.1); **(b)** spin-projected total density of states (TDOS); **(c)** partial density of states (PDOS) of Pd(s, p, d) orbitals in PdN; and **(d)** PDOS of N(s, p) orbitals in PdN.

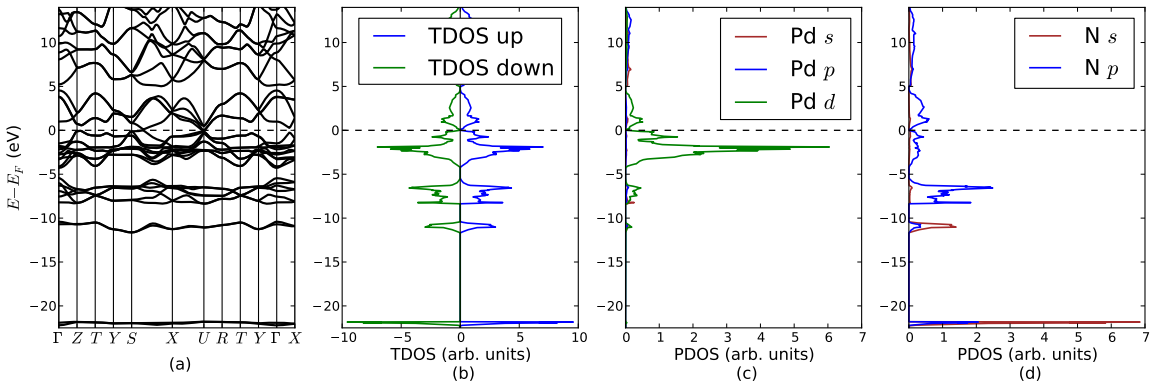

Figure 10.9: (Color online.) DFT calculated electronic structure for PdN_2 in the C18 structure: **(a)** band structure along the high-symmetry $\mathbf{k}$-points (see Table 8.1); **(b)** spin-projected total density of states (TDOS); **(c)** partial density of states (PDOS) of Pd(s, p, d) orbitals in PdN_2; and **(d)** PDOS of N(s, p) orbitals in PdN_2.

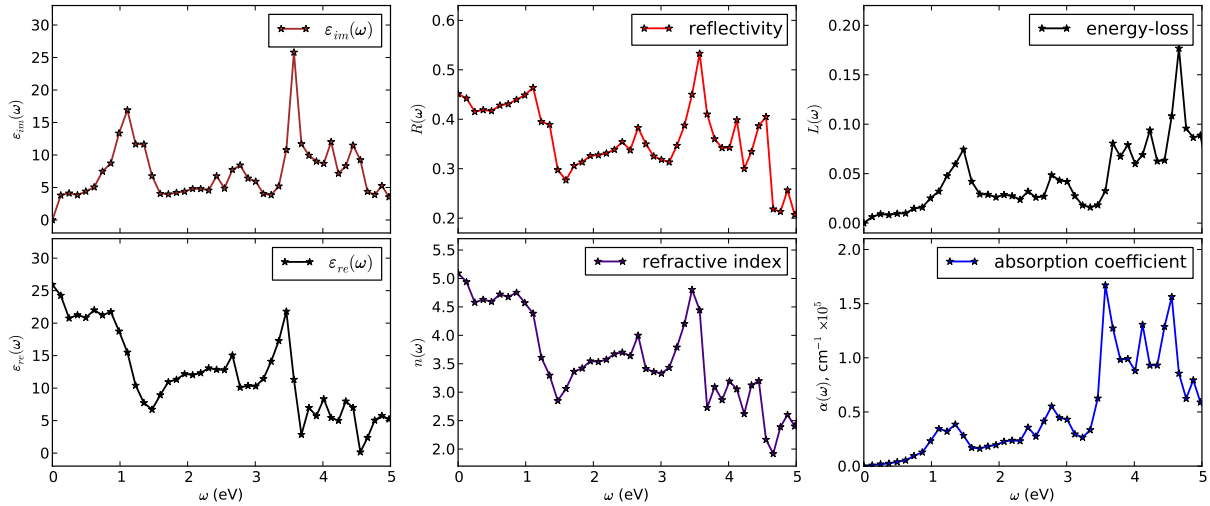

Figure 10.10: (Color online.) The GW calculated frequency-dependent optical spectra of PdN(B24): **(a)** the real $\varepsilon_{\text{re}}(\omega)$ and the imaginary $\varepsilon_{\text{im}}(\omega)$ parts of the dielectric function $\varepsilon_{\text{RPA}}(\omega)$; **(b)** reflectivity $R(\omega)$ and transmitivity $T(\omega)$; **(c)** refraction $n(\omega)$ and extinction $\kappa(\omega)$ coefficients; and **(d)** absorption coefficient $\alpha(\omega)$. The shaded area highlights the optical region.

10.2.7 Optical Properties

Fig. 10.10 displays the real and the imaginary parts of $\varepsilon_{\text{RPA}}(\omega)$ for PdN(B24) and the corresponding derived optical constants within the optical region $[\sim (3.183 - 1.655)\ eV \equiv (390 - 750)\ nm]$. With its non-zero value, it is clear from the absorption coefficient $\alpha\,(\omega)$ spectrum that our G_0W_0 calculations confirm that B24 is a metallic phase of PdN.

10.3 Platinum Nitrides

Cohesive energy E_{coh} versus atomic volume V_0 equation of state (EOS) for the different phases of Pt_3N, PtN_2 and PtN are displayed graphically in Fig. 10.11a, Fig. 10.11b and Fig. 10.11c, respectively. The corresponding obtained equilibrium structural parameters and energetic and elastic properties are presented in Table 10.3. In this table, as well as in Fig. 10.12, structures are first grouped according to the nitrogen content, starting with the stoichiometry with the lowest nitrogen content Pt_3N, followed by the 1:1 series and ending with the nitrogen-richest PtN_2 group. Within each series, structures are ordered according to their structural symmetry, starting from the highest symmetry (i.e. the highest space group number) to the least symmetry.

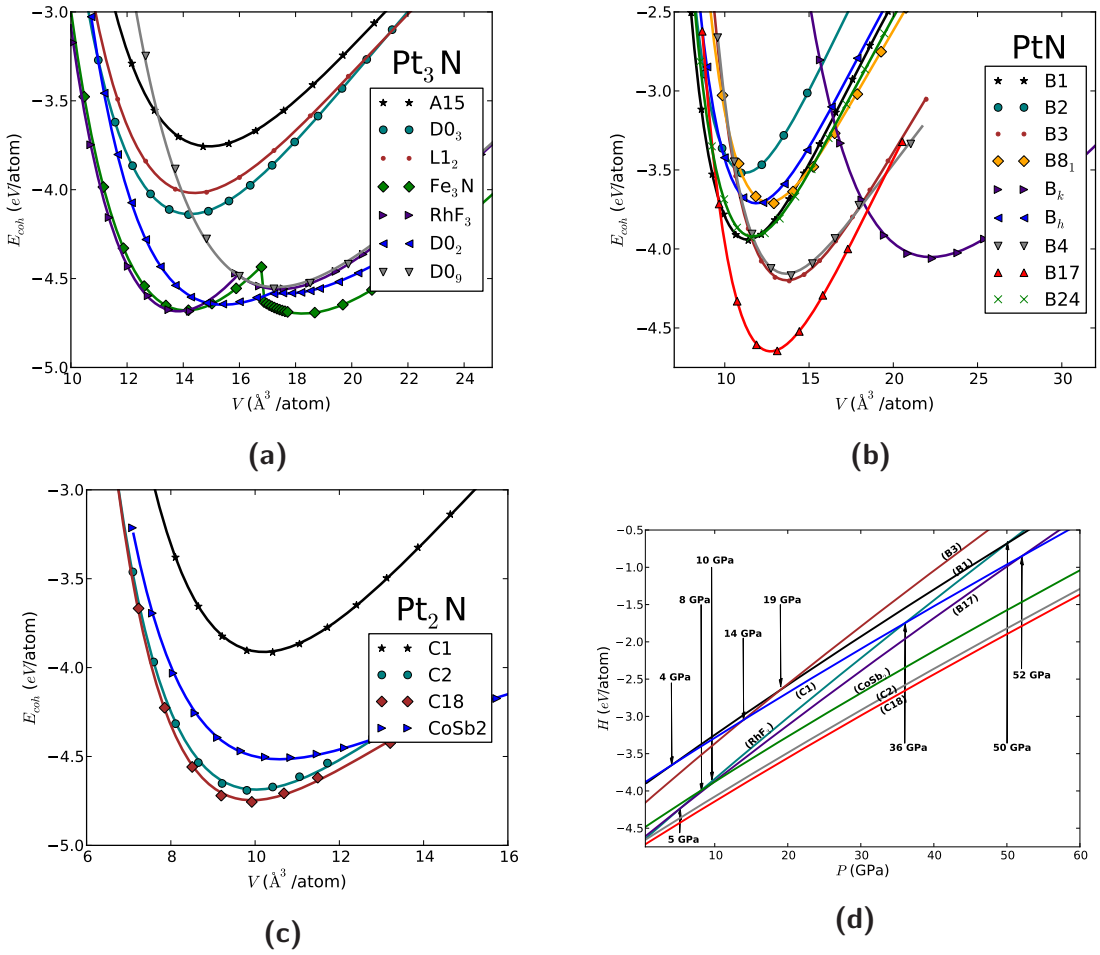

Figure 10.11: (Color online.) Cohesive energy $E_{\text{coh}}(eV/\text{atom})$ versus atomic volume V (Å^3/atom) for: **(a)** Pt_3N in seven different structural phases; **(b)** PtN in nine different structural phases; and **(c)** for PtN_2 in four different structural phases. **(d)** Enthalpy H *vs.* pressure P equation of state (EOS) for the most favorable Pt_3N phase (RhF_3), the three proposed PtN modifications (B1, B3 and B17), and the four considered PtN_2 structures in the present work (C1, C2, C18 and $CoSb_2$). The arrows indicate the pressures at which curves cross each other.

Whenever possible, our results are compared with experiment and with previous calculations. In the latter case, the calculations methods and the XC functionals are indicated in the Table footnotes. To study the effect of nitridation on the elemental Pt(A1) and to easly compare the properties of these phases relative to each other, the calculated equilibrium properties are displayed relative to the corresponding ones of Pt(A1) in Fig. 10.12.

Table 10.3: The calculated (*Pres.*) zero-pressure properties of the platinum nitrides and the results of previous calculations (*Comp.*). The available experimental data are given in the last row. Table footnotes are in the next page.

		$a(\AA)$	$b(\AA)$	$c(\AA)$	$\alpha(^\circ)$ or $\beta(^\circ)$	$V_0(\text{Å}^3/\text{atom})$	$E_{\text{coh}}(eV/\text{atom})$	$B_0(\text{GPa})$	B_0'	$E_f(eV/\text{atom})$
					Pt					
A1	*Pres.*	3.978	–	–	–	15.74	−5.451	242.999	5.486	
	Expt.	3.9233[a]	–	–	–	15.097[b]	−5.84[c]	278.3[c], 280[d]	5.18[e]	
		3.924[ee]	–	–	–			249[ee]	5.23[ee]	
	Comp.	3.90[g], 3.890[s],	–	–	–		−7.04[h],	305[g], 320[s],	5.16[k], 5.30[l],	
		3.967[t], 3.966[cc]	–	–	–		−5.53[j],	249[cc], 242[dd],	5.23[cc], 5.83[dd],	
		3.981[gg]	–	–	–		−3.74[i]	244.18[gg], 238[t]	5.25[m], 5.7[gg]	
					Pt_3N					
$D0_3$	*Pres.*	6.106	–	–	–	14.23	−4.140	218.097	5.282	1.247
A15	*Pres.*	4.924	–	–	–	14.92	−3.759	194.136	5.266	1.628
$D0_9$	*Pres.*	4.114	–	–	–	17.41	−4.558	167.839	5.241	0.829
$L1_2$	*Pres.*	3.863	–	–	–	14.41	−4.021	205.279	5.472	1.366
$D0_2$	*Pres.*	7.875	–	–	–	15.26	−4.644	147.174	12.098	0.743
ϵ-Fe_3N	*Pres.*	5.680	–	5.293	–	18.49	−4.713	217.035	6.779	0.674
RhF_3	*Pres.*	5.463	–	–	$\alpha = 58.640$	13.97	−4.688	224.419	5.412	0.699
					PtN					
B1	*Pres.*	4.495	–	–	–	11.35	−3.945	230.869	5.059	1.378
	Comp.	4.45[x], 4.50[y],	–	–	–			232[x], 230[y], 288[z]		
		4.471[cc], 4.41[z]	–	–	–	10.66[ff]		251[cc], 242[dd], 294[ff]	4.00[cc], 4.78[dd]	1.365[cc]
		4.491[gg]	–	–	–			229.76[gg]	4.9[gg]	0.375[hh]
B2	*Pres.*	2.819	–	–	–	11.20	−3.522	238.187	5.070	1.801
	Comp.	2.818[gg]	–	–	–			234.88[gg]	5.1[gg]	
B3	*Pres.*	4.782	–	–	–	13.67	−4.203	193.466	5.031	1.120
	Comp.	4.7217[n], 4.8250[o],	–	–	–			243.3[n], 196.3[o],	5.1[gg],	
		4.6833[p], 4.7889[q],	–	–	–			271.9[p], 192.7[q],		0.95[aa]
		4.692[s], 4.780[t],	–	–	–			244[s], 194[t], 213[cc],	4.00[cc]	1.1[cc]
		4.80[x,y], 4.70[z],	–	–	–			192[x], 190[y], 232[z],	3.62[dd]	0.21[hh]
		4.779[gg], 4.8114[r],	–	–	–			190.61[gg], 184[r],		
		4.760[cc], 4.699[hh]	–	–	–			217[dd]		
$B8_1$	*Pres.*	3.482	–	4.843	–	12.71	−3.713	210.165	4.945	1.610
B_k	*Pres.*	3.378	–	8.986	–	22.20	−4.061	108.968	4.553	1.262
B_h	*Pres.*	3.039	–	2.966	–	11.86	−3.716	222.279	5.014	1.607
B4	*Pres.*	3.382	–	5.539	–	13.72	−4.171	190.130	5.033	1.152
	Comp.	3.386[gg]	–	5.529[gg]	–			191.06[gg]	4.7[gg]	
B17	*Pres.*	3.069	–	5.403	–	12.72	−4.652	235.041	5.018	0.671
	Comp.	3.323[hh]	–	4.579[hh]	–					
B24	*Pres.*	4.216	4.472	4.948	–	11.66	−3.928	226.608	5.153	1.395
	Comp.[*]	3.972[hh]	3.977[hh]	6.022[hh]	–			270[hh]		0.085[hh]
					PtN_2					
C1	*Pres.*	4.963	–	–	–	10.19	−3.918	263.295	4.717	1.363
	Comp.	4.9428[n], 5.0403[o],	–	–	–			322.1[n], 267.2[o],	4.00[cc]	1.167[aa]
		4.866[s], 4.958[t],	–	–	–			316[s], 264[t],	4.73[dd]	1.317[dd]
		4.939[dd]	–	–	–			269[cc], 260[dd]		
C2	*Pres.*	4.912	–	–	–	9.882	−4.689	226.779	6.893	0.592
	Comp.	4.87[aa]	–	–	–	9.12[ff]		305[cc],	4.00[cc],	0.267[aa],
		4.848[cc], 4.874[ii]	–	–	–	9.65[ii]		285[dd], 300[ii]	5.50[dd]	0.64[cc],
			–	–	–					0.24[bb],
			–	–	–					0.212[ii]
C18	*Pres.*	3.036	3.984	4.862	–	9.800	−4.755	244.320	7.938	0.526
	Comp.	3.778[ii]	4.880[ii]	3.208[ii]	–	9.827[ii]		286[ii]		0.249[ii]
$CoSb_2$	*Pres.*	5.460	5.163	9.374	$\beta = 151.225$	10.60	−4.508	118.594	6.619	0.773
	Comp.	4.950[ii]	4.880[ii]	4.950[ii]	99.50[ii]	9.827[ii]		289[ii]		0.248[ii]
					Experiment					
		(4.8032 ± 5)[u,v],	–	–	–			(372 ± 5)[u],	4.0[u],	
		4.8041(2)[w]	–	–	–			(354 ± 5)[v]	5.26[v]	

Notes to Table 10.3 :

[a] Ref. [240]: This is an average of 23 experimental values (with a deviation ± 0.0007 Å), at room temperature.

[b] Ref. [240]: at room temperature.

[c] Ref. [172]: Cohesive energies are given at $0\ K$ and 1 atm $= 0.00010$ GPa; while bulk moduli are given at room temperature.

[d] Ref. (25) in [219]: at room temperature.

[e] See Refs. (8)–(11) in [219].

[g] Ref. [241]: using the full-potential linearized augmented plane waves (LAPW) method within LDA.

[h] Ref. [242]: using the projector augmented wave (PAW) method within LDA.

[i] Ref. [242]: using the projector augmented wave (PAW) method within GGA(PW91).

[j] Ref. [242]: using the projector augmented wave (PAW) method within GGA(PBE).

[k] Ref. [219]: using the so-called method of transition metal pseudopotential theory; a modified form of a method proposed by Wills and Harrison to represent the effective interatomic interaction.

[l] Ref. [219]: using a semi-empirical estimate based on the calculation of the slope of the shock velocity *vs.* particle velocity curves obtained from the dynamic high-pressure experiments. The given values are estimated at $\sim 298\ K$.

[m] Ref. [219]: using a semi-empirical method in which the experimental static $P - V$ data are fitted to an EOS form. The given values are estimated at $\sim 298\ K$.

[n] Ref. [26]: using the ultrasoft pseudopotential (USPP) method within LDA. B_0's are calculated from elastic constants.

[o] Ref. [26]: using the ultrasoft pseudopotential (USPP) method within GGA. B_0's are calculated from elastic constants.

[p] Ref. [26]: using the projector augmented wave (PAW) method within LDA. B_0' is set to be 4.

[q] Ref. [26]: using the projector augmented wave (PAW) method within GGA. B_0' is set to be 4.

[r] Ref. [26]: using fully relativistic full-potential linearized augmented plane waves (LAPW) method within GGA.

[s] Ref. [29]: using the full-potential linearized augmented plane waves (LAPW) method within LDA.

[t] Ref. [29]: using the full-potential linearized augmented plane waves (LAPW) method within GGA(PBE).

[u] Ref. [22]: The experimental evolution of the volume with pressure was fitted with a Birch-Murnaghan EOS, but B_0' was set to be 4.

[v] Ref. [22]: The experimental evolution of the volume with pressure was fitted with a Birch-Murnaghan EOS, but $B_{0,\mathrm{Pt}}' = 5.26$ was fixed.

[w] Ref. [22]: From XRD measurements at 0.1 MPa.

[x] Ref. [30]: using the full-potential linearized augmented plane waves (FPLAPW) method within GGA(PBE).

[y] Ref. [30]: using pseudopotentials method within GGA(PBE).

[z] Ref. [30]: using pseudopotentials method within LDA.

[aa] Ref. [25]: using the PAW method within GGA(PW91), but the experimental value of $E_{\mathrm{coh}}(\mathrm{N}_2^{\mathrm{gas}})$ in Eq. 7.5.3 was used.

[bb] Ref. [25]: using the full-potential linear-augmented plane-wave method.

[cc] Ref. [27]: using pseudopotentials method within GGA(PBE).

[dd] Ref. [27]: using pseudopotentials method within GGA(PBE).

[ee] Ref. [246].

[ff] Ref. [28]: using the pseudopotential method within LDA.

[gg] Ref. [194]: using the full potential augmented plane wave plus local orbitals (APW+lo) method within GGA(PBE).

[hh] Ref. [31]: using the Vanderbilt ultrasoft pseudopotentials within LDA. *The data from Ref. [31] are for a face-centered orthorhombic structure (space group Fddd) which is not the same as our studied face-centered orthorhombic B24 structure (space group Fmmm). The listed E_f are w.r.t $E_f(\mathrm{B17})$.

[ii] Ref. [66]: using Vanderbilt USPPs within GGA(PBE). B_0's are calculated from the elastic constants. $E_{\mathrm{coh}}(\mathrm{N}_2^{\mathrm{solid}})$ was used in Eq. 7.5.3 instead of $E_{\mathrm{coh}}(\mathrm{N}_2^{\mathrm{gas}})$.

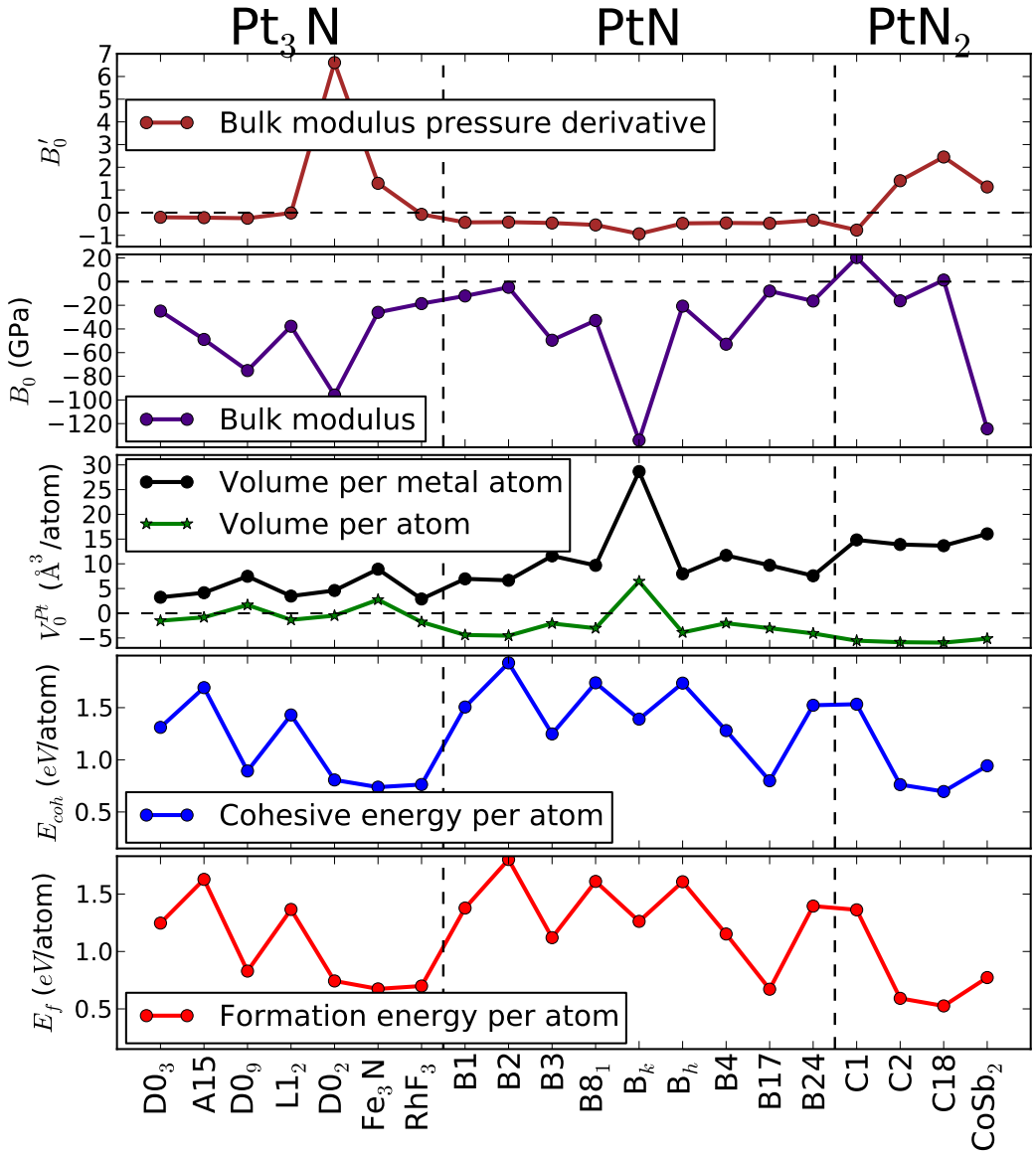

Figure 10.12: (Color online.) Calculated equilibrium properties of the twenty studied phases of platinum nitrides. All quantities are given relative to the corresponding ones of the *fcc* crystalline elemental platinum given in the first row of Table 10.3.

10.3.1 EOS and Relative Stabilities

Fig. 10.11a reveals that Pt_3N in its least symmetric phase, the trigonal (rhombohedric) structure of RhF_3, is the most favorable phase in this series. However, after ~ 15.9 Å^3/atom the EOS of $Pt_3N(RhF_3)$ is almost identical with the EOS of Pt_3N in the simple cubic structure of the anti-ReO_3 ($D0_9$). They share a minimum at $\sim (17.4$ Å^3/atom$, -4.56\ eV)$. Very close to this point, at $\sim (17.23$ Å^3/atom$, -4.59\ eV)$, the EOS of $Pt_3N(D0_2)$ has a kink due to a change in the positions of some Pt ions.

The EOS of $Pt_3N(Fe_3N)$ has two minima located at $(14.11$ Å^3/atom$, -4.697\ eV)$ and $(18.26$ Å^3/atom$, -4.679\ eV)$. Thus, the two minima are very close in energy but, due to the difference in V_0, they correspond to bulk moduli of 222.7 GP and 169.0 GP, respectively. The Pt ions are in the $6g$ Wyckoff positions: $(x,0,0),(0,x,0),(-x,-x,0),(-x,0,\frac{1}{2}),(0,-x,\frac{1}{2})$ and $(x,x,\frac{1}{2})$. Upon ion relaxation of $Pt_3N(Fe_3N)$, atomic positions change from $x \sim \frac{1}{3}$ to $x = \frac{1}{2}$ causing the sudden change in the potential surface (at ~ 16.83 Å^3/atom) as the bulk $Pt_3N(Fe_3N)$ being decompressed (Fig. 10.11a). It may be worth mentioning here that $Ag_3N(Fe_3N)$ [2] and $Cu_3N(Fe_3N)$ [3] were found to behave in a similar manner.

Hence, one of the two minima in the EOS of $Pt_3N(RhF_3)$ is shared with the minimum of the EOS of $Pt_3N(D0_9)$ and the other is shared with one of the two minima of $Pt_3N(Fe_3N)$.

The crossings of the less stable $D0_3$, $L1_2$ and A15 EOS curves with the more stable $D0_9$ EOS at the left side of their equilibria indicates that $D0_9$ would not survive under pressure and that possible pressure-induces phase transitions from the latter phase to the former ones may occur.

Fig. 10.12 shows that the Pt_3N most stable phases may energetically compete with the PtN and PtN_2 most stable ones. However, from the foregoing discussion, it seems that Pt_3N would not have a simple potential surface.

Using the full potential augmented plane wave plus local orbitals (APW+lo) method within GGA(PBE), the energy-volume EOS's for B1, B2, B3 and B4 have been studied by the authors of Ref. [194]. Some of their obtained equilibrium properties are included and referred to in Table 10.3. Within the considered parameter sub-space, our obtained EOS's (Fig. 10.11b), relative stabilities, and equilibrium structural parameters and mechanical properties (Table 10.3) are in excellent agreement with their findings. However, relaxing the c/a parameter, they obtained an additional EOS which lies below all the other considered ones, but its equilibrium B_0 is significantly

smaller.

From Fig. 10.11b, it is evident that PtN(B17) is the energetically most stable phase in the PtN series. The difference in the equilibrium E_{coh} between PtN(B17) and the next (less) stable phase, PtN(B3), is about $0.5\ eV$ (Table 10.3). This difference was found by other researchers [30] to be $0.9-1.05\ eV$. The crossings of the EOS curve of B17 with some of those of less stability at the left side of their equilibria reveals possible pressure-induces phase transitions. To closely investigate these transitions, we plot the corresponding relations between enthalpy $H = E(V) + PV$ and the imposed external pressure P. Possible transitions and the pressures at which they occur are carefully depicted. A point where two $H(P)$ curves (of two modifications with the same chemical stoichiometry [28]) meet represents a phase transition from the phase with the higher H to the one with the lower H [213]. From the $H(P)$ diagrams (not shown here) we found that PtN(B17) would transform to PtN(B1, B2, B_h or B24) at ~ 93 GPa, ~ 143 GPa, ~ 193 GPa or ~ 123 GPa, respectively.

It may be worth to mention here a few points about this B17 structure: (i) It was theoretically predicted to be the ground-state structure of CuN [3], AgN [2], AuN [6] and PdN [7]. (ii) The same foregoing phase PtN-PtN structural pressure-induced transitions have been predicted for PdN, but at relatively smaller pressures in the range $(25.8 \sim 62.1$ GPa$)$ [7]. (iii) B17 is the structure of PtS [179] and PtO [30]. (iv) It was found by other authors to be a possible ground state for PtN [30]. (v) The B17 structure has an fcc Pt sub-lattice (as the synthesized platinum nitride), but it is tetragonal and the sub-lattice are highly distorted ($c/a \approx \sqrt{3}$ versus $c/a = \sqrt{2}$ for ideal fcc), and probably because of this distortion it was rejected by the platinum nitride synthesizers [22]. (vi) Fig. 10.11d that B17 is energetically favorable over B1 and B3 at all pressures. Nevertheless, PtN(B17) was found to be elastically unstable [31].

Assuming 1:1 stoichiometry, the first platinum nitride synthesizers assigned the B3 structure for their product [22]. However, it was shown in the same work that PtN(B3) should break down or transform at pressures above 12 GPa. In agreement with this experimental prediction, Fig. 10.11d shows that PtN(B3) would not survive at pressures above 19 GPa where the B3→B1 phase transition occurs. Other theoretical works also predicted that B1 becomes more favorable than B3 structure above 13.3 GPa [30], ~ 15 GPa [28], 16.5 GPa [30], and 17.6 GPa [30].

Therefore, we support Ref. [30] on the judgment that, unless the PtN(B3) was formed upon

depressurization, its production at $45 - 50$ GPa [22] is questioned. Further, first-principles calculations showed that PtN(B3) is elastically unstable [26, 27, 29], and that it may distort spontaneously to a tetragonal lattice to lower the energy [29].

In the PtN_2 series, we can see from Table 10.3 and from Fig. 10.12 that PtN_2 in the simple orthorhombic structure of FeS_2 marcasite (C18) is the most stable phase, while the face-centered cubic structure of CaF_2 fluorite (C1) is significantly the least favorable structure. Yet, Fig. 10.11d reveals that the latter PtN_2(C1) is more favorable than the proposed PtN(B1, B3 and B17) at pressures above 4 GPa, 14 GPa and 52 GPa, respectively. Others [30] found PtN_2(C1) to be more favorable than PtN(B3) at pressures above 30 GPa.

In contrast to our enthalpy-pressure EOS's in Fig. 10.11d, Chen, Tse and Jiang [66] obtained an $H(P)$ curve for C18 which lies always above the curve for C2 and coincides with the one of $CoSb_2$. They concluded that C2 is the most stable structure among these three modifications. While we sticked to the original C18 relative dimensions, it seems that Chen, Tse and Jiang tried to optimize the lattice parameters ratios (see Table 10.3). However, the $c : a : b$ ratio they obtained is very close to our $a : b : c$ ratio, and the difference in V_0 is less than 0.03 Å^3/atom)[2]. Another difference is the atomic electronic configuration of Pt $5d^8 6s^2$ they used. Nevertheless, they agreed with us that in the $0 - 60$ GPa pressure range, no transition between these three phases occurs.

Comparing the relative stability of the three most stable compositions, we find from Table 10.3 and from Fig. 10.12 that PtN_2(C18) is the most favorable, followed by Pt_3N(RhF_3), and the least stable phase is PtN(B17). However, the differences in their equilibrium E_{coh} lies within a narrow range of 0.036 eV. Relative to their parent metal, all phases have higher E_{coh}, i.e. they are less bound than Pt(A1). Hence, we found, as other theoretical works [29], that platinum nitride can be stabilized in stoichiometries and structures other than that proposed by the first synthesizers [22].

In Ref. [30], the energy-volume EOS for B1, B3, B17, C1, and C2 have been studied using DFT-GGA. Within this parameter sub-space, our obtained EOS's (Figs. 10.11b, 10.11c and 10.12) are in excellent agreement with the findings of [30]. From the relative enthalpy-pressure diagrams

[2]Surprisingly, Chen, Tse and Jiang [66] got exactly the same V_0 values for C2 and C18 within both GGA and LDA; but the average values they gave are different! Thus, we suspect the equal V_0 values they gave for C2 and C18 in both GGA and LDA (see Table 1 in that article); and it may be a typo.

[3], Ref. [30] arrived at an astonishing result: the experimentally proposed PtN(B3) is an entirely unstable structure at any pressure.

To closely study the non-zero pressure stoichiometric and structural preferences, we displayed in Fig. 10.11d the enthalpy H *vs.* pressure P equation of states (EOS) for the most favorable Pt_3N phase (RhF_3), the three previously proposed PtN modifications (B1, B3 and B17), and the four considered PtN_2 structures in the present work (C1, C2, C18 and $CoSb_2$). The arrows indicate the pressures at which curves cross each other. From these curves, it is clear that PtN_2(C18), followed by PtN_2(C2), are the most energetically favorable phases at all pressure. At pressures above 10 GPa, $PtN_2(CoSb_2)$ has lower enthalpy than the rest of the modifications, including PtN(B17) and PtN_2(C1). At pressures higher than 8 GPa, PtN(B17) becomes more favorable than $Pt_3N(RhF_3)$, but the former never competes behind 52 GPa when PtN_2(C1) becomes more favorable. However, $Pt_3N(RhF_3)$ is more stable than PtN(B3) at all pressures. In summary, Fig. 10.11d reveals that even if a PtN phase has been observed (at pressures around 50 GPa), this phase must be unstable toward phase decomposition into solid constituents Pt and PtN_2 (see also Ref. [28]) or into Pt and Pt_3N. However, the series of the possible phase transitions must be carefully investigated.

10.3.2 Volume per Atom and Lattice Parameters

The obtained equilibrium volume per atom V_0, i.e. the inverse of the number density, for all the considered modifications are numerally presented in Table 10.3 and graphically depicted relative to the Pt(A1) in Fig. 10.12. On average, Pt_3N phases tend not to change the number density of the host parent Pt(A1); PtN phases tend to slightly increase it; while the PtN_2 increase it significantly.

It is also evident from Fig. 10.12 that in crossing the boarders between the Pt_3N and PtN and between the PtN and PtN_2 islands, i.e. in increasing the N content, V_0 tends to decrease while the volume per Pt atom V_0^{Pt}, a measure of the average Pt–Pt bond length, tends to increase. The latter finding has been found to be true for the nitrides of Cu [3] and Ag [2] as well.

[3] These are $H(P)$ diagrams but relative to their elemental constituents.

10.3.3 Bulk Modulus and its Pressure Derivative

With only a few exceptions, Fig. 10.12 and Table 10.3 reveal that nitridation of Pt apparently tends to reduce its bulk modulus. Relative to each other, the twenty B_0's show no clear trend. The most energetically favorable PtN phase, B17, has 42 GPa higher bulk modulus than the proposed PtN(B3).

As we mentioned somewhere else [2], B_0 is far more sensitive to any change in volume than the change in E_{coh}. The case of PtN(B2) is a clear example, in which the slight decrease in V_0 overcomes the significant increase in E_{coh} leading only to a very small decrease in B_0 (Fig. 10.12 and Table 10.3).

Given that all the considered phases have higher E_{coh} than Pt(A1), the foregoing argument fails to explain the decrease in B_0 in the case of the structures which have lower V_0 than their parent Pt(A1) and have lower E_{coh} than the extreme case PtN(B2). However, if one replaces V_0 in the argument above with V_0^{Pt}, the contradiction can be lifted. Therefore, we believe that the mechanical properties in these nitrides may be dominated by the effect of the Pt-Pt bond length more than the simple number density.

Although the GGA calculated B_0 values in the present and previous works (Table 10.3) are far smaller than the reported experimental value, our obtained bulk modulus for PtN_2(C1) is 20 GPa higher than that of Pt(A1). This is exactly the measured value for Pt after the PtN formation took place. The observation was considered by Gregoryanz et al. as an indication that some N is dissolved in Pt [22]. Recalling that the B_0 of the produced platinum nitride is ~ 100 GPa than that of Pt(A1) [22], our GGA-obtained B_0 for PtN_2(C1) is ~ 80 GPa less than the experimental value [4].

It may be worth to notice from Table 10.3 that the lattice parameter a of PtN_2(C1) is 0.13 Å higher than that of PtN(B3); yet the B_0 of the former is ~ 70 GPa higher than the latter. This difference in B_0 can be attributed to the fact that in B3, N atoms occupy only half of the tetrahedral interstitial sites of the Pt sub-lattice, while in C1, the four remaining tetrahedral interstitial sites are filled with N atoms [29, 30, 197]. This filling significantly reduces the compressibility but slightly increases the volume of the unit cell. This fact can also be seen readily as a consequence of the difference in the average volume per atom in the two cases (Table 10.3).

[4] Recall that we only consider values relative to Pt(A1) to eliminate systematic errors.

The pressure derivative of the bulk modulus, B_0', measures the sensitivity of B_0 to any external pressure. The top subfigure in Fig. 10.12 reveals that the bulk moduli of Pt_3N(Fe_3N) and PtN_2(C2, C18 and $CoSb_2$) increase upon application of external pressure. Pt_3N($D0_2$) is very sensitive and its B_0 will increase significantly under an infinitesimal excess of pressure. Pt_3N($L1_2$ and RhF_3) tend to be inert; while Pt_3N($D0_3$, A15 and $D0_9$), PtN_2(C1) and all PtN phases tend to decrease their bulk modulus upon application of external pressure. Although B_0' is a measurable quantity [219], we couldn't find any experimental value to test our obtained values against.

10.3.4 Formation Energies

From Fig. 10.12 and Table 10.3, it is evident that formation energy E_f has the same trend as the cohesive energy E_{coh}. If E_f is taken as a measure of synthesized, then the relatively most favorable Pt_3N phases have the same synthesized as the most favorable PtN and PtN_2.

A positive value of E_f means, in principle, that, at the temperature and pressure at which E_f is calculated, the phase is thermodynamically unstable (endothermic) and have a tendency to decompose into its constituent components. In our case, this observation is corroborated by the experimental fact that the synthesis of the platinum nitrides was achieved only at high temperature and temperature [27, 66].

Using different methods, other researchers [25, 27, 66] also obtained positive (zero-pressure and zero-temperature) formation energies for some PtN and/or PtN_2 phases. Some of their values are included in Table 10.3 with indication to the methods of calculations.

The obtained relative difference in E_f for PtN_2(C1) and PtN_2(C2) is in good agreement with Ref. [25]. However, the differences in our and their obtained E_f values can be attributed to three factors: First, the difference in the obtained lattice parameter (see Table 10.3). Second, the value of our calculated equilibrium free parameter u is 0.417 while Ref. [25] obtained 0.415 [5]. Third, and the most significant source of difference, the experimental value of $E_{\text{coh}}(N_2^{\text{gas}})$ in Eq. 7.5.3 was used by Ref. [25], while we calculated it as described in sub-section 7.5.

It may be worth mentioning here that a negative theoretical value of $E_f = -0.4\ eV$/atom was obtained for PtN_2(C2) at $P = 50$ GPa, showing excellent agreement with experiment [25].

[5] Fixing the lattice parameter at the experimental value $a = 4.8041$ Å, Ref. [27] relaxed the N ions and obtained the same value $u = 0.415$.

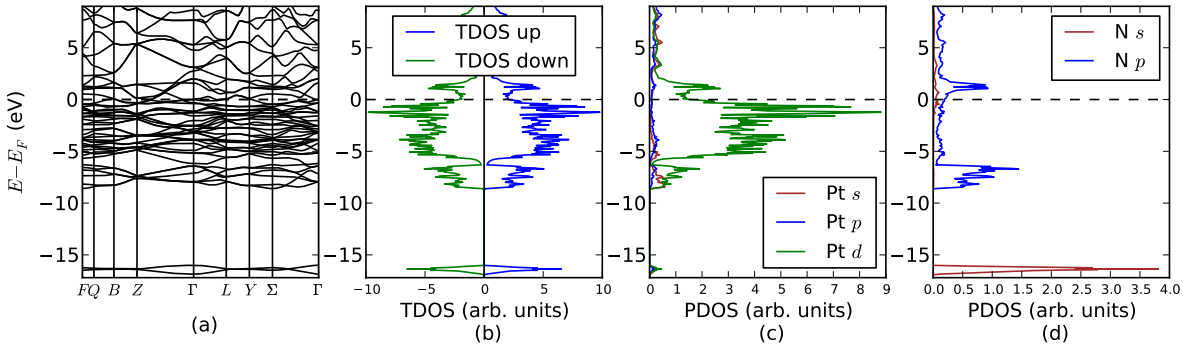

Figure 10.13: (Color online.) DFT calculated electronic structure for Pt_3N in the RhF_3 structure: **(a)** band structure along the high-symmetry $\mathbf{k}$-points (see Table 8.1); **(b)** spin-projected total density of states (TDOS); **(c)** partial density of states (PDOS) of Pt(s, p, d) orbitals in Pt_3N; and **(d)** PDOS of N(s, p) orbitals in Pt_3N.

Moreover, Young et al. [27] claimed that PtN_2 dissociates upon mild heating below $P = 10$ GPa.

10.3.5 Electronic Properties

The DFT obtained band diagrams $\epsilon_i^\sigma(\mathbf{k})$ and spin-projected total and partial density of states (DOS) of the most stable modifications: $Pt_3N(RhF_3)$, PtN(B3 and B17), and PtN_2(C18) are displayed in Figs. 10.13, 10.14[6], 10.15 and 10.16, respectively. Spin-projected total density of states (TDOS) are shown in sub-figure (b) in each case. Because in these four considered cases electrons occupy the spin-up and the spin-down bands equally, it was sufficient only to display spin-up DOS and spin-up band diagrams. Displaying the energy bands along densely sampled high-symmetry strings of $\mathbf{k}$-points allows us to extract information about the electronic structure of these phases. Moreover, to investigate the details of the orbital character of the bands, the Pt(s, p, d) and N(s, p) resolved DOS's are plotted at the same energy scale.

With The Fermi surface crossing the partly occupied bands. it is clear from Figs. 10.13, 10.14, and 10.15 that $Pt_3N(RhF_3)$ PtN(B3) and PtN(B17) are metals.

The TDOS of Fig. 10.16(b) reveal that PtN_2(C18) is a semiconductor with (Fig. 10.16(a)) its valence band maximum (VBM) at $(Y, -0.091\ eV)$ and its conduction band minimum (CBM) at $(Y, 0.044\ eV)$, resulting in a narrow direct energy band gap $E_g = 0.135\ eV$ of width. Below

[6] Note that, in Fig. 10.14, the coordinates of the W point is not as the same as in Ref. [203], but they are equivalent. Also, the coordinates of U and K are not given in Ref. [203]. The coordinates of U, K and the equivalent W were created by means of XCrySDen software!

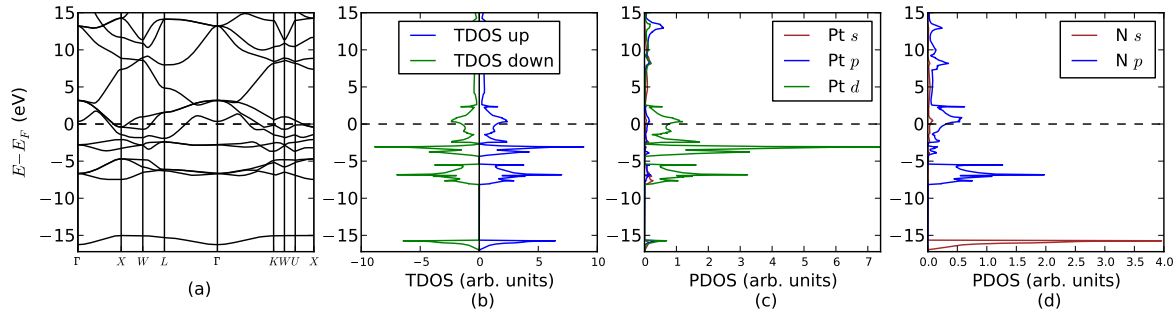

Figure 10.14: (Color online.) DFT calculated electronic structure for PtN in the B3 structure: **(a)** band structure along the high-symmetry $\mathbf{k}$-points (see Table 8.1); **(b)** spin-projected total density of states (TDOS); **(c)** partial density of states (PDOS) of Pt(s,p,d) orbitals in PtN; and **(d)** PDOS of N(s,p) orbitals in PtN.

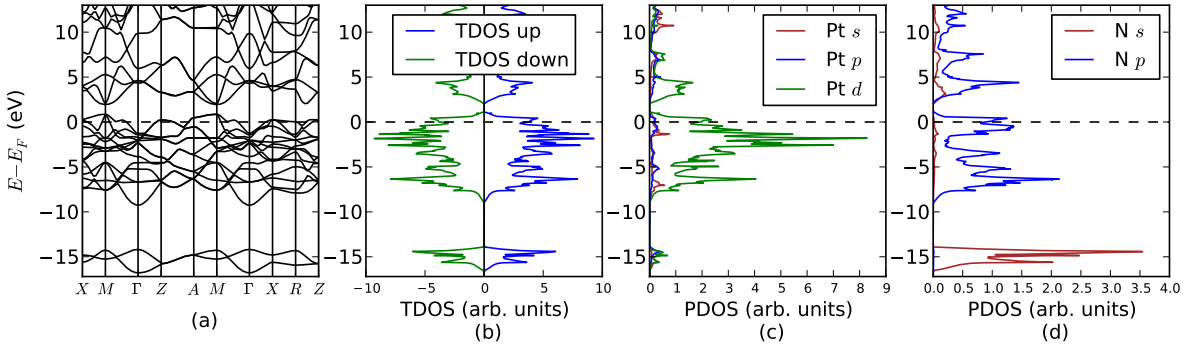

Figure 10.15: (Color online.) DFT calculated electronic structure for PtN in the B17 structure: **(a)** band structure along the high-symmetry $\mathbf{k}$-points (see Table 8.1); **(b)** spin-projected total density of states (TDOS); **(c)** partial density of states (PDOS) of Pt(s,p,d) orbitals in PtN; and **(d)** PDOS of N(s,p) orbitals in PtN.

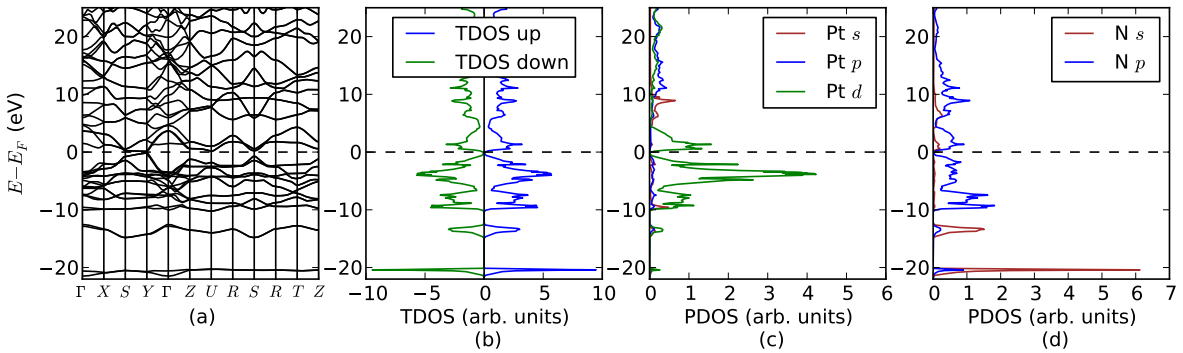

Figure 10.16: (Color online.) DFT calculated electronic structure for PtN_2 in the C18 structure: **(a)** band structure along the high-symmetry $\mathbf{k}$-points (see Table 8.1); **(b)** spin-projected total density of states (TDOS); **(c)** partial density of states (PDOS) of Pt(s,p,d) orbitals in PtN_2; and **(d)** PDOS of N(s,p) orbitals in PtN_2.

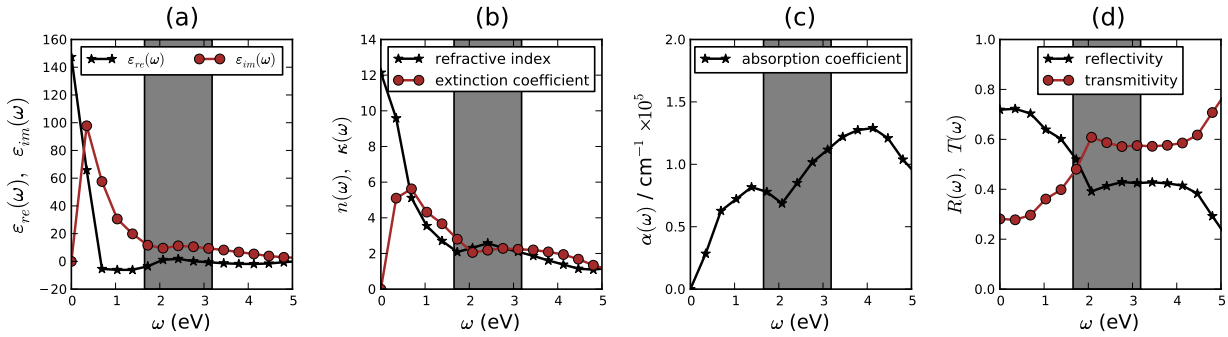

Figure 10.17: (Color online.) The GW calculated frequency-dependent optical spectra of PtN(B3): **(a)** the real $\varepsilon_{\text{re}}(\omega)$ and the imaginary $\varepsilon_{\text{im}}(\omega)$ parts of the dielectric function $\varepsilon_{\text{RPA}}(\omega)$; **(b)** refraction $n(\omega)$ and extinction $\kappa(\omega)$ coefficients; **(c)** absorption coefficient $\alpha(\omega)$; and **(d)** reflectivity $R(\omega)$ and transmitivity $T(\omega)$. The shaded window highlights the optical region.

this fundamental gap there are three bands: the deep one at $\sim -20.5\ eV$ consists mainly of the N$(2s)$ states. Its high DOS and sharp feature correspond to its little and slow energy variation in the $\mathbf{k}-$space. The second band is relatively narrow ($\sim 2.2\ eV$ of width) with low density and steming mainly from a mixture of the N states with Pt(d) states. The superposition Pt(d) and N(p) states in the region from $-10.314\ eV$ to $-0.091\ eV$ below the fundamental gap constitutes the third band with highly structured, intense and narrow series of peaks. Our obtained TDOS and PDOS show excellent agreement with Ref. [66] where also PtN_2(C18) was predicted to be a semiconductor, but band diagrams and E_g value are not given.

It may be worth mentioning here that PtN(B1) [31] and PtN(B4) [194] were found to be metallic, PtN_2(C1) was found to be a poor metal [29], $PtN_2(CoSb_2)$ [66] was found to be a semiconductor, and an indirect band gap between $1.2\ eV$ [66] and $1.5\ eV$ [27] has been obtained for PtN_2(C2).

10.3.6 Optical Properties

GW calculations were carried out for the PtN(B3) and PtN(B17) metallic phases at their equilibrium. Figs. 10.17 and 10.18 display the obtained real and imaginary parts of the frequency-dependent dielectric function $\varepsilon_{\text{RPA}}(\omega)$ of these two phases and the corresponding derived optical spectra (Eqs. D.2.12, D.2.13, D.2.17 and D.2.22). In each sub-figure, the optical region $[\sim (3.183 - 1.655)\ eV \equiv (390 - 750)\ nm]$ is shaded.

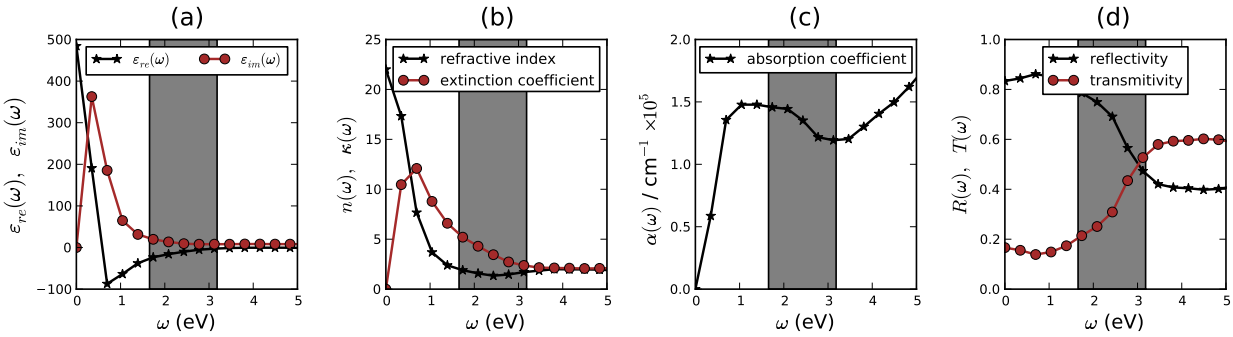

Figure 10.18: (Color online.) The GW calculated frequency-dependent optical spectra of PtN(B17): **(a)** the real $\varepsilon_{\text{re}}(\omega)$ and the imaginary $\varepsilon_{\text{im}}(\omega)$ parts of the dielectric function $\varepsilon_{\text{RPA}}(\omega)$; **(b)** refraction $n(\omega)$ and extinction $\kappa(\omega)$ coefficients; **(c)** absorption coefficient $\alpha(\omega)$; and **(d)** reflectivity $R(\omega)$ and transmitivity $T(\omega)$. The shaded window highlights the optical region.

The non-vanishing absorption coefficient $\alpha\,(\omega)$ in the whole range for both phases confirms their metallic character. As it should be the case, refraction $n(\omega)$ and extinction $\kappa(\omega)$ coefficients behave as the real $\varepsilon_{\text{re}}(\omega)$ and the imaginary $\varepsilon_{\text{im}}(\omega)$ dielectric functions, respectively.
As one can see from sub-figure 10.17(d), close to the edge of the optical region at $\sim (1.762\ eV = 703.768\ nm)$ PtN(B3) is 50% reflector and 50% transmitter. From $\sim (2.071\ eV = 598.579\ nm)$ to the UV region, PtN(B3) is only $\sim 40\%$ reflecting but $\sim 60\%$ transmitting. However, more of the transmitted portion in this region will be absorbed as the photon energy increases. This fact can be readily noticed if one compares sub-figures 10.17(c) and 10.17(d).
PtN(B17), as can be seen from sub-figure 10.18(d), is a very good reflector in the whole region until $\sim (3.000\ eV = 413.281\ nm)$ where it equally reflects and transmits the violet light. However, less of the transmitted portion in the optical region will be absorbed as the photon wavelength decreases. This fact can be readily observed in sub-figures 10.18(c).

According to the best of our knowledge, there is no available experimental optical spectra for the platinum nitride. However, from their visual appearance, all the synthesized platinum nitride samples look very shiny and darker than their parent platinum in reflected light and totally opaque in transmitted light. These features suggest that PtN is either a poor metal or a semiconductor with a small band gap [22].
From Figs. 10.18 and 10.15, the above mentioned properties are strongly met by PtN(B17), but purely seen (Figs. 10.17 and 10.14) in PtN(B3), as discussed above. Unfortunately, we did not

carry out optical calculations for PtN_2(C1 or C2).

10.3.7 PtN versus PtN_2

Using our own obtained results in the present work as well as the findings of other researchers, below we make a comparison between the PtN modifications (supported by the experimentalists) and the PtN_2 phases (supported by the theoreticians):

- Given that GGA calculated lattice parameters are usually overestimated [134, 135, 247], the obtained values of the a lattice parameter for PtN_2(C1 and C2) are the closest ones to the experimental value (to within 3 % and 2 %, respectively), while the PtN phases are in poor agreement with experiment, as can be seen in Table 10.3.

- First-principles studies of transition metals nitrides show that the B_0's of the elemental metals are generally enhanced by nitridation [16, 22]. Compared to experiment, Table 10.3 and Fig. 10.12 reveal that this trend is met by PtN_2(C1), while PtN(B3) has 50 GPa lower than Pt(A1).

- Like the first synthesized sample and the proposed PtN(B3) modification [22], PtN_2(C1 [29] and C2 [25]) have fcc sub-lattice of Pt.

- PtN_2(C1 [29], C2 [27, 66], C18 [66] and $CoSb_2$ [66]) have all been found to be elastically stable, while PtN(B3 [26, 27, 29, 31] and B17 [31]) were found to be elastically unstable.

- Formation and cohesive energies of PtN_2(C2, C18 and $CoSb_2$) are lower than that of PtN(B3) [Table 10.3 and Fig. 10.12.

- In excellent agreement with experiment, the calculated formation energy of PtN_2(C2) at $P = 50$ GPa was calculated to be negative [25], while calculations found PtN(B3) to be thermodynamically unstable at all pressures [30].

- The experimentally obtained Raman spectrum of the reproduced platinum nitride [25] matches closely that of pyrite (FeS2), i.e. in the C2 structure, but does not match the PtN(B3) spectrum that expected from group theory [25].

- The theoretically calculated [27,66] Raman spectrum for PtN_2(C2) shows good agreement with the first experimentally obtained one [22].

- In agreement with the experimental observation and the visual appearance of the first produced platinum nitrides [22], PtN_2(C1) was found to be a poor metal [29], and we found PtN_2(C18) to be a semiconductor with a small band gap.

Hence, in contrast to the proposed PtN modifications, PtN_2 phases possess many similar properties as the synthesized phase [7].

10.4 Copper Nitrides

Cohesive energy versus atomic volume data for the different phases of Cu_3N, CuN_2 and CuN are visualized graphically in Fig. 10.19a, Fig. 10.19b and Fig. 10.19c, respectively. The corresponding obtained equilibrium structural parameters and energetic and elastic properties are presented in Table 10.4. In this table, phases are first grouped according to the nitrogen content, starting with the stoichiometry with the lowest nitrogen content Cu_3N, followed by the 1:1 phases and ending with the nitrogen-richest CuN_2 ones. Within each group, phases are ordered according to their structural symmetry, starting from the highest symmetry (i.e. space group) to the least symmetry. Our results are compared with available experiment and with previous theoretical calculations; with the calculation methods and XC functional pointed out in the Table footnotes whenever appropriate.

[7] Such an observation was arrived at by other authors [29] for the PtN(C1). Here we are making more comprehensive comparison

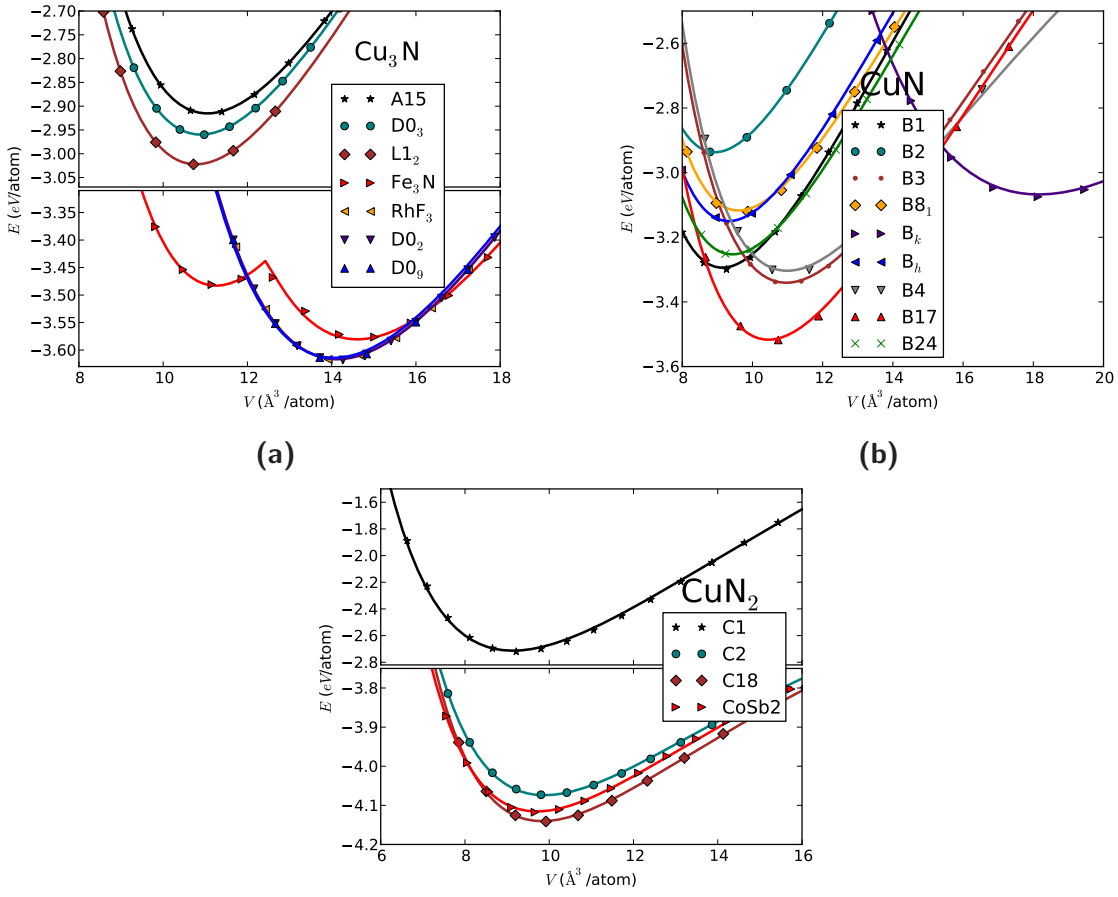

Figure 10.19: (Color online.) Cohesive energy $E_{\rm coh}(eV/{\rm atom})$ versus atomic volume V (Å^3/atom) for: **(a)** Cu_3N in seven different structural phases; **(b)** CuN in nine different structural phases; and **(c)** for CuN_2 in four different structural phases.

Table 10.4: Calculated and experimental zero-pressure properties of the twenty studied phases of Cu_3N, CuN and CuN_2**:** Lattice constants (a(Å), b(Å), c(Å), $\alpha(^\circ)$ and $\beta(^\circ)$), equilibrium atomic volume V_0(Å^3/atom), cohesive energy $E_{\text{coh}}(eV/\text{atom})$, bulk modulus $B_0(GPa)$ and its pressure derivative B_0', and formation energy $E_f(eV/\text{atom})$. The presented data are of the current work (*Pres.*), experimentally reported (*Exp.*) and of previous calculations (*Comp.*).

Structure		$a(\AA)$	$b(\AA)$	$c(\AA)$	$\alpha(^\circ)$ or $\beta(^\circ)$	$V_0(\AA^3/\text{atom})$	$E_{\text{coh}}(eV/\text{atom})$	B_0(GPa)	B_0'	$E_f(eV/\text{atom})$
					Cu					
	Pres..	3.636	–	–	–	12.02	−3.474	136.351	5.032	–
	Exp.	3.6148[c], 3.6077[f]	–	–	–	11.811[g], 11.810[f]	−3.49[i]	137[i], 137[p]	5.48[q]	–
A1[a,b]	*Comp.*	3.52[d,e]	–	–	–	11.009[h]	−4.29[j], −3.12[k],	189[d], 190[e]	4.46[r],	–
			–	–	–		−3.30[l], −4.66[m],		5.20[s],	
			–	–	–		−3.69[n,o]		5.14[t]	
					Cu_3N					
D0$_3$	*Pres.*.	5.585	–	–	–	10.89	−2.960	142.829	4.845	0.944
A15	*Pres.*	4.455	–	–	–	11.05	−2.915	138.164	4.845	0.989
	Pres.	3.827	–	–	–	14.05	−3.614	112.5	4.899	0.287
	Exp.	$(3.810 \sim 3.830)$[u],	–	–	–					
D0$_9$		(3.830 ± 0.005)[z],								
		3.815[x], 3.83[y],	–	–	–					
		3.855[aa], 3.82[gg],	–	–	–					
		(< 3.868)[dd]	–	–	–					
	Comp.	3.846[v], 3.82[w,ee],	–	–	–	13.94[w],	−4.863[w],	115.2[w],	4.066[w],	
		3.826[bb], 3.841[cc],	–	–	–	14.02[ee]	−4.865[ee]	116[bb],	4.47[bb],	
		3.83[ff]	–	–	–			104[ee]	5.26[ee]	
L1$_2$	*Pres.*	3.507	–	–	–	10.78	−3.022	147.516	4.817	
	Comp.	3.50[bb]	–	–	–			153[bb]	4.74[bb]	0.882
D0$_2$	*Pres.*	7.674	–	–	–	14.12	−3.616	111.776	4.757	0.286
ϵ-**Fe_3N**	*Pres.*	5.263	–	4.905	–	14.71	−3.579	109.798	4.819	0.325
RhF$_3$	*Pres.*	5.426	–	–	$\alpha = 60.003$	14.12	−3.615	111.192	4.758	0.286
					CuN					
	Pres.	4.182	–	–	–	9.143	−3.300	200.770	4.687	1.035
	Comp.	4.185[hh],	–	–	–			201.60[hh],	3.811[hh],	
B1		4.05[ii],	–	–	–			307[ii],	4.491[kk]	
		4.336[ij],	–	–	–			244.27[ij],		
		4.074[kk],	–	–	–			257.46[kk],		
		4.17[ll]	–	–	–			207[ll]		
	Pres.	2.615	–	–	–	8.936	−2.937	195.896	4.775	1.398
B2	*Comp.*	2.61[hh],	–	–	–			200.01[hh],	4.352[hh],	
		2.54[kk],	–	–	–			265.40[kk],	4.373[kk]	
		2.51[ll]	–	–	–			196[ll]		
	Pres.	4.445	–	–	–	10.98	−3.343	161.726	4.677	0.992
B3	*Comp.*	4.447[hh],	–	–	–			164.96[hh],	4.534[hh],	
		4.34[ii],	–	–	–			305[ii],		
		4.078[ij],	–	–	–			240.66[ij],		
		4.341[kk],	–	–	–			212.16[kk],	4.311[kk]	
		4.44[ll]	–	–	–			158[ll]		
B8$_1$	*Pres.*	3.174	–	4.415	–	9.603	−3.128	184.371	4.850	1.211
	Comp.	3.08[ll]	–	5.020[ll]	–			227[ll]		
B$_k$	*Pres.*	3.160	–	8.406	–	18.17	−3.074	86.124	4.494	1.261
B$_h$	*Pres.*	2.805	–	2.738	–	9.327	−3.149	192.9	4.779	1.186
B4	*Pres.*	3.148	–	5.155	–	11.06	−3.309	152.956	4.963	1.026
	Comp.	3.17[hh],	–	5.16[hh],	–			157.85[hh],	4.41[hh],	
		3.077[kk],	–	5.016[kk],	–			202.10[kk],		
		3.16[ll]	–	5.151[ll]	–			155[ll]	4.35[kk]	
B17	*Pres.*	2.870	–	5.052	–	10.40	−3.509	174.324	4.948	0.818
B24	*Pres.*	3.928	4.167	4.611	–	9.435	−3.253	189.745	4.708	1.082
					CuN_2					
C1	*Pres.*	4.8	–	–	–	9.214	−2.712	198.265	4.652	1.910
	Comp.	4.694[ij]	–	–	–			258.94[ij]		
C2	*Pres.*	4.919	–	–	–	9.920	−4.065	80.907	6.170	0.557
C18	*Pres.*	3.039	3.988	4.867	–	9.831	−4.132	92.680	6.317	0.490
$CoSb_2$	*Pres.*	5.303	5.015	9.106	$\beta = 151.225$	9.714	−4.110	92.028	6.167	0.512

Notes to Table 10.4 : ———————————-

[a] Ref. [248]: Information is given at RTP.

[b] Ref. [159].

[c] Ref. [240]: This is an average of 66 experimental values (with a deviation ± 0.0003 Å), at $20^{\circ}C$.

[d] Ref. [241]: using LAPW-TB.

[e] Ref. [241]: using LAPW-LDA.

[f] Ref. [227], with a deviation ± 0.0002 Å.

[g] See Ref. 15 in [249].

[h] Ref. [249]: using APW-MT-LDA.

[i] Ref. [172]: Cohesive energies are given at $0\ K$ and 1 atm $= 0.00010$ GPa; while bulk mudulii are given at room temperature.

[j] Ref. [216]: using LDA.

[k] Ref. [216]: using BP-GGA.

[l] Ref. [216]: using PW-GGA.

[m] Ref. [242]: using PAW-LDA.

[n] Ref. [242]: using PAW-PW91.

[o] Ref. [242]: using PAW-GGA(PBE).

[p] Ref. (25) in [219]: at room temperature.

[q] See Refs. (8)–(11) in [219].

[r] Ref. [219]: using the so-called method of transition metal pseudopotential theory; a modified form of a method proposed by Wills and Harrison to represent the effective interatomic interaction.

[s] Ref. [219]: using a semiempirical estimate based on the calculation of the slope of the shock velocity *vs.* particle velocity curves obtained from the dynamic high-pressure experiments. The given values are estimated at $\sim 298\ K$.

[t] Ref. [219]: using a semiempirical method in which the experimental static $P - V$ data are fitted to an EOS form where B_0 and B_0' are adjustable parameters. The given values are estimated at $\sim 298\ K$.

[u] Values obtained in the experimental work by Gallardo-Vega and Cruz [44] are between 3.810 Åand 3.830 Å.

[v] Ref. [46]: using PAW-GGA(Perdew-Wang).

[w] Ref. [187]: using FP-LAPW-GGA(PBE). Only the total energy ($-19.45\ eV$) is given.

[x] Ref. [47]; [y] Ref. [34]; [z] Ref. [39]; [aa] Ref. [250].

[bb] Ref. [188]: using FP-LAPW-GGA(PBE).

[cc] Ref. [251]: using USPP-GGA.

[dd] Ref. [252].

[ee] Ref. [18]: using FP-LAPW-GGA(PBE). Only the total energy ($-19.46\ eV$) is given.

[ff] Ref. [36]: using FP-LAPW+lo-GGA(PBE).

[gg] Ref. [253].

[hh] Ref. [65]: using FP-LAPW+lo method within GGA(PBE).

[ii] Ref. [189]: using FLAPW-LDA.

[jj] Ref. [254]: using USPP-GGA(PBE).

[kk] Ref. [65]: using FP-LAPW+lo method within LDA.

[ll] Ref. [192]: using full-potential linear muffin-tin orbital (FP-LMTO) method within GGA(PBE).

———————————————————————-

To deeper analyze and to compare the obtained equilibrium properties of the three stoichiometries series with respect to one another, these quantities are depicted again in Fig. 10.20. All quantities in this figure are given relative to the corresponding ones of the *fcc* crystalline elemental copper given in Table 10.4. This will allow us to study the effect of nitridation on pure crystalline Cu [8].

10.4.1 Relative Stability: Cohesive Energy

Considering E_{coh} in the Cu_3N series, one can use Fig. 10.20 to group these phases into two groups: a lower energy (more stable than the elemental Cu) group, containing $D0_9$, $D0_2$, RhF_3 and Fe_3N structures; and a higher energy (significantly less stable than the elemental Cu) group containing $L1_2$, $D0_3$ and A15 structures. The difference in cohesive energy between the least stable phase in the lower group (Fe_3N) and the relatively most stable phase in the higher group ($L1_2$) is $0.557\ eV$/atom, as one can see from Table 10.4. It is interesting to point out here that, except $Cu_3N(Fe_3N)$, all phases in the first group are insulators, while all the less stable phases are metallic[9].

Although this simple cubic $D0_9$ phase was indeed found to be stable, yet one interesting result we obtained is that, in their equilibrium, the $Cu_3N(RhF_3)$ and the $Cu_3N(D0_2)$ phases would be $0.001\ eV$/atom and $0.002\ eV$/atom more stable than $Cu_3N(D0_9)$, respectively. Moreover, Fig. 10.19a shows clearly that the $E(V)$ relations of Cu_3N in $D0_9$, $D0_2$ and in RhF_3 structures are almost identical. This marginal[10] difference in energy (Table 10.4) and the almost identical $E(V)$ curves (Fig. 10.19a) may indicate the possiblity of the co-existence of these phases during the copper nitride synthesis process. However, this behaviour in the EOS could be attributed to the structural relationships between these three structures that being discussed in Ref. [21, p. 265] and in Ref. [155].

The bcc skutterudite structure ($D0_2$) can be derived from the more symmetric sc $D0_9$ structure by simply displacing four of the N atoms located on parallel edges of the Cu cube to its center. This is done for two adjacent Cu cubes but in two vertical displacement directions, as nicely

[8] In Table 10.4, our computed properties of the elemental Cu are compared with experiment and with previous calculations as well. This may benchmark the accuracy of the rest of our calculations.

[9] The electronic structure of $D0_9$, $D0_2$ and RhF_3 phases are discussed in Sec. 10.4.6, while the rest are not shown here.

[10] In fact, the accuracy of the approximate XC functional (PBE and others) does not really allow us to make a distinction among these.

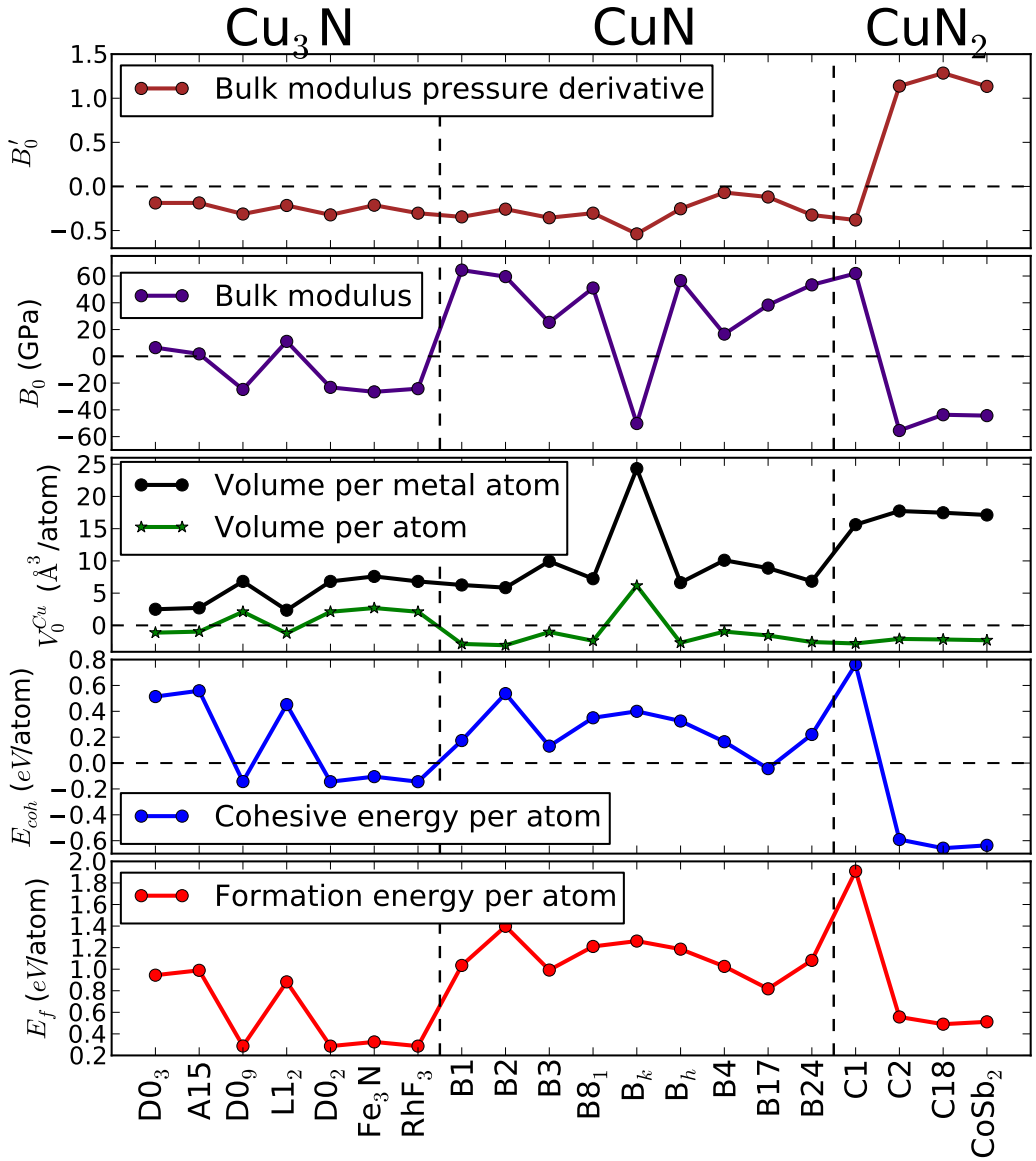

Figure 10.20: (Color online.) Calculated equilibrium properties of the twenty studied phases of copper nitrides. All quantities are given relative to the corresponding ones of the *fcc* crystalline elemental copper given in the first row of Table 10.4.

explained in Ref. [155]. On the other hand, to see the relation between $D0_9$ and RhF_3, it is better to think of $D0_9$ as built of Cu_6N octahedra (cf. Fig. I in Ref. [188]). A simple rotation of 60° of an octaheron about a shared vertex with another octahedron brings the system to a structure in which Cu atoms are in hcp positions. Interested readers are referred to Ref. [21, p. 266] for more details. Thus, both $D0_2$ and RhF_3 can simply be derived from $D0_9$. Hence it is not surprising that these structural relations reflect in their EOS's and in other physical properties.

The odd behaviour of the EOS of Fe_3N with the existence of two minima (Fig. 10.19a) shows that the first minima (to the left) is a metastable local minimum that cannot be maintained as the system is decompressed. Cu ions are in the $6g$ Wyckoff positions: $(x,0,0),(0,x,0),(-x,-x,0)$, $(-x,0,\frac{1}{2}),(0,-x,\frac{1}{2}),(x,x,\frac{1}{2})$; with $x=\frac{1}{3}$ to the left of the potential barrier (represented by the sharp peak in Fig. 10.19a), and $x=\frac{1}{2}$ to the right of the peak. It may be relevant to mention here that Wang and Xue [192] obtained an additional local minimum at high pressure (lower volume) in the $E(V)$ EOS of CuN(B1).

In the CuN series, all phases show less binding than the Cu(fcc), except that the simple tetragonal structure of cooperite (B17) is slightly more stable, with $0.043\ eV$/atom lower E_{coh}. This structure, B17, was theoretically predicted to be the ground-state structure of PtN [30].

In the CuN_2 nitrogen-richest phase series, we can see from Table 10.4 and from Fig. 10.20 that the phases of this group are significantly more stable than all the studied phases, except C1, which, in contrast, is the least stable among the twenty studied phases.

Comparing the relative stability of Cu_3N, CuN and CuN_2, we find from Table 10.4 and from Fig. 10.20 that CuN_2(C18) is the most energetically stable phase with $0.526\ eV$/atom lower than the experimentally reported $Cu_3N(D0_9)$ phase.

10.4.2 Volume per Atom and Lattice Parameters

Our obtained numerical values for the volume per atom V_0 are given in Table 10.4 and visualized in Fig. 10.20. Relative to the Cu(fcc), all phases tend to slightly lower the V_0 values except $CuN(B_k)$ and the semiconducting Cu_3N phases.

To study the structural effect of the nitrogen on the hosting Cu lattice, we, instead of using the commonly used average V_0, introduce the volume per metal atom V_0^{Cu}. In the case of CuN and CuN_2 it is numerically equivalent to the volume per formula unit, while for Cu_3N it equals

to (volume per formula unit)/3. Hence, this quantity (V_0^{Cu}) may be considered as a direct measure of the Cu-Cu bond length and, thus, as an indicator of the effect of nitridation on the mechanical properties of the elemental Cu. That is, for a given cohesive energy, an increase in V_0^{Cu} may/should lead to a decrease in B_0 and vise versa, as will be seen when we discuss the trends in B_0 values.

In the same sub-window as V_0, obtained V_0^{Cu} values are depicted relative to the Cu(fcc) in Fig. 10.20. Having a look at this figure, one can see a *general* behaviour: V_0^{Cu} *tends* to increase with the increase in the nitrogen content *and* with the decrease in the structural symmetry. There is only one phase which has a clear odd bevaviour, that is CuN(B_k). It is worth to mention here that this B_k is not an *hcp* structure, and we have not optimized its c/a ratio. Thus, this is the most open phase among all the investigated set. Nevertheless, all phases show an increase in V_0^{Cu} relative to the elemental Cu, and thus Cu-Cu bond is longer in all these nitrides than in the elemental Cu. This cannot be seen directly from the V_0 values given in Tabel 10.4.

10.4.3 Bulk Modulus and its Pressure Derivative

As can be seen in Fig. 10.20, compared to the parent Cu(fcc), the CuN phases tend to increase B_0. Such a conclusion has also been arrived at by Shimizu, Shirai and Suzuki [189] who calculated B_0 for a series of 1:1 TMNs, including CuN. On the other hand, the considered CuN_2 phases are all, except C1, more compressible than the Cu(fcc). Considering the 1:3 phases, one can easily see that the trend in E_{coh} manifests itself again and divides this series into two groups: a group of more compressible semiconductors containing $D0_9$, $D0_2$, RhF_3 and Fe_3N; and a group with almost no change in the Cu(fcc) bulk modulus containing $L1_2$, $D0_3$ and A15 metallic phases.

Having a look at Fig. 10.20, one may argue that, relative to Cu(fcc), the lower V_0 and the lower E_{coh} of the CuN_2(C2), CuN_2(C18) and $CuN_2(CoSb_2)$ phases must have led to higher B_0 values. Since this is not the case, we turn to our introduced V_0^{Cu}: Fig. 10.20 tells us that all these three nitrogen-rich phases have higher V_0^{Cu} relative to Cu(fcc). Hence, V_0^{Cu} won the competition with their relatively lower E_{coh}, leading to lower B_0. This, again,makes sense and justifies our introduction of V_0^{Cu} when dealing with such nitrides.

Take, for example CuN_2(C18). One can notice from Table 10.4 that, relative to $Cu_3N(D0_9)$, CuN_2(C18) has about 30% less atomic volume V_0 and about 14% less E_{coh}, but resulting in

about 30% *less* bulk modulus than $Cu_3N(D0_9)$. However, if we consider our introduced V_0^{Cu}, rather than the commonly used V_0, one can see that $CuN_2(C18)$ has about 57% more V_0^{Cu} than $Cu_3N(D0_9)$, which explains the lesser B_0 value. In fact, $CuN_2(C2)$, $CuN_2(C18)$ and $CuN_2(CoSb_2)$ share almost the same features when compared to $Cu_3N(D0_9)$, $Cu_3N(D0_2)$ and $Cu_3N(RhF_3)$ as $CuN_2(C18)$ when compared to $Cu_3N(D0_9)$.

Compared to the other CuN_2 phases, the relatively greater value of E_{coh} of C1 is overtaken by the relatively less V_0^{Cu} value, resulting in a greater B_0 than all the three other CuN_2 phases. It is also worth to notice from Table 10.4 that all the CuN phases, except the open $B_{\mathbf{k}}$, have higher bulk moduli than all Cu_3N and CuN_2 phases, except the least compressible phase, C1.

Hence, the isotropic elastic properties depend on, and are more appropriately described by, V_0^{Cu} rather than V_0. Fig. 10.20 tells that the more the nitrogen content, the longer the Cu-Cu bond length. Thus nitrogen tends to open the hosting Cu lattice and to reduce the bulk modulus. Nevertheless, bulk modulus is a result of the competition between the change in V_0^{Cu} and the change in E_{coh}.

Physically, the pressure dependence of B_0 can be quantified via its pressure derivative B_0' given by Eq. 7.2.3. Except for the last three CuN_2 phases in Fig. 10.20, all phases show almost equal sensitivity. However, the change in B_0 of the elemental Cu would be greater than all these phases. On the other hand $CuN_2(C2)$, $CuN_2(C18)$ and $CuN_2(CoSb_2)$ show high elastic sensitivity to any isotropic pressure. It is worth to mention here that this quantity is a measurable quantity [219], but we cannot find any experimental value for the synthesized $Cu_3N(D0_9)$ phase.

Table 10.4 shows that our obtained B_0 and B_0' values agree well with many other theoretical works. However, clear differences between the current and, and among, the theoretically obtained values exist. This can be traced back to two factors:

- From Eq. 7.2.2 and Eq. 7.2.3, one needs only to calculate E_{coh} from DFT. Hence, B_0' values depends on the DFT algorithm/method and functional. For example, in Table 10.4, the GGA (e.g. Refs. [65] and [254]) calculated B_0 values of B1, B2 and B3 are all lower than the obtained LDA (e.g. Refs. [65] and [189]) corresponding ones. This is, in fact, a well-known feature of GGA compared to LDA. That is, relative to the latter,the former understimates the cohesion and thus overstimates V_0 resulting in a lower B_0.

- Yet, there are considerable differences among the GGA values and among the LDA values!

Recalling that B_0 and B'_0 are obtained from the EOS fitting, the accuracy in the obtained values depends not only on the accuracy of the DFT calculated E_{coh}, but also on the numerical fitting; e.g. number of points around V_0 and how far these points are from both V_0 and E_0. Moreover, B'_0 is numerically more sensitive than B_0 [204], that why, we believe, there is no even clear/general trend/systematic in the calculated B'_0 values of Table 10.4.

10.4.4 Relative Stability: Formation Energy

The obtained formation energies E_f of the twenty relaxed phases are given in Table 10.4 and shown graphically in Fig. 10.20. All these values are positive; which means that all these twenty phases are, in principle, thermodynamically unstable (endothermic). However, these results have to be interpreted with some caution:

- Many other theoretical calculations found positive formation energy for experimentally synthesized transition metal nitrides; e.g. OsN_2 [255, using PP and PBE-GGA], PtN_2 [27, using PP and PBE-GGA] and InN [218, using PP with LDA and different GGAs] [256, using PW91-GGA].

- The fact that we obtained a positive formation energy for the successfully synthesized $Cu_3N(D0_9)$ phase means that it may be possible that other phases can still be synthesized, and it may indicate that there is a problem with our calculations method (i.e. with the approximations) and/or with the physical conditions assumed for the calculations (i.e. pressure and temperature); see below.

- These positive values are the result of static DFT calculations ($T = 0\ K$) at equilbrium volume ($P = 0$ GPa); while the fact is that most, if not all, of the successfully synthesized TMNs were obtained by subjecting their parent elements to extreme conditions of pressure and temperature ($c.f.$ Ref. [255]).

- Referring to Table 10.1, the difference between our calculated cohesive energy of N_2 and experiment (Ref. [159]) is about $-0.297\ eV$/atom; while for the bulk Cu the difference is about $0.016\ eV$/atom. Now, using Eq. 7.5.3 with this significant overestimation of $E_{\text{coh}}(N_2^{\text{gas}})$ and the reasonable value of $E_{\text{coh}}(Cu^{\text{solid}})$ will result in underestimation of

$E_f(\mathrm{Cu}_m\mathrm{N}_n^{\mathrm{solid}})$. This contribution has to be considered, as an apparent shortcoming of the PBE-GGA, whenever one deals with a dimeric crystal [204, 218].

- Nevertheless, since all formation energies are calculated as the difference between the *ab initio* cohesive energies, which in turn are calculated at the same level of accuracy, one can still use these formation energies to measure the *relative* thermodynamic stabilities of these structures. That is, the lower the formation energy, the lower the propensity to dissociate back into the constituent elements Cu and N_2 ($c.f.$ Ref. [255]).

- Moreover, because $Cu_3N(D0_9)$ has been synthesized, we can take it as a *reference measure* of stability. It is also worth to recall here that experiment found $Cu_3N(D0_9)$ to be metastable at room temperature [34].

Relative to each other, and within each series, E_f of the twenty phases shows almost the same trend as E_{coh}. However, the CuN phases tend to be relatively less stable than the Cu_3N and CuN_2 phases, except the odd C1 phase. In fact, C2, C18 and $CoSb_2$ are the most stable and share almost the same features when compared to $Cu_3N(D0_9)$, $Cu_3N(D0_2)$ and $Cu_3N(RhF_3)$. This may agree well with Armenta and Soto [36] who proved, from the study of formation energy, that the metallic phases of copper nitrides would be more stable than the semiconducting phase.

10.4.5 More Comparison with Experiment and with Theory

Comparing our obtained results with experiment, one can see from Table 10.4 that the lattice parameter a of $Cu_3N(D0_9)$ was reproduced very well. Excellent agreement with previous calculations is also clear, though, with respect to experiment (or: with respect to each other), the common overestimation of a by GGA and the underestimation of a by LDA (c.f. Refs. [46, 187, 188]; and Refs. [257, 258]) is showing up.

Using the full-potential (linearized) augmented plane waves plus local orbitals (FP-LAPW+lo) method within LDA and within GGA, Kanoun and Said [65] studied the $E(V)$ EOS for CuN in the B1, B2, B3 and B4 structures. While within GGA, they found equilibrium lattice parameters which are in excellent agreement with ours, their obtained LDA lattice parameter values show the common underestimation with respect to our and their GGA values (see Table 10.4). Also,

the relative stabilities of these phases they arrived at agree well with ours, and they concluded that B3 is the ground-state phase of CuN and is metalic.

Shimizu, Shirai and Suzuki [189] performed first-principles calculations using full-potential linearized augmented-plane-wave (FLAPW) method in the framework of LDA and found that CuN(B1) is less than $0.20\ eV$/atom more stable than CuN(B3), while we found that CuN(B3) is $0.043\ eV$/atom (GGA) more stable than CuN(B1). Some of their findings are shown in Table 10.4; and, again, their predicted LDA lattice constants are slightly less than our GGA values, while their obtained bulk moduli are overestimated when compared to ours.

Using full-potential linear muffin-tin orbital (FP-LMTO) method within GGA(PBE), Wang et al. [192] studied the $E(V)$ EOS of CuN in the B1, B2, B3, $B8_1$ and B4 structures. Their obtained equilibrium lattice parameters and bulk muduli are included in Table 10.4 which show good agreement with ours. However, Fig. 10.19b shows that, within this parameter space, equilibrium cohesive energy decreases as B2, $B8_1$, B4, B1 and B3. This is consistent with Wang et al. but $B8_1$ and B4 are swaped. Nevertheless, B3 is the most stable in both works, contrary to the findings of Shimizu, Shirai and Suzuki [189].

Whatever the case, in our wider parameter space, Fig. 10.19b and Table 10.4 reveal that CuN(B17) is $0.17\ eV$/atom and $0.21\ eV$/atom (GGA) more stable than CuN(B3) and CuN(B1), respectively. It may be worth to mention again here that B17 was theoretically predicted to be the ground-state structure of PtN [30].

Using norm-conserving ultra-soft pseudopotential within GGA and the so-called BFGS scheme for geometry optimization, Bouayed et al. [254] studied CuN in the B1 and B3 structures, and CuN_2 in the C1 structure. Although their obtained lattice constants (given in Table 10.4) are in good agreement with our findings, the noticable difference in bulk moduli may be traced back to the numerical fitting (see Subsection 10.4.3).

10.4.6 Electronic Properties

Band structure (i.e. $\epsilon_i^\sigma(\mathbf{k})$ curves) and spin-projected total and partial (i.e. orbital resolved) density of states (DOS) of the energetically most stable phases are presented in Figs. 10.21, 10.22, 10.23, 10.24 and 10.25. Spin-projected total density of states (TDOS) are shown in subfigure (b) in each case. In all cases, TDOS's are completely symmetrical in majority and minority spins. That

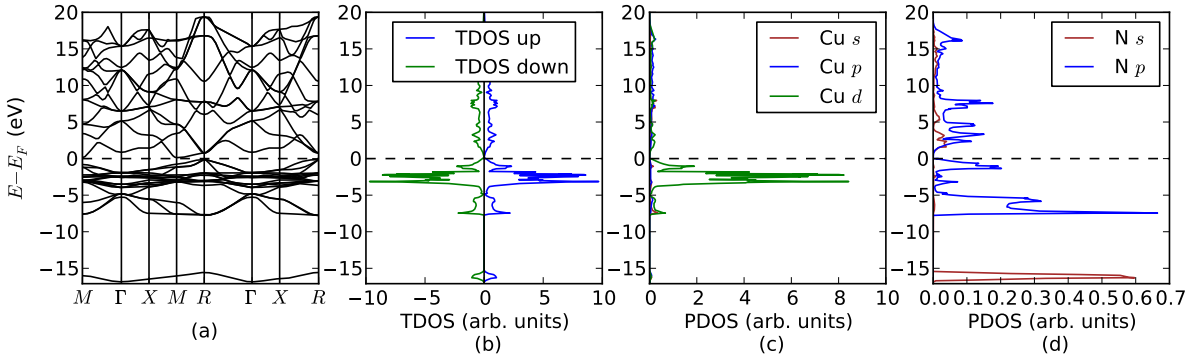

Figure 10.21: (Color online.) DFT calculated electronic structure for Cu_3N in the $D0_9$ structure: **(a)** band structure along the high-symmetry $\mathbf{k}$-points (see Table 8.1); **(b)** spin-projected total density of states (TDOS); **(c)** partial density of states (PDOS) of Cu(s,p,d) orbitals in Cu_3N; and **(d)** PDOS of N(s,p) orbitals in Cu_3N.

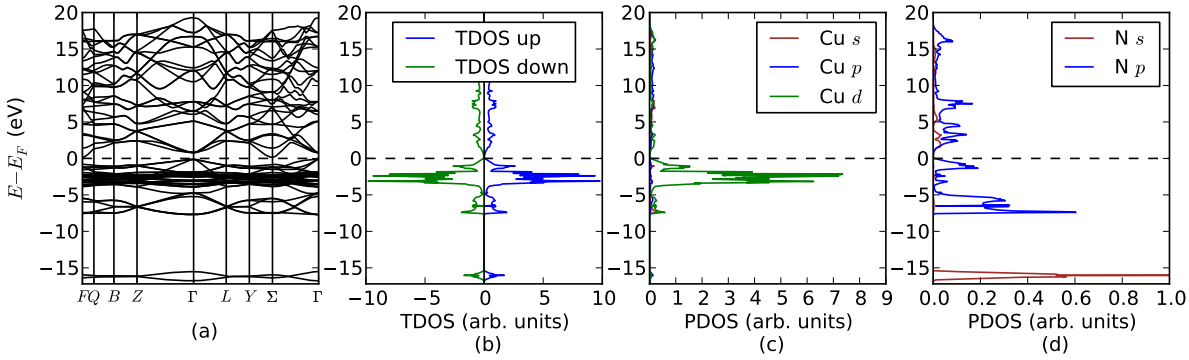

Figure 10.22: (Color online.) DFT calculated electronic structure for Cu_3N in the RhF_3 structure: **(a)** band structure along the high-symmetry $\mathbf{k}$-points (see Table 8.1); **(b)** spin-projected total density of states (TDOS); **(c)** partial density of states (PDOS) of Cu(s,p,d) orbitals in Cu_3N; and **(d)** PDOS of N(s,p) orbitals in Cu_3N.

is, electrons occupy the majority and minority spin bands equally and result in a zero total spin moment and a zero spin-polarization ratio: $\mathrm{SPR}_{\mathrm{DOS}}(E) = |\left(D_{\uparrow}(E) - D_{\downarrow}(E)\right) / \left(D_{\uparrow}(E) + D_{\downarrow}(E)\right)|$. That is why it was sufficient only to display spin-up partial density of states (PDOS) and spin-up band structures. To properly show details of the electronic structure of these phases, we plotted the energy bands along densely sampled high-symmetry string of neighbouring points in the $\mathbf{k}$-space; while displaying the Cu(s,p,d) and N(s,p) partial DOS allows us to extract information about the orbital character of these bands.

Energy bands $\epsilon_i^{\sigma}(\mathbf{k})$, total density of states (TDOS) and partial (orbital-resolved) density of states

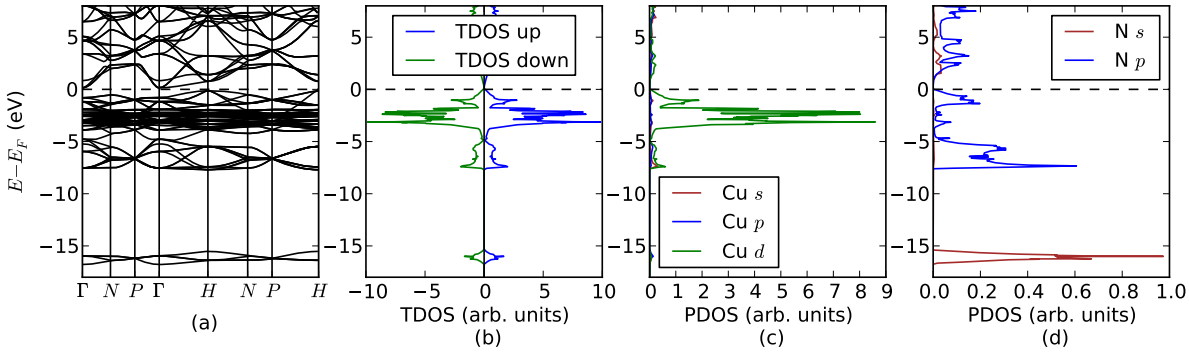

Figure 10.23: (Color online.) DFT calculated electronic structure for Cu_3N in the $D0_2$ structure: **(a)** band structure along the high-symmetry **k**-points (see Table 8.1); **(b)** spin-projected total density of states (TDOS); **(c)** partial density of states (PDOS) of Cu(s, p, d) orbitals in Cu_3N; and **(d)** PDOS of N(s, p) orbitals in Cu_3N.

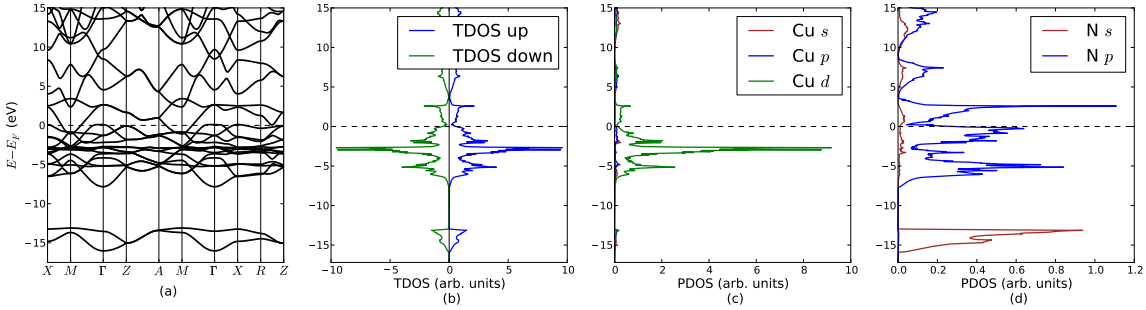

Figure 10.24: (Color online.) DFT calculated electronic structure for CuN in the B17 structure: **(a)** band structure along the high-symmetry **k**-points (see Table 8.1); **(b)** spin-projected total density of states (TDOS); **(c)** partial density of states (PDOS) of Cu(s, p, d) orbitals in CuN; and **(d)** PDOS of N(s, p) orbitals in CuN.

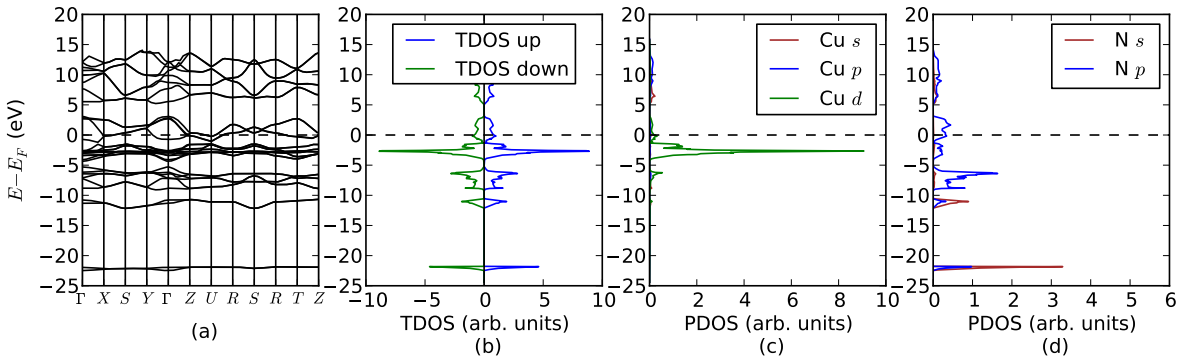

Figure 10.25: (Color online.) DFT calculated electronic structure for CuN_2 in the C18 structure: **(a)** band structure along the high-symmetry **k**-points (see Table 8.1); **(b)** spin-projected total density of states (TDOS); **(c)** partial density of states (PDOS) of Cu(s, p, d) orbitals in CuN_2; and **(d)** PDOS of N(s, p) orbitals in CuN_2.

(PDOS) of $Cu_3N(D0_9)$ are shown in Figs. 10.21. It is clear that $Cu_3N(D0_9)$ presents insulating character in its spin band. It has its valence band maximum (VBM) at R which lies $0.13\ eV$ below the Fermi energy E_F, and its conduction band minimum (CBM) at M which also lies $0.13\ eV$ above E_F, resulting in a narrow indirect gap of $0.26\ eV$. By looking at the PDOS plots, energy bands can be divided into three parts: a deep band around $\sim -16\ eV$ below E_F consists mainly of N$(2s)$, a broad group of 12 valence bands with $\sim 8\ eV$ of width that comes mostly from the $3d$ electrons of Cu plus smaller contribution from N$(2p)$, and the conduction bands.

Our obtained band structure of $Cu_3N(D0_9)$ agrees *qualitatively* well with many previous theoretical works [33, 46, 187]; however, depending on the calculation method, the value of the indirect band gap of $Cu_3N(D0_9)$ was predicted to be $0.23\ eV$ (LAPW+LDA) [33], $0.25\ eV$ (FP-LAPW+GGA(PBE)) [18,187], $0.355\ eV$ (UPP-GGA(Perdew-Wang)) [46] and $0.9\ eV$ (LCAO+LDA) [33]. Although our predicted band structure and gap value agree well with many theoretical calculations, the experimentally reported values of the energy gap E_g of $Cu_3N(D0_9)$ are larger, as will be discussed in Subsection 10.4.7. This is a well known drawback of Kohn-Sham DFT-based calculations to understimate the band gap.

Fig. 10.22 shows that the top of the valence band and the bottom of the conduction band of $Cu_3N(RhF_3)$ are about to touch the Fermi level at $(\Gamma, -0.13\ eV)$ and $(\Sigma, 0.15\ eV)$, respectively. Hence, we have an indirect band gap of $0.28\ eV$ with E_F slightly shifted towards the VBM.

The third most stable candidate in this 3:1 series is $Cu_3N(D0_2)$. Its band structure (shown in Fig. 10.23) has the VBM at $(H, -0.14\ eV)$, and the CBM at $(\Gamma, 0.14\ eV)$, resulting in an indirect energy gap of $0.28\ eV$.

The orbital resolved density of states (PDOS) of both $Cu_3N(D0_2)$ and $Cu_3N(RhF_3)$ share the same qualitative features with those of $Cu_3N(D0_9)$. As expected, the structural relation between these three phases are reflected into their electronic properties.

Energy bands $\epsilon_i^\sigma(\mathbf{k})$, total density of states (TDOS) and partial (orbital-resolved) density of states (PDOS) of CuN(B17) are shown in Figs. 10.24. It is clear that CuN(B17) would be a true metal at its equilibrium. The major contribution to the very low TDOS around Fermi energy E_F comes from the $2p$ states of the N atoms. Beneath E_F lies a band with $\sim 8\ eV$ of width, in which one can notice that the main contribution is due to the mixture of Cu$(3d)$ states with N$(2p)$ states. The N$(2s)$ states dominate the deep lowest region, while the unoccupied states stem mainly from the N$(2p)$ states. Fermi surface intersects two bands: a lower one in the M-Γ-X-R directions,

and a higher band in the Γ-M-A and M-X directions. Hence, E_F is not a continous surface contained entirely within the first BZ.

So, in CuN(B17), the nitridation effects on the pure Cu can be summarized from previous sections as: significant increase in the volume per atom V_0, increase in the bulk modulus resulting in a less compressible material than the pure metal, while the metallic character is preserved . Similar results for CuN(B3) were also arrived at by other researchers [254].

It may be worth to mention here that B1 [65, 254], B2 [65, 254], B3 [65] and B4 [65] phases of CuN were also theoretically predicted to be metallic.

With E_F crossing the finite TDOS, Fig. 10.25 shows that CuN_2(C18) is metallic at $0\ K$. The PDOS reveals that the major contribution to the TDOS at E_F comes from the N$(2p)$ states with minor contribution from the Cu$(3d)$ states. Compared to CuN(B17), a new feature of this 1:2 nitride is the contribution of N$(2p)$ states to N$(2s)$ states at the deep lowest region. However, variation in N$(2s)$ energy with respect to **k** is smaller than the variation of N$(2p)$ states, resulting in a narrower and higher PDOS. It may be instructive to mention here that CuN_2(C1) phase was also found to be metallic [254].

A common feature between all the studied cases is the higly structured, intense and narrow series of peaks in the TDOS valance band corresponding to superposition of N$(2p)$-states and Cu$(3d)$-states. In their $\mathbf{k}$-space, Cu$(3d)$ energies show little variation with respect to $\mathbf{k}$; hence the Hove singularities-like sharp features.

To summarize this section, we have found that the most stable phases of CuN and CuN_2 are metallic, while Cu_3N is a semiconductor. This finding agrees well with literature, specially with Armenta and Soto [36] who predicted theoretically that the semiconducting state is sensitive to the nitrogen concentration and changes to metallic when the composition is out of the ideal nitrogen to copper ratio, $x = 1/3$. Armenta and Soto, who studied the effect of introducing N atoms in one by one basis to the bulk cubic Cu matrix, also pointed out that as x increases, the TDOS at E_F, due to both N and Cu atoms, increases as well. Concerning this point, our findings are in excellent agreement with theirs, since we found for the most stable phases (i.e. Cu_3N, CuN and CuN_2, respectively) that TDOS$(x = 1/3) = 0$, TDOS$(x = 1) \sim 0.70$ and TDOS$(x = 2) \sim 0.85$, in relative arbitrary units.

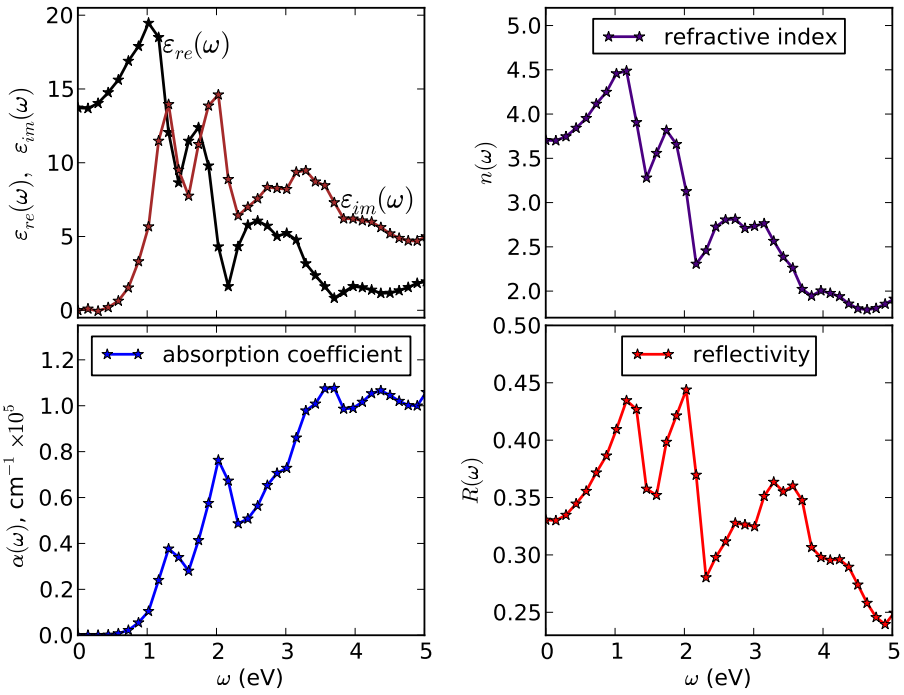

Figure 10.26: (Color online.) Normal-incidence frequency-dependent optical constants of $Cu_3N(D0_9)$.

10.4.7 Optical Properties

Fig. 10.26 displays the real and the imaginary parts of the frequency-dependent dielectric function $\varepsilon_{\text{RPA}}(\omega)$ of $Cu_3N(D0_9)$ and the corresponding derived optical constants within the optical region[11]. The real part $\varepsilon_{re}(\omega)$ shows an upward trend before $0.3\ eV$, reaches a maximum value at $1\ eV$ and generally decreases after that. The imaginary part $\varepsilon_{im}(\omega)$ has two main peaks located at $\sim 1.3\ eV$ and $\sim 2.0\ eV$. Niu et al. [251] carried out DFT(UPP-GGA) calculations and derived an $\varepsilon(\omega)$ spectrum with a real part that shows an upward trend before $1\ eV$, reaches the maximum value at $1\ eV$ (as ours) and decreases after that. The imaginary part they obtained has two main peaks, in the range $0\ eV$ to $5\ eV$, located at $2.07\ eV$ and $3.51\ eV$. By analyzing the DOS, Niu et al. claimed that these two peaks are mainly due to the electron transition from the Cu($3d$) band to the conduction band.

Refractive index $n\,(\omega)$ spectrum (Fig. 10.26) shows almost the same frequency dependance as $\varepsilon_{re}(\omega)$. Comparing our obtained $n\,(\omega)$ with the experimental results of Gordillo et al. [38], one can see a kind of general qualitative agreement between the experimental curve and the theoretical

[11] Recall that the optical region (visible spectrum) is about $(390 \sim 750)$ nm which corresponds to $(3.183 \sim 1.655)\ eV$.

one, represented by the increase in n with increase in the photon energy till reaching a maximum, then followed by a generally decreasing behaviour. However, the experimental peak of n is at $\sim (1.4\ eV, 3.65)$, while our obtained peak is at $\sim (1.2\ eV, 4.5)$. Surprisingly, the DFT(UPP-GGA)-refractive index spectrum derived by Niu et al. [251] shows far better agreement with the experimental results of Gordillo et al. [38] and they got the peak at $\sim (1.6\ eV, 3.9)$.

From the absorption coefficient $\alpha(\omega)$ spectrum (Fig. 10.26), it can be seen that $Cu_3N(D0_9)$ starts absorbing photons with $\sim 0.75\ eV$ energy. Hence, it is clear that GW_0 calculations give a band gap of $\sim 0.75\ eV$, which is a significant correction to the obtained DFT value. Our presented $\alpha(\omega)$ spectrum agrees qualitatively well with the experimental work of Gordillo et al. [38], who, in the $\sim (0.6\ -\ 1.4)\ eV$ region, obtained a smooth exponential-like curve. However, their obtained $\alpha(\omega)$ reaches 1×10^5 cm^{-1} in the visible range before $1.4\ eV$, while ours (Fig. 10.26) never reaches such a value before $3.3\ eV$. Niu et al. [251] got a curve that reaches this value at $\sim 3.6\ eV$. However, their $\alpha(\omega)$ spectrum starts to be non-zero from $\sim 0.71\ eV$!

Gordillo et al. [38] prepared nearly stoichiometric copper nitride polycrystalline films having nitrogen contents of $(27 \pm 2)\%$ with lattice parameter $a = 3.8621$ Å. They referred to it in their article as stoichiometric Cu_3N, and, at room temperature and with orientation along the $(1\ 0\ 0)$ crystallographic axis, they carried out some optical measurements and fitted the obtained data. From the fits, they managed to derive the refractive index and the absorption coefficient, while reflectance was measured directly. So, although our calculated optical properties show partial agreement with this experimental work, discrepancies may be attributed due to the lack of knowledge of the exact stoichiometry of the prepared samples. Wang, Nakamine, and Hayashi [43] also prepared nearly stoichiometric Cu_3N films at 67 Pa. Their experimentally obtained $\alpha(\omega)$ spectra reach 1×10^5 cm^{-1} at about $2.4\ eV$. However, α leaves the zero level only at about $(1.8 \sim 1.9)\ eV$. On the other hand, the used $E_{cut} = 290\ eV$ and $8 \times 8 \times 8$ $\mathbf{k}$-mesh in the DFT(UPP-GGA) calculations by Niu et al. [251] may not be sufficient to reproduce *qualitatively* similar spectra as those we obtained from GWA calculations. No quantitative correspondence is to be expected.

Experimentally reported values of the $Cu_3N(D0_9)$ optical gap spread over a wide range [34, 38]. Some of these values are: $(0.25 \sim 0.83)\ eV$ [45], $1.30\ eV$ [37, 252], $(1.7 \sim 1.84)\ eV$ [250], $1.85\ eV$ [35] and $(1.8 \sim 1.9)\ eV$ [43]. Hence, although GWA calculations give a band gap of $\sim 0.75\ eV$, which is a significant correction to the obtained DFT value of $0.26\ eV$, the difference

between theory and experiment is still considerable. This is a well known problem with GWA calculations on top of DFT eigenvalues and eigenstates that correspond to a very small bandgap compared to experiment.

Given that standard DFT functionals severely underestimate the band gaps while the Hartree-Fock (HF) approximation overestimates them [152], a potential solution is to combine local or semilocal DFT exchange with a portion of nonlocal exact exchange thereby constructing the so-called hybrid functional [259]. Much improved band gaps can be obtained by screening the nonlocal HF-type portion of exchange potential with a suitable screening parameter [260, 261]. A more appropriate approach is to apply the partially self-consistent GW method on eigenvalues obtained using hybrid functionals or DFT+U schemes [262] which readily provide better band gaps for insulators [263].

10.5 Silver Nitrides

The energy-volume equation of state (EOS) for the different structures of Ag_3N, AgN_2 and AgN are depicted in Figs. 10.27a, 10.27b and 10.27c, respectively. The corresponding calculated equilibrium properties are given in Table 10.5. In this table, we ordered the studied phases according to the increase in the nitrogen content; then within each series, structures are ordered in the direction of decreasing structural symmetry. For the sake of comparison, we also presented results from experiment and from previous *ab initio* calculations; and, whenever appropriate, the calculation method and the XC functional are also given in footnotes of the Table.

The calculated equilibrium properties: cohesive energies, formation energies, volume per atom, volume per Ag atom, and bulk modulus and its pressure derivative which are given Table 10.5, are visualized in Fig. 10.28. This kind of visualization allows us to study the effect of nitridation on the parent Ag(A1), since all quantities in this figure are given relative to the corresponding ones of the elemental Ag(A1) given in the first row of Table 10.5. Moreover, one can easly compare the properties of these phases relative to each other.

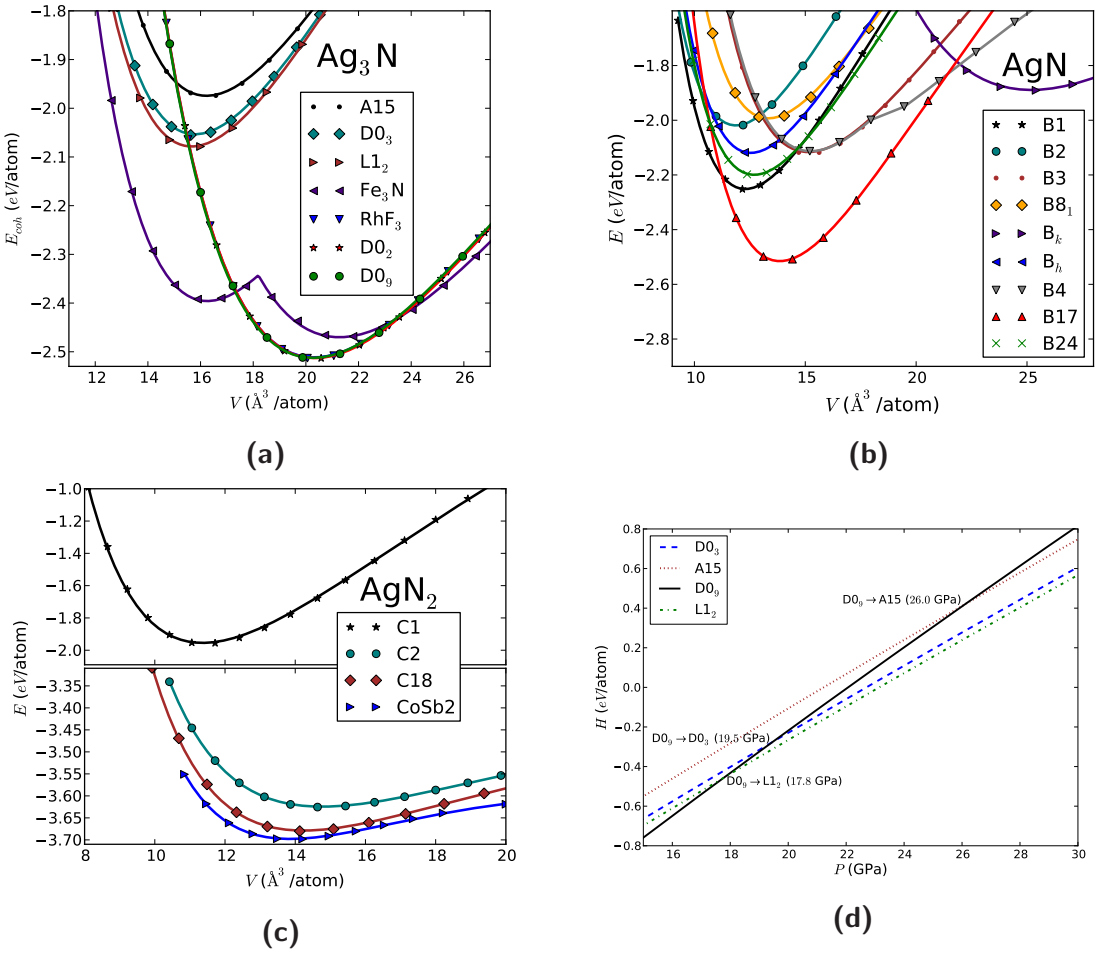

Figure 10.27: (Color online.) Cohesive energy $E_{\text{coh}}(eV/\text{atom})$ versus atomic volume V (Å^3/atom) for: **(a)** Ag_3N in seven different structural phases; **(b)** AgN in nine different structural phases; and **(c)** for AgN_2 in four different structural phases. **(d)** Enthalpy H *vs.* pressure P equation of state (EOS) for some Ag_3N phases in the range where $D0_9 \rightarrow A15$, $D0_9 \rightarrow D0_3$ and $D0_9 \rightarrow L1_2$ phase transitions occur.

Table 10.5: Calculated and experimental zero-pressure properties of the twenty studied phases of Ag_3N, AgN and AgN_2**:** Lattice constants (a(Å), b(Å), c(Å), $\alpha(^\circ)$ and $\beta(^\circ)$), equilibrium atomic volume V_0(Å^3/atom), cohesive energy $E_{\text{coh}}(eV/\text{atom})$, bulk modulus $B_0(GPa)$ and its pressure derivative B_0', and formation energy $E_f(eV/\text{atom})$. The presented data are of the current work (*Pres.*), experimentally reported (*Expt.*) and of previous calculations (*Comp.*).

Structure		$a(\AA)$	$b(\AA)$	$c(\AA)$	$\alpha(^\circ)$ or $\beta(^\circ)$	$V_0(\AA^3/\text{atom})$	$E_{\text{coh}}(eV/\text{atom})$	B_0(GPa)	B_0'	$E_f(eV/\text{atom})$
					Ag					
	Pres.	4.164	–	–	–	18.06	−2.484	88.188	5.793	
	Expt.	4.08570[a]	–	–	–		−2.95[b]	100.7[b], 101[c]	6.12[d]	
A1	*Comp.*	4.01[f]	–	–	–		−3.59[g],	142[f]	5.00[l],	
							−2.67[i],		5.97[k],	
			–	–	–		−2.66[h]		5.70[j]	
					Ag_3N					
D0$_3$	*Pres.*	6.322	–	–	–	15.79	−2.055	98.356	5.457	1.107
A15	*Pres.*	5.065	–	–	–	16.24	−1.976	92.280	5.470	1.186
	Pres.	4.328	–	–	–	20.27	−2.513	71.980	5.386	0.649
D0$_9$	*Comp.*	3.995[q],	–	–	–			95.7[r], 87.1[s]		
		4.169[r],	–	–	–					
		4.292[s]	–	–	–					
L1$_2$	*Pres.*	3.972	–	–	–	15.67	−2.081	100.743	5.530	1.081
D0$_2$	*Pres.*	8.662	–	–	–	20.31	−2.514	72.230	5.335	0.648
ϵ-**Fe$_3$N**	*Pres.*	5.967	–	5.560	–	21.43	−2.469	64.737	2.335	0.692
RhF$_3$	*Pres.*	6.126	–	–	$\alpha = 59.989$	20.31	−2.514	72.237	5.396	0.648
		4.369[u],	–	–						2.587 ± 0.364[w]
fcc[t]	**Expt.**	4.29[v],	–	–	–					
		4.378[x]	–	–	–					
					AgN					
	Pres.	4.617	–	–	–	12.30	−2.253	147.600	5.145	1.587
B1	*Comp.*	4.57[q], 4.506[r],	–	–	–			219.2[r],	4.653[p]	
		4.476[o],	–	–	–			197.18[o],	4.883[o]	
		4.606[p],	–	–	–			147.40[p],		
		4.619[s]	–	–	–			162.3[s]		
	Pres.	2.873	–	–	–	11.86	−2.021	146.157	5.260	1.819
B2	*Comp.*	2.833[q], 2.806[r],	–	–	–			138.96[p]	4.823[p]	
		2.78[o], 2.87[p]	–		–			204.10[o]	5.451[o]	
		2.876[s]	–	–	–					
	Pres.	4.950	–	–	–	15.16	−2.122	109.639	5.210	1.718
B3	*Comp.*	4.88[q], 4.816[r],	–	–	–			100.11[p]	5.825[p]	
		4.79[o], 4.94[p]	–	–	–			151.05[o]	4.542[o]	
		4.946[s]	–	–	–					
B8$_1$	*Pres.*	3.544	–	4.929	–	13.40	−1.996	130.485	5.240	1.844
B$_k$	*Pres.*	3.521	–	9.368	–	25.15	−1.891	57.077	5.110	1.949
B$_h$	*Pres.*	3.096	–	3.023	–	12.55	−2.121	141.385	5.285	1.719
	Pres.	3.501	–	5.734	–	15.22	−2.113	105.992	5.467	1.727
B4	*Comp.*	3.41[o],	–	5.52[o],	–			143.68[o],	4.82[o],	
		3.54[p]	–	5.69[p]	–			110.12[p]	4.663[p]	
B17	*Pres.*	Pres. 3.158	–	5.560	–	13.86	−2.517	132.556	5.185	1.323
B24	*Pres.*	4.337	4.601	5.091	–	12.70	−2.202	138.704	5.132	1.638
					AgN_2					
	Pres.	5.157	–	–	–	11.43	−1.959	164.844	4.996	2.333
C1	*Comp.*	5.055[r], 5.172[s],	–	–	–			181.3[r], 164.5[s]		
		5.013[m], 5.141[n],	–	–	–			215[m], 164[n]		
		5.124[q]	–	–	–					
C2	*Pres.*	5.617	–	–	–	14.77	−3.626	30.058	6.894	0.666
C18	*Pres.*	3.440	4.513	5.508	–	14.25	−3.680	35.878	7.269	0.612
CoSb$_2$	*Pres.*	5.976	5.651	10.261	$\beta = 151.225$	13.90	−3.699	35.117	7.822	0.593

Notes to Table 10.5 : ————————————

[a] Ref. [240]. This is an average of 56 experimental values (with a deviation ± 0.00018Å), at $20^{\circ}C$.

[b] Ref. [172]. Cohesive energies are given at $0\ K$ and 1 atm $= 0.00010$ GPa; while bulk mudulii are given at room temperature.

[c] Ref. (25) in [219]: at room temperature.

[d] See Refs. (8)–(11) in [219].

[f] Ref. [241]: using the full-potential linearized augmented plane waves (LAPW) method within LDA.

[g] Ref. [242]: using projector augmented wave (PAW) method within LDA.

[h] Ref. [242]: using projector augmented wave (PAW) method within GGA(PW91).

[i] Ref. [242]: using projector augmented wave (PAW) method within GGA(PBE).

[j] Ref. [219]: using a semiempirical estimate based on the calculation of the slope of the shock velocity *vs.* particle velocity curves obtained from the dynamic high-pressure experiments. The given values are estimated at $\sim 298\ K$.

[k] Ref. [219]: using a semiempirical method in which the experimental static $P - V$ data are fitted to an EOS form where B_0 and B_0' are adjustable parameters. The given values are estimated at $\sim 298\ K$.

[l] Ref. [219]: using the so-called method of transition metal pseudopotential theory; a modified form of a method proposed by Wills and Harrison to represent the effective interatomic interaction.

[m] Ref. [64]: using the full-potential linearized augmented plane waves (LAPW) method within LDA.

[n] Ref. [64]: using the full-potential linearized augmented plane waves (LAPW) method within GGA.

[o] Ref. [65]: using full-potential (linearized) augmented plane waves plus local orbitals (FP-LAPW+lo) method within LDA.

[p] Ref. [65]: using using full-potential (linearized) augmented plane waves plus local orbitals (FP-LAPW+lo) method within GGA(PBE).

[q] Ref. [264]: using pseudopotential (PP) method within LDA.

[r] Ref. [264]: using linear combinations of atomic orbitals (LCAO) method within LDA. B_0's are calculated from elastic constants.

[s] Ref. [264]: using linear combinations of atomic orbitals (LCAO) method within GGA. B_0's are calculated from elastic constants.

[t] This is the face centered cubic (fcc) structure with $Z = 4/3$ (i.e. 4 Ag atoms in the unit cell) suggested by Hahn and Gilbert according to some measurements (Ref. [55]).

[u] Ref. [55].

[v] Ref. [54].

[w] This is the average of the experimental values: $(+314.4 \mp 2.5)$ kJ/mol [53] $= (3.25853 \pm 0.02591)\ eV$/atom, $+199$ kJ/mol [57] $= 2.062\ eV$/atom, $+255$ kJ/mol [55] $= 2.643\ eV$/atom, and $+230$ kJ/mol [56] $= 2.384\ eV$/atom. We used the conversion relation: 1 eV/atom $= 96.521$ kJ/mol or equivalently 1 kJ/mol $= 0.010364$ eV/atom.

[x] Ref. [58].

10.5.1 EOS and Relative Stabilities

Considering E_{coh} in the Ag_3N series, Fig. 10.27a shows clearly that the $E(V)$ relations of Ag_3N in $D0_9$, $D0_2$ and RhF_3 phases are almost identical, corresponding to equilibrium cohesive energy (Table 10.5) of -2.513, -2.514 and $-2.514\ \ eV$/atom, respectively. This behavior in the EOS could be traced back to the structural relationships between these three structures, since both $D0_2$ and RhF_3 can simply be derived from the more symmetric $D0_9$ (see Ref. [3] and references therein). These structural relations may reflect in the EOS's and in other physical properties, and the three phases may co-exist during the Ag_3N synthesis process. Relative to the elemental Ag,

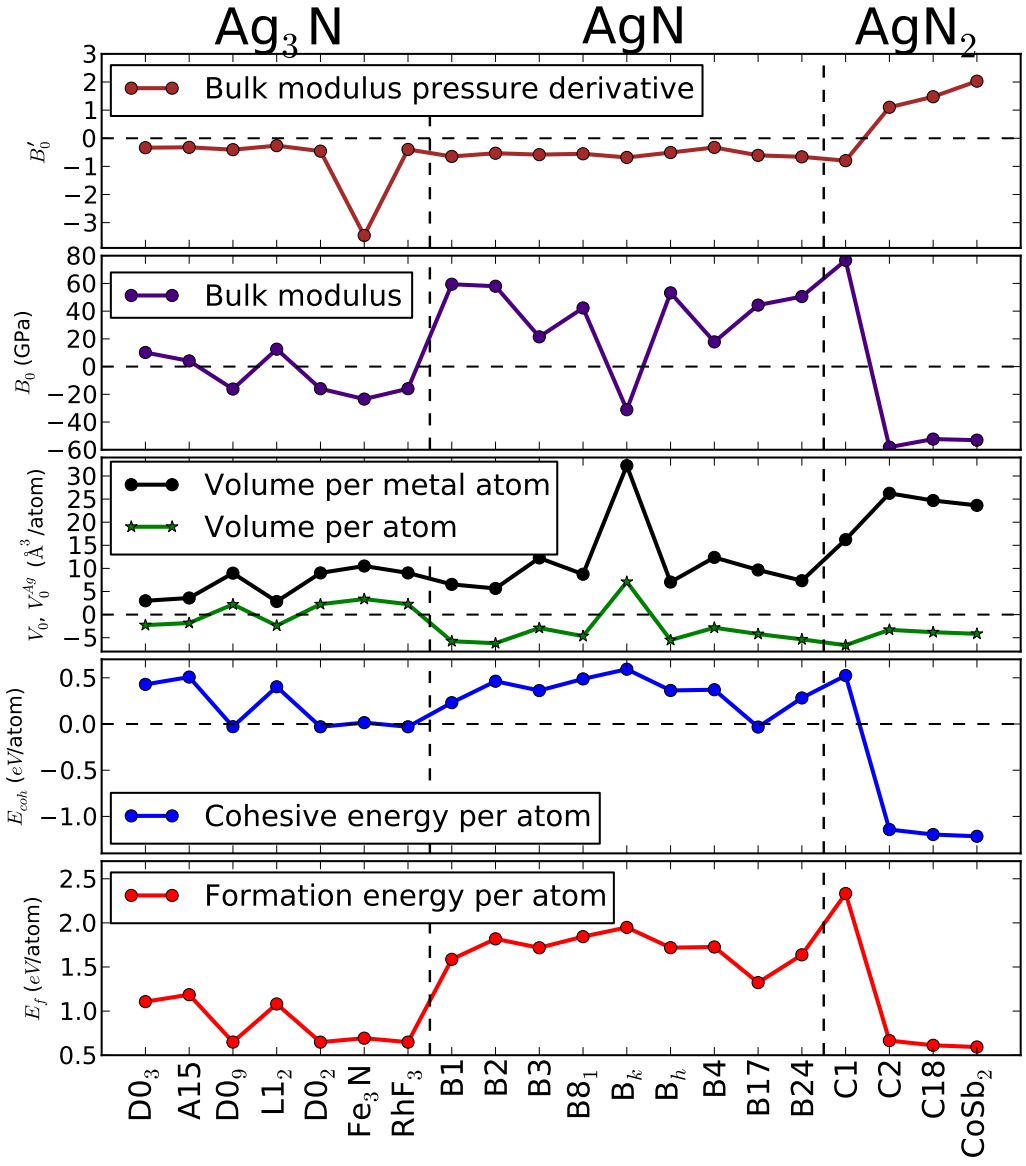

Figure 10.28: (Color online.) Calculated equilibrium properties of the twenty studied phases of silver nitrides. All quantities are given relative to the corresponding ones of the *fcc* crystalline elemental silver given in the first row of Table 10.5. The vertical dashed lines separate between the different stoichoimetries.

these three phases tend not to change the E_{coh} (Fig. 10.28), lowering it only by $\sim 0.03\ eV$/atom, as can been seen from Table 10.5. It may be worth to mention here that the simple cubic $D0_9$ phase is the stable phase of the synthesized Cu_3N [32, 33].

The odd behavior of the EOS of Ag_3N(Fe_3N) with the existence of two minima (Fig. 10.27a) shows that the first minima (to the left) is a metastable local minimum that cannot be maintained as the system is decompressed. Ag ions are in the $6g$ Wyckoff positions: $(x,0,0),(0,x,0)$, $(-x,-x,0),(-x,0,\frac{1}{2}),(0,-x,\frac{1}{2})$ and $(x,x,\frac{1}{2})$; with $x \sim \frac{1}{3}$ to the left of the potential barrier (represented by the sharp peak at ~ 18.2 Å^3/atom), and $x = \frac{1}{2}$ to the right of the peak. It may be relevant to mention here that Cu_3N(Fe_3N) was found to behave in a similar manner [3].

The crossings of the less stable A15, $D0_3$ and $L1_2$ EOS curves with the more stable $D0_9$, $D0_2$ and RhF_3 ones at the left side of their equilibrium points reveals pressure-induces phase transitions from the latter phases to the former. To show this, we plotted the corresponding relation between enthalpy $H = E(V)+PV$ and the imposed pressure P in Fig. 10.27d. Since $D0_9$, $D0_2$ and RhF_3 phases have identical $E(V)$ curves, the corresponding $H(P)$ curves are also identical. Hence, only the $H(P)$ of $D0_9$ is displayed in Fig. 10.27d. A point where the enthalpies of two phases are equal determine the phase transition pressure P_t; and, indeed, the direction of the transition is from the higher H to the lower H [213]. As depicted in Fig. 10.27d, $P_t(D0_9 \rightarrow L1_2) = 17.8$ GPa, $P_t(D0_9 \rightarrow D0_3) = 19.5$ GPa and $P_t(D0_9 \rightarrow A15) = 26.0$ GPa. Thus, $D0_9$, $D0_2$ and RhF_3 would not survive behind these P_t's and A15, $D0_3$ and $L1_2$ are preferred at high pressure.

Fig. 10.28 reveals that the AgN group contains the least stable phase among all the twenty studied phases: the hexagonal B_k. Fig. 10.27b and Table 10.5 show that the simple tetragonal structure of cooperite (B17) is the most stable phase in this AgN series. In fact, one can see from Fig. 10.28 and Table 10.5 that all the considered AgN phases possess less binding than their parent Ag(fcc), except AgN(B17) which is slightly more stable, with $0.033\ eV$/atom lower E_{coh}. It is interesting to notice that AgN(B17) is $\sim 0.003\ eV$/atom more stable than the Ag_3N most stable phases. Moreover, this B17 structure was theoretically predicted to be the ground-state structure of CuN [3], AuN [6], PdN [7] and PtN [30].

Using the full-potential (linearized) augmented plane waves plus local orbitals (FP-LAPW+lo) method within LDA and within GGA, Kanoun and Said [65] studied the $E(V)$ EOS for AgN in the B1, B2, B3 and B4 structures. The equilibrium energies they obtained from the $E(V)$ EOS

revealed that B1 is the most stable phase, and the relative stability they arrived at is in the order B1–B3–B4–B2, with a significant difference in total energy between B3 and B4 (see Fig. 2(b) in that article). Within this subset of structures, the numerical values of E_{coh} in Table 10.5 do have the same order. However, the difference between the equilibrium E_{coh}(B3) and E_{coh}(B4) is only $\sim 0.009\ eV$, and the $E(V)$ EOS of B3 and B4 match/overlap over a wide range of volumes around the equilibrium point. This discrepancy may be attributed to the unphysical/ill-defined measure of stability that Kanoun and Said used, the *total* energy, while the number of the AgN formula units per unit cell in the B4 structure differs from that in the others[12]. Nevertheless, it may be worth mentioning here that AgN(B3) was found to be elastically unstable [264].

In the CuN_2 nitrogen-richest phase series, we can see from Table 10.5 and from Fig. 10.28 that the phases of this group are significantly more stable than all the other studied phases, except C1, which is, in contrast, the second least stable among the twenty studied phases, with $0.017\ eV$/atom more than AgN(B_k). From Fig. 10.27c, Fig. 10.28 and Table 10.5, one can see that in this series, the lower the structural symmetry, the more stable is the phase. It was found that CuN_2 phases have the same trend [3].

Comparing the relative stability of Ag_3N, AgN and AgN_2, we find from Table 10.5 and from Fig. 10.28 that AgN_2 in its least symmetric phase, the simple monoclinc structure of $CoSb_2$, is the most energetically stable phase with $E_{\text{coh}} = -3.699\ eV$/atom.

10.5.2 Volume per Atom and Lattice Parameters

The numerical values of the lattice parameters and the average equilibrium volume per atom V_0 for the twenty modifications are presented in Table 10.5. The middle subwindow of Fig. 10.28 depicts the V_0 values relative to the Ag(fcc). To measure the average of the Ag–Ag bond length in the silver nitride, the equilibrium average volume per Ag atom (V_0^{Ag}), which is simply the ratio of the volume the unit cell to the number of Ag atoms in the unit cell, is visualized in the same subwindow.

From the V_0 curve in Fig. 10.28, we can see that, all AgN and AgN_2 modifications, except the open AgN(B_k) phase, decrease V_0; while the Ag_3N phases tend, on average, not to change the number density of the parent Ag(A1).

[12] In their original article [65], Kanoun and Said stated that "*... there are two atom in wurtzite unit cell, and one in all the other cases.*" which is a clear typo!

On the other hand, the V_0^{Ag} curve in Fig. 10.28 reveals that, relative to the elemental Ag and to each other, V_0^{Ag} *tends* to increase with the increase in the nitrogen content. Thus, in all these nitrides, the introduced N ions displace apart the ions of the host lattice causing longer Ag-Ag bonds than in the elemental Ag. This cannot be seen directly from the V_0 values depicted in the same figure.

For AgN in the B1, B2, B3 and B4 structures, Kanoun and Said (Ref. [65] described in Sec. 10.2.1 above) obtained GGA equilibrium lattice parameters which are in very good agreement with ours. Their obtained LDA lattice parameter values show the common underestimation with respect to their and our GGA values (see Table 10.5).

Gordienko and Zhuravlev [264] studied the structural, mechanical and electronic properties of AgN(B1) , AgN(B2), AgN(B3), AgN_2(C1) and $Ag_3N(D0_9)$ cubic phases. Their DFT calculations were based on pseudopotential (PP) method within LDA, and on linear combinations of atomic orbitals (LCAO) method within both LDA and GGA. For comparison, some of their findings are included in Table 10.5. Within the parameter subspace they considered, our GGA values of the a lattice parameter agree very well with theirs. On the other hand, although their PP a values are closer to the GGA ones (ours and theirs), all their LDA values are less than the GGA ones. This confirms the well-known behavior of LDA compared to GGA [134, 135, 247]. Gordienko and Zhuravlev also found that the Ag–Ag interatomic distance increases in the order Ag_3N–AgN–AgN_2. This agrees with the general trend shown in Fig. 10.28, since the V_0^{Ag} curve shows an average increase in the same direction.

10.5.3 Bulk Modulus and its Pressure Derivative

Fig. 10.28 reveals that Ag_3N phases tend, on average, to preserve the B_0 value of the parent Ag(A1). Increasing the nitrogen content to get AgN phases will increase the B_0 value of the parent Ag(A1), except in the case of B_k. While the nitrogen in AgN_2 tends to lower the B_0 value of the parent Ag(A1), the cubic C1 phase posses the highest B_0 value. This could be seen from Fig. 10.27c, where the curvature of the $E_{\mathrm{coh}}(V)$ curve of C1 is higher compared to the shallow minima of the C2, C18 and $CoSb_2$ curves.

From the definition of the equilibrium bulk modulus (Eq. 7.2.2), one would expect B_0 to increase as E_{coh} or V_0 decreases. This is because of the minus sign of the former and the inverse propor-

tionality of the latter. That is, *roughly speaking*, the B_0 curve should have a mirror reflection-like behavior with respect to the E_{coh} and V_0 curves. Nevertheless, if E_{coh} or V_0 are increasing and the other is decreasing, then the dominant net effect will be of the one with the higher change [13]. For example, Fig. 10.28 shows that in going from $D0_3$ to A15, both E_{coh} and V_0 increase resulting in a negative change in B_0. In going from A15 to $D0_9$, E_{coh} is decreasing while V_0 is increasing, but, in the end, the latter won the competition and lowered the value of B_0. This argument stays true throughout the three series. When there is no significant change in both E_{coh} and V_0, there is no significant change in B_0. This is the case when one goes from C18 to $CoSb_2$. A close look at the B_0 curve in Fig. 10.28, reveals that the huge decrease in E_{coh} between C1 and C2 defeats the relatively small increase in V_0. This is simply because, according to Eq. 7.2.2, the value of B_0 is proportional to the *absolute* change in E_{coh}, while it is far more sensitive to any change in V_0 because it is proportional to $(\Delta V_0)^{-1}$.

It is common to measure the pressure dependence of B_0 by its derivative B_0' (Eq. 7.2.3). Fig. 10.28 shows that the B_0 value of the C2, C18 and $CoSb_2$ phases increases as these phases are put under pressure. While the B_0 values of the rest of the phases shows very low sensitivity to pressure and they tend to slightly lower the bulk modulus, the Fe_3N phase is the most sensitive phase and tends to significantly lower its B_0 upon application of pressure. This high sensitivity may indicate that the corresponding minimum on the potential surface is not global, but another local minimum as the one at 16.2 $\mathring{A}^3$/atom (Fig. 10.27a).

From the elastic constants they obtained, Gordienko and Zhuravlev [264] calculated the corresponding macroscopic bulk moduli (included in Table 10.5). They found the highest LDA B_0 value for AgN(B1) among all phases they considered, but, in agreement with the present work, they obtained the highest GGA B_0 value for AgN_2(C1). Since LDA relative to GGA overestimates E_{coh} and thus underestimates V_0, *each* of these two factors (see Subsection 10.2.4) would separately lead to the odd LDA value of 219.2 GPa which they obtained. Nevertheless, due to this fact, Gordienko and Zhuravlev argued that one should consider the LDA and GGA average value of B_0.

[13] Since Eq. 7.2.2 does not refer to any stoichiometry or any species (that is, it does not consider the way that the change in energy or volume was done), we may take the change in volume (or energy) with respect to itself, with respect to the parent Ag(A1), or with respect to any of the other nineteen considered modifications.

10.5.4 Formation Energies

Formation energies in the present work are used as a measure of the *relative* thermodynamic stabilities of the phases under consideration. That is, the lower the formation energy, the lower the tendency to dissociate back into the constituent components Ag and N_2.

The obtained formation energies E_f of the twenty relaxed phases are given in Table 10.5 and depicted graphically in Fig. 10.28. The latter shows that, relative to each other and within each series, the formation energy E_f (defined by Eqs. 7.5.2 and 7.5.3) of the studied phases has the same trend as the cohesive energy[14]. That is, all phases have the same relative stabilities in the E_f space as in the E_{coh} space. However, while Ag_3N phases tend to have equal E_{coh} as the AgN phases, all Ag_3N modifications have a lower E_f than the AgN ones. Hence, silver nitride is more likely to be formed in the former stoichiometry. However, all the twenty obtained E_f values are positive; which, in principle, means that all these phases are thermodynamically unstable (endothermic) [15].

Some of the experimental values of E_f for the synthesized Ag_3N phase (which is claimed to be in an fcc structure) are $+199$ kJ/mol [57] $= 2.062\ eV$/atom, $+230$ kJ/mol [56] $= 2.384\ eV$/atom, $+255$ kJ/mol [55] $= 2.643\ eV$/atom and $(+314.4 \mp 2.5)$ kJ/mol [53] $= (3.25853 \pm 0.02591)\ eV$; with an average value of $2.587 \pm 0.364\ eV$. Among the considered phases in the present work, there is only one phase wich has E_f value that fits in this range, the AgN_2(C1). Interestingly, this C1 structure has an fcc underlying Bravia lattice; however, the chemical formula differs from that of the synthesized phase.

10.5.5 Electronic Properties

The DFT(GGA) calculated band diagrams (i.e. $\epsilon_i^\sigma(\mathbf{k})$ curves) and spin-projected total and orbital resolved (i.e. partial) density of states (DOS) of the most stable phases: $D0_9$, RhF_3, $D0_2$, B17, and C18 are presented in Figs. 10.29, 10.30, 10.31, 10.32 and 10.33, respectively. Spin-projected total density of states (TDOS) are shown in sub-figure (b) in each case. In all the six considered cases, electrons occupy the spin-up and spin-down bands equally, resulting in zero

[14] Surely, this needs not to be so. Compare the definition 7.1.2 with the definition 7.5.3.

[15] It is common that one obtains positive DFT formation energy for (even the experimentally synthesized) transition-metal nitrides. Moreover, the zero-pressure zero-temperature DFT calculations have to be corrected for the conditions of formation of these nitrides. Another source of this apparent shortcoming stems from the PBE-GGA underestimation of the cohesion in N_2. We have discussed this point further in Ref. [3].

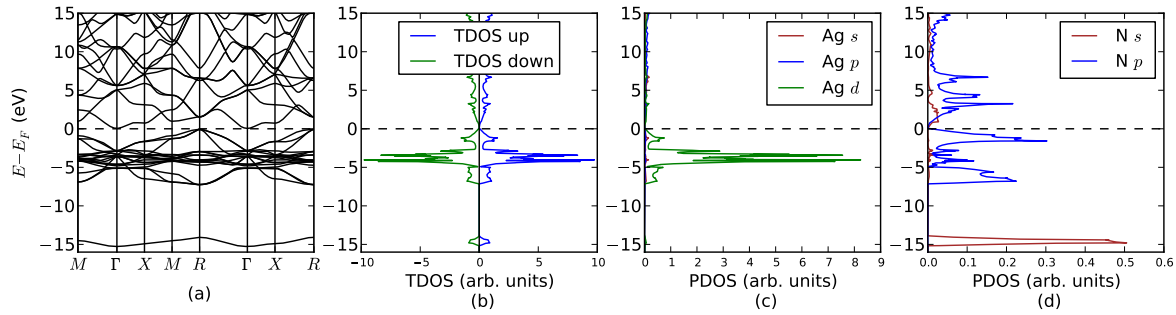

Figure 10.29: (Color online.) DFT calculated electronic structure for Ag_3N in the $D0_9$ structure: **(a)** band structure along the high-symmetry $\mathbf{k}$-points (see Table 8.1); **(b)** spin-projected total density of states (TDOS); **(c)** partial density of states (PDOS) of Ag(s,p,d) orbitals in Ag_3N; and **(d)** PDOS of N(s,p) orbitals in Ag_3N,.

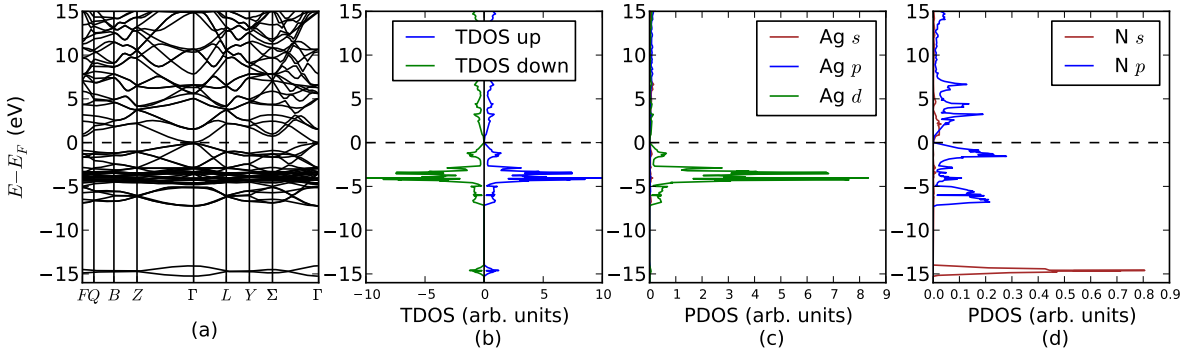

Figure 10.30: (Color online.) DFT calculated electronic structure for Ag_3N in the RhF_3 structure: **(a)** band structure along the high-symmetry $\mathbf{k}$-points (see Table 8.1); **(b)** spin-projected total density of states (TDOS); **(c)** partial density of states (PDOS) of Ag(s,p,d) orbitals in Ag_3N; and **(d)** PDOS of N(s,p) orbitals in Ag_3N.

spin-polarization density of states: $\zeta(\epsilon) = n_\uparrow(\epsilon) - n_\downarrow(\epsilon)$. Thus, it is sufficient only to display spin-up (or spin-down) density of states (DOS) and spin-up (or spin-down) band diagrams. In order to investigate the details of the electronic structure of these phases, energy bands are plotted along densely sampled high-symmetry string of neighboring $\mathbf{k}$-points. Moreover, to extract information about the orbital character of the bands, the Ag(s,p,d) and N(s,p) partial DOS are displayed at the same energy scale.

Fig. 10.29(a) shows the band structure $\epsilon_i^\sigma(\mathbf{k})$ of $Ag_3N(D0_9)$. With its valence band maximum (VBM) at $(R, -0.086\ eV)$ and its conduction band minimum (CBM) at $(\Gamma, 0.049\ eV)$, $Ag_3N(D0_9)$ presents a semiconducting character with a narrow indirect band gap E_g of $0.134\ eV$. From sub-figures 10.29(c) and (d), it is seen clearly that the Ag(d)-N(p) mixture in the region

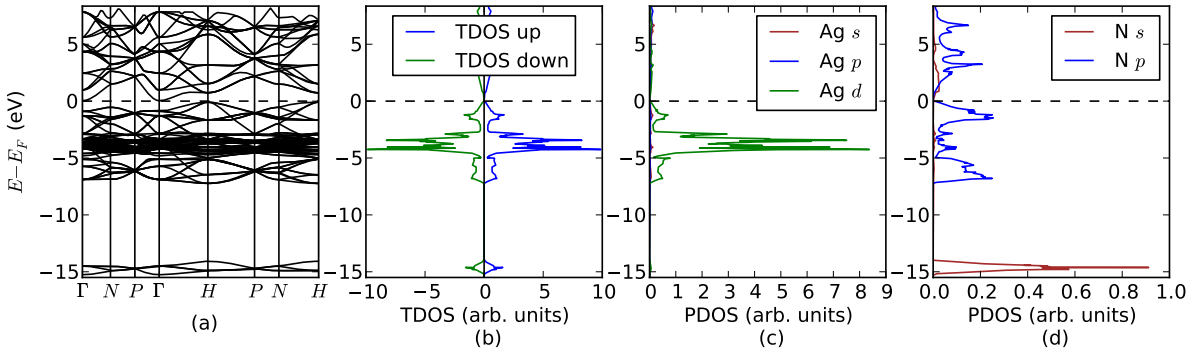

Figure 10.31: (Color online.) DFT calculated electronic structure for Ag_3N in the $D0_2$ structure: **(a)** band structure along the high-symmetry $\mathbf{k}$-points (see Table 8.1); **(b)** spin-projected total density of states (TDOS); **(c)** partial density of states (PDOS) of Ag(s, p, d) orbitals in Ag_3N; and **(d)** PDOS of N(s, p) orbitals in Ag_3N.

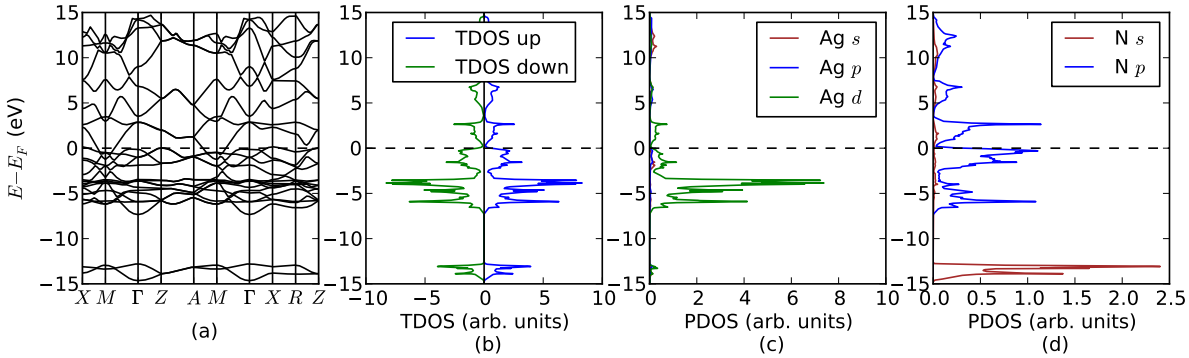

Figure 10.32: (Color online.) DFT calculated electronic structure for AgN in the B17 structure: **(a)** band structure along the high-symmetry $\mathbf{k}$-points (see Table 8.1); **(b)** spin-projected total density of states (TDOS); **(c)** partial density of states (PDOS) of Ag(s, p, d) orbitals in AgN; and **(d)** PDOS of N(s, p) orbitals in AgN.

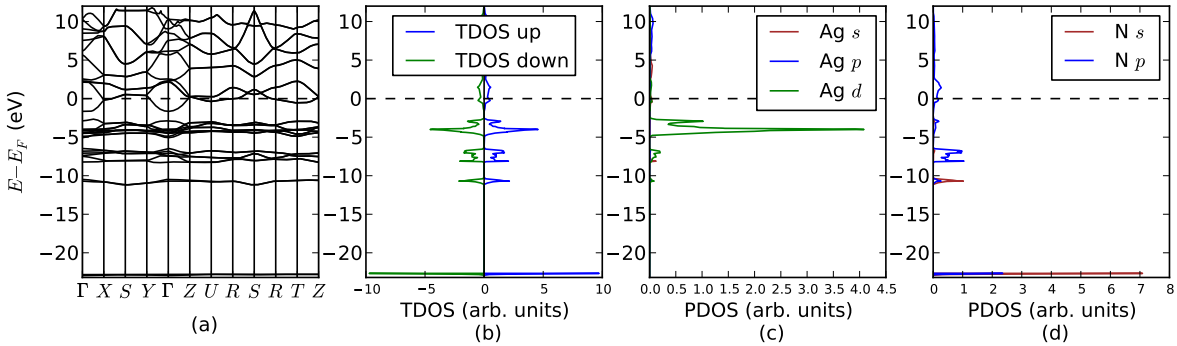

Figure 10.33: (Color online.) DFT calculated electronic structure for AgN_2 in the C18 structure: **(a)** band structure along the high-symmetry $\mathbf{k}$-points (see Table 8.1); **(b)** spin-projected total density of states (TDOS); **(c)** partial density of states (PDOS) of Ag(s, p, d) orbitals in AgN_2; and **(d)** PDOS of N(s, p) orbitals in AgN_2.

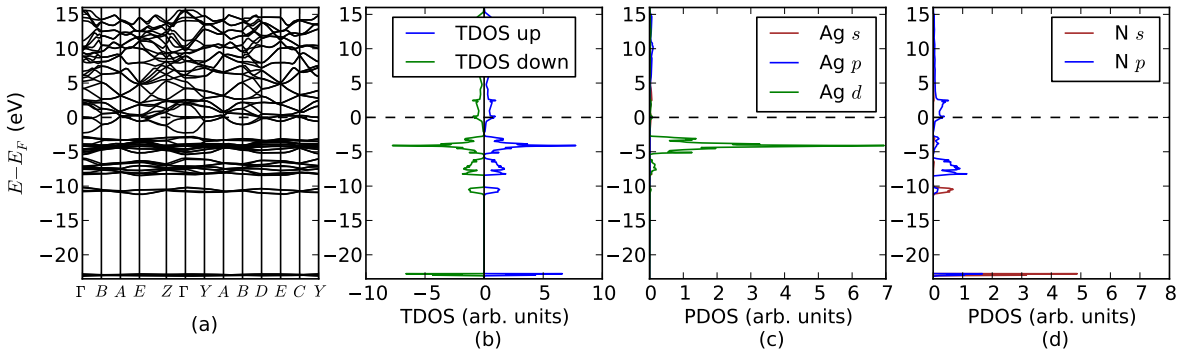

Figure 10.34: (Color online.) DFT calculated electronic structure for AgN_2 in the $CoSb_2$ structure: **(a)** band structure along the high-symmetry $\mathbf{k}$-points (see Table 8.1); **(b)** spin-projected total density of states (TDOS); **(c)** partial density of states (PDOS) of Ag(s, p, d) orbitals in AgN_2; and **(d)** PDOS of N(s, p) orbitals in AgN_2.

from $-7.286\ eV$ to $-0.086\ eV$ beneath E_F, with two peaks: a low density peak around $-1.5\ eV$ and a high density peak around $-4.0\ eV$ stemming mainly from the bands of silver d electrons. Our obtained PDOS, TDOS and band structure of $Ag_3N(D0_9)$ agree qualitatively well with Gordienko and Zhuravlev [264]; however, using LCAO method within GGA, the value of the indirect E_g of $Ag_3N(D0_9)$ they predicted is $0.25\ eV$.

To the best of our knowledge, there is no experimentally reported E_g value for Ag_3N. However, Tong [54] prepared $Ag_{3+x}N$ samples, and carried out XRD measurements to confirm the fcc symmetry of the prapared samples. Using a TB-LMTO code within LDA, Tong then calculated the band structure of Ag_3N and obtained an indirect energy gap of $1.35\ eV$. Nevertheless, we could not figure out the positions of the N ions Tong's model.

It is a well known drawback of Kohn-Sham DFT-based calculations to underestimate the band gap. Thus the more demanding GW calculations were carried out, and the obtained E_g value will be presented in Sec. 10.2.7.

Calculated electronic properties of $Ag_3N(D0_2)$ are displayed in Fig. 10.31. sub-figure 10.31(a) shows the energy bands $\epsilon_i^\sigma(\mathbf{k})$ of $Ag_3N(D0_2)$. With its valence band maximum (VBM) at $(H, -0.091\ eV)$ and its conduction band minimum (CBM) at $(\Gamma, 0.039\ eV)$, $Ag_3N(D0_9)$ presents semiconducting character with a narrow indirect band gap E_g of $0.130\ eV$. From sub-figures 10.31(c) and (d), one can notice clearly the Ag(d)-N(p) mixture in the region from $-7.249\ eV$ to $-0.091\ eV$ below E_F, with two peaks: a low density peak around $-1.3\ eV$ stemming from an almost equal mixture of Ag(d) and N(p), and a high density peak around $-4.3\ eV$ steming mainly from the bands of silver d electrons plus a relatively very low contribution from the N(p) states.

Fig. 10.30 depicts the band diagram and DOS's of $Ag_3N(RhF_3)$. In contrast to $Ag_3N(D0_9)$ and $Ag_3N(D0_2)$, sub-figure 10.30(a) shows that $Ag_3N(RhF_3)$ is a semiconductor with a narrow *direct* band gap of $0.129\ eV$ of width located at Γ point. The VBM is at $-0.089\ eV$ and the CBM is at $0.040\ eV$. From sub-figures 10.30(c) and (d), one can see the Ag(d)-N(p) mixture is in the region from $-7.286\ eV$ to $-0.089\ eV$ beneath E_F, with two peaks: a low density peak around $-1.366\ eV$ stemming from an almost equal mixture of Ag(d) and N(p), and a high density peak around $-4.382\ eV$ stemming mainly from the bands of silver d electrons plus a relatively very low contribution from the N(p) states.

The relationship between $D0_9$, $D0_2$ and RhF_3 structures manifests itself in many common features

between the electronic structure of these three Ag_3N nitrides: (i) equal E_g of $\sim 0.13\ eV$; (ii) a deep bound band around $\sim -14.6\ eV$ below E_F consists mainly of the N$(2s)$ states; (iii) a broad valence band with $\sim 7.2\ eV$ of width that comes mostly from the $4d$ electrons of Ag plus a very small contribution from N$(2p)$; and (iv) the relatively low TDOS of the conduction bands.

Energy bands $\epsilon_i^\sigma(\mathbf{k})$, total density of states (TDOS) and partial (orbital-resolved) density of states (PDOS) of AgN(B17) are shown in Figs. 10.32. It is clear that AgN(B17) would be a true metal at its equilibrium. The major contribution to the very low TDOS around Fermi energy E_F comes from the $2p$ states of the N atoms as it is evident from sub-figure 10.32(d). Beneath E_F lies a band with $\sim 7.3\ eV$ of width, in which the main contribution is due to the Ag$(4d)$ states plus a small contribution from the N$(2p)$ states. While the N$(2s)$ states dominate the deep lowest region around $13.5\ eV$, the low density unoccupied bands stem mainly from the N$(2p)$ states. The Fermi surface crosses two partly occupied bands: a lower one in the X-M, Γ-Z-A and Γ-X-R directions, and a higher band in the X-M-Γ and M-A directions. Thus, E_F is not a continuous surface contained entirely within the first BZ.

It may be worth mentioning here that AgN(B1) [65, 72] and AgN(B3) [65, 265] phases were also theoretically predicted to be metallic.

Although $AgN_2(CoSb_2)$ is the most stable phase, but the difference in cohesive energy between $AgN_2(CoSb_2)$ and AgN_2(C18) is less than $0.02\ eV$/atom, and we decided to examine the electronic structure of both phases. With E_F crossing the finite TDOS, Fig. 10.33 shows that AgN_2(C18) is metallic at $0\ K$. The orbital resolved DOS's reveal that the major contribution to the low TDOS at E_F comes from the N$(2p)$ states with tiny contributions from the $5s$, $4d$ and $3p$ states of Ag, respectively. As one can see from sub-figure 10.33(a), the E_F surface crosses the edges of the first Brillouin zone in the Z-U-R-S-T-X and T-Z directions.

The calculated electronic properties of $AgN_2(CoSb_2)$ are displayed in Fig. 10.34. Band structure, TDOS and orbital resolved DOS's have almost the same features as the corresponding ones of AgN_2(C18). It may be worth to mention here that C1 phase of AgN_2 was also theoretically predicted to be metallic [264].

Compared to the metallic AgN(B17), three new features of these 1:2 nitrides are evident: (i) Deep at $\sim -22.7\ eV$ there is a highly-localized mixture of the N(s)-N(p) states. However, the variation in N$(2s)$ energy with respect to **k** is smaller than the variation of N$(2p)$ states, resulting in a narrower and higher PDOS. (ii) Below the band that is crossed by E_F there are four bands

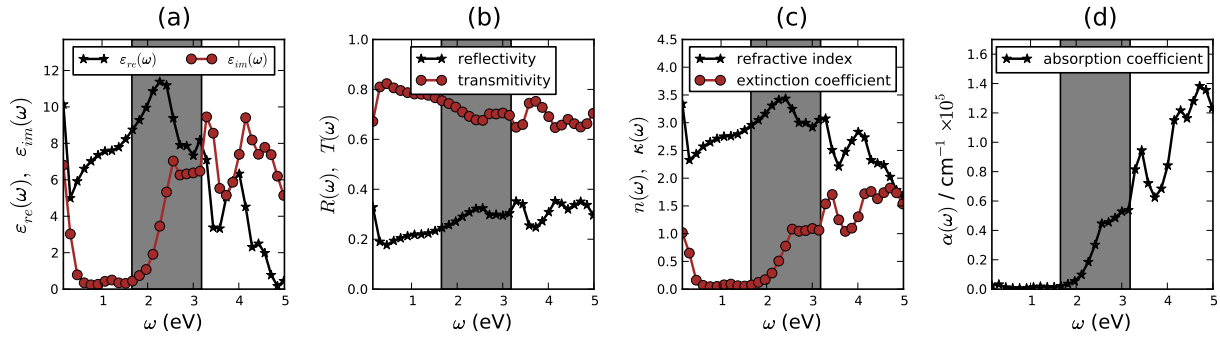

Figure 10.35: (Color online.) The GW calculated frequency-dependent optical spectra of $Ag_3N(D0_9)$: **(a)** the real $\varepsilon_{re}(\omega)$ and the imaginary $\varepsilon_{im}(\omega)$ parts of the dielectric function $\varepsilon_{RPA}(\omega)$; **(b)** reflectivity $R(\omega)$ and transmitivity $T(\omega)$; **(c)** refraction $n(\omega)$ and extinction $\kappa(\omega)$ coefficients; and **(d)** absorption coefficient $\alpha(\omega)$. The shaded area highlights the optical region.

separated by $\sim 11.4\ eV$, $\sim 1.6\ eV$, $\sim 0.38\ eV$ and $\sim 0.28\ eV$ energy gaps, respectively. (iii) The very tiny contribution of the N(p) states to the N($2p$)-Ag($4d$) band.

A common feature of all the studied cases is that Ag(p)-orbitals do not contribute significantly to the hybrid bands. Another common feature is the highly structured, intense and narrow series of peaks in the TDOS valance band corresponding to the superposition of N($2p$) and Ag($4d$) states. In their $\mathbf{k}$-space, Ag($4d$) energies show little variation with respect to $\mathbf{k}$; hence the Van Hove singularities-like sharp features.

To summarize, we have found that the most stable phases of AgN and AgN_2 are metallic, while those of Ag_3N are semiconductors. A close look at Fig. 10.32 up to Fig. 10.29 reveals that as the nitrogen to silver ratio increases from $x = 1$ to $x = 1/2$, the TDOS at E_F decreases; and by arriving at $x = 1/3$ a gap opens. This finding agrees well with Gordienko and Zhuravlev [264]. Moreover, it may be worth mentioning here that such behavior was theoretically predicted to be true for copper nitrides as well [3, 36].

10.5.6 Optical Properties

Fig. 10.35 depicts the GW calculated real and imaginary parts of the frequency-dependent dielectric function $\varepsilon_{RPA}(\omega)$ of $Ag_3N(D0_9)$ and the corresponding derived optical constants. The optical region[16] is shaded in each sub-figure.

[16] Recall that the optical region (i.e. the visible spectrum) is about $(390 \sim 750)\ nm$ which corresponds to $(3.183 \sim 1.655)\ eV$.

The real part $\varepsilon_{\text{re}}(\omega)$ (sub-figure 10.35(a)) shows an upward trend before $\sim 2.3\ eV$, where it reaches its maximum value and generally decreases after that. The imaginary part $\varepsilon_{\text{im}}(\omega)$ (same sub-figure 10.35(a)) shows an upward trend before $\sim 1.0\ eV$ and it has three main peaks located at $\sim 2.6\ eV$ in the optical region, $\sim 3.3\ eV$ at the right edge of the optical region, and at $\sim 4.1\ eV$ in the UV range.

Calculated reflectivity $R(\omega)$ and transmitivity $T(\omega)$ are displayed in sub-figure 10.35(b). With $0.6 \leq R(\omega) \leq 0.8$, it is evident that $Ag_3N(D0_9)$ is a good reflector, specially in the red and the infrared regions. In the visible range, the maximum transmitivity $T(\omega)$ is at $\sim 2.54\ eV \equiv 489$ nm, which is at the blue-green edge.

sub-figure 10.35(c) depicts the calculated refraction $n(\omega)$ and extinction $\kappa(\omega)$ coefficients. As they should, these two spectra have, in general, the same qualitative frequency dependence as the real $\varepsilon_{\text{re}}(\omega)$ and the imaginary $\varepsilon_{\text{im}}(\omega)$ dielectric functions, respectively.

From the absorption coefficient $\alpha(\omega)$ spectrum (sub-figure 10.35(d)), it can be seen that $Ag_3N(D0_9)$ starts absorbing photons with $\sim 0.9\ eV$ energy. Hence, it is clear that GW_0 calculations give a band gap of $\sim 0.9\ eV$, which is a significant improvement over the value obtained from DFT. The non-vanishing $\alpha(\omega)$ in the whole optical region agrees with the experiment, since it may explain the observed black color of the synthesized Ag_3N.

To the best of our knowledge, the present work is the first trial to theoretically investigate the optical properties of silver nitride. However, for more accurate optical characterization (e.g. more accurate positions and amplitudes of the characteristic peaks), electron-hole excitations should be calculated. This can be done by evaluating the two-body Green function G_2 on the basis of our obtained GW one-particle Green function G and QP energies, then solving the so-called Bethe-Salpeter equation, the equation of motion of G_2 [151].

10.6 Gold Nitrides

Cohesive energy E_{coh} versus atomic volume V_0 equation of state (EOS) for the considered modifications of Au_3N, AuN and AuN_2 are displayed graphically in Figs. 10.36a, 10.36b and 10.36c, respectively. The corresponding calculated equilibrium structural, energetic and mechanical properties of these twenty phases and of Au(A1) are presented in Table 10.6. Modifications in this table are ordered in the same way as in Table 5.1. Whenever possible, our results are compared

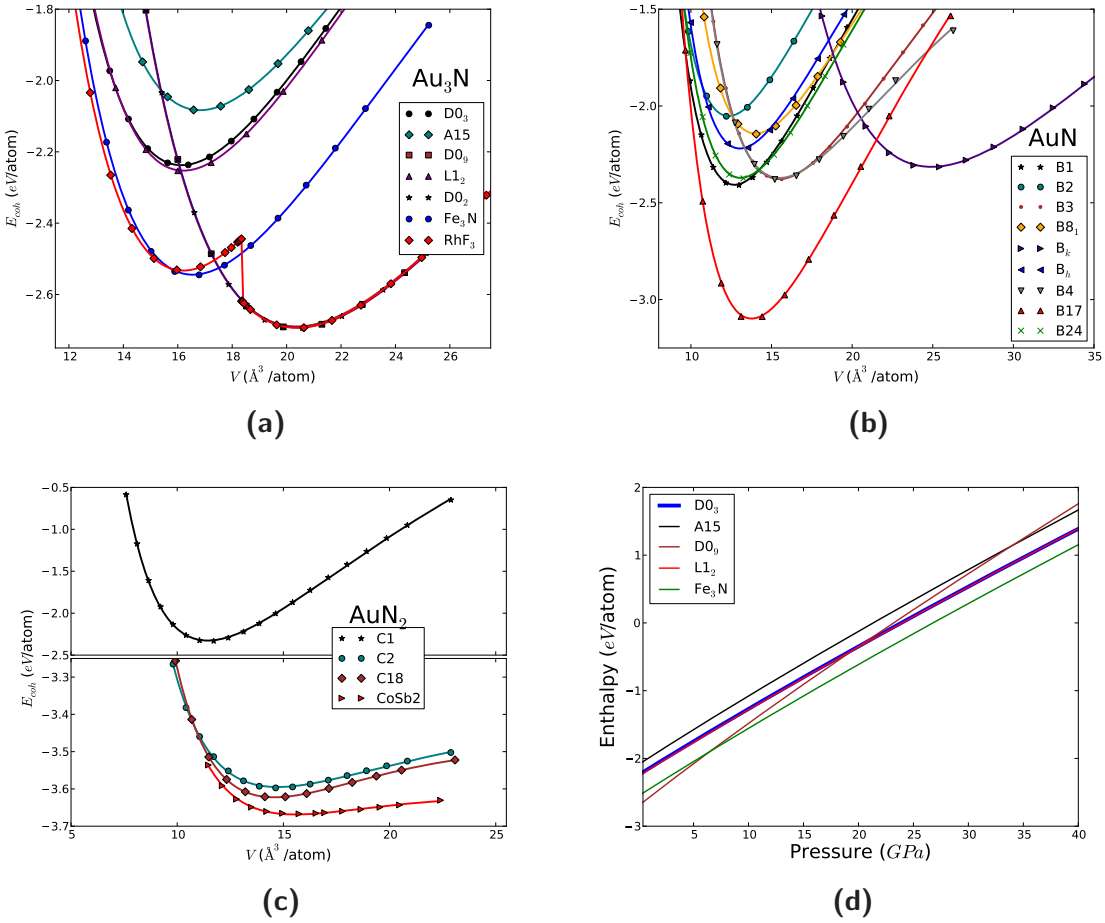

Figure 10.36: (Color online.) Cohesive energy $E_{\text{coh}}(eV/\text{atom})$ versus atomic volume V ($\text{Å}^3/\text{atom}$) for: **(a)** Au_3N in seven different structural phases; **(b)** AuN in nine different structural phases; and **(c)** for AuN_2 in four different structural phases. **(d)** Enthalpy H versus pressure P for Au_3N in five structures.

with experiment and with previous calculations. In the latter case, the calculations methods and the XC functionals are indicated in the Table footnotes.

Table 10.6: Calculated and experimental zero-pressure properties of Au(A1) and of the twenty studied phases of Au_3N, AuN and AuN_2**:** Lattice constants [a(Å), b(Å), c(Å), $\alpha(^\circ)$ and $\beta(^\circ)$], equilibrium atomic volume V_0(Å^3/atom), cohesive energy $E_{\text{coh}}(eV/\text{atom})$, bulk modulus $B_0(GPa)$ and its pressure derivative B_0', and formation energy $E_{\text{f}}(eV/\text{atom})$. The presented data are of the current work (*Pres.*), experimentally reported (*Expt.*) and of previous calculations (*Comp.*).

Structure		a(Å)	b(Å)	c(Å)	$\alpha(^\circ)$ or $\beta(^\circ)$	V_0(Å^3/atom)	$E_{\text{coh}}(eV/\text{atom})$	B_0(GPa)	B_0'	$E_{\text{f}}(eV/\text{atom})$
					Au					
A1	*Pres.*	4.174	–	–	–	18.18	−2.982	135.363	5.926	
	Exp.	4.0782[a]	–	–	–		−3.81[b]	173.2[b], 173[c]	6.29[d]	
	Comp.	4.06[e,f]	–	–	–		−4.38[g], −3.17[h],	187[e], 205[f]	4.68[i], 6.00[j],	
			–	–	–		−3.19[l]		5.23[k]	
					Au_3N					
D0$_3$	*Pres.*	6.368	–	–	–	16.14	−2.238	133.110	5.656	1.297
A15	*Pres.*	5.124	–	–	–	16.82	−2.084	121.792	5.645	1.451
D0$_9$	*Pres.*	4.336	–	–	–	20.38	−2.695	95.370	5.518	0.840
	Comp.	4.239[m]	–	–	–					
L1$_2$	*Pres.*	4.017	–	–	–	16.20	−2.254	135.621	5.686	1.281
D0$_2$	*Pres.*	8.672	–	–	–	20.38	−2.695	95.692	5.551	0.840
ϵ-Fe$_3$N	*Pres.*	5.473	–	5.100	–	16.54	−2.546	125.363	5.551	0.989
RhF$_3$	*Pres.*	6.075	–	–	$\alpha = 61.269$	20.38	−2.694	95.859	5.534	0.841
					AuN					
B1	*Pres.*	4.670	–	–	–	12.73	−2.411	170.385	5.178	1.678
B2	*Pres.*	2.912	–	–	–	12.35	−2.054	170.874	5.269	2.035
B3	*Pres.*	4.989	–	–	–	15.52	−2.378	126.414	5.119	1.711
B8$_1$	*Pres.*	3.600	–	5.007	–	14.05	−2.144	151.504	5.271	1.945
B$_k$	*Pres.*	3.508	–	9.332	–	24.86	−2.317	73.343	5.126	1.772
B$_h$	*Pres.*	3.138	–	3.063	–	13.06	−2.223	163.369	5.285	1.866
B4	*Pres.*	3.526	–	5.774	–	15.54	−2.382	120.842	5.711	1.707
B17	*Pres.*	3.149	–	5.543	–	13.74	−3.105	176.760	5.334	0.984
B24	*Pres.*	4.380	4.647	5.141	–	13.08	−2.375	161.383	5.092	1.714
					AuN_2					
C1	*Pres.*	5.162	–	–	–	11.46	−2.334	195.138	4.890	2.124
	Comp.	5.035[n]	–	–	–			246[n]		
		5.144[o]	–	–	–			198[o]		
C2	*Pres.*	5.607	–	–	–	14.69	−3.597	26.129	7.643	0.861
	Comp.	5.471[p]	–	–	–			41[p]		0.727[p]
		5.157[q]	–	–	–			126[q]		
C18	*Pres.*	3.467	4.549	5.551	–	14.59	−3.622	27.178	7.609	0.836
	Comp.	6.160[p]	5.013[p]	2.936[p]	–			27[p]		0.554[p]
		5.410[q]	4.938[q]	2.874[q]	–			57[q]		
CoSb$_2$	*Pres.*	6.219	5.882	10.679	$\beta = 151.225$	15.67	−3.667	11.430	7.529	0.791
	Comp.	8.149[p]	5.350[p]	5.361[p]	131.09[p]			36[p]		0.529[p]
		7.715[q]	5.215[q]	5.172[q]	132.11[q]			81[q]		

Notes to Table 10.6 :

[a] Ref. [240]. This is an average of 40 experimental values, at $20\ ^{\circ}C$, with a deviation: ± 0.0002 Å.

[b] Ref. [172]. Cohesive energies are given at $0\ K$ and 1 atm $= 0.00010$GPa; while bulk moduli are given at room temperature.

[c] Ref. (25) in [219]: at room temperature.

[d] See Refs. (8)–(11) in [219].

[e] Ref. [241]. LAPW-TB.

[f] Ref. [241]. LAPW-LDA.

[g] Ref. [242]: PAW-LDA.

[h] Ref. [242]: PAW-PW91.

[i] Ref. [219]: using the so-called method of transition metal pseudopotential theory; a modified form of a method proposed by Wills and Harrison to represent the effective interatomic interaction.

[j] Ref. [219]: using a semi-empirical estimate based on the calculation of the slope of the shock velocity *vs.* particle velocity curves obtained from the dynamic high-pressure experiments. The given values are estimated at $\sim 298\ K$.

[k] Ref. [219]: using a semi-empirical method in which the experimental static $P - V$ data are fitted to an EOS form where B_0 and B_0' are adjustable parameters. The given values are estimated at $\sim 298\ K$.

[l] Ref. [242]: PAW-PBE.

[m] Ref. [63]: Using the AIMPRO code, in which a Gaussian orbital basis set is used with the separable dual-space pseudopotentials of Hutter *et al*.

[n] Ref. [64]: Using the full-potential linearized augmented plane waves (LAPW) method within LDA.

[o] Ref. [64]: Using the full-potential linearized augmented plane waves (LAPW) method within GGA(PBE).

[p] Ref. [66]: using Vanderbilt USPPs within GGA(PBE). B_0's were calculated from the elastic constants. $E_{\rm coh}(\mathrm{N}_2^{\rm solid})$ was used in Eq. 7.5.3 instead of $E_{\rm coh}(\mathrm{N}_2^{\rm gas})$.

[q] Ref. [66]: using Vanderbilt USPPs within LDA. B_0's were calculated from the elastic constants.

To compare and to deeper analyze the obtained equilibrium properties of the three stoichiometries series with respect to one another, the calculated equilibrium properties are depicted graphically in Fig. 10.37. All quantities in this figure are given relative to the corresponding ones of Au(A1) given in Table 10.6. In this way, one will be able to investigate the effect of nitridation on the parent crystalline Au as well [17].

[17] In Table 10.6, our computed properties of the elemental Au are compared with experiment and with previous calculations as well. This may benchmark the accuracy of the rest of our calculations.

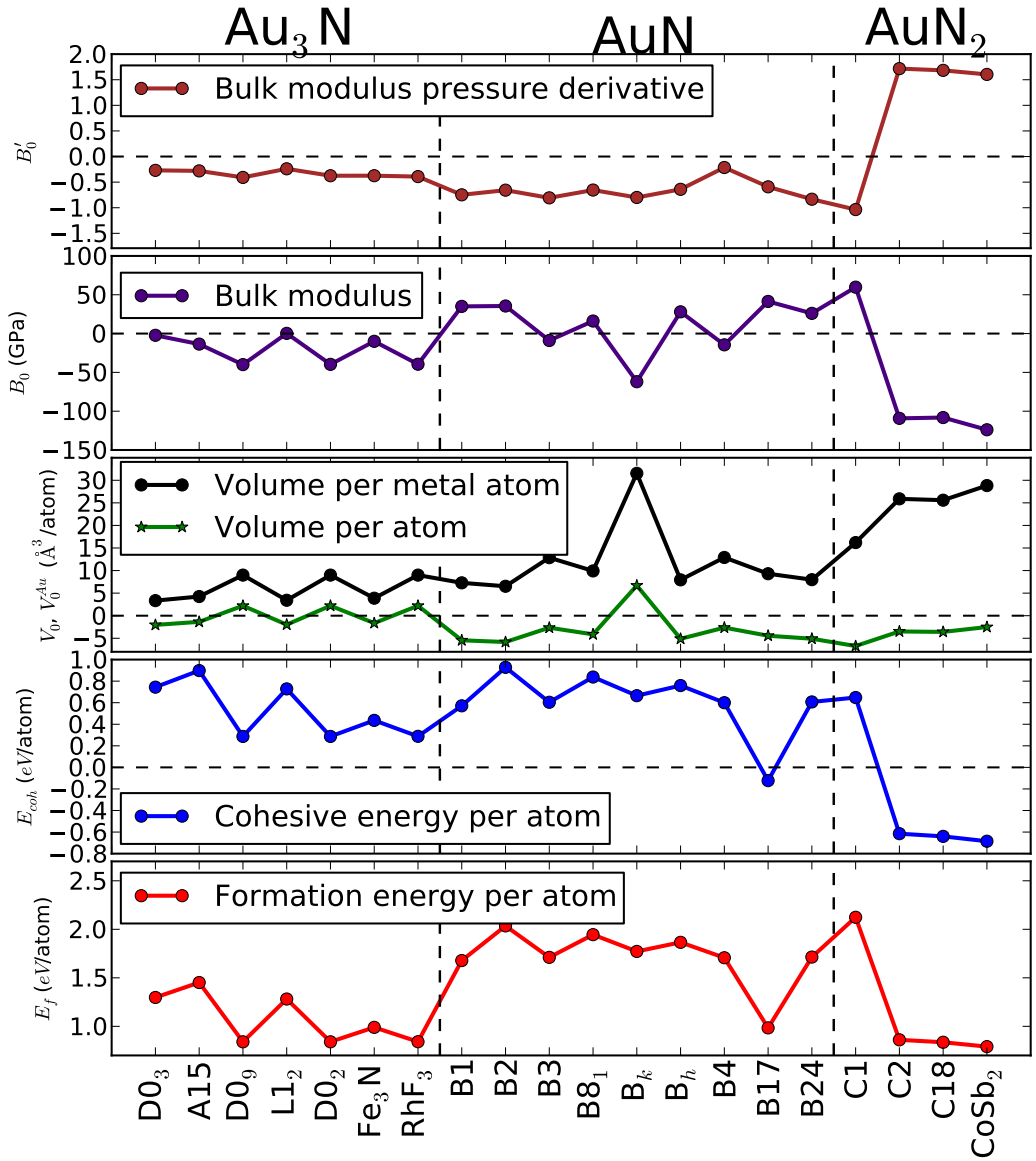

Figure 10.37: (Color online.) Calculated equilibrium properties of the twenty studied phases of gold nitrides. All quantities are given relative to the corresponding ones of the *fcc* crystalline elemental gold given in the first row of Table 10.6.

10.6.1 EOS and Relative Stabilities

Fig. 10.36a shows that the most stable phases in the studied Au_3N series are $D0_9$, $D0_2$ and RhF_3. From the figure, it is also clear that the $E_{coh}(V)$ curves of these three phases are almost identical around their equilibria. In fact the $D0_9$ curve can hardly be seen in the whole range (compare with Fig. 1(c) in Ref. [6]). We found the same behavior in the EOS to be true for Ag_3N in the same phases (see Ref. [2]), and we traced back this behavior to the structural relationships between these three phases (For more details, see Ref. [3] and references therein). As can readily be seen from Fig. 10.37 and Table 10.6, these structural relations have manifested themselves in all the presented structural, energetic and mechanical properties, giving rise to almost identical values. Therefore, one may conclude that, if one phase is synthesizable, the three phases may co-exist during the Au_3N synthesis process.

Noting that Cu, Ag and Au share the same group in the periodic table of elements, it may be worth to mention here that $D0_9$ structure is known to be the structure of the synthesized Cu_3N [34, 47, 253] and, as mentioned above, we found it to be the most stable structure of Ag_3N [2].

Assuming that it is the most likely stoichiometry, Krishnamurthy *et al.* [63] undertook *ab initio* pseudopotential calculations on Au_3N and studied all the Au_3N structures in Table 5.1. Although they found $D0_9$ to be the most stable modification in this sub-parameter space, yet, they identified a triclinic crystal structure with $0.25\ eV$/atom lower energy than the $D0_9$. Krishnamurthy and co-workers determined the triclinic phase to be metallic. It must be mentioned here that all the 3:1 structures we have investigated in the present study were taken mainly from the work of Krishnamurthy *et al.* [63]. However, Krishnamurthy et. al. gave only the *lattice vectors* of their triclinic structure, but no *basis vectors* were given. So, we were not able to properly place the atoms inside the cell they gave. Allowing them to relax, ions keep moving over the potential surface with no sign of a local minimum, and the structure seems to be very *soft*!

The odd behavior of the EOS curve of $Au_3N(RhF_3)$ with the existence of two minima (Fig. 10.36a) reveals that the first minimum (the one with higher E_{coh}) is a metastable local minimum on the potential surface that cannot be maintained as the material is decompressed. The potential barrier, represented by the sudden drop of the $Au_3N(RhF_3)$ curve, at $\sim 18.4\ eV$/atom is due to the change of positions of those metal ions which possess internal degrees of freedom.

Concerning the AuN series, it is evident from Fig. 10.36b that the simple tetragonal structure of cooperite (B17) would be the energetically most stable structure, with $0.694eV$/atom less than B1. This B17 structure was theoretically predicted to be the ground-state structure of CuN [3], AgN [2] and PtN [1, 30].
Kanoun and Said [65] studied the $E(V)$ EOS for AuN in the B1, B2, B3 and B4 structures. Within this parameter sub-space, the relative stabilities they arrived at agree in general with ours. However, they predicted that B3 is *always* more stable than B4, while Fig. 10.36b shows that B4 is preferred against B3 only at low pressures.
In the AuN_2 series, the least symmetric simple $CoSb_2$ monoclinc structure is found to be the most stable (Fig. 10.36c). This agrees with the conclusion of Ref. [66], where it is suggested that AuN_2 may be synthesized at extreme conditions (higher pressure and temperature) and/or it may have other Au:N stoichiometric ratios than 1:2.

10.6.2 Pressure-induced phase transitions

Enthalpy-pressure relations of Au_3N for five considered structures are displayed in Fig. 10.36d. A point at which enthalpies $H = E_{\text{coh}}(V) + PV$ of two structures are equal defines the transition pressure P_t, where transition from the phase with higher enthalpy to the phase with lower enthalpy may occur.
Fig. 10.36d shows that a transition from $D0_9$ phase to the Fe_3N phase would take place at a very low pressure ~ 6.3 GPa; and it is clear that the $D0_9$ phase is favourable only at low pressures below ~ 6.3 GPa, while the Fe_3N hexagonal structure of Ni_3N is favoured at higher pressures. Fig. 10.36d also reveals that $L1_2$ and $D0_3$ phases may co-exist over a wide range of pressure and that they are both favoured over $D0_9$ phase at pressures higher than ~ 20 GPa, while A15 would be favoured over $D0_9$ only at pressures higher than ~ 33 GPa.

10.6.3 Volume per Atom and Lattice Parameters

The numerical values of the equilibrium lattice parameters and the corresponding volume per atom V_0 for the twenty modifications are presented in Table 10.6. The middle sub-window of Fig. 10.37 depicts the V_0 values relative to Au(A1). To measure the average of the Au–Au bond length in the silver nitride, the equilibrium average volume per Au atom (V_0^{Au}), which is simply

the ratio of the volume the unit cell to the number of Au atoms in that unit cell, is visualized in the same subwindow.

From the V_0 curve in Fig. 10.37, we can see that, all AuN and AuN_2 modifications, except the open AuN(B_k) phase, decrease V_0 ; while the Au_3N phases tend, on average, not to change the number density of the parent Au(A1). The metal-metal bond length, as represented by the volume per metal atom V_0^{Au}, increases (on average) in the direction of increasing nitrogen content and decreasing structural symmetry.

Both trends in V_0 and in V_0^M were found to be true for copper [3], silver [2] and platinum [1] nitrides. The trend in V_0^M, however, reveals the fact that in all these nitrides, the introduced N ions displace apart the ions of the host lattice causing longer metal-metal bonds than in the elemental parent metal. This cannot be seen directly from the V_0 values depicted in the same figure.

10.6.4 Bulk Modulus and its Pressure Derivative

The numerical values of the equilibrium bulk moduli and their pressure derivatives for the twenty modifications are presented in Table 10.6. The second from top and the top sub-windows of Fig. 10.37 visualize these values relative to Au(A1).

In the Au_3N series, one can see from the second top subfigure of Fig. 10.37 that less stable phases tend to preserve the B_0 value of their parent Au(A1), while the most stable phases ($D0_9$, $D0_2$ and RhF_3) posses lower B_0 values.

Except B_k, AuN modifications and AuN_2(C1) tend, on average, to increase the B_0 value of their parent Au(A1), with the highest B_0 value possessed by the most stable AuN phase: B17.

The last least symmetric structures AuN_2(C2, C18 and $CoSb_2$) possess the lowest B_0 values among the 20 studied modifications. The B_0 values of AuN_2's have the same trend as their corresponding E_{coh}'s and opposite trend as their corresponding V_0^{Au}'s.

From the top subfigure of Fig. 10.37 one can see that upon application of external pressure, all Au_3N and AuN phases and C1 phase tend to lower their B_0. The last AuN_2 three modifications, however, are more sensitive to external pressure, and their bulk moduli tend to increase under pressure.

10.6.5 Thermodynamic Stability

The numerical values of the calculated formation energy E_f (Table 10.6) and their graphical representation (Fig. 10.37) show clearly that all the twenty obtained E_f values are positive. This, in principle, means that all these phases are thermodynamically unstable (endothermic). However, it is common that one obtains positive DFT-calculated E_f for (even the experimentally synthesized) transition-metal nitrides. Moreover, the zero-pressure zero-temperature DFT calculations have to be corrected for the conditions of formation of these nitrides. Another source of this apparent shortcoming stems from the PBE-GGA underestimation of the cohesion in N_2. We have discussed this point further in Ref. [3]. Nevertheless, formation energies in the present work are used as a measure of the *relative* thermodynamic stabilities of the phases under consideration. That is, the lower the formation energy, the lower the tendency to dissociate back into the constituent components Au and N_2.

Fig. 10.37 shows that, relative to each other and within each series, the formation energy E_f (defined by Eqs. 7.5.2 and 7.5.3) of the studied phases has the same trend as the cohesive energy[18]. That is, all phases have the same relative stabilities in the E_f space as in the E_{coh} space. This trend was found to be true for the nitrides of Cu [3] and Ag [2] as well. However, while Au_3N phases tend to have comparable E_{coh} as the AuN phases, all Au_3N modifications have a lower E_f than the AuN ones, except B17. In fact, Fig. 10.37 indicates that it may be relatively hard to form a 1:1 gold nitride other than B17. Moreover, it is apparent that the tendency of AuN_2(C2, C18 and $CoSb_2$) phases to decompose back to Au and N_2 is comparable with that of Au_3N($D0_2$, $D0_9$ and RhF_3).

Using Vanderbilt USPPs within GGA(PBE), Chen, Tse and Jiang [66] calculated E_f of C2, C18 and $CoSb_2$ phases. Their results are included in Table 10.6 for comparison. Although they got positive values, as expected, the differences between our obtained values and theirs can be traced back to the fact that they used $E_{coh}(N_2^{solid})$ in Eq. 7.5.3 instead of $E_{coh}(N_2^{gas})$. Moreover, the smaller the difference between our obtained values and their obtained equilibrium lattice parameters, the smaller the difference in E_f.

Unfortunately, no experimental values of E_f for the synthesized gold nitride phases are available.

[18] **Surely, this needs not to be so. Compare the definition 7.1.2 with the definition 7.5.2.**

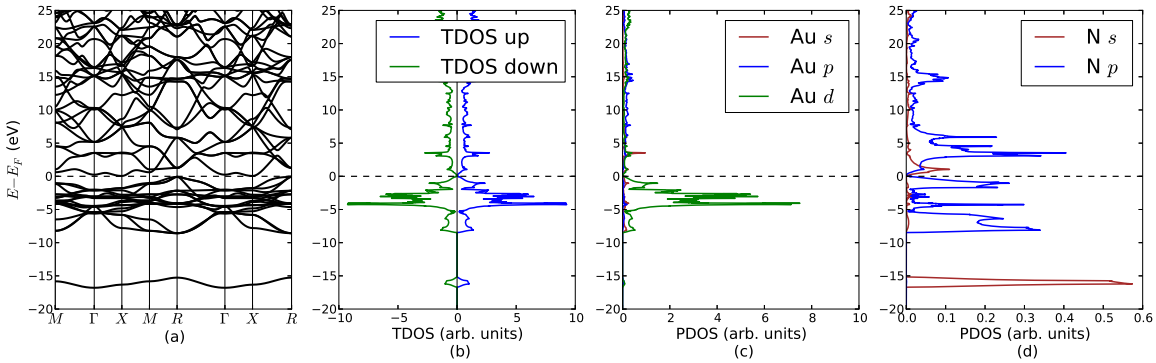

Figure 10.38: (Color online.) DFT calculated electronic structure for Au_3N in the $D0_9$ structure: **(a)** band structure along the high-symmetry $\mathbf{k}$-points (see Table 8.1); **(b)** spin-projected total density of states (TDOS); **(c)** partial density of states (PDOS) of Au(s, p, d) orbitals in Au_3N; and **(d)** PDOS of N(s, p) orbitals in Au_3N.

10.6.6 Electronic Properties

In this subsection, the DFT calculated electronic structure for the most energetically stable phases are shown graphically. In each case, presented information include **(a)** spin-projected total density of states (TDOS); **(b)** partial density of states (PDOS) of Au(s, p, d) orbitals in Au_3N; **(c)** PDOS of N(s, p) orbitals in Au_3N, and **(d)** band structure along the high-symmetry $\mathbf{k}$-points.

Beside $D0_9$ (Fig. 10.38), the equilibrium electronic structure of its two competing phases: $D0_2$ and RhF_3, are presented in Figs. 10.39 and 10.40, respectively. This is because the foregoing similarity in their EOS's may reflect in their electronic properties.

Krishnamurthy *et al.* [63] predicted $Au_3N(D0_9)$ to be an indirect band-gap semiconductor, but they did not give a value. Fig. 10.38 shows that it is indeed a semiconductor with an $(R - X)$ indirect DFT band gap of $0.139\ eV$ GGA value. According to the fact that the produced gold nitrides are metallic, the $D0_9$ structure may not be the true candidate for the most likely stoichiometry, Au_3N.

Fig. 10.39 shows that $Au_3N(D0_2)$ has its CBM at $(H, 0.065\ eV)$, and its VBM is at $(H, -0.073\ eV)$, resulting in a direct energy band gap at H: $E_g = 0.139\ eV$. This is exactly equal to E_g of $Au_3N(D0_9)$.

The Fermi surface E_F in $Au_3N(RhF_3)$ crosses the valence band at Γ and the phase seems to have a poor metallic character, since there is only a very narrow width of energy of the unoccupied

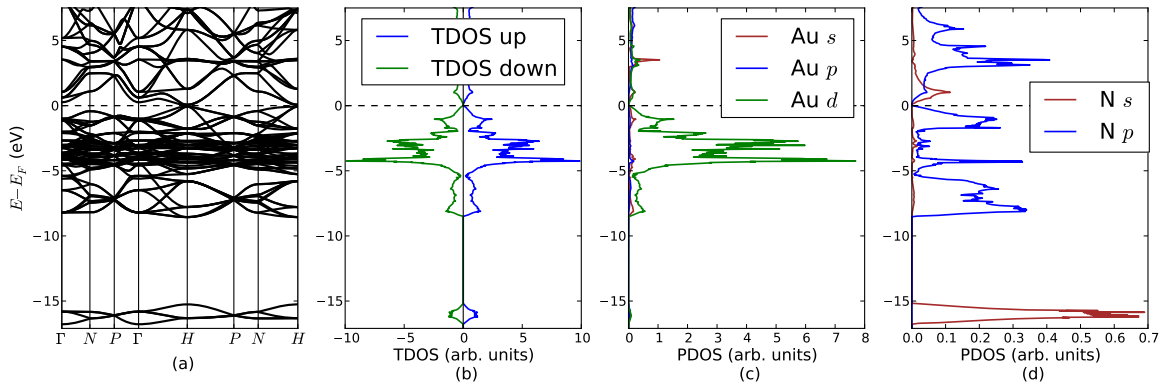

Figure 10.39: (Color online.) DFT calculated electronic structure for Au_3N in the $D0_2$ structure: **(a)** band structure along the high-symmetry $\mathbf{k}$-points (see Table 8.1); **(b)** spin-projected total density of states (TDOS); **(c)** partial density of states (PDOS) of Au(s, p, d) orbitals in Au_3N; and **(d)** PDOS of N(s, p) orbitals in Au_3N.

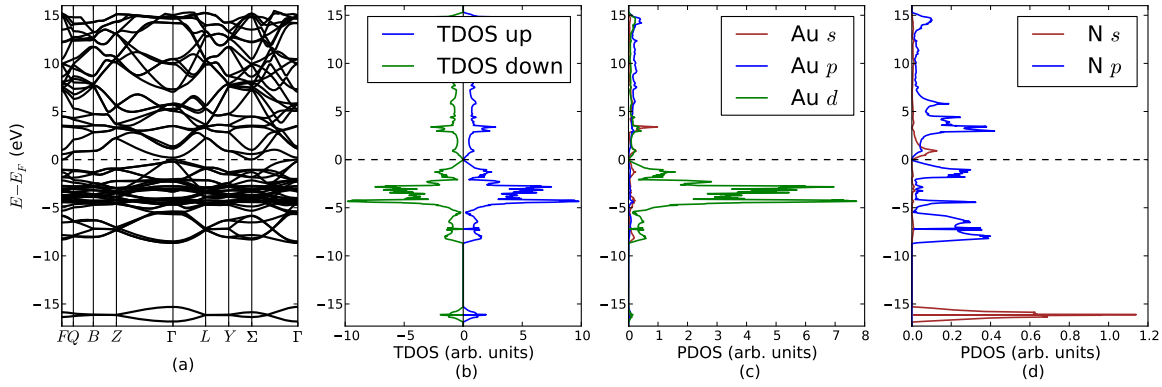

Figure 10.40: (Color online.) DFT calculated electronic structure for Au_3N in the RhF_3 structure: **(a)** band structure along the high-symmetry $\mathbf{k}$-points (see Table 8.1); **(b)** spin-projected total density of states (TDOS); **(c)** partial density of states (PDOS) of Au(s, p, d) orbitals in Au_3N; and **(d)** PDOS of N(s, p) orbitals in Au_3N.

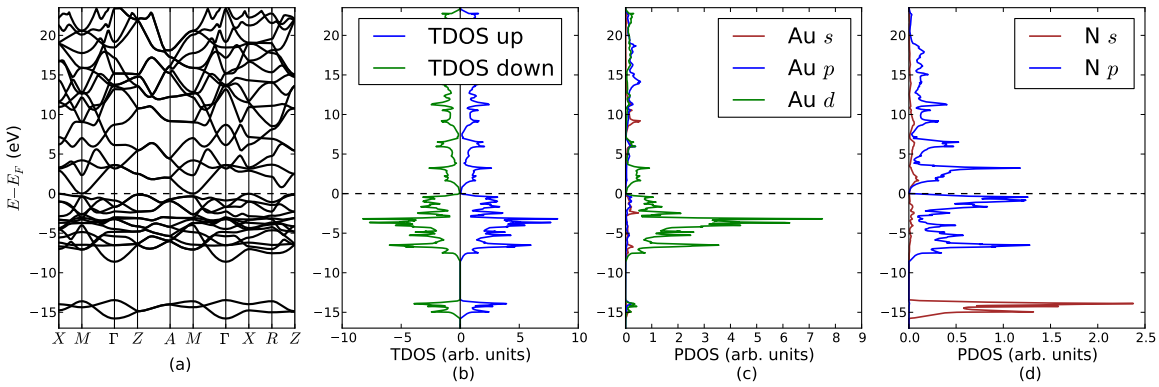

Figure 10.41: (Color online.) DFT calculated electronic structure for AuN in the B17 structure: **(a)** band structure along the high-symmetry $\mathbf{k}$-points (see Table 8.1); **(b)** spin-projected total density of states (TDOS); **(c)** partial density of states (PDOS) of Au(s, p, d) orbitals in AuN; and **(d)** PDOS of N(s, p) orbitals in AuN.

states above E_F and around Γ.

A common feature in these three Au_3N phases, there is an Au(d)-N(p) mixture in the range $\sim -8.8 - E_{\mathrm{F}}$ which becomes stronger around $-4.45\ eV$.

Although it might not be clear on the graph, Fig. 10.41(a) shows that AuN(B17) is a DFT(GGA) indirect band gap semiconductor. With its valence band maximum (VBM) at $(X, -0.012)$ and its conduction band minimum (CBM) very close to E_{F} at $(M, 0.001\ eV)$, AuN(B17) possesses a very narrow band gap of width: $E_g = 0.013\ eV$.

This insulating feature is in contrast to PdN [7], PtN [1], CuN [3] and AgN [2] which were all found to be metallic in this B17 structure.

With the Fermi surface crossing many partly occupied bands, it is evident from Fig. 10.42 that $AuN_2(CoSb_2)$ is a metal.

10.6.7 Optical Properties

Within a frequency range that includes the optical region (i.e. the visible spectrum: $[(390 \sim 750\ \text{nm}) \equiv (3.183 \sim 1.655\ eV)]$), Fig. 10.43 displays the real and the imaginary parts of the frequency-dependent dielectric function $\varepsilon_{\mathrm{RPA}}(\omega)$ of $Au_3N(D0_9)$ and the corresponding derived optical constants (Eqs. D.2.12, D.2.13, D.2.17 and D.2.22).

From the absorption coefficient $\alpha\,(\omega)$ spectrum, it can be seen that $Au_3N(D0_9)$ starts absorbing

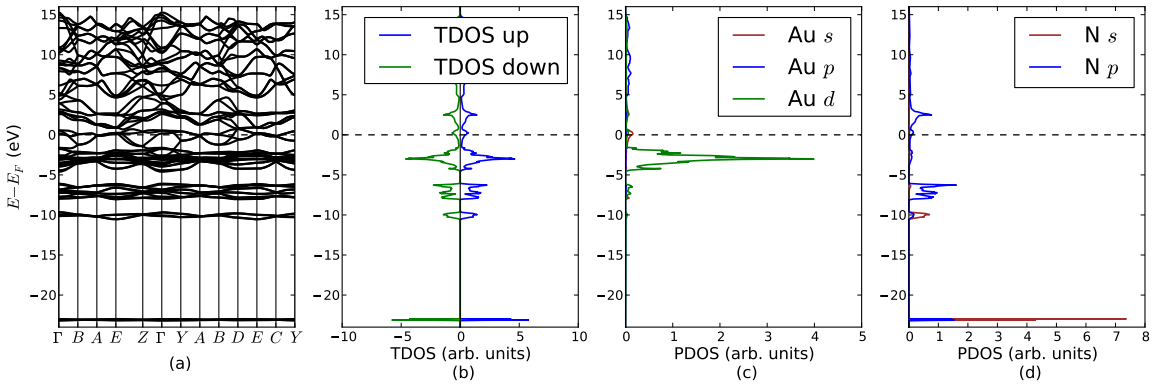

Figure 10.42: (Color online.) DFT calculated electronic structure for AuN_2 in the $CoSb_2$ structure: **(a)** band structure along the high-symmetry $\mathbf{k}$-points (see Table 8.1); **(b)** spin-projected total density of states (TDOS); **(c)** partial density of states (PDOS) of Au(s, p, d) orbitals in AuN_2; and **(d)** PDOS of N(s, p) orbitals in AuN_2.

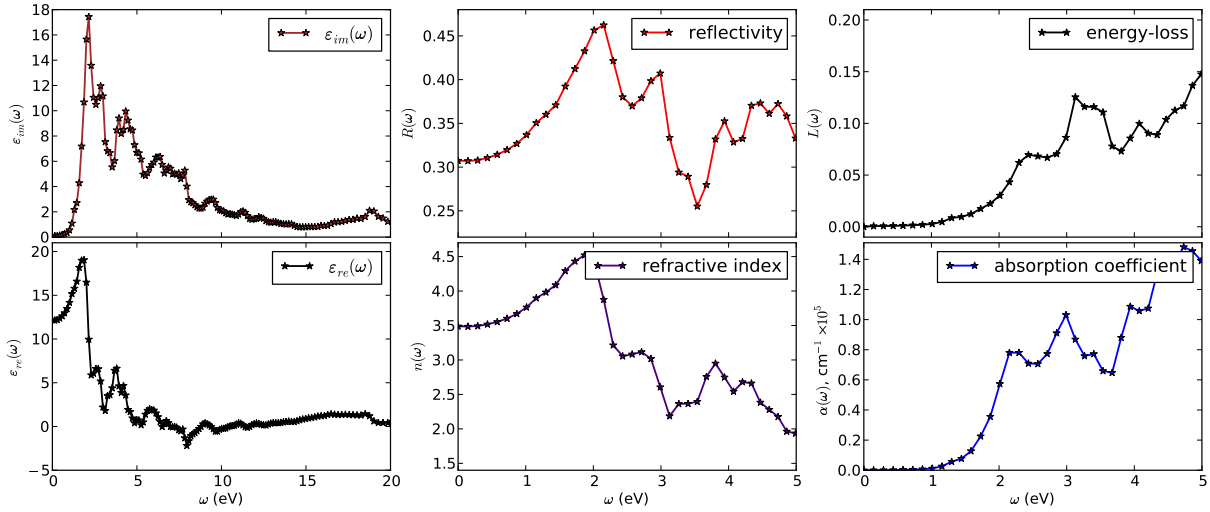

Figure 10.43: (Color online.) Normal-incidence frequency-dependent optical spectra of $Au_3N(D0_9)$ obtained using Eqs. (D.2.12, D.2.13, D.2.17 and D.2.22) and GW_0 eigenvalues.

photons with ~ 0.9 eV energy. Hence, it is clear that GW_0 calculations give a band gap of ~ 0.9 eV, which is a significant improvement to the obtained DFT-GGA value. Therefore, our presented $\alpha(\omega)$ spectrum confirms that $Au_3N(D0_9)$ would be a true semiconductor and that $D0_9$ cannot be the true structure of the most likely Au_3N stoichiometry.

10.7 Hypothetical ZnN

As most of the transition metals, different formulas of zinc nitride have been reported: Zn_3N_2, ZnN_2, α-ZnN_6 and β-ZnN_6; each with its own crystal structure [71]. However, it is a common practice in first-principles calculations to study phases that have not been synthesized yet (cf. Refs. [72, 73]). In the present section, we replace the sulfur ion in the well-known ZnS(B3) and ZnS(B4) by an N ion and perform *ab initio* calculations to study the structural and electronic properties of these hypothetical ZnN(B3) and ZnN(B4) phases. We followed calculations method described in Part II, and, as usual, we investigated the effect of nitridation on the elemental Zn(A3).

The energy-volume equations of state (EOS) for the two phases are depicted in Fig. 10.44. The corresponding calculated equilibrium properties are given in Table 10.7. It is clear from the Figure that the two phases have almost identical EOSs, especially at high pressures (low volumes). Table 10.7 shows that both ZnN(B3) and ZnN(B4) have quite similar equilibrium V_0 and E_{coh}; however, due to the slight difference in the curvature of the two EOS curves around the equilibrium, bulk moduli differ and ZnS(B3) has ~ 17 GPa higher B_0 than ZnS(B4). However, B_0 of the latter is more sensitive to external pressure than the former, as can be noticed from the difference in the B_0' values.

The obtained values of formation energies E_f shows that Zn(B3) has slightly lower tendency to dissociate back into the constituent components Zn and N_2 than Zn(B4). The positive sign of the obtained E_f does not mean that these phases are thermodynamically unstable (endothermic), but the same argument of our article Ref. [3] applies. Moreover, the present values are far less than those of the B3 and B4 phases of CuN [3] and PtN [1] for which we have argued to be

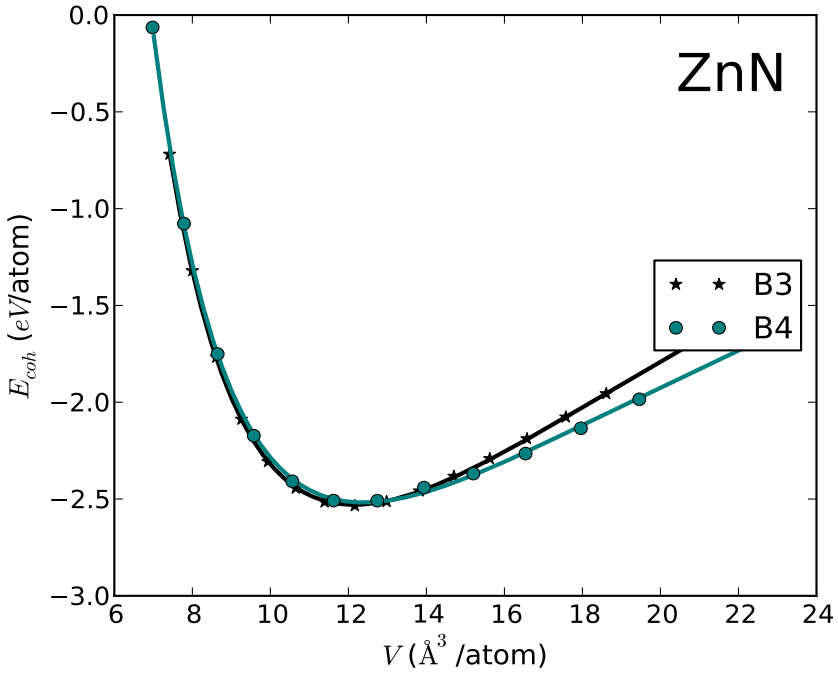

Figure 10.44: (Color online.) Cohesive energy $E_{\text{coh}}(eV/\text{atom})$ versus atomic volume V (Å^3/atom) for ZnN(B3) and ZnN(B4).

thermodynamically stable and synthesizable.

The obtained band diagrams $\epsilon_i^\sigma(\mathbf{k})$ and spin- and ℓ-projected density of states (DOS) of the slightly more stable phase, ZnN(B3), are displayed in Fig. 10.45. From the spin-projected total density of states (TDOS), sub-figure (b), it is evident that electrons occupy the spin-up and the spin-down bands equally. Therefore, it is sufficient to display either spin-up DOS or spin-down band diagrams. Depicting the energy bands along densely sampled high-symmetry strings of $\mathbf{k}$-points[19] allows us to extract information about the electronic structure of this phase. Moreover, to investigate the details of the orbital character of the bands, the Zn(s,p,d)- and N(s,p)-resolved DOS's are plotted at the same energy scale.

[19] The coordinates of the W point is not as the same as in Ref. [203], but they are equivalent. Also, the coordinates of U and K are not given in Ref. [203]. The coordinates of U, K and the equivalent W were created by means of XCrySDen!

Table 10.7: Equilibrium properties of Zn(A3), ZnN(B3) and ZnN(B4)**:** Lattice constants (a(Å), b(Å), c(Å), $\alpha(^\circ)$ and $\beta(^\circ)$), equilibrium atomic volume V_0(Å^3/atom), cohesive energy $E_{\text{coh}}(eV/\text{atom})$, bulk modulus $B_0(GPa)$ and its pressure derivative B_0', and formation energy $E_f(eV/\text{atom})$. The presented data are of the current work (*Pres.*), experimentally reported (*Expt.*) and of previous calculations (*Comp.*).

Structure		$a(\AA)$	$b(\AA)$	$c(\AA)$	$\alpha(^\circ)$ or $\beta(^\circ)$	$V_0(\AA^3/\text{atom})$	$E_{\text{coh}}(eV/\text{atom})$	B_0(GPa)	B_0'	$E_f(eV/\text{atom})$
				Zn						
A3	*Pres.*	2.668	–	4.952	–	15.26	−1.179	70.745	5.474	
	Exp.	(2.6644 ± 0.0003)[a], 2.66[c]	–	(4.9454 ± 0.0003)[a], 4.95[c]	–	(15.202 ± 0.003)[b]	−1.35[c,g]	59.8[c]		
	Comp.		–		–		1.91[d], 0.98[e], 1.17[f]			
				ZnN						
B3	*Pres.*	4.593	–	–	–	12.11	−2.534	127.991	4.873	0.571
B4	*Pres.*	3.247	–	5.318	–	12.14	−2.514	111.009	6.646	0.591

[a] Ref. [240]: These are averages of 23 experimental values, at $20^\circ C$.
[b] Ref. [240]: at room temperature and atmospheric pressure.
[c] Ref. [172]: Cohesive energies are given at $0\ K$ and 1 atm $= 0.00010$ GPa; while bulk moduli are given at room temperature.
[d] Ref. [216]: LDA.
[e] Ref. [216]: BP-GGA.
[f] Ref. [216]: PW-GGA.
[g] Ref. [86].
[h] Ref. [266].

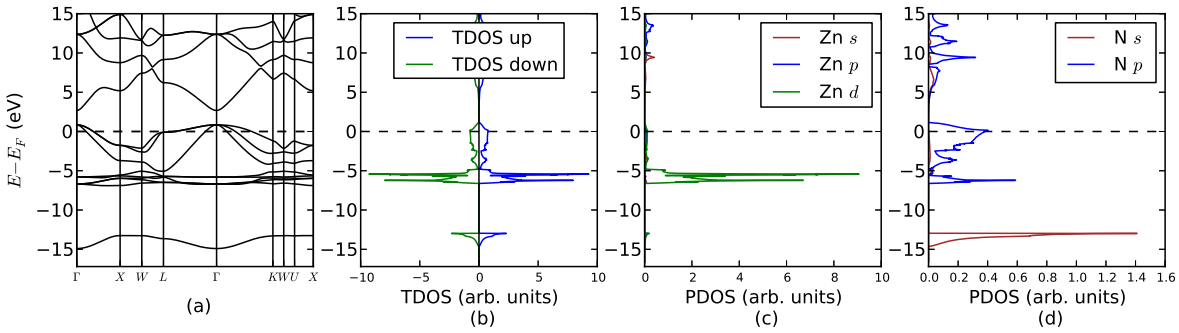

Figure 10.45: (Color online.) DFT calculated equilibrium electronic structure for ZnN in the B3 structure: **(a)** band structure along the high-symmetry $\mathbf{k}$-points which are labeled according to Ref. [203]. Their coordinates w.r.t. the reciprocal lattice basis vectors are: $\Gamma(0.0, 0.0, 0.0)$, $X(0.0, 0.5, 0.0)$, $W(0.75, 0.25, 0.5)$, $L(0.5, 0.5, 0.5)$, $K(0.750, 0.375, 0.375)$, $U(0.625, 0.250, 0.625)$; **(b)** spin-projected total density of states (TDOS); **(c)** partial density of states (PDOS) of Zn(s, p, d) orbitals in ZnN; and **(d)** PDOS of N(s, p) orbitals in ZnN.

With The Fermi surface ε_F crossing the partly occupied bands, it is clear from Fig. 10.45 that ZnN(B3) is a metal. The only evident contribution to DOS at ε_F is from the p states of the N atoms. The bonding in the material is due to the Zn(d)-N(p) mixing around $-6.2\ eV$. The very low contributions (less than 0.15 in the PDOS scale) from Zn(s) and Zn(p) in the range from about $-6.5\ eV$ and crossing ε_F is not clear in Fig. 10.45 due to the PDOS scale.

Compared to the elemental Zn(A3), it is clear that nitridation lowers the cohesive energy (per atom) leading to a significant increase in the bulk modulus. Therefore, to conclude, it is evident that the 1:1 nitridation of Zn significantly enhances its mechanical properties while, in contrast to the reported semiconducting Zn_3N_2 [267, 268], it preserves its metallic character.

11. Conclusions and Future Work

Below we briefly summarize the general achievements of the present thesis investigations and the progress made toward the main proposed goals of the study. Then we suggest some future research directions which have emerged naturally during the course of this study.

11.1 Conclusions

In general, the present theoretical investigation yield an insight into the structural, stability, mechanical, electronic and optical properties of Pd, Pt, Cu, Ag, Au, and Zn nitrides. Each nitride was attached to twenty different structures distributed among 1:1, 1:2 and 3:1 stoichiometries. Some of these modifications have been experimentally reported for some of the nitrides under investigation, some were proposed by other researchers, and some were proposed for the first time in this work. Zinc nitride was studied only in two simple hypothetical phases.

Obtained results were analyzed within the introduced theoretical framework (Part I) and calculation methods (Part II). Extensive comparisons with experiment and with previous calculations were carried out. In many cases we obtained excellent agreement with previous works. This was justified within the limitations of and trends in the employed calculation methods. In other cases, cf. Paper [1], we successfully argued even against some experimental proposals. This, however, reveals the power of the employed DFT and GWA calculations-based schemes in dealing with such realistic and technologically important materials.

From our comparison of the obtained properties of the nitrides each with the corresponding ones of its parent metal, we found it possible to control the physical properties of such systems. For example, one can preserve the metallic character of the parent metal and enhance its bulk modulus in the same time.

To the best of our knowledge, most of, if not all, our GWA-based calculations of the optical properties are the first theoretical calculations of the optical spectra of these technologically important materials. Nevertheless, for more accurate optical characterization, exciton energies must

be calculated. This can be achieved by means of the evaluation of the two-body Green's function G_2 on top of the basis of the calculated GW one-particle Green's function G and quasi-particle energies, then solving the equation of motion of G_2, the so-called Bethe-Salpeter equation.

We hope that the present work would serve as a reference source for meaningful comparisons which may be made among the largely different calculations. We also hope that some of our predictions will be confirmed in future experimentally and/or theoretically.

11.1.1 Palladium Nitrides

We have applied first-principles methods to investigate the structural, electronic and optical properties of some possible stoichiometries and crystal structures of the recently discovered palladium nitride.

From the study of the equation of state (EOS), we identified the energetically most stable phases and determined their equilibrium structural parameters. B17 and C18 were found to be the most energetically favored structures in the PdN and PdN_2 series, respectively. Band diagrams and total and partial density of states reveal that PdN(B17 and B24) and PdN_2(C18) are all metallic. The considerable differences found with and among the earlier reported structural properties (of PdN and PdN_2) may invoke the need for deeper and more expensive calculation schemes such as in Ref. [245].

The more sophisticated GW approach was employed to investigate excitation energies and optical properties of this promising material. The obtained absorption coefficient spectrum confirmed that the high-pressure competing phase PdN(B24) is metallic.

In the present investigation, we have studied a wider parameter sub-space than previous works, and to the best of our knowledge, the present study is the first to propose and to investigate the physical properties of Pd_3N. If synthesized, Pd_3N will likely be in the ϵ-Fe_3N hexagonal structure of Ni_3N. This Pd_3N modification is thermodynamically more stable (and thus it is more possible to be synthesized) than all the previously proposed PdN and PdN_2 modifications, and has better cohesive energy than all the previously proposed PdN and PdN_2(C1) modifications. Compared to all these PdN and PdN_2 modifications, Pd_3N(ϵ-Fe_3N) has the shortest Pd-Pd bond length. Moreover, Pd_3N(ϵ-Fe_3N) possesses slightly higher bulk modulus B_0 than its parent Pd, and

B_0 increases significantly under pressure. Pd_3N(ϵ-Fe_3N) preserves the metallic character of its parent Pd. These properties together may make this phase, if synthesized, important to possible high-pressure applications.

11.1.2 Platinum Nitrides

We presented a systematic series of first-principles calculations of the energy-optimized geometries, phase stabilities and electronic and optical properties of bulk Pt_3N, PtN and PtN_2 in twenty different crystal structures. Comprehensive comparison with experiment and with previous calculations has been made, and excellent agreement has been achieved. We found that both the lowest energy and the highest bulk modulus phases belong to the PtN_2 series and not to the PtN family. Moreover, the calculated electronic and optical properties of the PtN_2 phases show stronger consistency with experiment than the claimed PtN(B3) phase. In the present work, we have investigated a wider parameter sub-space than previous calculations, and to the best of our knowledge, the present work is the first to propose and to study the physical properties of Pt_3N, as well as the first to theoretically calculate the optical spectra of this new material. However, optical properties of PtN_2(C1 and C2) have not been investigated, and we strongly recommend optical calculations for these phases and obtained results should be tested against experiment. Moreover, experimentalists should provide the community with more data.

11.1.3 Copper Nitrides

DFT-based first-principles calculations on bulk crystalline Cu_3N, CuN and CuN_2 over a series of twenty structural phases have been successfully carried out. The studied structural properties include energy-volume equation of state (EOS), equilibrium lattice structural parameters, cohesive and formation energies, relative phase stabilities, bulk modulus and its presssure derivative. Electronic characterization of the energetically most stable phases was done via the analysis of their band structure and their total and partial density of states (DOS). Further, we carried out GW_0 calculations within the random-phase approximation (RPA) to the dielectric tensor $\varepsilon_{\mathrm{RPA}}(\omega)$. The frequency-dependent optical constants (absorption coefficient, reflectivity and refractive index spectra) of the experimentally reported phase $Cu_3N(D0_9)$ were derived from the updated $\varepsilon_{\mathrm{RPA}}(\omega)$. Obtained results were compared with experiment and/or with previous calculations

whenever possible. The main conclusions which we can derive from all these calculations are the followings:

- The calculated lattice constants are in good agreement with experiment and with theory.
- From the obtained cohesive energies, the energetically most stable phases are $D0_9$, B17, and C18 in the Cu_3N, CuN and CuN_2 stoichiometric series, respectively. However, other Cu_3N phases show similar stability to $Cu_3N(D0_9)$ and may present during the nitridation process.
- Including the successfully synthesized $Cu_3N(D0_9)$ phase, all obtained formation energies are positive, yet they can be used to measure the relative thermodynamic stabilities of these phases.
- Although CuN_2(C18) is the most bound phase, its tendency to decompose back into its elemental constituents is more than the less bound Cu_3N phases.
- The volume dependence of the bulk modulus is more precisely described by the change in volume of the Cu sublattice rather than the common average atomic volume of the nitride.
- The most stable Cu_3N phases are predicted to be indirect-gap semiconducing materials with lower bulk modulus than the pure metal, while CuN(B17) preserves the metallicity and improves the bulk modulus. However, the CuN_2(C18) phase substantially increases the compressibility while preserving the metallicity.
- Our GWA calculated optical properties show partial agreement with experiment and with the available theoretical work (Ref. [251]). Discrepancies are probably due to the lack of knowledge of the exact stoichiometry of the prepared samples, and due to the big difference in the used plane waves cut-off energy and in the density of the $\mathbf{k}$-mesh. Convergence criterion with respect to these two quantities have not been referred to in Ref. [251].
- Our GWA calculated energy gap of $Cu_3N(D0_9)$ shows significant improvement over the calculated DFT value.

11.1.4 Silver Nitrides

We have succesfully employed first-principles calculation methods to investigate the structural, stability, electronic and optical properties of Ag_3N, AgN and AgN_2. Within the accuracy of the employed methods, the obtained structural parameters, EOS, B_0, B'_0 and electronic properties show good agreement with the few avialable previous calculations. On the other hand, our obtained results show, at least, partial agreement with three experimental facts: (i) the lattice parameter of $Ag_3N(D0_9)$ is close to the experimentally reported one; (ii) the positive formation energies reveals the endothermic (unstable) nature of silver nitrides, and (iii) absorption spectrum explains its observed black color. Moreover, the present work may be considered as the first trial to theoretically investigate the optical properties of silver nitride. We hope that some of our obtained results will be confirmed in future experimentally and/or theoretically.

11.1.5 Gold Nitrides

We have successfully applied first-principles calculation methods to investigate the structural, stability, electronic and optical properties of Au_3N, AuN and AuN_2. Within the accuracy of the employed methods, the obtained structural parameters, EOS, B_0, B'_0 and electronic properties show acceptable agreement with some of the available previous calculations.
Among the studied modifications, we determined metallic (RhF_3 and $CoSb_2$) and semiconducting ($D0_9$ and B17) phases.
According to the fact that the produced gold nitride phases are metallic, our DFT-GGA and GW calculations confirmed that $D0_9$ structure cannot be the true candidate for the Au_3N stoichiometry that has been suggested by experimentalists.
From experiment, *ab initio* calculations of Krishnamurthy *et al.* [63], and from the present work, one may conclude that if Au_3N is the true stoichiometry, it must have a metallic character only at low crystal symmetries: i.e. RhF_3 (present work) or a triclinic (Ref. [63]). However, the better hardness -compared to pure gold- of the synthesized phases [12] remains a mystery and may be a property of gold nitride at low dimensions only.
The low symmetry AuN_2 phases have far lower cohesive energy than all Au_3N, have comparable formation energy with the most favorable Au_3N modifications, and their bulk moduli become higher under pressure.

11.1.6 Zinc Nitrides

The two studied hypothetical phases of zinc nitride, ZnN(B3) and ZnN(B4), were found to have almost identical EOSs as well as quite similar equilibrium number density and cohesive energy. However, ZnS(B3) has $\sim 17\ \mathrm{GPa}$ higher equilibrium bulk modulus than ZnS(B4); but the latter is more sensitive to external pressure than the former.
Compared to the elemental Zn(A3), it is clear that nitridation lowers the cohesive energy (per atom) leading to a significant increase in the bulk modulus. Therefore, we conclude that the 1:1 nitridation of Zn significantly enhances its mechanical properties while, in contrast to the reported semiconducting Zn_3N_2 [267, 268], it preserves its metallic character.

11.2 Directions for Future Work

"*... it is still early to sing praises.*" G. Soto [215]

The present work reveals a number of open problems that should be solved and a variety of research directions:

1. Study elastic, thermal, transport and magnetic *properties* of the most stable phases among these *bulk* compounds.

2. Since most of the considered nitrides have been prepared in form of thin films, it is important to study the structural and physical properties of these materials at *low dimensions*. This would be more realistic and should be application-oriented.

3. Although some *trends* in the physical properties of the target TMNs have been discussed (e.g. B17 is the most energetically favorable phase in all the studied 1:1 nitrides; all equilibrium phases in the $D0_9$ structure are semiconductors.), extensive and more formal investigation may reveal interesting common features in this family of materials.

4. Due to the expensive nature of the GWA calculations, optical properties of many important phases (e.g. PtN_2(C1 and C2)) have not been studied. Therefore, we strongly recommend the completion of the optical calculations.

5. Inclusion of the excitonic effects in the calculations of the optical properties is a crucial step toward comparison of the theoretically calculated optical spectra with those obtained experimentally.

Part IV

Appendices

Appendix A. Crystal Structure of Solids

"The 7 crystal systems and 14 Bravais lattices ... exhaust the possibilities. This is far from obvious ... . However, it is of no practical importance to understand why these are the only distinct cases. It is enough to understand why the categories exist, and what they are."

Ashcroft and Mermin [89, p. 119].

The well-ordered state of matter in which the positions of its atomic nuclei are repeated periodically in space is known as *crystal* [78]. The geometrical description of a given physical crystal can be fully described by giving the underlying *Bravais lattice* and the positions of its atomic constituent (known as *basis*) within a particular primitive unit cell [89]. Below, we define these terms and summarize some consequent notions.

The so-called *Bravais lattice* is a fundamental concept in the description of crystalline solids. A $3D$ Bravais lattice consists of all points

$$\mathbf{R} = \sum_{i}^{3} n_i \, \mathbf{a}_i = n_1\mathbf{a_1} + n_2\mathbf{a_2} + n_3\mathbf{a_3} \, , \qquad n_1, n_2, n_3 = \text{integers} \tag{A.0.1}$$

where the three linear independent unit vectors $\mathbf{a_1}$, $\mathbf{a_2}$ and $\mathbf{a_3}$ define the parallelepiped of the *primitive unit cell*. The region that fills the space without any overlapping when translated through $\mathbf{T} \in \{\mathbf{R}\}$ is known as *conventional unit cell* [89][1]. According to which unit cell one uses, a full geometrical description of a given crystal structure can be given by two sets of vectors: Either the *primitive vectors* of the lattice, $\mathbf{a_1}$, $\mathbf{a_2}$ and $\mathbf{a_3}$ above; or a set of the lengths of the edges of the conventional unit cell $\mathbf{a}$, $\mathbf{b}$ and $\mathbf{c}$ plus a set of the three interaxial (lattice) angles $\alpha = \mathbf{a} \wedge \mathbf{c}$, $\beta = \mathbf{b} \wedge \mathbf{c}$ and $\gamma = \mathbf{a} \wedge \mathbf{b}$ [79]. The group of the last two sets is usually referred to in the literature as cell or *lattice parameters*.

The *volume* Ω of a primitive unit cell can always be given by

$$\Omega = \mathbf{a}_1 \cdot \mathbf{a}_2 \times \mathbf{a}_3 \tag{A.0.2}$$

[1] When the term *unit cell* is used in the present thesis, we refer to the latter.

The region of space (usually a polyhedron) which is closer to a point in the Bravais lattice than to any other lattice point uniquely defines the *Wigner-Seitz (primitive) cell* about that point [89].

Atomic species and positions in a primitive unit cell are known as *basis* [78]. *Basis vectors* give the position of each atom within the unit cell relative to a chosen origin. The number of these vectors equals the number of the atoms within the unit cell. These coordinates can either be provided in the direct coordinates, i.e. with respect to the pre-defined lattice primitive vectors

$$\mathbf{R}_I = x_1\mathbf{a}_1 + x_2\mathbf{a}_2 + x_3\mathbf{a}_3 \tag{A.0.3}$$

or in the Cartesian coordinates

$$\mathbf{R}_I = s\left(x_1\hat{\mathbf{i}} + x_2\hat{\mathbf{j}} + x_3\hat{\mathbf{k}}\right). \tag{A.0.4}$$

where $x_{1\ldots3}$ are the coordinates, I labels atoms, $\hat{\mathbf{i}}$, $\hat{\mathbf{j}}$ and $\hat{\mathbf{k}}$ are the conventional orthonormal Cartesian basis vectors, and s may represent an arbitrary scaling factor.

The term *basis* introduced above refers to one of the identical copies physical of the same unit (i.e. of atoms) which when translated through all the Bravais lattice vectors gives rise to a *crystal structure* [89]. When dealing with conventional unit cell (or an artificial super cell), the number of basis copies (i.e. number of chemical formula units) within the cell is usually labeled by the letter Z.

Crystal Systems and Space Groups

From symmetry point of view, a crystal is characterized by all rigid symmetry operations (i.e. operations that leaves the distance between all lattice points invariant) that take the lattice into itself. The set of *all* such operations is referred to as *space group*, or symmetry group. The subset of all the translations that leave the crystal invariant is called the *translation group*. The (sub)set of all *non*-translational symmetry operations (that leave a particular point of the lattice fixed) is known as the *point group* [79, 89].

There are only 7 distinct Bravais point groups, known as the 7 *crystal systems* to which all crystal structures belong. When translational symmetry operations are considered, only 14 *Bravais lattices* (i.e. space groups) can be arrived at. These are the cubic (simple, body-centered and face-centered), the hexagonal, the tetragonal (simple and body-centered), the orthorhombic (simple, base-centered, body-centered and face-centered), monoclinic (simple and base-centered), the triclinic and the trigonal crystal system [79, 89].

When an atomic basis is attached to a Bravais lattice, 230 *space groups* can be obtained, with the 32 *point groups* recovered by setting all the translations equal to zero [79, 89, 230]. It may be worth mentioning here that these 230 are not just simple combinations of translational and point symmetry operations as the 14 Bravais lattices. By attaching to each lattice point (that belong to a certain crystal system) an atomic basis that has the same point group as the crystal system, one generate only 73 groups, known as the 73 *symmorphic space groups*. Each of the 157 *non-symmorphic space groups*, on the other hand, involves at least a screw axis or a glide plane translational symmetry operations [230]. For further details on this last point particularly, we refer to [203, pp. 44–45], [89, pp. 125–126] or [79, pp. 104–105].

There are different ways for naming and labeling the 230 space groups. In the International Tables for Crystallography [http://it.iucr.org/] each space group is assigned to a unique number from 1 to 230. In these Tables, space groups within the same crystal system are given consecutive numbers, starting with the cubic system and ending with the monoclinic system. A different designation most commonly used by crystallographers is the *international notation* or *Hermann–Mauguin notation*. Each symbol in this nomenclature consists in general of a set of four symbols. The first is a capital letter (P, I, F, R, A, B or C) designating the Bravais lattice centering [174][2], while the rest of the symbol characterizes the underlying point group using the involved symmetry operations [89].

[2] The symbol P stands for primitive lattices, I for body-centered lattice, F for all-face centered lattice, R for a trigonal lattice; and the symbols A, B, or C describe one-face centered lattices centered at the corresponding A, B, or C faces [174].

For a brief decent mathematical discussion of groups and symmetry operations, interested readers are referred to Kaxiras [79, Ch. 3]. For comprehensive materials, the International Tables for Crystallography [http://it.iucr.org/] and Bradley and Cracknell [203] are good references.

Appendix B. Bloch's Theorem and Band-Structure

Within the independent-particle approximation to the many-electron problem of bulk crystalline solids, Bloch's theorem [269] states that the eigenfunctions φ of the one-electron Hamiltonian [89]

$$\hat{\mathcal{H}}_{\mathsf{B}} = -\frac{\hbar^2}{2m_e}\nabla^2_{\mathbf{r}} + v_{\mathsf{ext}}(\mathbf{r}) \ , \tag{B.0.1}$$

where the effective potential $v_{\mathsf{ext}}(\mathbf{r})$ satisfies

$$v_{\mathsf{ext}}(\mathbf{r}+\mathbf{R}) = v_{\mathsf{ext}}(\mathbf{r}) \quad \text{for all } \mathbf{R} \text{ in the Bravais lattice} \ , \tag{B.0.2}$$

can be chosen to have the form

$$\varphi_{i,\mathbf{k}}(\mathbf{r}) = e^{\jmath\mathbf{k}\cdot\mathbf{r}}\, u_{i,\mathbf{k}}(\mathbf{r}) \ , \tag{B.0.3}$$

where

$$u_{i,\mathbf{k}}(\mathbf{r}+\mathbf{R}) = u_{i,\mathbf{k}}(\mathbf{r}) \quad \text{for all } \mathbf{R} \text{ in the Bravais lattice.} \tag{B.0.4}$$

Note that:

- The wave function $\varphi_{i,\mathbf{k}}(\mathbf{r})$ itself is, in general, not periodic in the configuration space, but the electronic density is, since

$$\varphi_{i,\mathbf{k}}(\mathbf{r}+\mathbf{R}) = e^{\jmath\mathbf{k}\cdot\mathbf{R}}\, \varphi_{i,\mathbf{k}}(\mathbf{r}) \quad \Rightarrow \quad |\varphi_{i,\mathbf{k}}(\mathbf{r}+\mathbf{R})|^2 = |\varphi_{i,\mathbf{k}}(\mathbf{r})|^2 \ . \tag{B.0.5}$$

- For a given $\mathbf{k}$, there are infinitely many independent eigenstates with discretely spaced corresponding eigenvalues that are labeled by the band index i. Conversely, for a given i, the eigenstates and eigenvalues are (quasi-continuous) periodic functions $\varepsilon_i(\mathbf{k})$ (or $\varepsilon_{i,\mathbf{k}}$) of $\mathbf{k}$. The information contained in these functions is referred to as "*band structure*". For each given i, the set of electronic levels specified by the band of eigenvalues $\varepsilon_i(\mathbf{k})$ is called "*energy band*" [89]. Examining band structure of a material provides a nuanced view of its electronic structure [127].

- By imposing the so-called Born-von Karman boundary conditions on the Bloch wave functions $\varphi_{i,\mathbf{k}}(\mathbf{r})$

$$\varphi_{i,\mathbf{k}}(\mathbf{r}) = \varphi_{i,\mathbf{k}}(\mathbf{r} + N_j \mathbf{a}_j) \ , \tag{B.0.6}$$

  where N_j is the number of the primitive cells in the $\mathbf{a}_j$ direction, it is straightforward to show that the number of the allowed wave vectors $\mathbf{k}$ in a primitive cell of the reciprocal lattice (e.g. the first Brillouin zone) is equal to the number of primitive cells $(N = N_1 \times N_2 \times N_3)$ in the direct crystal. Each $i, \mathbf{k}$ level can accommodate two electrons (one of each spin) at max [79, 89].

- Being continuous and periodic in $\mathbf{k}$, each $\varepsilon_i(\mathbf{k})$ must be bound; i.e. has at least one minimum and one maximum[1] at which $\nabla_{\mathbf{k}}\, \varepsilon_i(\mathbf{k}) = 0$.

From practical computational cost point of view, the most important appealing result of Bloch's theorem is that instead of dealing with an infinite number of interacting electrons in the perfectly ordered infinite solid, it is sufficient only to calculate the wave function of a finite number of electrons within one primitive unit cell. The wave function in any neighboring unit cell[2] is exactly the same, up to a phase factor (Eq. B.0.5) [8, 75].

[1] Saddle points are possible.
[2] Hence, all the quantum mechanical information and physical properties of the whole solid [8].

Appendix C. The $\mathbf{k}$ vector and the Brillouin zone

"The concepts associated with reciprocal space are fundamental to much of solid-state physics; that there are many physicists who can barely fathom the possibility that anyone might find them slightly mysterious."

David S. Sholl and Janice A. Steckel [127, p. 50].

From Eq. B.0.3, it is easy to see that there is a set of wave vectors $\{\mathbf{K}\}$

$$\mathbf{K} = \sum_i^3 n_i \mathbf{b}_i = n_1\mathbf{b}_1 + n_2\mathbf{b}_2 + n_3\mathbf{b}_3 \; ; \qquad n_1, n_2, n_3 = \text{integers} \; , \tag{C.0.1}$$

such that

$$\varphi_{i,\mathbf{K}}(\mathbf{r} + \mathbf{R}) = \varphi_{i,\mathbf{K}}(\mathbf{r}) \qquad \Rightarrow \qquad e^{j\mathbf{K}\cdot\mathbf{R}} = 1 \; , \tag{C.0.2}$$

where $\mathbf{R}$ defines the (direct) lattice as given by Eq. A.0.1.

Thus, with $\mathbf{k} \in \{\mathbf{K}\}$, Bloch's wave functions B.0.3 are periodic in $\mathbf{R}$. The set of the smallest independent $\mathbf{b}_j$ vectors C.0.1 that spans the *reciprocal lattice* $\{\mathbf{K}\}$ can be given by

$$\mathbf{b}_i = 2\pi \, \frac{\mathbf{a}_j \times \mathbf{a}_k}{\mathbf{a}_i \cdot \mathbf{a}_j \times \mathbf{b}_k} \; , \qquad i, j, k = 1, 2, 3 \quad , \tag{C.0.3}$$

with

$$\mathbf{a}_i \cdot \mathbf{b}_j = 2\pi\delta_{ij} \quad , \tag{C.0.4}$$

where $\mathbf{a}_i$ are the primitive vectors that span the direct lattice (Eq. A.0.1), and where the permutation between their indices is cyclic.

The Wigner–Seitz cell (App. A) in the reciprocal space is known as the first *Brillouin Zone*, or

simply Brillouin Zone (BZ). Its volume Ω_{R} is equivalent to

$$\Omega_{\mathsf{R}} = \mathbf{b}_i \cdot \mathbf{b}_j \times \mathbf{b}_k = \frac{(2\pi)^3}{\Omega} \,, \tag{C.0.5}$$

where Ω is the volume of the unit cell in the direct space (Eq. A.0.2).

Any vector $\mathbf{k}'$ outside the BZ can always be written in terms of another vector $\mathbf{k}$ inside the BZ as $\mathbf{k}' = \mathbf{k} + \mathbf{K}_0$, where $\mathbf{K}_0 \in \{\mathbf{K}\}$. Now, expanding the periodic part $u_{i,\mathbf{k}}(\mathbf{r})$ of the Bloch wave function B.0.3 yields

$$\begin{aligned} \varphi_{i,\mathbf{k}'}(\mathbf{r}) = \quad & e^{\jmath\mathbf{k}'\cdot\mathbf{r}}\, u_{i,\mathbf{k}'}(\mathbf{r}) = e^{\jmath\mathbf{k}'\cdot\mathbf{r}} \sum_{\mathbf{K}} C_{i,\mathbf{k}'+\mathbf{K}}\, e^{\jmath\mathbf{K}\cdot\mathbf{r}} = e^{\jmath(\mathbf{k}+\mathbf{K}_0)\cdot\mathbf{r}} \sum_{\mathbf{K}} C_{i,\mathbf{k}+\mathbf{K}_0+\mathbf{K}}\, e^{\jmath\mathbf{K}\cdot\mathbf{r}} \\ = \quad & e^{\jmath\mathbf{k}\cdot\mathbf{r}} \sum_{\mathbf{K}} C_{i,\mathbf{k}+\mathbf{K}_0+\mathbf{K}}\, e^{\jmath(\mathbf{K}+\mathbf{K}_0)\cdot\mathbf{r}} = e^{\jmath\mathbf{k}\cdot\mathbf{r}} \sum_{\mathbf{K}'} C_{i,\mathbf{k}+\mathbf{K}'}\, e^{\jmath\mathbf{K}'\cdot\mathbf{r}} = \varphi_{i,\mathbf{k}}(\mathbf{r}) \,. \end{aligned} \tag{C.0.6}$$

where the first (and, hence, the last) summation is over *all* the reciprocal lattice vectors $\mathbf{K}$. This proofs the major result that the wave vector $\mathbf{k}$ appearing in the Bloch theorem (App. B) can always be restricted to the first BZ and

$$\varphi_{i,\mathbf{k}+\mathbf{K}}(\mathbf{r}) = \varphi_{i,\mathbf{k}}(\mathbf{r}) \quad \text{and} \quad \varepsilon_{i,\mathbf{k}+\mathbf{K}} = \varepsilon_{i,\mathbf{k}} \quad \text{for all } \mathbf{K} \text{ in the reciprocal lattice.} \tag{C.0.7}$$

Hence, beside the introduction of $\mathbf{k}$ as a quantum number, Bloch's theorem (App. B) also shows that the wave vector $\mathbf{k}$ characterizes the translational symmetry of the periodic potential v_{ext} [89]. In fact, $\mathbf{k}$ plays a fundamental role in describing electrons in a solid.

The Irreducible Brillouin Zone (IBZ)

Using group theory, one can show that the Bloch energy spectrum $\varepsilon_{i,\mathbf{k}}$ has the full symmetry of the point group of the reciprocal lattice. Moreover, using group theory, one can also show that it is sufficient only to solve the single-particle Bloch equations in a minimal portion of the Brillouin Zone, called the *Irreducible Brillouin Zone* (IBZ). All the solutions in the entire BZ can then be obtained by *unfolding* the IBZ using the symmetry operations of the point group. This offers great savings in computation [79]. For example, the IBZ of the fcc BZ corresponds to $1/48$ of

the latter. Therefore, to count the number of the one-electron states in the BZ, one counts only each $\mathbf{k}$ point in the IBZ with a proper weight $w_{\mathbf{k}}$ to represent the whole BZ. The weight $w_{\mathbf{k}}$ of a $\mathbf{k}$-point in the IBZ is defined to be the total number of the distinguishable $\mathbf{k}$-points which are related by point symmetry to this $\mathbf{k}$, including $\mathbf{k}$ itself [78].

From Eq. C.0.1, it is clear that once the full Bravais lattice is correctly identified, the reciprocal lattice and its BZ structure are determined *uniquely from the translational symmetry of the direct lattice* and independent of the detailed configuration of the atomic basis within the primitive cell. Consequently, one has only 14 distinct BZ's [148, 203]. Unfortunately, the one-electron energy bands $\varepsilon_{i,\mathbf{k}}$ possess symmetry associated with one of the 230 space groups. Thus, although it is tempting, one can not simply use the geometrical symmetry of the BZ to find the corresponding IBZ [148].

An easily programmable procedure to find the IBZ is as follows: First, one divides the three $\mathbf{b}_i$ vectors by an integer number of times. This yields a (more-or-less) uniform grid of $\mathbf{k}$-points. Second, by applying to each $\mathbf{k}$-point in the generated grid the *point-group operations*, one can extract a list of non-equivalent $\mathbf{k}$-points. If a $\mathbf{k}$-point is found to be already in the list, its weight $w_{\mathbf{k}}$ is increased by 1, otherwise it is added to the list [148]. Because it is shared with other wedges, a $\mathbf{k}$-point at the boundaries of an IBZ carries a smaller weight with a *multiplicity* factor $m = 1/W_s$, where W_s is the number of IBZ's that share the point. Indeed, any point inside the IBZ have $m = 1$; however, the Γ point has $m = 1/W_{\text{tot}}$, where W_{tot} is the total number of IBZ's required by the BZ to be stuffed with. At the end, the weights $w_{\mathbf{k}}$ should be normalized such that [75]

$$\sum w_{\mathbf{k}} = 1 \; . \tag{C.0.8}$$

Appendix D. Classical Electrodynamics of Solids

D.1 Electromagnetic Waves in Linear Macroscopic Media

To macroscopically describe the interaction of electromagnetic fields with a solid, one needs two sets of equations [270–273]: Maxwell equations and the so-called material (or constitutive) equations. Below, we give these equations and summarize some of their implications that are relevant to our study.

Maxwell equations in vacuum

The four classical Maxwell equations in vacuum are (in Gaussian units):

$$\nabla \cdot \mathbf{E}(\mathbf{r},t) = 4\pi\rho(\mathbf{r},t) \qquad \text{(Gauss's law)}, \tag{D.1.1a}$$

$$\nabla \cdot \mathbf{B}(\mathbf{r},t) = 0 \qquad \text{(No free magnetic monopole)}, \tag{D.1.1b}$$

$$\nabla \times \mathbf{E}(\mathbf{r},t) + \frac{1}{c}\frac{\partial \mathbf{B}(\mathbf{r},t)}{\partial t} = 0 \qquad \text{(Faraday's law)}, \tag{D.1.1c}$$

$$\nabla \times \mathbf{B}(\mathbf{r},t) - \frac{1}{c}\frac{\partial \mathbf{E}(\mathbf{r},t)}{\partial t} = \frac{4\pi}{c}\mathbf{J}(\mathbf{r},t) \qquad \text{(Ampere's law)}. \tag{D.1.1d}$$

In these equations, $\mathbf{E}$ is the electric field vector, $\mathbf{B}$ is the magnetic induction field vector, ρ is the electric charge density, $\mathbf{J}$ is the electric current density, c is the speed of light in vacuum, and $(\mathbf{r},t)$ indicates the spatial and temporal dependence of these quantities. For convenience, fields ($\mathbf{E}$ and $\mathbf{B}$) are put on the left while sources (ρ and $\mathbf{J}$) are put on the right.

Material equations

In the presence of a medium that is subject to electric and magnetic fields, the total charge density $\rho = \rho_{\text{total}}$ that appears in Gauss's law (Eq. D.1.1a) has two contributions, free external charge ρ_{ext} and bound charge ρ_{pol} due to polarization $\mathbf{P}$

$$\rho_{\text{total}}(\mathbf{r},t) = \rho_{\text{ext}}(\mathbf{r},t) + \rho_{\text{pol}}(\mathbf{r},t) = \rho_{\text{ext}}(\mathbf{r},t) - \nabla \cdot \mathbf{P}(\mathbf{r},t)\ . \tag{D.1.2}$$

If there is no external current $\mathbf{J}_{\rm ext}$, the total current density $\mathbf{J} = \mathbf{J}_{\rm total}$ that appears in Ampere's law (Eq. D.1.1d) can be written as

$$\mathbf{J}_{\rm total}(\mathbf{r},t) = \mathbf{J}_{\rm cond}(\mathbf{r},t) + \mathbf{J}_{\rm bound}(\mathbf{r},t) = \mathbf{J}_{\rm cond}(\mathbf{r},t) + \frac{\partial \mathbf{P}(\mathbf{r},t)}{\partial t} + c\nabla \times \mathbf{M}(\mathbf{r},t), \qquad \text{(D.1.3)}$$

where $\mathbf{J}_{\rm cond}$ arises from the transport of electrons in the presence of electric field, while the time dependent polarization $\frac{\partial \mathbf{P}}{\partial t}$ and the spatially dependent magnetization $\nabla \times \mathbf{M}$ contribute to the bound (or displacement) current $\mathbf{J}_{\rm bound}$ component.

By substituting Eqs. D.1.2 and D.1.3 into Eqs. D.1.1a and D.1.1d, one arrives at the so-called material (or constitutive) equations:

$$\mathbf{D}(\mathbf{r},t) = \varepsilon_1 \mathbf{E}(\mathbf{r},t) = \mathbf{E}(\mathbf{r},t) + 4\pi \mathbf{P}(\mathbf{r},t) = (1 + 4\pi\chi_e)\mathbf{E}(\mathbf{r},t), \qquad \text{(D.1.4a)}$$

$$\mathbf{B}(\mathbf{r},t) = \mu_1 \mathbf{H}(\mathbf{r},t) = \mathbf{H}(\mathbf{r},t) + 4\pi \mathbf{M}(\mathbf{r},t) = (1 + 4\pi\chi_m)\mathbf{H}(\mathbf{r},t), \qquad \text{(D.1.4b)}$$

$$\mathbf{J}_{\rm cond}(\mathbf{r},t) = \sigma_1 \mathbf{E}(\mathbf{r},t) \qquad \text{(Ohm's law)}, \qquad \text{(D.1.4c)}$$

which define the auxiliary vectors: the electric displacement field $\mathbf{D}$ and the magnetic field strength $\mathbf{H}$. The material parameters which connect the fields are the dielectric constant or permitivity (ε_1), the permeability (μ_1), the conductivity (σ_1), the dielectric susceptibility (χ_e), and the magnetic susceptibility (χ_m).

Eq. D.1.4a simply says that the difference between the $\mathbf{D}$-field and the $\mathbf{E}$-field which is caused be the induced polarization $\mathbf{P}$ is described by ε_1. The *linear* proportionality between $\mathbf{E}$ and $\mathbf{P}$ is given by χ_e. Similarly, Eq. D.1.4b shows that the difference between the $\mathbf{B}$-filed and the $\mathbf{H}$-field which is caused be the induced magnetization $\mathbf{M}$ is described by μ_1. The *linear* proportionality between $\mathbf{H}$ and $\mathbf{M}$ is given by χ_m.

Maxwell equations in matter

Using these definitions (i.e. Eqs. D.1.2, D.1.3 and D.1.4), one can now write Maxwell equations (Eqs. D.1.1) in matter as

$$\nabla \cdot \mathbf{D}(\mathbf{r},t) = 4\pi\rho_{\text{ext}}(\mathbf{r},t), \tag{D.1.5a}$$

$$\nabla \cdot \mathbf{B}(\mathbf{r},t) = 0, \tag{D.1.5b}$$

$$\nabla \times \mathbf{E}(\mathbf{r},t) + \frac{1}{c}\frac{\partial \mathbf{B}(\mathbf{r},t)}{\partial t} = 0, \tag{D.1.5c}$$

$$\nabla \times \mathbf{H}(\mathbf{r},t) - \frac{1}{c}\frac{\partial \mathbf{D}(\mathbf{r},t)}{\partial t} = \frac{4\pi}{c}\mathbf{J}_{\text{cond}}(\mathbf{r},t). \tag{D.1.5d}$$

Wave equations in matter

Recall the vector identity

$$\nabla \times (\nabla \times \mathbf{A}) = -\nabla^2\mathbf{A} + \nabla(\nabla \cdot \mathbf{A}) \,, \tag{D.1.6}$$

and take $\nabla \times (\nabla \times \mathbf{E})$, where $(\nabla \times \mathbf{E})$ is given by Eq. D.1.5c while $\mathbf{E}$ itself is given by Eq. D.1.4a, to obtain

$$\nabla^2\mathbf{E} - \frac{\varepsilon_1\mu_1}{c^2}\frac{\partial^2\mathbf{E}}{\partial t^2} + \frac{4\pi\mu_1\sigma_1}{c^2}\frac{\partial \mathbf{E}}{\partial t} = 0. \tag{D.1.7}$$

Similarly, taking $\nabla \times (\nabla \times \mathbf{H})$, where $(\nabla \times \mathbf{H})$ is given by Eq. D.1.5d while $\mathbf{H}$ itself is given by Eq. D.1.4b, one obtains

$$\nabla^2\mathbf{H} - \frac{\varepsilon_1\mu_1}{c^2}\frac{\partial^2\mathbf{H}}{\partial t^2} + \frac{4\pi\mu_1\sigma_1}{c^2}\frac{\partial \mathbf{H}}{\partial t} = 0. \tag{D.1.8}$$

Eqs. D.1.7 and D.1.8 above describe the propagation of the electric and magnetic fields in matter. A possible solution to them is the mono-harmonic plane wave fields in the following form

$$\mathbf{E}(\mathbf{r},t) = \mathbf{E}_0 e^{j(\mathbf{q}\cdot\mathbf{r}-\omega t)} \,, \tag{D.1.9a}$$

$$\mathbf{H}(\mathbf{r},t) = \mathbf{H}_0 e^{j(\mathbf{q}\cdot\mathbf{r}-\omega t+\phi)} \,, \tag{D.1.9b}$$

where $\mathbf{E}_0$ and $\mathbf{H}_0$ are the maximum amplitudes, $\mathbf{q}$ is the wavevector, ω is the angular frequency, ϕ is a phase factor and $j = \sqrt{-1}$.

The wavevector

By substituting Eq. D.1.9a into Eq. D.1.7, or substituting Eq. D.1.9b into Eq. D.1.8, one obtains a dispersion relation between the wavevector $\mathbf{q}$ and the frequency ω

$$\mathbf{q} = \frac{\omega}{c}\left[\varepsilon_1\mu_1 + j\frac{4\pi\mu_1\sigma_1}{\omega}\right]^{\frac{1}{2}}\mathbf{n}_\mathbf{q} \ , \tag{D.1.10}$$

where $\mathbf{n}_\mathbf{q}$ is the unit vector in the direction of $\mathbf{q}$.

The relation between $\mathbf{E}$ and $\mathbf{H}$

Consider Eqs. D.1.9, it is straightforward to verify that

$$\nabla \times \mathbf{E} = j(\mathbf{q} \times \mathbf{E}_0)e^{j(\mathbf{q}\cdot\mathbf{r}-\omega t)}. \tag{D.1.11}$$

Substituting Eqs. D.1.11 and D.1.9b into Eq. D.1.5c and using $\mathbf{B} = \mu_1\mathbf{H}$ yield

$$\mathbf{H}_0 = \frac{c}{\omega}\frac{1}{\mu_1}(\mathbf{q} \times \mathbf{E}_0)\, e^{-j\phi} \ . \tag{D.1.12}$$

Substituting Eq. D.1.12 above back into Eq. D.1.9b gives the relation between $\mathbf{E}$ and $\mathbf{H}$[1]

$$\mathbf{H} = \frac{c}{\omega\mu_1}\mathbf{q} \times \mathbf{E} \ . \tag{D.1.13}$$

Poynting vector

Recall that the energy flux density (energy transported per unit area per unit time) of an electromagnetic wave is given by the so-called Poyinting vector $\mathbf{S}$

$$\mathbf{S} = \frac{c}{4\pi}(\mathbf{E} \times \mathbf{H}), \tag{D.1.14}$$

where c is the phase velocity of the wave.

[1] Eq. D.1.13 is Eq. 2.2.17 in Ref. [271] exactly; however it is a very general relation. If one considers the special case in which $\sigma = 0$, then, from Eq. D.1.10, we have $\mathbf{q} = \frac{\omega}{c}\sqrt{\varepsilon_1\mu_1}\mathbf{n}_\mathbf{q}$. Substituting this back into Eq. D.1.13 yields: $\mathbf{H} = \sqrt{\frac{\varepsilon_1}{\mu_1}}\ \mathbf{n}_\mathbf{q} \times \mathbf{E}$, which is the well-known relation for the non-conducting materials (cf. Eq. 2.2.21 in Ref. [271]).

Wave intensity

Intensity I of a wave is defined as its time averaged power per unit area. That is

$$I = \langle \mathbf{S}(t) \rangle = \frac{1}{T} \int_0^T \mathrm{d}t \, |\mathbf{S}(t)| \, , \tag{D.1.15}$$

where the integral is taken over one time period $T = \frac{2\pi}{\omega}$ (cf. [272, p. 381]). Assuming that the fields have the form of Eqs. D.1.9 and using Eq. D.1.13, the integral above reads

$$\begin{aligned} I = \langle \mathbf{S}(t) \rangle &= \frac{c}{4\pi} \frac{1}{T} \int_0^T \mathrm{d}t \; |\mathbf{E} \times \mathbf{H}| \\ &= \frac{c}{4\pi} \frac{1}{T} \int_0^T \mathrm{d}t \; \left| \mathbf{E} \times \left(\frac{c}{\omega \mu_1} \mathbf{q} \times \mathbf{E} \right) \right| \\ &= \frac{c}{4\pi} \frac{c}{\omega \mu_1} \frac{1}{T} \int_0^T \mathrm{d}t \; |\mathbf{q}| \, |\mathbf{E}_0|^2 \\ &= \frac{c}{4\pi} \frac{c}{\omega \mu_1} \; |\mathbf{q}| \, |\mathbf{E}_0|^2 \; , \end{aligned} \tag{D.1.16}$$

where we made use of the vector identity

$$\mathbf{A} \times (\mathbf{B} \times \mathbf{C}) = \mathbf{B}(\mathbf{A} \cdot \mathbf{C}) - \mathbf{C}(\mathbf{A} \cdot \mathbf{B}) \, . \tag{D.1.17}$$

Eq. D.1.16 above confirms the well-known fact that the intensity of a plane wave is proportional to the square of its maximum amplitude.

D.2 Optical Constants

Using the introduced definitions and relations in the previous section, we are going to derive all optical constants and show that they can all be calculated from the complex dielectric function solely.

Dielectric constant (ε)

Substituting Eqs.D.1.4a and D.1.9a into Eq. D.1.5d yields

$$c \nabla \times \mathbf{H} = -j\omega\varepsilon_1 \mathbf{E} + 4\pi\sigma_1 \mathbf{E} = -j\omega(\varepsilon_1 + j\frac{4\pi\sigma_1}{\omega})\mathbf{E}. \tag{D.2.1}$$

This defines the complex dielectric function ε as

$$\varepsilon = \varepsilon_1 + j\frac{4\pi\sigma_1}{\omega} = \varepsilon_1 + j\varepsilon_2, \tag{D.2.2}$$

and Eq. D.1.4a can be generalized to

$$\mathbf{D}(\mathbf{r}, t) = \varepsilon\mathbf{E}(\mathbf{r}, t), \tag{D.2.3}$$

to reflect the fact that the field inside the material $\mathbf{E}$ may change magnitude and phase with respect to the field in vacuum $\mathbf{D}$. This is, however, more general and not restricted to ε; the response of the material can have a time delay with respect to the applied perturbation. Thus, one can define a complex permeability μ

$$\mu = \mu_1 + j\mu_2 \ , \tag{D.2.4}$$

and a complex conductivity σ

$$\sigma = \sigma_1 + j\sigma_2 \ . \tag{D.2.5}$$

This generalizes the material equations D.1.4b and D.1.4c to read

$$\mathbf{B} = \mu\mathbf{H} \ , \tag{D.2.6}$$

$$\mathbf{J}_{\text{tot}} = \sigma\mathbf{E} \ . \tag{D.2.7}$$

Refractive index and attenuation coefficient

The refractive index N of a medium is defined as the ratio between the speed of light in vacuum c and the wave phase velocity $v_{ph} = \omega/q$ in the medium

$$N = \frac{c}{v_{ph}} = \frac{c}{\omega}q = \frac{c}{\omega}\frac{\omega}{c}\left[\varepsilon_1\mu_1 + j\frac{4\pi\mu_1\sigma_1}{\omega}\right]^{\frac{1}{2}} = \left[\mu_1\left(\varepsilon_1 + j\varepsilon_2\right)\right]^{\frac{1}{2}} = n + j\kappa \ \ , \tag{D.2.8}$$

where we have made use of Eq. D.1.10, and put $\varepsilon_2 = \frac{4\pi\sigma_1}{\omega}$ as defined by Eq. D.2.2. Thus, Eq. D.2.8 above defines a complex refractive index. To relate the real part n and the imaginar part κ of N to ε_1 and ε_2, we square both sides of Eq. D.2.2 and equate the real parts and imaginary parts to get

$$n^2 - \kappa^2 = \varepsilon_1\mu_1, \tag{D.2.9}$$

$$2n\kappa = \varepsilon_2\mu_1. \tag{D.2.10}$$

Multiplying the last two parts in Eq. D.2.8 by their complex conjugates yields

$$n^2 + \kappa^2 = \left[\mu_1^2\left(\varepsilon_1^2 + \varepsilon_2^2\right)\right]^{\frac{1}{2}}. \tag{D.2.11}$$

Adding Eq. D.2.9 to Eq. D.2.11 and making some arrangements yield

$$n = \sqrt{\frac{\mu_1}{2}}\left(\left[\varepsilon_1^2 + \varepsilon_2^2\right]^{\frac{1}{2}} + \varepsilon_1\right)^{\frac{1}{2}} \tag{D.2.12}$$

Subtracting Eq. D.2.9 from Eq. D.2.11 and making some arrangements yield

$$\kappa = \sqrt{\frac{\mu_1}{2}}\left(\left[\varepsilon_1^2 + \varepsilon_2^2\right]^{\frac{1}{2}} - \varepsilon_1\right)^{\frac{1}{2}} \tag{D.2.13}$$

To understand the meaning of n and κ, we rewrite Eq. D.1.9a using the fact that $\mathbf{q} = \frac{\omega}{c}N\mathbf{n_q} = \frac{\omega}{c}(n + j\kappa)\mathbf{n_q}$, as defined in Eq. D.2.8, to get

$$\mathbf{E}(\mathbf{r}, t) = \mathbf{E}_0 e^{j((\frac{\omega}{c}(n+j\kappa)\mathbf{n_q})\cdot\mathbf{r} - \omega t)} = \left(\mathbf{E}_0 e^{-\left(\frac{\omega\kappa}{c}\mathbf{n_q}\cdot\mathbf{r}\right)}\right) e^{j\omega\left(\frac{n}{c}\mathbf{n_q}\cdot\mathbf{r} - t\right)}. \tag{D.2.14}$$

From Eq. D.2.14 above, and at a given time $t = t'$, the second exponent expresses the change in the wavevector magnitude (i.e. change in wavelength and phase velocity), while the first exponent reflects the damping feature of the wave amplitude in its spatial domain. For this reason, the real part n is commonly referred to as the *refractive index*, while the imaginary part κ is known in the literature as the *attenuation (or extinction) coefficient*.

Absorption coefficient

The absorption coefficient α of a medium is defined via Beer-Lambert law

$$\alpha = -\frac{1}{I(r)}\frac{\mathrm{d}I(r)}{\mathrm{d}r} \quad \text{or} \quad I(r) = I_0 e^{-\alpha r}, \tag{D.2.15}$$

where I refers to the intensity of the wave. If we assume that the plane wave of Eq. D.2.14 travels in the z direction, then the intensity I (Eq. D.1.16) of this wave is[2]

$$I(z) \propto |\mathbf{E}_0|^2 \, e^{-2\frac{\omega\kappa}{c}z} \, . \tag{D.2.16}$$

Substituting Eq. D.2.16 above into Beer-Lambert law (Eq. D.2.15) yields

$$\alpha = -\frac{1}{I(z)}\frac{\mathrm{d}I(z)}{\mathrm{d}z} = 2\frac{\omega}{c}\kappa = \frac{\sqrt{2\mu_1}\omega}{c}\left(\left[\varepsilon_1^2 + \varepsilon_2^2\right]^{\frac{1}{2}} - \varepsilon_1\right)^{\frac{1}{2}}, \tag{D.2.17}$$

where we made use of Eq. D.2.13 in the last part.

Reflectivity

Consider two linear media (1) and (2), the boundary between them is in the xy plane. And consider a plane wave (Eqs. D.1.9) traveling in the z direction (i.e. its wavevector $\mathbf{q}^{(i)} = q^{(i)}\,\hat{\mathbf{z}}$ is perpendicular to the plane interface) and its $\mathbf{E}^{(i)}$ and $\mathbf{H}^{(i)}$ fields point in the x- and y- direction, respectively. A portion of this wave will be reflected off the surface and travels back in medium (1), while the other portion will enter medium (2). By carefully examining this situation, one can arrive at the following relations between the maximum amplitudes of the three portions at the boundary[3]

$$\mathbf{E}_{0x}^{(t)} = \mathbf{E}_{0x}^{(i)} + \mathbf{E}_{0x}^{(r)} \, , \tag{D.2.18}$$

$$\mathbf{H}_{0y}^{(t)} = \mathbf{H}_{0y}^{(i)} - \mathbf{H}_{0y}^{(r)} \, . \tag{D.2.19}$$

[2] We have neglected the prefactor $(\frac{c}{4\pi}\frac{c}{\omega\mu_1}\,\frac{1}{2})$ since it would be common between the numerator and the denominator in Eq. D.2.15 and cancels out.

[3] For details, cf. Refs. [271, 272].

Here, the superscripts, t, i and r stand for the transmitted, the incident and the reflected portion, respectively. The x and y subscripts are to remind us about the polarization directions of the fields. Now, using Eqs. D.1.12 to write the H_0 components in Eq. D.1.12 above in terms of the E_0 components[4], and substituting $q = \frac{w}{c}N$ as defined in Eq. D.2.8, Eq. D.1.12 above reads

$$\frac{N^{(2)}}{\mu_1^{(2)}}\mathbf{E}_{0x}^{(t)} = \frac{N^{(1)}}{\mu_1^{(1)}}\left(\mathbf{E}_{0x}^{(i)} - \mathbf{E}_{0x}^{(r)}\right) \ , \tag{D.2.20}$$

Reflectivity R is defined as the ratio of the time averaged flux of the reflected portion $\langle \mathbf{S}^{(r)}(t)\rangle$ to that of the incident portion $\langle \mathbf{S}^{(i)}(t)\rangle$. Using Eq. D.1.16, an expression for R can be written as

$$R = \frac{\langle \mathbf{S}^{(r)}(t)\rangle}{\langle \mathbf{S}^{(i)}(t)\rangle} = \frac{\frac{\left(v^{(1)}\right)^2}{8\pi\omega\mu_1^{(1)}}\left|\mathbf{q}^{(r)}\right|\left|\mathbf{E}_{0x}^{(r)}\right|^2}{\frac{\left(v^{(1)}\right)^2}{8\pi\omega\mu_1^{(1)}}\left|\mathbf{q}^{(i)}\right|\left|\mathbf{E}_{0x}^{(i)}\right|^2} = \frac{\left|\mathbf{E}_{0x}^{(r)}\right|^2}{\left|\mathbf{E}_{0x}^{(i)}\right|^2} = \frac{\left|\frac{N^{(1)}}{\mu_1^{(1)}} - \frac{N^{(2)}}{\mu_1^{(2)}}\right|^2}{\left|\frac{N^{(1)}}{\mu_1^{(1)}} + \frac{N^{(2)}}{\mu_1^{(2)}}\right|^2} \tag{D.2.21}$$

Here, the last part was obtained by first solving Eqs. D.2.20 and D.2.18 for $\mathbf{E}_{0x}^{(r)}$, then for $\mathbf{E}_{0x}^{(i)}$. Eq. D.2.21 above is a general equation, but if one considers the case in which $N^{(1)} = 1$ (i.e. free space), and $\mu_1^{(1)} = \mu_1^{(2)} \simeq 1$ as for most materials, then R becomes

$$R = \frac{\left|1 - N^{(2)}\right|^2}{\left|1 + N^{(2)}\right|^2} = \frac{(1-n)^2 + k^2}{(1+n)^2 + k^2} \tag{D.2.22}$$

which is a commonly used equation (cf. Eq. 2.4.15 in Ref. [271]).

Transmitivity

Transmitivity (or transmission) T is defined as the ratio of the time averaged flux of the transmitted portion $\langle \mathbf{S}^{(t)}(t)\rangle$ to that of the incident portion $\langle \mathbf{S}^{(i)}(t)\rangle$. Using Eq. D.1.16, an expression

[4] Note that phase factors have been embedded in the maximum amplitudes, which are considered here to be complex.

for T can be written as

$$T = \frac{\langle \mathbf{S}^{(t)}(t) \rangle}{\langle \mathbf{S}^{(i)}(t) \rangle} = \frac{\frac{c^2}{\mu_1^{(2)}} \left| \mathbf{q}^{(t)} \right| \left| \mathbf{E}_{0x}^{(t)} \right|^2}{\frac{c^2}{\mu_1^{(1)}} \left| \mathbf{q}^{(i)} \right| \left| \mathbf{E}_{0x}^{(i)} \right|^2} = \frac{\frac{c^2}{\mu_1^{(2)}} \left| \mathbf{q}^{(t)} \right|}{\frac{c^2}{\mu_1^{(1)}} \left| \mathbf{q}^{(i)} \right|} \frac{\left| 2 \frac{N^{(1)}}{\mu_1^{(1)}} \right|^2}{\left| \frac{N^{(1)}}{\mu_1^{(1)}} + \frac{N^{(2)}}{\mu_1^{(2)}} \right|^2} \tag{D.2.23}$$

Here, the last part was obtained by first solving Eqs. D.2.20 and D.2.18 for $\mathbf{E}_{0x}^{(t)}$, then for $\mathbf{E}_{0x}^{(i)}$. Again, Eq. D.2.21 above is a general equation, but if one considers medium (1) to be the free space, then it is straightforward forward to show that T becomes

$$T = \frac{4n}{(n+1)^2 + k^2} = 1 - R \tag{D.2.24}$$

as one expects from the conservation of energy.

Appendix E. Functionals and Functional Derivatives

Functionals play a central rule in the formulation of electronic structure calculations methods [78]. In fact, most of what is called "calculus of variation" is a branch of the calculus of functionals. Following Refs. [76, Appendix A] and [75, Subsection 4.1.1], in this appendix we briefly quote some basic definitions and properties of functionals and their derivatives. For a compact description, readers are referred to Ref. [76, Appendix A] and to the clear notes by Svetitsky (Ref. [97]).

E.1 What is a Functional?

A functional $F[f]$ is a mapping of an entire function f onto a number [78, Appendix A]. For example, the expectation $\langle Q \rangle = \langle \psi | \hat{Q} | \psi \rangle$ of a quantum dynamical variable Q is a functional that maps ψ onto a number $\langle Q \rangle$ [76].

E.2 Functional Derivative

The functional derivative $\delta F / \delta f(x)$ of F with respect to f at point x is defined via

$$\delta F[f(x)] = \int \mathrm{d}x \, \frac{\delta F}{\delta f(x)} \delta f(x) \tag{E.2.1}$$

where the deferential δF of the functional is the part of the difference $F[f + \delta f] - F[f]$ that depends linearly on δf [76]. The expression E.5.1 can be looked at as a generalization of the usual expression for the multivariable function differential [75, 76]

$$dF(f_1, f_2, \cdots) = \sum_i \frac{\partial F}{\partial f_i} \, \mathrm{d}f_i \quad . \tag{E.2.2}$$

E.3 Properties of Functional Derivative

A number of rules analogue to those of usual derivatives can be derived for functional derivatives. Below are some of these which are relevant for the present work [75]:

$$\frac{\delta}{\delta f(x)}\left(\int \mathrm{d}x\; g[f(x)]\right) = \frac{\partial g[f]}{\partial f(x)} \tag{E.3.1}$$

$$\frac{\delta}{\delta f(x)}\left(\int \mathrm{d}x\; g[f(x)]f(x)\right) = \frac{\partial g[f]}{\partial f(x)}f(x) + g[f(x)] \tag{E.3.2}$$

$$\frac{\delta}{\delta f(x)}\left(\frac{1}{2}\int \mathrm{d}x\,\mathrm{d}x'\; g(x,x')f(x)f(x')\right) = \int \mathrm{d}x'\; g(x,x')f(x') \tag{E.3.3}$$

E.4 Higher-Order Functional Derivatives

The extension to second and higher-order functional derivatives is straightforward [75, 76], and the order of differentiation is usually not important [76]

$$\frac{\delta^2 F}{\delta f(x)\delta f(x')} = \frac{\delta^2 F}{\delta f(x')\delta f(x)} \quad . \tag{E.4.1}$$

E.5 The Chain Rule

Let $F = F[f(x)]$ and $f = f[g(x), x]$; then the basic chain rule for functional derivative states [76]

$$\frac{\delta F}{\delta g(x')} = \int \mathrm{d}x\; \frac{\delta F}{\delta f(x)}\frac{\delta f(x)}{\delta g(x')} \quad . \tag{E.5.1}$$

Appendix F. Crystal Structures: Numerical Data

Information about each chosen crystal structure are given in Sec. 5.2, summarized in Table 5.1 therein and pictures of the unit cells are depectied. In the present appendix we explicitly give numerical data for their lattice geometry (i.e. primitive vectors) and ionic positions (i.e. *initial* basis vectors)[1]. All vectors are given up to a universal scaling factor which scales all lattice vectors and all atomic coordinates. All atomic coordinates are given with respect to the lattice vectors. The additional flag, T or F, for each atom signals whether the respective coordinate(s) of a given atom possess an internal free parameter[2] or not, respectively. We believe that presenting such numerical information allows other researchers to check and/or redo the same calculations we presented in this Thesis.

M_3N structures

1. **$D0_3$:**

```
Primitive vectors
 0.000000000000    0.500000000000    0.500000000000
 0.500000000000    0.000000000000    0.500000000000
 0.500000000000    0.500000000000    0.000000000000
Basis vectors
M  -.5000000000000000  0.5000000000000000  0.5000000000000000   F  F  F
M  -.2500000000000000  -.2500000000000000  -.2500000000000000   F  F  F
M  0.2500000000000000  0.2500000000000000  0.2500000000000000   F  F  F
N  0.0000000000000000  0.0000000000000000  0.0000000000000000   F  F  F
```

2. **A15:**

```
Primitive vectors
 1.00000000  0.00000000  0.00000000
```

[1] For definitions of these terms see App. A

[2] Such coordinate(s) are allowed to change during the ionic relaxation. See Sections 7.3 and 7.4.

```
 0.00000000  1.00000000  0.00000000
 0.00000000  0.00000000  1.00000000
Basis vectors
M  0.25000000  0.50000000  0.00000000     F  F  F
M  0.75000000  0.50000000  0.00000000     F  F  F
M  0.00000000  0.25000000  0.50000000     F  F  F
M  0.00000000  0.75000000  0.50000000     F  F  F
M  0.50000000  0.00000000  0.25000000     F  F  F
M  0.50000000  0.00000000  0.75000000     F  F  F
N  0.00000000  0.00000000  0.00000000     F  F  F
N  0.50000000  0.50000000  0.50000000     F  F  F
```

3. **$D0_9$:**

```
Primitive vectors
 1.00000000  0.00000000  0.00000000
 0.00000000  1.00000000  0.00000000
 0.00000000  0.00000000  1.00000000
Basis vectors
M   0.50000000   .00000000   .00000000     F F F
M   0.00000000   .50000000   .00000000     F F F
M   0.00000000   .00000000   .50000000     F F F
N   0.00000000   .00000000   .00000000     F F F
```

4. **$L1_2$:**

```
Primitive vectors
 1.00000000  0.00000000  0.00000000
 0.00000000  1.00000000  0.00000000
 0.00000000  0.00000000  1.00000000
Basis vectors
M   0.00000000   .50000000   .50000000     F F F
M   0.50000000   .00000000   .50000000     F F F
M   0.50000000   .50000000   .00000000     F F F
N   0.00000000   .00000000   .00000000     F F F
```

5. **$D0_2$:**

```
Primitive vectors
  -0.5000000000000000    0.5000000000000000    0.5000000000000000
   0.5000000000000000   -0.5000000000000000    0.5000000000000000
   0.5000000000000000    0.5000000000000000   -0.5000000000000000
Basis vectors
M  0.49560002   .15140004   .34419999   T T T
M  0.19279995  -.15140004   .34419999   T T T
M  0.34419999   .49560002   .15140004   T T T
M  0.34419999   .19279995  -.15140004   T T T
M  0.15140004   .34419999   .49560002   T T T
M  -.15140004   .34419999   .19279995   T T T
M  -.49560002  -.15140004  -.34419999   T T T
M  -.19279995   .15140004  -.34419999   T T T
M  -.34419999  -.49560002  -.15140004   T T T
M  -.34419999  -.19279995   .15140004   T T T
M  -.15140004  -.34419999  -.49560002   T T T
M  0.15140004  -.34419999  -.19279995   T T T
N  0.50000000   .50000000   .50000000   F F F
N  0.50000000   .00000000   .00000000   F F F
N  0.00000000   .50000000   .00000000   F F F
N  0.00000000   .00000000   .50000000   F F F
```

6. ϵ-**Fe_3N:**

```
Primitive vectors
     1.0000000000         0.0000000000         0.0000000000
    -0.5000000000         0.8660254040         0.0000000000
     0.0000000000         0.0000000000         0.9318713710
Basis vectors
M     0.328000009         0.000000000         0.000000000       T T T
M     0.000000000         0.328000009         0.000000000       T T T
M     0.671999991         0.671999991         0.000000000       T T T
M     0.671999991         0.000000000         0.500000000       T T T
M     0.000000000         0.671999991         0.500000000       T T T
M     0.328000009         0.328000009         0.500000000       T T T
N     0.333333343         0.666666687         0.250000000       F F F
N     0.666666627         0.333333313         0.750000000       F F F
```

7. **RhF_3:**

```
Primitive vectors
1.000000000000      0.000000000000      0.000000000000
0.581839108853      0.813303910853      0.000000000000
0.581839108853      0.299153068140      0.756287440879
Basis vectors
M -.08300000000      0.58300000000      0.25000000000   T   T   T
M 0.08300000000      -.58300000000      -.25000000000   T   T   T
M 0.58300000000      0.25000000000      -.08300000000   T   T   T
M -.58300000000      -.25000000000      0.08300000000   T   T   T
M 0.25000000000      -.08300000000      0.58300000000   T   T   T
M -.25000000000      0.08300000000      -.58300000000   T   T   T
N 0.00000000000      0.00000000000      0.00000000000   F   F   F
N 0.50000000000      0.50000000000      0.50000000000   F   F   F
```

MN structures

1. **B1:**

```
Primitive vectors
0.00000000  0.50000000  0.50000000
0.50000000  0.00000000  0.50000000
0.50000000  0.50000000  0.00000000
Basis vectors
M 0.00000000  0.00000000  0.00000000      F F F
N 0.50000000  0.50000000  0.50000000      F F F
```

2. **B2:**

```
Primitive vectors
1.00000000  0.00000000  0.00000000
0.00000000  1.00000000  0.00000000
0.00000000  0.00000000  1.00000000
Basis vectors
M 0.00000000  0.00000000  0.00000000      F F F
N 0.50000000  0.50000000  0.50000000      F F F
```

3. **B3:**

```
Primitive vectors
0.00000000  0.50000000  0.50000000
0.50000000  0.00000000  0.50000000
0.50000000  0.50000000  0.00000000
Basis vectors
M 0.00000000  0.00000000  0.00000000      F F F
N 0.25000000  0.25000000  0.25000000      F F F
```

4. **B8$_1$:**

```
Primitive vectors
0.500000000 -0.866025404  0.000000000
0.500000000  0.866025404  0.000000000
0.000000000  0.000000000  1.390991986
Basis vectors
M 0.00000000  0.00000000  0.00000000      F F F
M 0.00000000  0.00000000  0.50000000      F F F
N 0.33333333  0.66666667  0.25000000      F F F
N 0.66666667  0.33333333  0.75000000      F F F
```

5. **B$_k$:**

```
Primitive vectors
0.187954122 -0.325546089  0.00000000
0.187954122  0.325546089  0.00000000
0.000000000  0.000000000  1.00000000
Basis vectors
M 0.33333333  0.66666667  0.25000000      F F F
M 0.66666667  0.33333333  0.75000000      F F F
N 0.66666667  0.33333333  0.25000000      F F F
N 0.33333333  0.66666667  0.75000000      F F F
```

6. **B$_h$:**

```
Primitive vectors
0.512160733  -0.88708841  0.00000000
```

```
0.512160733   0.88708841  0.00000000
0.000000000   0.00000000  1.00000000
Basis vectors
M 0.000000000   0.000000000   0.00000000  F F F
N 0.666666666   0.333333333   0.50000000  F F F
```

7. **B4:**

```
Primitive vectors
0.50000000  -.866025404  0.000000000
0.50000000  0.866025404  0.000000000
0.00000000  0.000000000  1.637769116
Basis vectors
M 0.33333333  0.66666667  0.00000000      F F F
M 0.66666667  0.33333333  0.50000000      F F F
N 0.33333333  0.66666667  0.37480000      F F T
N 0.66666667  0.33333333 -0.12520000      F F T
```

8. **B17:**

```
Primitive vectors
1.000000000  0.000000000  0.000000000
0.000000000  1.000000000  0.000000000
0.000000000  0.000000000  1.760525633
Basis vectors
M 0.00000000  0.50000000  0.00000000      F F F
M 0.50000000  0.00000000  0.50000000      F F F
N 0.00000000  0.00000000  0.25000000      F F F
N 0.00000000  0.00000000  0.75000000      F F F
```

9. **B24:**

```
Primitive vectors
0.000000000  0.530405405  0.586872587
0.500000000  0.000000000  0.586872587
0.500000000  0.530405405  0.000000000
Basis vectors
0.000000000  0.000000000  0.000000000   F F F
0.500000000  0.500000000 -0.500000000   F F F
```

MN_2 structures

1. **C1:**

```
Primitive vectors
0.00000000  0.50000000  0.50000000
0.50000000  0.00000000  0.50000000
0.50000000  0.50000000  0.00000000
Basis vectors
M 0.00000000  0.00000000  0.00000000      F F F
N 0.25000000  0.25000000  0.25000000      F F F
N 0.75000000  0.75000000  0.75000000      F F F
```

2. **C2:**

```
Primitive vectors
1.0000000000 0.0000000000  0.0000000000
0.0000000000 1.0000000000  0.0000000000
0.0000000000 0.0000000000  1.0000000000
Basis vectors
M 0.0000000000   0.0000000000   0.0000000000      F F F
M 0.0000000000   0.5000000000   0.5000000000      F F F
M 0.5000000000   0.0000000000   0.5000000000      F F F
M 0.5000000000   0.5000000000   0.0000000000      F F F
N 0.3850000000   0.3850000000   0.3850000000      T T T
N -.3850000000   -.3850000000   -.3850000000      T T T
N 0.8850000000   0.1150000000   0.3850000000      T T T
N 0.1150000000   0.8850000000   -.3850000000      T T T
N 0.3850000000   0.1150000000   0.8850000000      T T T
N -.3850000000   0.8850000000   0.1150000000      T T T
N 0.8850000000   0.3850000000   0.1150000000      T T T
N 0.1150000000  -.38500000000   0.8850000000      T T T
```

3. **C18:**

```
Primitive vectors
1.000000000  0.000000000  0.000000000
0.000000000  1.220468891  0.000000000
```

```
0.000000000  0.000000000  0.762173129
Basis vectors
M 0.00000000  0.00000000  0.00000000   F F F
M 0.50000000  0.50000000  0.50000000   F F F
N 0.20000000  0.37800000  0.00000000   T T F
N -.20000000  -.37800000  0.00000000   T T F
N 0.30000000  0.87800000  0.50000000   T T F
N 0.70000000  0.12200000  0.50000000   T T F
```

4. **$CoSb_2$:**

```
Primitive vectors
        1.0000000000         0.0000000000         0.0000000000
        0.0000000000         0.9815910200         0.0000000000
       -0.4667420000         0.0000000000         0.8905223700
Basis vectors
M     0.270000011         0.000000000         0.280000001         T F T
M     0.730000019         0.000000000         0.720000029         T F T
M     0.730000019         0.500000000         0.219999999         T F T
M     0.270000011         0.500000000         0.779999971         T F T
N     0.354000002         0.358999997         0.167999998         T T T
N     0.646000028         0.641000032         0.832000017         T T T
N     0.646000028         0.858999968         0.332000017         T T T
N     0.354000002         0.141000003         0.667999983         T T T
N     0.162000000         0.638000011         0.368000001         T T T
N     0.838000000         0.361999989         0.631999969         T T T
N     0.838000000         0.138000011         0.131999999         T T T
N     0.162000000         0.861999989         0.868000031         T T T
```

Appendix G. Presentations and Activities

Conferences, workshops, schools, courses, seminars and symposia in which I participated during the course of this study, and oral and poster presentations I gave out of this study are listed below in a reverse chronological order:

1. Mohammed S. H. Suleiman and Daniel P. Joubert; *Ab initio calculations on the structural, electronic and optical properties of the hazardous silver nitrides*; a talk (no. 557) presented on Friday, 12 July 2013 at the South African Institute of Physics 58th Annual Conference (SAIP 2013), 8–12 July 2013, University of Zululand, Richards Bay, **South Africa**.

2. 19 – 30 January 2013, 1st Khartoum Workshop On Advances In Materials Science (KWAMS13), University of Khartoum, Khartoum, **Sudan**.

3. Mohammed Suleiman Hussein Suleiman; *Electronic Structure Calculations for Solids: Basic Concepts and some Applications*; a two-hours talk presented on Thursday, 17 January 2013 at the College of Science Seminar, Sudan University of Science and Technology (SUST), Khartoum, **Sudan**.

4. Mohammed S. H. Suleiman and Daniel P. Joubert; *Noble Metals: from South African Mines to Computer Nitridation*; a talk presented on Monday, 22 October 2012 at the Wits 4th Cross Faculty Graduate Symposium, 19–22 October 2012, University of the Witwatersrand, Johannesburg, **South Africa**.

5. Mohammed S H Suleiman and Daniel P Joubert; *Structural, electronic and optical properties of gold nitrides*; a talk (no. 298) presented on Wednesday 11 July 2012 at the South African Institute of Physics 57th Annual Conference (SAIP 2012), 9–13 July 2012, University of Pretoria, Pretoria, **South Africa**.

6. Mohammed S H Suleiman and Daniel P Joubert; *First-principles calculations of the structural, electronic and optical properties of PdN and PdN_2*; a poster (no. 299) presented on

Thursday 12 July 2012 at the South African Institute of Physics 57th Annual Conference (SAIP 2012), 9–13 July 2012, University of Pretoria, Pretoria, **South Africa**.

7. 11 - 13 June 2012, VASP Workshop; The Institut des Matériaux Jean Rouxel (IMN), Nantes, **France**.

8. Mohammed S. H. Suleiman, Daniel P. Joubert and Mahlaga P. Molepo; *Computational Study of the Structural, Electronic and Optical Properties of Copper Nitrides*; a poster (no. 28) presented at the 2nd edition of the International Conference on Advanced Materials Modelling (ICAMM 2012), 14 – 16 June 2012, The Institut des Matériaux Jean Rouxel (IMN), Nantes, **France**.

9. 28 November – 03 December 2011, CHPC Introductory Scientific Programming School, Meraka Institute, Council for Scientific and Industrial Research (CSIR), Pretoria, **South Africa**.

10. 12 – 21 July 2011, Hands-on Tutorial Workshop 2011 on Ab Initio Molecular Simulations: Toward a First-Principles Understanding of Materials Properties and Functions, Fritz-Haber-Institut der Max-Planck-Gesellschaft, Berlin, **Germany**.
    Presented a poster : Mohammed S. H. Suleiman, Daniel P. Joubert and Mahlaga P. Molepo; *A Theoretical Investigation of Structural, Mechanical, Electronic and Optical Properties of some Bulk Late Transition-Metal Nitrides.*

11. 29 November – 10 December 2010, The High Performance Computing School, the Centre for High Performance Computing (CHPC) of the Council for Scientific and Industrial Research (CSIR), Cape Town, **South Africa**.

12. Mohammed Suleiman and Daniel P Joubert, *Ab initio Study of the Crystal Structures and Mechanical Properties of some Late Transition-Metal Nitrides*; a poster (no. 209) presented at the South African Institute of Physics 55th Annual Conference (SAIP 2010), 27 September – 1 October 2010, Council for Scientific and Industrial Research (CSIR), Pretoria, **South Africa**.
    Abstracts are available online at `http://events.saip.org.za/saip2010/`, ISBN: 978-0-620-46211-2.

13. 14 – 20 August 2010 CAMD Summer School 2010 on the Electronic Structure Theory and Materials Design, Centre for Atomic-Scale Materials Design, Technical University of Denmark (DTU), Copenhagen, **Denmark**.
    Presented a poster: M S H Suleiman and D P Joubert; *A Theoretical Investigation of some Ground-State Properties of Group 10 and 11 Transition-Metal Mono-Nitrides.*

14. 19 - 30 July 2010, African School on Electronic Structure Methods and Applications (AS-ESMA 2010), African Institute for Mathematical Sciences (AIMS), Cape Town, **South Africa**.

15. 24 January – 11 February 2010, attended a postgraduate course on *Statistical Mechanics*, taught by Prof. Stephane Ouvry at the African Institute for Mathematical Sciences (AIMS), Cape Town, **South Africa**.

List of Publications

E-Prints

1. Mohammed S. H. Suleiman and Daniel P. Joubert. *Structural, electronic and optical characterization of bulk platinum nitrides: a first-principles study*. ArXiv e-prints, January 2013 [http://arxiv.org/abs/1301.5490].

2. Mohammed S. H. Suleiman and Daniel P. Joubert. *Theoretical calculations on the structural, electronic and optical properties of bulk silver nitrides*. ArXiv e-prints, December 2012 [http://arxiv.org/abs/1212.6507].

3. Mohammed S. H. Suleiman, Mahlaga P. Molepo and Daniel P. Joubert. *A theoretical investigation of structural, electronic and optical properties of bulk copper nitrides*. ArXiv e-prints, November 2012 [http://arxiv.org/abs/1211.0179].

4. Mohammed S. H. Suleiman and Daniel P. Joubert. *Computational study of the structural, electronic and optical properties of bulk palladium nitrides*. ArXiv e-prints, October 2013 [http://arxiv.org/a/suleiman_m_1].

5. Mohammed S. H. Suleiman and Daniel P. Joubert. *Quantum mechanical ab initio calculations of the structural, electronic and optical properties of bulk gold nitrides*. ArXiv e-prints, September 2013 [http://arxiv.org/abs/1309.3753].

Conference Proceedings

6. Mohammed S H Suleiman and Daniel P Joubert. *Structural, electronic and optical properties of gold nitrides*. In South African Institute of Physics 57th Annual Conference (SAIP 2012), No. 298, July 2012 .

7. Mohammed S H Suleiman and Daniel P Joubert. *First-principles calculations of the structural, electronic and optical properties of PdN and PdN_2*. In South African Institute of Physics 57th Annual Conference (SAIP 2012), No. 299, July 2012.

Bibliography

[1] Mohammed S. H. Suleiman and Daniel P. Joubert. Structural, electronic and optical characterization of bulk platinum nitrides: a first-principles study. *ArXiv e-prints*, January 2013.

[2] Mohammed S. H. Suleiman and Daniel P. Joubert. Theoretical calculations on the structural, electronic and optical properties of bulk silver nitrides. *ArXiv e-prints*, December 2012.

[3] Mohammed S. H. Suleiman, Mahlaga P. Molepo, and Daniel P. Joubert. A theoretical investigation of structural, electronic and optical properties of bulk copper nitrides. *ArXiv e-prints*, November 2012.

[4] Mohammed S. H. Suleiman and Daniel P. Joubert. Computational study of the structural, electronic and optical properties of bulk palladium nitrides. *ArXiv e-prints*, October 2013.

[5] Mohammed S. H. Suleiman and Daniel P. Joubert. Quantum mechanical ab initio calculations of the structural, electronic and optical properties of bulk gold nitrides. *ArXiv e-prints*, September 2013.

[6] Mohammed S H Suleiman and Daniel P Joubert. Structural, electronic and optical properties of gold nitrides. In *South African Institute of Physics 57th Annual Conference (SAIP 2012), No. 298*, July 2012.

[7] Mohammed S H Suleiman and Daniel P Joubert. First-principles calculations of the structural, electronic and optical properties of PdN and PdN_2. In *South African Institute of Physics 57th Annual Conference (SAIP 2012), No. 299*, July 2012.

[8] C. Colinet. Ab-initio calculation of enthalpies of formation of intermetallic compounds and enthalpies of mixing of solid solutions. *Intermetallics*, 11(1112):1095 – 1102, 2003. Special Issue Dedicated to the International Meeting on Thermodynamics of Alloys – TOFA 2002.

[9] Seung-Hoon Jhi, Jisoon Ihm, Steven G. Louie, and Marvin L. Cohen. Electronic mechanism of hardness enhancement in transition-metal carbonitrides. *Nature*, 399:132 – 134, 1999.

[10] A. Fernández Guillermet, J. Häglund, and G. Grimvall. Cohesive properties of 4*d*-transition-metal carbides and nitrides in the NaCl-type structure. *Physical Review B*, 45:11557–11567, May 1992.

[11] Leif I. Johansson. Electronic and structural properties of transition-metal carbide and nitride surfaces. *Surface Science Reports*, 21(56):177 – 250, 1995.

[12] L. Šiller, N. Peltekis, S. Krishnamurthy, Y. Chao, S. J. Bull, and M. R. C. Hunt. Gold film with gold nitride—A conductor but harder than gold. *Applied Physics Letters*, 86(22):221912, 2005.

[13] Jian Zhou, Zhimei Sun, and Rajeev Ahuja. Ab initio Study of the Phase Stability and Mechanical Properties of 5d Transition Metal Nitrides MN_2. *Journal of Alloys and Compounds*, 472(12):425 – 428, 2009.

[14] Jamal Uddin and Gustavo E. Scuseria. Structures and electronic properties of platinum nitride by density functional theory. *Physical Review B*, 72:035101, Jul 2005.

[15] L.H. Yu, K.L. Yao, Z.L. Liu, and Y.S. Zhang. Structural property of platinum mononitride. *Physica B: Condensed Matter*, 399(1):50 – 54, 2007.

[16] Jeffrey C. Grossman, Ari Mizel, Michel Côté, Marvin L. Cohen, and Steven G. Louie. Transition metals and their carbides and nitrides: Trends in electronic and structural properties. *Physical Review B*, 60:6343–6347, Sep 1999.

[17] A. C. Brieva, L. Alves, S. Krishnamurthy, and L. Šiller. Gold surface with gold nitride–a surface enhanced Raman scattering active substrate. *Journal of Applied Physics*, 105(5):054302, 2009.

[18] Ma Guadalupe Moreno-Armenta, Alejandro Martínez-Ruiz, and Noboru Takeuchi. Ab initio total energy calculations of copper nitride: the effect of lattice parameters and Cu content in the electronic properties. *Solid State Sciences*, 6(1):9 – 14, 2004.

[19] Bernhard Eck, Richard Dronskowski, Masao Takahashi, and Shinichi Kikkawa. Theoretical Calculations on the Structures, Electronic and Magnetic Properties of Binary 3d Transition Metal Nitrides. *Journal of Materials Chemistry*, 9:1527–1537, 1999.

[20] Jonathan C. Crowhurst, Alexander F. Goncharov, B. Sadigh, J.M. Zaug, D. Aberga, Yue Meng, and Vitali B. Prakapenka. Synthesis and characterization of nitrides of iridium and palladium. *Journal of Materials Research*, 23:1 – 5, 2008.

[21] Alexander Frank Wells. *Structural Inorganic Chemistry*. Oxford University Press, 5th edition, 1984.

[22] Eugene Gregoryanz, Chrystele Sanloup, M. Somayazulu, James Badro, Guillaume Fiquet, Ho kwang Mao, and Russell J. Hemley. Synthesis and characterization of a binary noble metal nitride. *Nature Materials*, 3:294 – 297, 2004.

[23] Angelo Citra, Xuefeng Wang, William D. Bare, and Lester Andrews. Reactions of Laser-Ablated Platinum with Nitrogen: Matrix Infrared Spectra of Platinum Nitride, Complexes, and Anions. *The Journal of Physical Chemistry A*, 105(33):7799–7811, 2001.

[24] G Soto. Synthesis of PtNx films by reactive laser ablation. *Materials Letters*, 58(16):2178 – 2180, 2004.

[25] Jonathan C. Crowhurst, Alexander F. Goncharov, Babak Sadigh, Cheryl L. Evans, Peter G. Morrall, James L. Ferreira, and A. J. Nelson. Synthesis and Characterization of the Nitrides of Platinum and Iridium. *Science*, 311(5765):1275 – 1278, 2006.

[26] Fan Chang-Zeng, Sun Li-Ling, Wang Yuan-Xu, Wei Zun-Jie, Liu Ri-Ping, Zeng Song-Yan, and Wang Wen-Kui. First-Principles Study on the Elastic Properties of Platinum Nitride. *Chinese Physics Letters*, 22(10):2637, 2005.

[27] Andrea F. Young, Javier A. Montoya, Chrystele Sanloup, Michele Lazzeri, Eugene Gregoryanz, and Sandro Scandolo. Interstitial dinitrogen Makes PtN_2 an Insulating Hard Solid. *Physical Review B*, 73:153102, Apr 2006.

[28] Xiuwen Zhang, Giancarlo Trimarchi, and Alex Zunger. Possible pitfalls in theoretical determination of ground-state crystal structures: The case of platinum nitride. *Physical Review B*, 79:092102, Mar 2009.

[29] R. Yu, Q. Zhan, and X. F. Zhang. Elastic stability and electronic structure of pyrite type PtN[sub 2]: A hard semiconductor. *Applied Physics Letters*, 88(5):051913, 2006.

[30] Jörg von Appen, Marck-Willem Lumey, and Richard Dronskowski. Mysterious Platinum Nitride. *Angewandte Chemie International Edition*, 45(26):4365–4368, 2006.

[31] S. K. R. Patil, S. V. Khare, B. R. Tuttle, J. K. Bording, and S. Kodambaka. Mechanical stability of possible structures of PtN investigated using first-principles calculations. *Physical Review B*, 73:104118, Mar 2006.

[32] Robert Juza and Harry Hahn. Kupfernitrid, Metallamide und Metallnitride VII. *Zeitschrift für anorganische und allgemeine Chemie*, 241(2-3):172–178, 1939.

[33] U. Hahn and W. Weber. Electronic Structure and Chemical-Bonding Mechanism of Cu_3N, Cu_3NPd, and Related Cu(I) Compounds. *Physical Review B*, 53:12684–12693, May 1996.

[34] A.L. Ji, R. Huang, Y. Du, C.R. Li, Y.Q. Wang, and Z.X. Cao. Growth of Stoichiometric Cu_3N Thin Films by Reactive Magnetron Sputtering. *Journal of Crystal Growth*, 295(1):79 – 83, 2006.

[35] Y. Du, A.L. Ji, L.B. Ma, Y.Q. Wang, and Z.X. Cao. Electrical conductivity and photoreflectance of nanocrystalline copper nitride thin films deposited at low temperature. *Journal of Crystal Growth*, 280(34):490 – 494, 2005.

[36] Ma. Guadalupe Moreno-Armenta and Gerardo Soto. Stability and Electronic Structure of Intrinsic and Intercalated Copper Nitride Alloys. *Solid State Sciences*, 10(5):573–579, 2008.

[37] S Ghosh, F Singh, D Choudhary, D.K Avasthi, V Ganesan, P Shah, and A Gupta. Effect of substrate temperature on the physical properties of copper nitride films by r.f. reactive sputtering. *Surface and Coatings Technology*, 142144(0):1034 – 1039, 2001. ¡ce:title¿Proceedings of the 7th International Conference on Plasma Surface Engineering¡/ce:title¿.

[38] N Gordillo, R Gonzalez-Arrabal, A Ivarez Herrero, and F Agull-Lpez. Free-carrier contribution to the optical response of N-rich Cu_3N thin films. *Journal of Physics D: Applied Physics*, 42(16):165101, 2009.

[39] Rainer Cremer, Mirjam Witthaut, Dieter Neuschtz, Cyril Trappe, Martin Laurenzis, Olaf Winkler, and Heinrich Kurz. Deposition and Characterization of Metastable Cu_3N Layers for Applications in Optical Data Storage. *Microchimica Acta*, 133:299–302, 2000. 10.1007/s006040070109.

[40] Toshiro Maruyama and Tomonor Morishita. Copper Nitride and Tin Nitride Thin Films for Write-Once Optical Recording Media. *Applied Physics Letters*, 69(7):890–891, 1996.

[41] Masaaki Asano, Kazuo Umeda, and Akira Tasaki. Cu_3N Thin Film for a New Light Recording Media. *Japanese Journal of Applied Physics*, 29(Part 1, No. 10):1985–1986, 1990.

[42] Leon Maya. Covalent nitrides for maskless laser writing of microscopic metal lines. volume 282, pages 203–208, 1993.

[43] Dao yuan Wang, Norio Nakamine, and Yasunori Hayashi. Properties of various sputter-deposited Cu–N thin films. *Journal of Vacuum Science & Technology A: Vacuum, Surfaces, and Films*, 16(4):2084 – 2092, 1998.

[44] C. Gallardo-Vega and W. de la Cruz. Study of the structure and electrical properties of the copper nitride thin films deposited by pulsed laser deposition. *Applied Surface Science*, 252(22):8001 – 8004, 2006.

[45] J.F Pierson. Structure and properties of copper nitride films formed by reactive magnetron sputtering. *Vacuum*, 66(1):59 – 64, 2002.

[46] Z.F. Hou. Effects of Cu, N, and Li Intercalation on the Structural Stability and Electronic Structure of Cubic Cu_3N. *Solid State Sciences*, 10(11):1651–1657, 2008.

[47] S. Terada, H. Tanaka, and K. Kubota. Heteroepitaxial growth of Cu_3N thin films. *Journal of Crystal Growth*, 94(2):567 – 568, 1989.

[48] Jian-Ning Ding, Ning-Yi Yuan, Feng Li, Gu-Qiao Ding, Zhi-Gang Chen, Xiao-Shuang Chen, , and Wei Lu. Geometry and Stability of $Cu_{(}n)N$ (n=1-6) and $Cu_{(}3n)N_{(}n)$ (n=1-5) Clusters. *Journal of Chemical Physics*, 131(17):174102, 2009.

[49] G.H. Yue, P.X. Yan, and J. Wang. Study on the preparation and properties of copper nitride thin films. *Journal of Crystal Growth*, 274(34):464 – 468, 2005.

[50] G Soto, J.A Daz, and W de la Cruz. Copper nitride films produced by reactive pulsed laser deposition. *Materials Letters*, 57(2627):4130 – 4133, 2003.

[51] Fakhili Gulo, Arndt Simon, Jrgen Khler, and Reinhard K. Kremer. Li–Cu Exchange in Intercalated Cu_3N – With a Remark on Cu_4N. *Angewandte Chemie International Edition*, 43(15):2032–2034, 2004.

[52] J. Blucher, K. Bang, and B.C. Giessen. Preparation of the metastable interstitial copper nitride, Cu_4N, by d.c. plasma ion nitriding. *Materials Science and Engineering: A*, 117(0):L1–L3, 1989.

[53] Edward S. Shanley and John L. Ennis. The chemistry and free energy of formation of silver nitride. *Industrial & Engineering Chemistry Research*, 30(11):2503–2506, 1991.

[54] Jianwei Tong. *Darstellung, Strukturen und Eigenschaften ausgewählter Perowskit-Materialien und Molekülkristalle*. PhD thesis, Max-Planck-Institut für Festkörperforschung, Stuttgart, 2010.

[55] Harry Hahn and Edmund Gilbert. Silbernitrid. Metallamide und Metallnitride, 19. Mitteilung. *Zeitschrift fr anorganische Chemie*, 258(1-2):77–93, 1949.

[56] R.N. Anderson and N.A.D. Parlee. Standard Free Energy of Nitride Formation from the Elements, an Estimation Technique. *High Temperature Science*, 2:289–292, 1970.

[57] Robert Juza and Harry Hahn. Über die Nitride der Metalle der ersten Nebengruppen des periodischen Systems. Metallamide und Metallnitride. X. Mitteilung. *Zeitschrift fr anorganische und allgemeine Chemie*, 244(2):133–148, 1940.

[58] M. Haisa. The Origin of the Crystallographic Pedigree. *Acta Crystallographica Section A*, 38(4):443–453, Jul 1982.

[59] John L. Ennis and Edward S. Shanley. On hazardous silver compounds. *Journal of Chemical Education*, 68(1):A6, 1991.

[60] L. Šiller, M. R. C. Hunt, J. W. Brown, J-M. Coquel, and P. Rudolf. Nitrogen ion irradiation of Au(110): formation of gold nitride. *Surface Science*, 513(1):78–82, 2002.

[61] L. Alves, T. P. A. Hase, M. R. C. Hunt, A. C. Brieva, and L. Šiller. X-ray diffraction study of gold nitride films: Observation of a solid solution phase. *Journal of Applied Physics*, 104(11):113527, 2008.

[62] L. Šiller, L. Alves, A. C. Brieva, Yu. V. Butenko, and M. R. C. Hunt. Gold Nitride: Preparation and Properties. *Topics in Catalysis*, 52:1604–1610, 2009.

[63] S. Krishnamurthy, M. Montalti, M. G. Wardle, M. J. Shaw, P. R. Briddon, K. Svensson, M. R. C. Hunt, and L. Šiller. Nitrogen ion irradiation of $\mathrm{Au}(110)$: Photoemission spectroscopy and possible crystal structures of gold nitride. *Physical Review B*, 70:045414, Jul 2004.

[64] R. Yu and X. F. Zhang. Family of Noble Metal Nitrides: First Principles Calculations of the Elastic Stability. *Physical Review B*, 72:054103, Aug 2005.

[65] M.B. Kanoun and S. Goumri-Said. Investigation of Structural Stability and Electronic Properties of CuN, AgN and AuN by First Principles Calculations. *Physics Letters A*, 362(1):73–83, 2007.

[66] W. Chen, J.S. Tse, and J.Z. Jiang. An ab initio study of $5d$ noble metal nitrides: OsN_2, IrN_2, PtN_2 and AuN_2. *Solid State Communications*, 150(34):181 – 186, 2010.

[67] J H Quintero, R Ospina, O O Cárdenas, G I Alzate, and A Devia. Electrical properties of AuN thin films. *Physica Scripta*, 2008(T131):014013, 2008.

[68] Yu.V. Butenko, L. Alves, A.C. Brieva, J. Yang, S. Krishnamurthy, and L. Šiller. X-ray induced decomposition of gold nitride. *Chemical Physics Letters*, 430(1–3):89 – 92, 2006.

[69] Robert Juza and Harry Hahn. Über die Kristallstrukturen von Zn_3N_2, Cd_3N_2 und Ge_3N_4. Metallamide und Metallnitride. IX. Mitteilung. *Zeitschrift für anorganische und allgemeine Chemie*, 244(2):125–132, 1940.

[70] Fujian Zong, Honglei Ma, Jin Ma, Wei Du, Xijian Zhang, Hongdi Xiao, Feng Ji, and Chengshan Xue. Structural properties and photoluminescence of zinc nitride nanowires. *Applied Physics Letters*, 87(23):233104, 2005.

[71] H.A. Wriedt. The N–Zn (Nitrogen-Zinc) system. *Bulletin of Alloy Phase Diagrams*, 9:247–251, 1988.

[72] Deligoz Engin, Colakoglu Kemal, and Ciftci Yasemin Oztekin. Ab Initio Study on Hypothetical Silver Nitride. *Chinese Physics Letters*, 25(6):2154, 2008.

[73] P. J. LIN-CHUNG. Energy-band structures of $\mathrm{cd_3as_2}$ and $\mathrm{zn_3as_2}$. *Physical Review*, 188:1272–1280, Dec 1969.

[74] P. A. M. Dirac. Quantum Mechanics of Many-Electron Systems. *Proceedings of the Royal Society of London. Series A, Containing Papers of a Mathematical and Physical Character*, 123(792):pp. 714–733, 1929.

[75] Jorge Kohanoff. *Electronic Structure Calculations for Solids and Molecules : Theory and Computational Methods*. Cambridge University Press; Cambridge, 2006.

[76] Robert G. Parr and Yang Weitao. *Density-Functional Theory of Atoms and Molecules*. Oxford University Press, 1989.

[77] John C. Inkson. *Many-Body Theory of Solids: An Introduction*. Springer, 1984.

[78] Richard M. Martin. *Electronic Structure, Basic Theory and Practical Methods*. Cambridge University Press, 2004.

[79] Efthimios Kaxiras. *Atomic and Electronic Structure of Solids*. Cambridge University Press, 2003.

[80] Wilfried G. Aulbur, Lars Jönsson, and John W. Wilkins. Quasiparticle Calculations in Solids. *Solid State Physics*, 54:1 – 218, 1999.

[81] Max Born and J. Robert Oppenheimer. On the Quantum Theory of Molecules. *Annalen der Physik*, 84:457, 1927.

[82] David J. Griffiths. *Introduction to Quantum Mechanics*. Prentice Hall, Upper Saddle River, NJ, 2nd edition, 2005.

[83] P. Güttinger. Das Verhalten von Atomen im magnetischen Drehfeld. *Zeitschrift für Physik*, 73:169–184, 1932.

[84] Hans Hellmann. *Quantenchemie*. Leipzig, 1937.

[85] Richard P. Feynman. Forces in Molecules. *Physical Review*, 56:340–343, August 1939.

[86] Michael P. Marder. *Condensed Matter Physics*. Wiley-Interscience, 2000.

[87] G. Kresse and J. Furthmüller. Efficiency of ab-initio total energy calculations for metals and semiconductors using a plane-wave basis set. *Computational Materials Science*, 6(1):15 – 50, 1996.

[88] Peter David Haynes. *Linear-scaling methods in ab initio quantum-mechanical calculations*. PhD thesis, Christ's College, Cambridge, 1998.

[89] Neil W. Ashcroft and N. David Mermin. *Solid State Physics*. Brooks Cole, 1976.

[90] Wolfgang Pauli. Ueber den Zusammenhang des Abschlusses der Elektronengruppen im Atom mit der Komplexstruktur der Spektren. *Zeitschrift für Physik*, 31:765–783, 1925.

[91] P. A. M. Dirac. On the Theory of Quantum Mechanics. *Proceedings of the Royal Society of London. Series A*, 112:661–677, October 1926.

[92] W. Heisenberg. Mehrkörperproblem und Resonanz in der Quantenmechanik. *Zeitschrift fr Physik*, 38(6-7):411–426, 1926.

[93] Christian Schilling, David Gross, and Matthias Christandl. Pinning of Fermionic Occupation Numbers. *Physical Review Letters*, 110:040404, Jan 2013.

[94] R. McWeeny. Some Recent Advances in Density Matrix Theory. *Review of Modern Physics*, 32:335–369, April 1960.

[95] Peter E. Blöchl. Theory and Practice of Density-Functional Theory. *ArXiv e-prints*, August 2011.

[96] Daniel P. Joubert. *Applications of Quantum Mechanics (lecture notes)*. School of Physics, University of the Witwatersrand, Johannesburg, South Africa, 2004.

[97] Benjamin Svetitsky. Notes on Functionals. Available on-line at http://julian.tau.ac.il/bqs/functionals/functionals.html; last accessed December 2012., December 1998. Available on-line at http://julian.tau.ac.il/bqs/functionals/functionals.html. Last accessed December 2012.

[98] D. R. Hartree. The Wave Mechanics of an Atom with a Non-Coulomb Central Field. Part I. Theory and Methods. *Mathematical Proceedings of the Cambridge Philosophical Society*, 24(01):89–110, 1928.

[99] J. C. Slater. The Self Consistent Field and the Structure of Atoms. *Physical Review*, 32:339–348, Sep 1928.

[100] V. Fock. Näherungsmethode zur Lösung des quantenmechanischen Mehrkörperproblems. *Zeitschrift fr Physik A Hadrons and Nuclei*, 61:126–148, 1930.

[101] J. C. Slater. A Simplification of the Hartree-Fock Method. *Physical Review*, 81:385–390, Feb 1951.

[102] O. Gunnarsson and B. I. Lundqvist. Exchange and correlation in atoms, molecules, and solids by the spin-density-functional formalism. *Physical Review B*, 13:4274–4298, May 1976.

[103] P. Ravindran, Lars Fast, P. A. Korzhavyi, B. Johansson, J. Wills, and O. Eriksson. Density functional theory for calculation of elastic properties of orthorhombic crystals: Application to TiSi[sub 2]. *Journal of Applied Physics*, 84(9):4891–4904, 1998.

[104] Mihai V. Putz. Density Functionals of Chemical Bonding. *International Journal of Molecular Sciences*, 9(6):1050–1095, 2008.

[105] John E. Klepeis. Introduction to First-Principles Electronic Structure Methods: Application to Actinide Materials. *Journal of Materials Research*, 21:2979–2985, 2006.

[106] P. Hohenberg and W. Kohn. Inhomogeneous Electron Gas. *Physical Review*, 136:B864–B871, November 1964.

[107] W. Kohn and L. J. Sham. Self-Consistent Equations Including Exchange and Correlation Effects. *Physical Review*, 140:A1133–A1138, November 1965.

[108] E.K.U. Gross and R.M. Dreizler, editors. *Density Functional Theory*. NATO ASI Series: Physics. Plenum Press, 1995.

[109] C. Fiolhais, F. Nogueira, and M. Marques, editors. *A Primer in Density Functional Theory*. Lecture Notes in Physics. Springer, 2003.

[110] Lars Hedin. New Method for Calculating the One-Particle Green's Function with Application to the Electron-Gas Problem. *Physical Review*, 139:A796–A823, Aug 1965.

[111] Paola Gori-Giorgi and Andreas Savin. Study of the discontinuity of the exchange-correlation potential in an exactly soluble case. *International Journal of Quantum Chemistry*, 109(11):2410–2415, 2009.

[112] John P. Perdew, Adrienn Ruzsinszky, Jianmin Tao, Viktor N. Staroverov, Gustavo E. Scuseria, and Gabor I. Csonka. Prescription for the design and selection of density functional approximations: More constraint satisfaction with fewer fits. *The Journal of Chemical Physics*, 123(6):062201, 2005.

[113] I V Solovyev. Combining DFT and many-body methods to understand correlated materials. *Journal of Physics: Condensed Matter*, 20(29):293201, 2008.

[114] L. H. Thomas. The calculation of atomic fields. *Mathematical Proceedings of the Cambridge Philosophical Society*, 23:542–548, January 1927.

[115] Enrico Fermi. Un Metodo Statistico per la Determinazione di alcune Prioprietá dell'Atomo. *Accademia Nazionale dei Lincei*, 6:602–607, 1927.

[116] P. A. M. Dirac. Note on Exchange Phenomena in the Thomas Atom. *Mathematical Proceedings of the Cambridge Philosophical Society*, 26:376–385, July 1930.

[117] Walter Kohn. Fundamentals of Density Functional Theory. In Daniel Joubert, editor, *Density Functionals: Theory and Applications: Proceedings of the Tenth Chris Engelbrecht Summer School in Theoretical Physics Held at Meerensee, near Cape Town, 19-29 January 1997 (Lecture Notes in Physics)*, pages 1–7. Springer, 2002.

[118] Mel Levy. Electron densities in search of Hamiltonians. *Physical Review A*, 26:1200–1208, Sep 1982.

[119] Elliott H. Lieb. Density Functionals for Coulomb Systems. In A. Shimony and H. Feshbach, editors, *Physics As Natural Philosophy: Essays in Honor of Laszlo Tisza on his 75th Birthday*, pages 111–149. Mit Press, 1982.

[120] Elliott H. Lieb. Density functionals for coulomb systems. *International Journal of Quantum Chemistry*, 24(3):243–277, 1983.

[121] Ken F. Riley, Michael P. Hobson, and Stephen J. Bence. *Mathimatical Methods for Physics and Engineering*. Cambridge University Press, 2006.

[122] Stefan Kurth, John P. Perdew, and Peter Blaha. Molecular and solid-state tests of density functional approximations: LSD, GGAs, and meta-GGAs. *International Journal of Quantum Chemistry*, 75(4-5):889–909, 1999.

[123] John P. Perdew, Adrienn Ruzsinszky, Lucian A. Constantin, Jianwei Sun, and Gábor I. Csonka. Some Fundamental Issues in Ground-State Density Functional Theory: A Guide for the Perplexed. *Journal of Chemical Theory and Computation*, 5(4):902–908, 2009.

[124] Tomás A. Arias. Notes on the *ab initio* theory of molecules and solids: Density functional theory (DFT), January 2004. Available on-line at `http://people.ccmr.cornell.edu/~muchomas/P480/Notes/dft/dft.html`. Last accessed February 2013.

[125] U von Barth and L Hedin. A local exchange-correlation potential for the spin polarized case. i. *Journal of Physics C: Solid State Physics*, 5(13):1629, 1972.

[126] Klaus Capelle. A bird's-eye view of density-functional theory. *Brazilian Journal of Physics*, 36:1318 – 1343, 12 2006.

[127] David S. Sholl and Janice A. Steckel. *Density Functional Theory: A Practical Introduction*. John Wiley and Sons, Inc., 2009.

[128] Jürgen Hafner. Ab-initio simulations of materials using VASP: Density-functional theory and beyond. *Journal of Computational Chemistry*, 29(13):2044–2078, 2008.

[129] Peter E. Blöchl, O. Jepsen, and O. K. Andersen. Improved tetrahedron method for Brillouin-zone integrations. *Physical Review B*, 49:16223–16233, June 1994.

[130] Hendrik J. Monkhorst and James D. Pack. Special points for Brillouin-zone integrations. *Physical Review B*, 13:5188–5192, Jun 1976.

[131] O. Jepson and O.K. Anderson. The electronic structure of h.c.p. Ytterbium. *Solid State Communications*, 9(20):1763 – 1767, 1971.

[132] G. Lehmann and M. Taut. On the Numerical Calculation of the Density of States and Related Properties. *physica status solidi (b)*, 54(2):469–477, 1972.

[133] M. Methfessel and A. T. Paxton. High-precision sampling for Brillouin-zone integration in metals. *Physical Review B*, 40:3616–3621, Aug 1989.

[134] John P. Perdew and Stefan Kurth. Chapter 1: Density Functionals for Non-relativistic Coulomb Systems in the New Century. In C. Fiolhais, F. Nogueira, and M. Marques, editors, *A Primer in Density Functional Theory*, Lecture Notes in Physics. Springer, 2003.

[135] Viktor N. Staroverov, Gustavo E. Scuseria, Jianmin Tao, and John P. Perdew. Tests of a ladder of density functionals for bulk solids and surfaces. *Physical Review B*, 69:075102, Feb 2004.

[136] John P. Perdew, J. A. Chevary, S. H. Vosko, Koblar A. Jackson, Mark R. Pederson, D. J. Singh, and Carlos Fiolhais. Atoms, molecules, solids, and surfaces: Applications of the generalized gradient approximation for exchange and correlation. *Physical Review B*, 46:6671–6687, Sep 1992.

[137] In-Ho Lee and Richard M. Martin. Applications of the generalized-gradient approximation to atoms, clusters, and solids. *Physical Review B*, 56:7197–7205, Sep 1997.

[138] Matthias Ernzerhof and Gustavo E. Scuseria. Assessment of the Perdew–Burke–Ernzerhof exchange-correlation functional. *The Journal of Chemical Physics*, 110(11):5029 – 5036, 1999.

[139] John P. Perdew, Kieron Burke, and Matthias Ernzerhof. Generalized Gradient Approximation Made Simple. *Physical Review Letters*, 77:3865–3868, Oct 1996.

[140] John P. Perdew, Kieron Burke, and Matthias Ernzerhof. Generalized Gradient Approximation Made Simple [Phys. Rev. Lett. 77, 3865 (1996)]. *Physical Review Letters*, 78:1396–1396, Feb 1997.

[141] Elliott H. Lieb and Stephen Oxford. Improved lower bound on the indirect coulomb energy. *International Journal of Quantum Chemistry*, 19(3):427–439, 1981.

[142] Conyers Herring. A New Method for Calculating Wave Functions in Crystals. *Physical Review*, 57:1169–1177, June 1940.

[143] P. E. Blöchl. Projector Augmented-Wave Method. *Physical Review B*, 50:17953–17979, Dec 1994.

[144] Georg Kresse and Daniel P. Joubert. From Ultrasoft Pseudopotentials to the Projector Augmented-Wave Method. *Physical Review B*, 59:1758–1775, Jan 1999.

[145] Carsten Rostgaard. The Projector Augmented-wave Method. *ArXiv e-prints*, October 2009.

[146] P. A. M. Dirac. The Quantum Theory of the Electron. *Proceedings of the Royal Society of London. Series A*, 117(778):610–624, 1928.

[147] D D Koelling and B N Harmon. A technique for relativistic spin-polarised calculations. *Journal of Physics C: Solid State Physics*, 10(16):3107, 1977.

[148] K. Schwarz. Chapter 2.2: Electrons. In *International Tables for Crystallography, Volume D: Physical Properties of Crystals.*, pages 294 – 313. 2006.

[149] Reiner M. Dreizler and Eberhard Engel. Relativistic Density Functional Theory. In Daniel Joubert, editor, *Density Functionals: Theory and Applications: Proceedings of the Tenth Chris Engelbrecht Summer School in Theoretical Physics Held at Meerensee, near Cape Town, 19-29 January 1997 (Lecture Notes in Physics)*, pages 147–189. Springer, 2002.

[150] M. Shishkin and G. Kresse. Implementation and performance of the frequency-dependent GW method within the PAW framework. *Physical Review B*, 74:035101, Jul 2006.

[151] Michael Rohlfing and Steven G. Louie. Electron-hole excitations and optical spectra from first principles. *Physical Review B*, 62:4927–4944, Aug 2000.

[152] Giovanni Onida, Lucia Reining, and Angel Rubio. Electronic excitations: density-functional versus many-body Green's-function approaches. *Reviews of Modern Physics*, 74:601–659, Jun 2002.

[153] Judith Harl. *The Linear Response Function in Density Functional Theory: Optical Spectra and Improved Description of the Electron Correlation*. PhD thesis, University of Vienna, 2008.

[154] Georg Kresse, Martijn Marsman, and Jürgen Furthmüller. Vasp the guide, 2011. Available on-line at `http://cms.mpi.univie.ac.at/vasp/vasp/`. Last accessed February 2013.

[155] Miquel Llunell, Santiago Alvarez, and Pere Alemany. Skutterudite vs. ReO_3 Structures for MX_3 Solids: Electronic Requirements. *Journal of the Chemical Society, Dalton Transactions*, pages 1195–1200, 1998.

[156] International Union of Pure and Applied Chemistry (IUPAC). Compendium of Chemical Terminology, 2nd ed. (the "Gold Book"). Compiled by A. D. McNaught and A. Wilkinson. Blackwell Scientific Publications, Oxford (1997). XML on-line corrected version: `http://goldbook.iupac.org` (2006-) created by M. Nic, J. Jirat, B. Kosata; updates compiled by A. Jenkins. ISBN 0-9678550-9-8. doi:10.1351/goldbook. Last update: 2012-03-23; version: 2.3.1. DOI of this term: doi:10.1351/goldbook.M03940.

[157] F. Albert Cotton and Geoffrey Wilkinson. *Advanced Inorganic Chemistry, A Comprehensive Text*. J. Wiley, New York, 5th edition, 1988.

[158] Naval Research Laboratory, Centre for Computational Materials Science (CCMS). Crystal Lattice Structures database. Available on-line at http://cst-www.nrl.navy.mil/lattice/.

[159] D. R. Lide, editor. *CRC Handbook of Chemistry and Physics: A Ready-reference Book of Chemical and Physical Data, 2001-2002*. CRC Handbook of Chemistry & Physics. Taylor & Francis Group, 2001.

[160] M. L. Fornasini. Ca_8In_3, a structure related to the BiF_3 type. *Acta Crystallographica Section C*, 43(4):613–616, Apr 1987.

[161] Marc De Graef and Michael E. McHenry. *Structure of materials : An Introduction to Crystallography, Diffraction and Symmetry*. Cambridge University Press, 2007.

[162] R. L. Moss and I. Woodward. The structure of evaporated tungsten films. *Acta Crystallographica*, 12(3):255–256, Mar 1959.

[163] M. V. Nevitt. Chapter 13: Miscellaneous structures of fixed stiochiometry. In J. H. Westbrook, editor, *Intermetallic Compounds*, Wiley series on the science and technology of materials, pages 217–229. John Wiley & Sons, Inc., 1967.

[164] Karl Meisel. Rheniumtrioxyd. III. Mitteilung. Über die Kristallstruktur des Rheniumtrioxyds. *Zeitschrift für anorganische und allgemeine Chemie*, 207(1):121–128, 1932.

[165] T.-S. Chang and P. Trucano. Lattice parameter and thermal expansion of ReO_3 between 291 and 464 K. *Journal of Applied Crystallography*, 11(4):286–288, Aug 1978.

[166] Jan T. Szymanski, Louis J. Cabri, and J. H. Gilles Laflamme. The Crystal Structure and Calculated Powder-Diffraction Data for Zvyagintsevite, Pd_3Pb. *The Canadian Mineralogist*, 35:773 – 776, 1997.

[167] M. L. Bhatia. On the Packing of $AuCu_3$ and Cu_2Mg Structures. *Philosophical Magazine*, 83(19):2293–2300, 2003.

[168] John W. Anthony, Richard A. Bideaux, Kenneth W. Bladh, and Monte C. Nichols, editors. *Handbook of Mineralogy*. Mineralogical Society of America, Chantilly, VA 20151-1110,

USA, 2012. Online version available at http://www.handbookofmineralogy.org/, last accessed December 2012.

[169] H. Jacobs, D. Rechenbach, and U. Zachwieja. Structure determination of γ'-Fe_4N and ϵ-Fe_3N. *Journal of Alloys and Compounds*, 227(1):10 – 17, 1995.

[170] Andreas Leineweber, Herbert Jacobs, and Steve Hull. Ordering of Nitrogen in Nickel Nitride Ni_3N Determined by Neutron Diffraction. *Inorganic Chemistry*, 40(23):5818–5822, 2001.

[171] M. A. Hepworth, K. H. Jack, R. D. Peacock, and G. J. Westland. The Crystal Structures of the Trifluorides of Iron, Cobalt, Ruthenium, Rhodium, Palladium and Iridium. *Acta Crystallographica*, 10(1):63–69, Jan 1957.

[172] C. Kittel. *Introduction to Solid State Physics*. John Wiley & Sons, Inc., eigth edition, 2005.

[173] Theo Hahn, editor. *International Tables for Crystallography*, volume A: Space-Group Symmetry. Reidel Publishing, Dordrecht, 5th edition, 2005.

[174] N. Gonzalez Szwacki and T. Szwacka. *Basic Elements of Crystallography*. Pan Stanford Publishing Pte. Ltd., 2010.

[175] Nils and Schnberg. The tungsten carbide and nickel arsenide structures. *Acta Metallurgica*, 2(3):427 – 432, 1954.

[176] Ambarish J. Kulkarni, Min Zhou, Kanoknan Sarasamak, and Sukit Limpijumnong. Novel Phase Transformation in ZnO Nanowires under Tensile Loading. *Physical Review Letters*, 97:105502, Sep 2006.

[177] E. H. Kisi and M. M. Elcombe. *u* parameters for the wurtzite structure of ZnS and ZnO using powder neutron diffraction. *Acta Crystallographica Section C*, 45(12):1867–1870, Dec 1989.

[178] S. K. R. Patil, S. V. Khare, B. R. Tuttle, J. K. Bording, and S. Kodambaka. Mechanical stability of possible structures of PtN investigated using first-principles calculations. *Physical Review B*, 73:104118, Mar 2006.

[179] Louis J. Cabri, J. H. Gilles Laflamme, John M. Stewart, Kent Turner, and Brian J. Skinner. On cooperite, braggite, and vysotskite. *American Mineralogist*, 63:832 – 839, 1978.

[180] P. Berastegui and S. Hull. The Crystal Structures of Thallium(I) Fluoride. *Journal of Solid State Chemistry*, 150(2):266 – 275, 2000.

[181] Mario Birkholz. The crystal energy of pyrite. *Journal of Physics: Condensed Matter*, 4(29):6227, 1992.

[182] Gunnar Brostigen and Arne Kjekshus. On the Relationships between the Structure Types Pyrite, Marcasite, and Arsenopyrite. *Acta Chemica Scandinavica*, 24:2983 – 2992, 1970.

[183] Bruce Hyde and Michael O'keeffe. Marcasite and Pyrite (FeS_2). *Australian Journal of Chemistry*, 49(8):867 – 872, 1996.

[184] Arne Kjekshus. On the Properties of Binary Compounds with the $CoSb_2$ Type Crystal Structure. *Acta Chemica Scandinavica*, 25:411–422, 1971.

[185] Richard J. D. Tilley. *Crystals and Crystal Structures*. John Wiley and Sons Ltd., England, 2006.

[186] R.C. Evans. *An Introduction to Crystal Chemistry*. Cambridge University Press, 2 edition, 1964.

[187] Ma. Guadalupe Moreno-Armenta, William López Pórez, and Noboru Takeuchi. First-principles calculations of the structural and electronic properties of Cu_3MN compounds with M = Ni, Cu, Zn, Pd, Ag, and Cd. *Solid State Sciences*, 9(2):166–172, 2007.

[188] Wen Yu, Linyan Li, and Changqing Jin. Pressure Induced Metallization of Cu_3N. *Journal of Materials Science*, 40:4661–4664, 2005. 10.1007/s10853-005-0638-3.

[189] Hisashi Shimizu, Masafumi Shirai, and Naoshi Suzuki. Electronic, Structural and Magnetic Properties of Transition-Metal Mononitrides. *Journal of the Physical Society of Japan*, 66(10):3147–3152, 1997.

[190] William Burton Pearson. *Handbook of Lattice Spacings & Structures of Metals & Alloys (International Series of Monographs on Metals Physics & Physical Metallurgy)*. Franklin Book Co, 1964.

[191] J. Häglund, G. Grimvall, T. Jarlborg, and A. Fernández Guillermet. Band Structure and Cohesive Properties of 3*d*-Transition-Metal Carbides and Nitrides with the NaCl-type Structure. *Physical Review B*, 43:14400–14408, Jun 1991.

[192] Wang Hong-Bo and Xue De-Sheng. Electronic Structures and Magnetic Properties of CoN, NiN and CuN. *Chinese Physics Letters*, 21(8):1612–1615, 2004.

[193] E. Deligoz, K. Colakoglu, and Y. O. Ciftci. Electronic and mechanical properties of the PdN: A first-principles study. *physica status solidi (b)*, 247(9):2155–2160, 2010.

[194] L.H. Yu, K.L. Yao, Z.L. Liu, and Y.S. Zhang. Structural property of platinum mononitride. *Physica B: Condensed Matter*, 399(1):50 – 54, 2007.

[195] K. Suzuki, H. Morita, T. Kaneko, H. Yoshida, and H. Fujimori. Crystal Structure and Magnetic Properties of the Compound FeN. *Journal of Alloys and Compounds*, 201(12):11 – 16, 1993.

[196] K. Suzuki, T. Kaneko, H. Yoshida, H. Morita, and H. Fujimori. Crystal Structure and Magnetic Properties of the Compound CoN. *Journal of Alloys and Compounds*, 224(2):232 – 236, 1995.

[197] R. Yu, Q. Zhan, and X. F. Zhang. Elastic stability and electronic structure of pyrite type PtN_2: A hard semiconductor. *Applied Physics Letters*, 88(5):051913, 2006.

[198] Alexandra Friedrich, Björn Winkler, Erick A. Juarez-Arellano, and Lkhamsuren Bayarjargal. Synthesis of Binary Transition Metal Nitrides, Carbides and Borides from the Elements in the Laser-Heated Diamond Anvil Cell and Their Structure-Property Relations. *Materials*, 4(10):1648–1692, 2011.

[199] G. Kresse and J. Hafner. *Ab initio* molecular dynamics for liquid metals. *Physical Review B*, 47:558–561, Jan 1993.

[200] G. Kresse and J. Hafner. *Ab initio* molecular-dynamics simulation of the liquid-metal–amorphous-semiconductor transition in germanium. *Physical Review B*, 49:14251–14269, May 1994.

[201] Georg Kresse and J. Furthmüller. Efficient Iterative Schemes for *ab initio* Total-Energy Calculations Using a Plane-Wave Basis Set. *Physical Review B*, 54:11169–11186, Oct 1996.

[202] Andrew M. Rappe, Karin M. Rabe, Efthimios Kaxiras, and J. D. Joannopoulos. Optimized pseudopotentials. *Physical Review B*, 41:1227–1230, Jan 1990.

[203] Christopher John Bradley and Arthur Philip Cracknell. *The Mathematical Theory of Symmetry in Solids: Representation Theory for Point Groups and Space Groups*. Clarendon Press, 1972.

[204] Kurt Lejaeghere, Veronique Van Speybroeck, Guido Van Oost, and Stefaan Cottenier. Error bars for solid-state density-functional theory predictions: an overview by means of the ground-state elemental crystals. August 2012.

[205] Michael P. Teter, Michael C. Payne, and Douglas C. Allan. Solution of Schrödinger's equation for large systems. *Physical Review B*, 40:12255–12263, Dec 1989.

[206] D. M. Bylander, Leonard Kleinman, and Seongbok Lee. Self-consistent calculations of the energy bands and bonding properties of $B_{12}C_3$. *Physical Review B*, 42:1394–1403, Jul 1990.

[207] Ernest R. Davidson. The iterative calculation of a few of the lowest eigenvalues and corresponding eigenvectors of large real-symmetric matrices. *Journal of Computational Physics*, 17(1):87 – 94, 1975.

[208] D M Wood and A Zunger. A new method for diagonalising large matrices. *Journal of Physics A: Mathematical and General*, 18(9):1343, 1985.

[209] Péter Pulay. Convergence Acceleration of Iterative Sequences - the Case of Scf Iteration. *Chemical Physics Letters*, 73:393–398., 1980.

[210] D. D. Johnson. Modified Broyden's method for accelerating convergence in self-consistent calculations. *Physical Review B*, 38:12807–12813, Dec 1988.

[211] M. T. Yin and Marvin L. Cohen. Theory of static structural properties, crystal stability,and phase transformations: Application to Si and Ge. *Physical Review B*, 26:5668–5687, November 1982.

[212] Walter A. Harrison. *Electronic Structure and the Properties of Solids: The Physics of the Chemical Bond*. W H Freeman & Co (Sd), 1980.

[213] G. Grimvall. *Thermophysical Properties of Materials*. Elsevier Science, 1999.

[214] Amitava Banerjea and John R. Smith. Origins of the universal binding-energy relation. *Physical Review B*, 37:6632–6645, April 1988.

[215] G. Soto. Study on the formation and the decomposition of AgN_3 and a hypothetical compound ReN_3 by using density functional calculations. *ArXiv e-prints*, November 2012.

[216] P. H. T. Philipsen and E. J. Baerends. Cohesive energy of 3*d* transition metals: Density functional theory atomic and bulk calculations. *Physical Review B*, 54:5326–5333, Aug 1996.

[217] Y. Mishin, D. Farkas, M. J. Mehl, and D. A. Papaconstantopoulos. Interatomic Potentials for Monoatomic Metals from Experimental Data and *ab initio* Calculations. *Physical Review B*, 59:3393–3407, Feb 1999.

[218] M. Fuchs, J. L. F. Da Silva, C. Stampfl, J. Neugebauer, and M. Scheffler. Cohesive properties of group-III nitrides: A comparative study of all-electron and pseudopotential calculations using the generalized gradient approximation. *Physical Review B*, 65:245212, Jun 2002.

[219] S. Raju, E. Mohandas, and V.S. Raghunathan. The pressure derivative of bulk modulus of transition metals: An estimation using the method of model potentials and a study of the systematics. *Journal of Physics and Chemistry of Solids*, 58(9):1367 – 1373, 1997.

[220] Francis Birch. Finite Elastic Strain of Cubic Crystals. *Physical Review*, 71:809–824, Jun 1947.

[221] J. K. Dewhurst. EOS version 1.2, August 2005. Equation of State (EOS) program for fitting energy-volume data (`http://elk.sourceforge.net`, `http://exciting.sourceforge.net`).

[222] F. D. Murnaghan. The Compressibility of Media under Extreme Pressures. *Proceedings of the National Academy of Sciences*, 30(9):244–247, 1944.

[223] Marcus Frederick Charles Ladd. *Introduction to Physical Chemistry*. Cambridge University Press, 1998.

[224] Na Wang, Wei-Yang Yu, Bi-Yu Tang, Li-Ming Peng, and Wen-Jiang Ding. Structural and mechanical properties of $Mg_{17}Al_{12}$ and $Mg_{24}Y_5$ from first-principles calculations. *Journal of Physics D: Applied Physics*, 41(19):195408, 2008.

[225] C. Stampfl and A. J. Freeman. Metallic to insulating nature of TaN_x : Role of Ta and N vacancies. *Physical Review B*, 67:064108, Feb 2003.

[226] Peter Atkins and Julio De Paula. *Atkins' Physical Chemistry*. Oxford University Press, 2009.

[227] Ralph Walter Graystone Wyckoff. *The Structure of Crystals*. The Chemical Catalog Co., New York, 1935.

[228] Xiuwen Zhang, Giancarlo Trimarchi, and Alex Zunger. Possible pitfalls in theoretical determination of ground-state crystal structures: The case of platinum nitride. *Physical Review B*, 79:092102, March 2009.

[229] Wai-Yim Ching and Paul Rulis. *Electronic Structure Methods for Complex Materials: The orthogonalized linear combination of atomic orbitals*. Oxford University Press, 2012.

[230] Stephen R. Elliott. *The Physics and Chemistry of Solids*. John Wiley & Sons, 1998.

[231] M. Gajdoš, K. Hummer, G. Kresse, J. Furthmüller, and F. Bechstedt. Linear Optical Properties in the Projector-Augmented Wave Methodology. *Physical Review B*, 73:045112, Jan 2006.

[232] H. Ehrenreich and M. H. Cohen. Self-Consistent Field Approach to the Many-Electron Problem. *Physical Review*, 115:786–790, Aug 1959.

[233] Stephen L. Adler. Quantum Theory of the Dielectric Constant in Real Solids. *Physical Review*, 126:413–420, Apr 1962.

[234] Stefano Baroni and Raffaele Resta. *Ab initio* calculation of the macroscopic dielectric constant in silicon. *Physical Review B*, 33:7017–7021, May 1986.

[235] Nathan Wiser. Dielectric Constant with Local Field Effects Included. *Physical Review*, 129:62–69, Jan 1963.

[236] David Pines. *Elementary Excitations in Solids*. Advanced Book Classics. Perseus Books Publishing, 1999.

[237] H. Ibach and H. Lüth. *Solid-State Physics: An Introduction to Principles of Materials Science ; with 100 Problems*. Advanced texts in physics. Springer, 2003.

[238] F Aryasetiawan and O Gunnarsson. The GW method. *Reports on Progress in Physics*, 61(3):237, 1998.

[239] L. E. Sutton, editor. *Tables of interatomic distances and configuration in molecules and ions*. The Chemical Society, London, UK, 1958.

[240] Jerry Donohue. *The structures of the elements*. A Wiley-interscience publication. John Wiley & Sons Inc., 1974.

[241] Michael J. Mehl and Dimitrios A. Papaconstantopoulos. Applications of a tight-binding total-energy method for transition and noble metals: Elastic constants, vacancies, and surfaces of monatomic metals. *Physical Review B*, 54:4519–4530, Aug 1996.

[242] E.Yu. Zarechnaya, N.V. Skorodumova, S.I. Simak, B. Johansson, and E.I. Isaev. Theoretical study of linear monoatomic nanowires, dimer and bulk of Cu, Ag, Au, Ni, Pd and Pt. *Computational Materials Science*, 43(3):522 – 530, 2008.

[243] W Chen, J S Tse, and J Z Jiang. Stability, Elastic and Electronic Properties of Palladium Nitride. *Journal of Physics: Condensed Matter*, 22(1):015404, 2010.

[244] Zhao Wen-Jie and Wang Yuan-Xu. Elastic Stability and Electronic Structure of Low Energy Tetragonal and Monoclinic PdN_2 and PtN_2. *Chinese Physics B*, 18(9):3934, 2009.

[245] Daniel Åberg, Paul Erhart, Jonathan Crowhurst, Joseph M. Zaug, Alexander F. Goncharov, and Babak Sadigh. Pressure-induced phase transition in the electronic structure of palladium nitride. *Physical Review B*, 82:104116, Sep 2010.

[246] Agnès Dewaele, Paul Loubeyre, and Mohamed Mezouar. Equations of state of six metals above 94 GPa. *Phys. Rev. B*, 70:094112, Sep 2004.

[247] Zhigang Wu and R. E. Cohen. More accurate generalized gradient approximation for solids. *Physical Review B*, 73:235116, Jun 2006.

[248] David A. Young. *Phase Diagrams of the Elements*. University of California Press, 1991.

[249] M. Sigalas, D. A. Papaconstantopoulos, and N. C. Bacalis. Total energy and band structure of the 3*d*, 4*d*, and 5*d* metals. *Physical Review B*, 45:5777–5783, Mar 1992.

[250] Jianrong Xiao, Yanwei Li, and Aihua Jiang. Structure, Optical Property and Thermal Stability of Copper Nitride Films Prepared by Reactive Radio Frequency Magnetron Sputtering. *Journal of Materials Science & Technology*, 27(5):403 – 407, 2011.

[251] Jian Gang Niu, Wei Gao, Xiao Ping Dong, Li Guan, and Fei Xie. First Principles Calculations of Optical Properties of Cu_3N and Cu_4N. *Advanced Materials Research (Volumes 150–151)*, Advances in Composites:1290–1293, October 2010.

[252] Toshiro Maruyama and Tomonor Morishita. Copper Nitride Thin Films Prepared by Radio-Frequency Reactive Sputtering. *Journal of Applied Physics*, 78(6):4104–4107, 1995.

[253] Leon Maya. Deposition of Crystalline Binary Nitride Films of Tin, Copper, and Nickel by Reactive Sputtering. *Journal of Vacuum Science & Technology A*, 11:604–608, May 1993.

[254] Nawel Kanoun-Bouayed, Mohammed BenaliKanoun, and Souraya Goumri-Said. Structural Stability, Elastic Constants, Bonding Characteristics and Thermal Properties of Zincblende, Rocksalt and Fluorite Phases in Copper Nitrides: Plane-Wave Pseudo-Potential *ab initio* Calculations. *Central European Journal of Physics*, 9:205–212, 2011. 10.2478/s11534-010-0063-3.

[255] Javier A. Montoya, Alexander D. Hernandez, Chrystele Sanloup, Eugene Gregoryanz, and Sandro Scandolo. OsN_2: Crystal structure and electronic properties. *Applied Physics Letters*, 90(1):011909, 2007.

[256] C. Stampfl and C. G. Van de Walle. Density-functional calculations for III-V nitrides using the local-density approximation and the generalized gradient approximation. *Physical Review B*, 59:5521–5535, Feb 1999.

[257] Shobhana Narasimhan and Stefano de Gironcoli. *Ab initio* calculation of the thermal properties of Cu: Performance of the LDA and GGA. *Physical Review B*, 65:064302, Jan 2002.

[258] Blazej Grabowski, Tilmann Hickel, and Jörg Neugebauer. *ab initio*study of the thermodynamic properties of nonmagnetic elementary fcc metals: exchange-correlation-related error bars and chemical trends. *Phys. Rev. B*, 76:024309, Jul 2007.

[259] Axel D. Becke. Density-functional thermochemistry. III. The role of exact exchange. *The Journal of Chemical Physics*, 98(7):5648–5652, 1993.

[260] Konstantin N. Kudin, Gustavo E. Scuseria, and Richard L. Martin. Hybrid Density-Functional Theory and the Insulating Gap of UO_2. *Phys. Rev. Lett.*, 89:266402, Dec 2002.

[261] Edward N. Brothers, Artur F. Izmaylov, Jacques O. Normand, Veronica Barone, and Gustavo E. Scuseria. Accurate solid-state band gaps via screened hybrid electronic structure calculations. *The Journal of Chemical Physics*, 129(1):011102, 2008.

[262] Wei-Guo Yin, Dmitri Volja, and Wei Ku. Orbital Ordering in $LaMnO_3$: Electron-Electron versus Electron-Lattice Interactions. *Physical Review Letters*, 96:116405, Mar 2006.

[263] C. Franchini, R. Kovacik, M. Marsman, S. Sathyanarayana Murthy, J. He, C. Ederer, and G. Kresse. Maximally localized wannier functions in $LaMnO_3$ within PBE+U, hybrid functionals, and partially self-consistent GW: an efficient route to construct ab-initio tight-binding parameters for eg perovskites. May 2012.

[264] A. Gordienko and Yu. Zhuravlev. *ab initio* calculations of structural, elastic, and electronic properties of silver nitrides. *Journal of Structural Chemistry*, 51:401–408, 2010.

[265] R. de Paiva, R. A. Nogueira, and J. L. A. Alves. Atomic and electronic structures of $4d$ transition-metal nitrides. *Physical Review B*, 75:085105, Feb 2007.

[266] Nicola Gaston, Dirk Andrae, Beate Paulus, Ulrich Wedig, and Martin Jansen. Understanding the hcp anisotropy in Cd and Zn: the role of electron correlation in determining the potential energy surface. *Physical Chemistry Chemical Physics*, 12:681–687, 2010.

[267] Kazuaki Toyoura, Hiroyuki Tsujimura, Takuya Goto, Kan Hachiya, Rika Hagiwara, and Yasuhiko Ito. Optical properties of zinc nitride formed by molten salt electrochemical process. *Thin Solid Films*, 492(1–2):88 – 92, 2005.

[268] K. Kuriyama, Yukimi Takahashi, and F. Sunohara. Optical band gap of Zn_3N_2 films. *Physical Review B*, 48:2781–2782, Jul 1993.

[269] Felix Bloch. Über die Quantenmechanik der Elektronen in Kristallgittern. *Zeitschrift für Physik*, 52:555–600, 1929.

[270] Dan Wei. *Solid State Physics*. Cengage Learning Asia, 2008.

[271] Martin Dressel and George Grüner. *Electrodynamics of solids : optical properties of electrons in matter*. Cambridge University Press, Cambridge New York, 2002.

[272] David J. Griffiths. *Introduction to Electrodynamics*. Prentice Hall, Upper Saddle River, NJ, 3rd edition, 1999.

[273] Amnon Yariv and Pochi Yeh. *Optical Waves in Crystals: Propagation and Control of Laser Radiation*. Wiley Classics Library. John Wiley & Sons, 1984.

Acknowledgements

"WHO DOES NOT THANK PEOPLE WILL NEVER THANK **ALLAH**"

First of all, I thank Allah, the Beneficent, the Merciful; the Owner of the Day of Judgment, thee alone I worship; thee alone I ask for help. In the name of Him I started this work. I thank Him - the true god, the One Who is Besought of all, the One Who needing none; the One Who neither begot anyone, nor was He begotten, and equal to Him has never been anyone - I thank Him for the uncountable granted blessings and for the help in completion of this work.

Thanks to my supervisor, Professor Daniel P. Joubert, who has offered me the best support I could wish for. I am indeed indebted to the guidance and encouragement I received from him. He very patiently provided me with adequate materials and encouraged me to go a head with this work in spite of many setbacks. I would like to say *baie dankie* for sharing your knowledge of physics! Moreover, heartiest congratulations on your latest honor!

I am at loss when I think of expressing my sincere gratitude to Dr Mahlaga Molepo who helped me in this work right from the begining. He listened to my problems and helped me to get closer to the solutions. He read most of my thesis, all the listed manuscripts and helped to decrease the number of errors. I also appreciate being helped, in the early stage of my DFT-VASP calculations of this work, by Dr Kris T Delaney and Ms Sinead Griffin (ASESMA 2010 tutors). Their help was priceless.

I extend my warm thanks to all my mates at the School of Physics. Special thanks to Ross McIntosh, Abd ElLateef Abbas (from SUST) and Jonah Kurian for their carefull reading of Chapter 2. In fact, the Scottish red pen of Mr Ross McIntosh has always been there correcting the language! Thanks are due to Dr Badr A. Mohammed for his critical reading of the manuscript of Appendix D and for teaching me group theory. I would like also to thank George S. Manyali for his assistance with XCrySDen, and more. Special thanks to Dr Mustafa A. A. Ahmed, from the TU Dortmund University, for assistance with German language and for correcting the typos in the e-prints.

I want to acknowledge the financial support I received from the University of the Witwatersrand (Wits), African Institute for Mathematucal Sciences (AIMS) and the German Academic Exchange Service (DAAD), Sudan University of Science and Technology (SUST), Ministry of Higher Education and Scientific Research in Sudan, Centre for High Performance Computing (CHPC) in Cape Town, ASESMA group and the Abdus Salam International Center for Theoretical Physics (ICTP), Center for Atomic-scale Materials Design (CAMD) at the DTU Department of Physics, Fritz Haber Institute of the Max Planck Society (FHI), and the Centre Européen de Calcul Atomique et Moléculaire (CECAM).

I will be failing if I do not express my profound gratitude to all brothers at the Wits *Musalla*. Without their *duaa* and enthusiasm my work would have been much heavier! I am grateful for all the support from the Sudanese people in Gauteng; in particular AlAmeen Shabashah for his assistance in various forms at various times during these four years. Special thanks to Mr Anas AbdAlWahhab for taking care of my managmental issues at SUST while away.

أتقدّمُ بأسمى ءايات الشّكر والامتنان والتقدير والمحبّة، إلى ينبوع الصّبر والتّفاؤل والأمل، إلى من كان دعاؤها سرّ نجاحي .. الوالدة الغالية .. اللّهَ أسأل بمنّه وكرمه أن يمتّعنا بوجودك عمراً مديداً في عافية وعمل صالح.

إلى الوجوه المفعمة بالبراءة، و لمحتّها أزهرت أيّامي وتفتّحت براعمُ لِلْغَد .. إلى أزهار النّرجس الّتي تفيض حبّاً وطفولةً ونقاءاً وعطراً .. أبنائي: تفاؤل، ترتيل و خطّاب. ها هي ثمرة صبركم .. فكم كانت تتردّد على ألسنتكم: «أبي.. متى تنتهي من هذا العمل، وتفرغ لنا؟!» اللّهَ أسألُ أن يحفظكم و يوفّقكم. إلى زوجتي: أمّ خطّاب، صبرها السّنين و دعائها .. جزاك اللّه خيراً ..

إلى إخواني: أبي حمزة، أمّ محمّد و أمّ عبد العزيز .. أشكر لهم تشجعيهم، دعمَهم و دعائهم..

إلى أهلي ورحمي ومعيني و نخوتي .. إلى كل من أحبّني في اللّه وأحببته فيه .. أشكر لكم وقوفكم بجانبي و أشكر لكم دعواتكم ..

إلى كلّ مَن علّمني حرفاً ..

إليكم جميعاً: ها هو نتاج غرسكم لعلّه أثمر و أينع .. فأنتم تقطفونه، و هو أحقّ لكم به من نفسي ...

Mohammed S. H. Suleiman

★★★★★★★★★★★★★★★★★★★